UC Riverside

UC Riverside Electronic Theses and Dissertations

Title

Nonequilibrium Effects in Strongly Driven Correlated Systems

Permalink

https://escholarship.org/uc/item/1sv44142

Author

Hamilton, Kathleen

Publication Date

2014

Peer reviewed|Thesis/dissertation

eScholarship.org Powered by the California Digital Library
University of California

UNIVERSITY OF CALIFORNIA
RIVERSIDE

Nonequilibrium Effects in Strongly Driven Correlated Systems

A Dissertation submitted in partial satisfaction
of the requirements for the degree of

Doctor of Philosophy

in

Physics

by

Kathleen Elizabeth Hamilton

December 2014

Dissertation Committee:

Dr. Leonid P. Pryadko, Chairperson
Dr. Kiril Shtengel
Dr. Vivek Aji

Copyright by
Kathleen Elizabeth Hamilton
2014

The Dissertation of Kathleen Elizabeth Hamilton is approved:

Committee Chairperson

University of California, Riverside

Acknowledgments

I am grateful to my advisor, Dr. Leonid Pryadko, without whose help, I would not have been here. Also many thanks to the post-doctoral scholars Dr. Alexey Kovalev and Dr. Amrit De for their help and advice.

The work in this dissertation was made possible by funding from:

- The work in Chapter 5 was supported in part by the U.S. Army Research Office Grant No. W911NF-11-1-0027, and by the NSF Grant No. 1018935.
- The work discussed in Chapter 7 was supported in part by the U.S. Army Research Office under Grant No. W911NF-11-1-0027, and by the NSF under Grant No. 1018935.

The work in this dissertation would not be possible without the love and support of my family and friends.

ABSTRACT OF THE DISSERTATION

Nonequilibrium Effects in Strongly Driven Correlated Systems

by

Kathleen Elizabeth Hamilton

Doctor of Philosophy, Graduate Program in Physics
University of California, Riverside, December 2014
Dr. Leonid P. Pryadko, Chairperson

At the heart of this dissertation is the phenomenon of correlations between members of a system. Many systems exhibit correlated behavior and those described in this work are divided into two classes: strongly driven correlated electron systems and networks formed by correlations. The work on correlated electron systems focuses initially on using a strong external AC field to drive a system into new phases, far from equilibrium: *e.g.* dynamical stabilization of a pendulum, band-gap suppression, and inversion of electronic bandwidths. Several of these effects are further investigated with the addition of a DC field, leading to effects such as: doubling of an electron's Bloch oscillation period, generation of a non-zero net current in a metal-insulator transition or higher harmonic generation for electrons whose conduction bands are inverted. For correlations on networks, the focus was on bounds for the percolation transition threshold. The effects of correlated percolation are discussed in the second part of this dissertation, where a random process can affect a cluster of sites simultaneously. First, a mapping between a graph and a tree is derived, and an extended mean-field approach is used to determine a lower bound on the percolation threshold for quasi-transitive graphs. To study correlated percolation, three models are used: the first is an approximation of each lattice animal by a covering shape, second is an approximation of the additional connections created by lattice animals as a single auxiliary vertex, the third is analysis based on the adjacency matrix of the random graph created through the overlap of lattice animals. In all three models a lower bound on the percolation threshold can be established, and this bound is dependent on the size of clusters present. Initial disagreement between the models is ameliorated by reducing the dimensionality of the covering shapes.

Contents

List of Figures

Chapter 1

Introduction

The study of correlated systems has been a fundamental area of condensed matter research. Correlations between particles in a system, that the existence of other members of a system affects the physics and dynamics of a single particle, is of importance on many length scales and system sizes, from classical systems to quantum systems to large-scale networks. Such systems are complex, involving many degrees of freedom. The complexity of these interacting many body systems is compounded by the addition of large amplitude driving forces which oscillate at large frequencies. It is the ability of correlations on small scales to affect behavior on large scale quantities that is important. Similarly, correlations between random systems can lead to changes in thresholds which determine phase transitions.

This dissertation is organized into two sections: Chapters (3)-(5) study the dynamics of correlated systems which are driven with strong fields which oscillate at high frequency, and Chapters (7), and (8) delve into the phenomenon of percolation on random graphs and how correlations affect large-scale transitions. As a result, the methodology pertinent to the first section and the second sections are separated. Chapter (2) discusses the methods used for driven systems, while Chapter (6) gives the definitions and methods needed to discuss random graphs and percolation. The central theme to this work is the nonlinear effects in systems with correlations, whether it's the change due to strong external fields or the sudden change in percolating systems.

The first section explores the effects of strong field driving on correlated systems. In the classical model, the driven Sine-Gordon model, the result is the transformation of unstable points of the system into stable points. In the quantum two-band model, the result is delocalization of a particle by closing gaps in the energy bands. In the quantum single-band model, the result is the inversion of a single energy band, leading to harmonic generation.

In the second section, the growth of random networks is studied. First, a method for establishing the percolation threshold on a random graph is designed which connects the mean-field methods of tree networks to the more complex structure of random graphs. Second, the growth of a random graph is studied for process which grow networks through the overlap of groups of graph nodes, rather than by connecting individual nodes. The random sizes of these groups determines the threshold of percolation and the methods used provide a way to extend continuum based models to discrete spaces and random networks.

The two sections of this dissertation are at first glance, unrelated. However both are studying effects on highly connected, complex systems. The approximations of mean-field theory are used across all sections. From reducing the complexity of many-body electron systems to describing the growth of clusters on random networks, the approximations due to mean-field theory help to give phenomenological insight into driven correlated systems.

1.1 Strongly driven correlated systems

1.1.1 Driven pendulum

A simple model of an oscillator is the physical pendulum. The dynamics of a pendulum under the influence of a strong external oscillating force was introduced by Stephenson [1], where the support of a pendulum is vertically oscillating. Such a dynamic system exhibits unique behavior, particularly the inversion of the pendulum [1]. Further study by Kapitza [2], described the motion of the pendulum along two time scales (slow and fast dynamics), and introduced the concept of an effective potential governing the slow dynamics. The general problem of a classical system under high frequency driving was described by Landau [3]. The oscillation of the pendulum mass about the vertical position (above the support) has been called "dynamical stabilization." The ability to invert multiple, stacked, pendulums, was studied by Acheson [4]. A driven system with friction has also been studied [5]. Experimental and numerical studies of the driven, vertical pendulum show agreement with the effective potential approach [6–8]. A horizontal set of coupled pendulums which are driven by a time-dependent torque applied at points of support for each pendulum, which is a physical interpretation of the driven Sine-Gordon model, is studied. In contrast to the model studied by Kapitza, the point of support is not driven but rather the driving is incorporated into the relative angle time dependence for the coupled pendulums.

1.1.2 Classical field theory: the Sine-Gordon model

An example of a correlated classical system is the Sine-Gordon model. Physically, it can be interpreted as a system of horizontal pendulums with a coupling existing between their individual pivot points. The relative angle of each pendulum is coupled to its neighbors and used to define a classical field theory [9]. Physically, the Sine-Gordon model is useful in treating Josephson junctions [10] and the dynamics of the Frenkel-Kontorova model [11]. Once the field theory is quantized, and proper quantum operators are defined, it is possible to use the Sine-Gordon model to describe the dynamics of correlated boson models [12].

In the Sine-Gordon model, the equations of motion for a stationary solution can be rewritten as the equations of motion for a single particle in the Sine-Gordon potential [13]. In Chapter (3) the effective potential approach is applied to the driven Sine-Gordon model. From the effective potential, the possibility of dynamical stabilization for a horizontal chain of coupled oscillators is investigated. In the Kapitza model, dynamical stabilization occurred when a pendulum, with its support vertically driven, was stable in an inverted position (above the support). For the horizontal chain of pendulums, dynamical stabilization is defined by a subset of pendulums being stable above the support.

Studies on strongly driven Sine-Gordon models have established the existence of π-solitons, excitations in the system with half the width of an un-driven soliton. Such excitations have a natural interpretation as domain walls in ferromagnetic systems. Through the application of strong driving forces it is seen how the width of such a domain wall can be affected. The physical interpretation of the Sine-Gordon model as a chain of coupled pendulum lead to the identification of the stable driven positions above the support and it is seen in Chapter (3) how multiple pendulum can be stabilized in an inverted position. In a ferromagnetic system this would correspond to a broadening of a domain wall.

The classical Sine-Gordon model can be connected to a variety of correlated, quantum systems. When the classical Sine-Gordon equation is quantized, it defines a quantum field theory which is identical to that of spin-less bosons with a gapped mass spectrum. The gap is due to backscattering. Additionally, the π-soliton of the Sine-Gordon model can be interpreted as a "true" domain wall in ferromagnetic systems [14]. In a one-dimensional, interacting electron system, such a domain wall would correspond to an excitation in the charge or spin spectra. It is of interest how the strong field effect of dynamical stabilization in the classical system is manifested in the quantum system.

1.1.3 Correlated many-body quantum systems

One-dimensional, correlated many-body quantum systems are incredibly complex systems. The dimensionality of the systems raises complications with the Fermi liquid model [15–17] and the quasi-particle description of excitations. Interactions and correlations due to the spin and charge of electrons cannot be exactly accounted for without prohibitively large computing resources. However, there are a range of approximations to correlated systems and the result recast is a representation which is more tractable to analysis. For the gap suppression discussed in Chapter (4), a phenomenological model is derived using the Hartree-Fock approximation to a one-dimensional Hubbard model.

The Hartree-Fock approximation has been established as a perturbative approach to interacting quantum systems [18]; describing orbital energies of atoms or molecules [19, 20], interacting electron systems [21, 22] and interacting spins in ferromagnets [23, 24]. The self-consistent field central to the method is an effective potential which describes independent electrons interacting with a mean field due to the remaining electron density. Through the Hartree-Fock approximation, an interacting system can be decomposed into terms which account for Coulumb repulsion, exchange and correlation interactions without the use of two-body operator products.

A class of systems which have been treated with the Hartree-Fock approximation is the Mott-Hubbard model, a correlated system with a metal-insulator transition at low-temperature [25–28]. Specifically, the use of the Hartree-Fock model gives an approximate description of the gap opening due to interactions (and subsequent metal-insulator transition) [29]. Originally derived for correlated spin systems, the Hubbard model can also be mapped to spinless fermion models, discussed further in Section (2.3).

One-dimensional, electron systems can be described in the Luttinger liquid picture. The theory of the Luttinger liquid is well-established in the literature (see Refs: [30, 31]). Excitations of an interacting system no longer produce quasi-particles (as in the Fermi liquid theory), but rather density waves in the charge or spin spectrum. Additionally, one-dimensional systems exhibit spin-charge separation [32, 33]. Further simplification is done by using bosonization to rewrite the fermionic operators as bosonic ones [34, 35]. Also, considering a system at the Luther-Emery point, results in a gapped spectrum in either the spin or charge spectra [30, 36]. As a result, the physics of a many-body, electron system in one-dimension can be studied using a system of spinless fermions.

1.2 Driven quantum systems

The dynamics of charged particles in external fields, magnetic or electric, have been studied in stationary fields and oscillatory fields. The results have shaped the understanding of transport in quantum systems. The effects in stationary electric fields, time-dependent fields and large amplitude fields are discussed. In the systems studied in this dissertation the fundamental effects are due to large amplitude, time-dependent fields. The verification of these effects are probed using weak stationary fields (see Chapters (4), (5)). As the work in this dissertation is focused on electric field driving, the effects discussed here are due to electric fields.

1.2.1 Stationary field driving

The behavior of a particle trapped in a potential well and subject to a static external electromagnetic force has been an active area of research for over a century and has unexpected results. Intuitively, it is expected that the particle in a potential can be driven far from its initial position with a strong enough external force. However, when driving a system with a static (DC) field, it is possible to localize a particle in a spatially periodic well. This localization has been explained by Bloch oscillations [37, 38], and Wannier-Stark ladder formation [39]. The observation of these effects was made possible in superlattice structures [40, 41] and optical lattices [42–45].

In Chaper (4), Bloch oscillations are used to further probe the effects of oscillating field driving. The dynamics of electrons under DC field driving are determined by the periodicity of the Brillouin zone. It is expected that if a system is driven through a gap closure then the resulting DC field dynamics will show the effects of the zone width increase.

1.2.2 Oscillating field driving

The effective potential approach, and the concept of a system evolving along slow and fast time scales, has been used to describe quantum systems and atomic dynamics in rapidly oscillating external fields [46–49]. Using the Floquet quasi-energy spectrum allows for time-independent analysis.

For a periodically driven quantum system, the Floquet-Bloch theorem recasts a time-dependent system as a series of time-independent Hamiltonians and has been well-established in the study of quantum systems interacting with oscillatory external fields [50–53]. The work in this dissertation is inspired by two known effects of electrons in a strongly oscillating field, coherent destruction of tunneling and dynamical localization.

Coherent destruction of tunneling (CDoT) was proposed in 1991, as a perturbative effect seen in a two-level system driven by a strong AC field [54]. In a double-well system, the degeneracy between neighboring well levels is removed through tunnel splitting. When a strong AC field is applied it was shown that particles could be localized in one well [54] by suppressing the tunnel splitting. This effect was later confirmed in optical lattices [55, 56]. An inverse effect is discussed in Chapter (4), the delocalization of a particle by strong AC field driving. Using the perturbative approach of the Hartree-Fock model, the phenomenological effects of AC driving at Thz frequencies on an interaction-induced gap, are studied; in particular, gap suppression analogous to the suppression of tunnel splitting in CDoT. However, if an interaction-induced gap can be suppressed, this would lead to delocalization of electrons, rather than localization.

Another effect of strong AC driving is dynamical localization (DL) [57], later described in terms of Floquet band collapse [58], and verified experimentally in optical lattices [59]. While CDoT is a perturbative effect, DL is an exact result, describing the renormalization of a system's bandwidth [60]. When dynamical localization occurs, the effective bandwidth of a system is suppressed (band collapse). This bandwidth renormalization has inspired research into what occurs as a system is driven past the point of band suppression. It is possible to invert a bandwidth, and this has been studied as a dynamical renormalization of particle interactions, turning repulsive interactions to attractive [61].

The behavior of a collection of particles driven into an inverted Floquet band and higher harmonic generation, is discussed in Chapter (5). In particular an amplification of the third harmonic of the driving field is sought. Higher harmonic generation in strongly driven crystal structures has been studied theoretically [62, 63] and observed experimentally [64]. In a similar approach which has been applied to topological insulators (see [65] and [66] for theoretical and experimental results), lead to the investigation of the driven dynamics of a system: if they will be determined by the renormalized Floquet spectrum, rather than the un-driven spectrum.

The theoretical predictions of Floquet states that have been verified by experiment lead us to study how a system can be driven through renormalized Floquet bands. For a two-band system with a band-gap the effects of gap closure on the stationary field driving effects such as Bloch oscillations and how an initially full band can be driven into an effectively half-filled band are investigated. In the inverted band system this is extended to the study of whether a system can equilibrate to the renormalized (inverted) Floquet quasi-energy band, rather than the original energy bands. It has come to our attention that similar work on band-gap suppression in a two-band model has

been carried out [67].

1.2.3 Strong field driving

Non-equilibrium transport has gained a lot of attention as electronics have been scaled down to the nanoscale and the ability to generate intense laser fields has been refined. Many experimental measurements of high drift velocities in graphene and semiconductor materials driven by high electric fields exist (for examples, see [68, 69]), and many theoretical reviews are available, [70, 71]. There are many challenges in the study of strong driving fields including incoherence, heating, and the lack of equilibrium statistical mechanics. The use of non-equilibrium (Keldysh) Green's functions [72, 73] provides a connection to the quantum kinetic equation, used to describe charge transport.

1.3 Dynamics of quantum systems and percolation

The theory of percolation in quantum systems has been used to describe a variety of critical phenomena, including: ferromagnetism, charge and magnetic transport. Many of these systems rely on an underlying lattice which may have defects that affect the large-scale qualities of transport. Percolation theory can describe phase transitions due to spin interactions between particles. It can also describe transport in systems of nano-scale objects. distributed in a substrate, which form networks. Additionally, lower-dimensional objects such as quantum dots can be collected into networks used for charge transport. Percolation theory can be applied to predict the possibility of conduction in such systems, or to investigate the robustness of such systems to failure.

The work discussed in Chapters (7) derives an extension to mean field theory in order to find a percolation threshold on a quasi-regular graph. Chapter (8) explores correlated percolation on: regular lattice structures, quasi-regular lattice structures and random graphs. Correlation refers to a random process which affects multiple vertices, rather than site or bond percolation which only affects individual vertices or edges. The lower bound on the percolation threshold is established using continuum percolation methods, an auxiliary vertex model and using the adjacency matrix to define a bound on the mean cluster size. These methods can be applied to the variety of physical systems that have been studied through percolation theory, expanded by the role of correlations. Physical examples of correlations are discussed in this section and their possible connections to the work in Chapter (7) and (8) are emphasized.

1.3.1 Percolation theory and ferromagnetism

Magnetic behavior of materials is a direct bridge between correlated quantum systems and percolation theory. In interacting spin systems, the correlations between particles lead to large-scale phenomena, such as the parallel (or anti-parallel) alignment of spins. One of the earliest atomic systems studied with percolation theory is the ferromagnetic phase transition in a metal at the Curie temperature [74–76]. Theoretical descriptions of how correlations between neighboring particles lead to large-scale effects have been made using mean-field theory introduced by Weiss [77], and Bethe [78, 79]. It was discussed in Section (1.1.3) that a correlated system in one-dimension can be described in terms of independent electrons interacting with a mean field due to the remaining system electrons. The mean-field approach to percolation systems (such as magnetic transitions) does not include all possible interactions between particles, only nearest neighbors. This mean-field approach is the basis for the extended-mean field theory discussed in Chapter (7). Ferromagnetism can also be studied in semiconductor systems, where the Curie temperature is affected by impurities or clustering of dopants [80–83].

1.3.2 Percolation theory and semiconductor transport

Charge and magnetic transport have been studied in semiconductors and interpreted as a percolation process. Transport can be affected by the connections available in the system, either by design, or by the amount of dopants in a semiconductor.

Conductivity can be studied as the transport of charge through a given system, modeled by a resistor network, which is a randomly connected network [84, 85]. The system can be affected by the presence of impurities, defects and the geometry or deformation of the lattice [86–89]. Such methods can be applied to magnetic transport [90–92] or transport in systems of nanocomposites [93]. Semiconductors formed through the addition of dopants in a material are also modeled as percolating systems. The clustering of dopants leads to systems which could exhibit correlated percolation, as described in Chapter (8).

1.3.3 Networks of nanoscale objects

With the advance of nano-scale fabrication, systems comprised of many nanoscale objects distributed in an environment can be created. The density and distribution of such objects exhibits a crossover point where the behavior can be treated not as a collection of individual objects, but as singular object. For example, quantum dots

on a surface can exhibit behavior of a thin metal film [94, 95], or sheets of exfoliated graphene can behave as a carbon surface [96] Additionally, conductivity in materials with suspended nano-structures has been studied [93, 97, 98]. Quantum dot networks have also lead to new designs of highly-efficient solar cells [99].

Such networks of finite-sized shapes and their collective effects are related to correlated percolation, discussed in Chapter (8). Percolation theory can be applied to such networks to determine when the system will no longer behave as a collection of disconnected shapes, but rather as a large cluster. The emergence of this behavior can be interpreted as forming a percolating cluster on a random graph through the connection of finite-sized lattice animals.

1.4 Percolation theory

The modern age is defined by relationships and networks [100]. In addition to the physical systems described in the previous section, large-scale events can be defined in social, economic, biological, chemical, technological and ecological systems [101–104]. For example, it is possible for members of a society to become infected by a virus, which will spread throughout the network defined by social connections. On a power grid, the failure of one node can lead to catastrophic failure which can destroy the whole network.

The conditions that lead to the existence of large-scale clusters is of great interest. The probability of a large cluster, or *giant component* forming on a network exhibits a phase transition. There exists a threshold value of the probability, below where there is no giant component. Above this threshold the existence of a giant component is certain. The existence of a percolation threshold is dependent on the structure of the network or graph. While it may be possible on some graphs and systems to define an exact value for the percolation threshold, on others it may only be possible to define an upper or lower bound on the probability of percolation.

1.4.1 Percolation thresholds on graphs and trees

The study of percolation has lead to many estimates to the percolation threshold on trees, regular lattices and random graphs. On trees, graphs with no cycles, the mean field theory approach leads to exact results [74,105–107]. The mean field approach is based on determining the probability that a branch grown from some arbitrary point on a graph, can grow to an infinitely long length. Additionally, bounds on the percolation threshold have been established on many kinds of regular lattices (*e.g.* site percolation on the square and honeycomb lattice [108], site and bond percolation on

triangular, honeycomb or quadratic lattices [109]). Many estimates for the percolation threshold on random graphs exist [110, 111]. To determine these thresholds, methods which incorporate degree correlations, small-world arguments are used. In Chapter (7), the methods of mean field analysis are applied to a quasi-random graph. A bound on the percolation threshold of a random graph is sought by establishing a mapping between a graph with cycles and a tree. The mean field analysis is based on the connections between vertices, rather than the number of neighbors for a given vertex.

1.4.2 Percolation thresholds in continuum

On a graph of discrete nodes and connections, it is straightforward to define percolation by considering processes which affect single nodes. In a continuum model, it is difficult to define a discrete point, and it is through the continuum model of percolation that the process of correlated percolation is first studied. In a 2008 paper by Gouéré [112], a lower bound on the percolation threshold was established. By considering the size of the cluster formed by overlapping spheres in a continuum model, it was found that the threshold for percolation is proportional to the average covered fraction of the full space. Our studies of correlated percolation on random graphs begins from the discretization of these results: establishing a percolation threshold by studying the connected cluster formed by overlapping spheres on a regular lattice. Modifications to this method are needed to study correlated percolation on random lattices.

1.4.3 Correlation in percolation

Correlated percolation as used in this dissertation, describes a percolation process wherein a random graph is generated from an initial graph through a random selection of vertices. However, the probabilities of a vertex and its neighbors being open are no longer independent. Correlated percolation can be described as percolation by shapes, known as *lattice animals*. These are collections of adjacent vertices and the percolation process is defined as follows: if a vertex (i) of a graph is contained inside a lattice animal it is open, and a. s. all vertices connected to (i) through the lattice animal are also open. Now on a lattice, percolation will occur when a large cluster is formed through the overlap of shapes, rather than connecting individual vertices.

Lattice animals are found throughout the study of percolation [74, 113], and research has focused on enumerating the many kinds of animals that can be formed on different graphs, or the distribution of animal sizes [114–118]. Percolation with lattice animals has been studied in terms of the critical exponents of percolation [119, 120].

In this work the lattice animals are distributed with a known probability distribution and what is studied is how the average size determined the percolation threshold of the overall system.

The concept of percolation by shapes, or by objects that contain more than one vertex of a graph, has ties to the study of adsorption of polymers on surfaces [121–124]. Random sequential adsorption describes how a surface is covered by a random application of shapes, and the surface is modeled as a continuum or a lattice. However, these studies are restricted to systems covered by shapes that do not overlap and instead establish conditions for jamming coverage. I extend results for continuum percolation models to study how a lattice can be covered by overlapping shapes by first extending the Gouéré results to a discrete lattice.

The discrete lattice leads to promising results, where it is seen that the percolation threshold due to overlapping circles scales proportionally to the covered volume of lattice points. However, on a tree or random graph, the percolation threshold scales exponentially, leading to an infinitesimally small threshold. In order to get a bound on the percolation threshold which is not trivial, the adjacency matrix approach of Ref [125] for the random graph system, is modified to incorporate lattice animal connections.

A note on units: throughout this dissertation, natural units are used ($\hbar = k_B = c = 1$).

Chapter 2

Theory of driven correlated systems

Dynamics of particles in strong external fields have many degrees of complexity. In this chapter we discuss the methods which are used to reduce the complexity through the reduction of degrees of freedom, assumptions about the time-evolution of systems and the definition of perturbation series expansions. For the classical Sine-Gordon systems (discussed in Chapter (3)), the method of effective potentials is discussed. For the two-band quantum system (discussed in Chapter (4)), the derivation of a phenomenological theory is discussed using the Hartree-Fock approximation, the Hubbard model and the Luttinger liquid. The result is a description of the physics for a many-body, interacting electron system in one-dimension as a two-band model of spin-less fermions. Finally, for the single-band theory (discussed in Chapter (5)), the Keldysh formalism and Boltzmann master equations are discussed.

In the three physical systems considered in the first part of this dissertation, systems of many particles are strongly driven by an external force which is rapidly oscillating in time. It is expected that the effects of such an external force on the system will occur on two time scales. The dynamics of the system will evolve along a slow time scale and a fast time scale. On the slow time scale, driving effects gradually accumulate over several periods of the driving force. On the fast time scale, effects on the system are rapidly oscillating and will have zero mean value when averaged over a period of the driving force, resulting in no net changes to the system. This separation of time scales results in expressions for slow dynamics which show the dynamical effects due to the driving field. It is also investigated how robust these effects are against externals perturbations due to phonon scattering. In the presence of the external field,

all three systems are recast in a moving reference frame and the effects of the driving field are described through classical effective potentials, or quantum quasi-energy models (renormalization of the Floquet spectrum). The methods discussed in this chapter are for dynamical systems only, the methods for percolation theory are discussed in Chapter (6).

2.1 Effective potential

One method for deriving the classical dynamics of a particle moving in an external potential begins with the Lagrangian density. From the kinetic and potential energy of a particle (or system of particles), the Euler-Lagrange equations of motions are found through a variational method [3]. For simple potentials, or simple forces, these equations are easily found. However, complex systems, either through multi-dimensional motion or a potential field plus an external force, can obscure the physics described by the equations of motion. It is useful to define an *effective potential*, a rearrangement of the equations of motion such that the form is reminiscent of a particle moving under the influence of a single external potential. Such an approach is standard in classical mechanics textbooks when describing orbital motion or systems with external driving [3]. From a generic Lagrangian:

$$\mathcal{L}(\dot{x}, x, t) = \frac{1}{2}(\dot{x})^2 - U(x), \tag{2.1}$$

the Euler-Lagrange equations of motion have the form:

$$m(\ddot{x}) = -\frac{\partial U(x)}{\partial x}. \tag{2.2}$$

2.2 Correlated systems

The systems studied in Chapters (4) and (5) are interacting electron systems in one-dimension. They will be treated using models of spin-less fermions. The discussion in this section begins with the general treatment of interacting electron systems, with focus on approximations to many-body operators (the Hartree-Fock model) and the treatment of strongly localized interactions (the Hubbard model).

2.2.1 Hartree-Fock approximation

In a non-interacting electron system, the Hamiltonian can be written as a sum over single-body operators,

$$H_0 = \sum_k \epsilon_k a_k^\dagger a_k, \tag{2.3}$$

and the ground state of such a system is just a collection of non-interacting particles. When interactions between particles are included, the Hamiltonian must include two-body operators,

$$H = H_0 + H' = H_0 + \sum_{k,k',q} V_q a^\dagger_{k+q} a^\dagger_{k'-q} a_{k'} a_k. \tag{2.4}$$

To determine the effects of interactions on the non-interacting ground state, a mean-field analysis is used. An electron in the system is treated as an independent particle interacting with the mean field due to the remaining electrons in the system. To find the mean field of the two-body term, $\langle a^\dagger_{k+q} a^\dagger_{k'-q} a_{k'} a_k \rangle$, requires the use of Wick's theorem [126,127]. This theorem allows for multi-body operators to be written in terms of single-body operators. This is done by expanding a product of N operators into a sum, where each term accounts for a possible pair contraction of operators. For the four operators in the two-body interaction, that would result in the expansion,

$$\begin{aligned} \langle a^\dagger_{k+q} a^\dagger_{k'-q} a_{k'} a_k \rangle = & \\ & \langle a^\dagger_{k+q} a_k \rangle a^\dagger_{k'-q} a_{k'} + a^\dagger_{k+q} a_k \langle a^\dagger_{k'-q} a_{k'} \rangle \\ & - \langle a^\dagger_{k+q} a_{k'} \rangle a^\dagger_{k'-q} a_k - a^\dagger_{k+q} a_{k'} \langle a^\dagger_{k'-q} a_k \rangle \end{aligned} \tag{2.5}$$

The two-body operator is now a sum of single-body operators, and the averaging $\langle \dots \rangle$ is done with respects to a Hartree-Fock ground state. the full Hartree-Fock Hamiltonian has three terms. It is noted that the creation and annihilation operators $a^\dagger_k, a_k$ are dependent on position, wave-number and spin ($a_k = a_{k,\sigma}(\bar{r})$). Likewise the interaction potential in Eq.(2.4) may depend on position and spin, not just transferred momenta. The position dependence of the operators $a^\dagger_k, a_k$ and the interaction will be discussed in Section (2.2.2) where the interacting system is studied in a strongly correlated lattice. The separation of charge and spin variables will be discussed in Section (2.3.1).

2.2.2 The Hubbard model

The Hubbard model is a description of strongly interacting particles (in this dissertation, electrons). The Hamiltonian has two terms, one describing the hopping of electrons between sites (with hopping parameter t) and the second describing the on-site interaction energy (U),

$$H = -t \sum_i (a^\dagger_i a_{i+1} + a^\dagger_{i+1} a_i) + U \sum_i n_i n_{i+1} \tag{2.6}$$

where $n_i = a^\dagger_i a_i$. In the previous section it was mentioned that an interaction term can be dependent on many different parameters. The Hubbard model treats the interaction term as acting at lattice sites only.

Applying the Hartree-Fock approximation to the Hubbard model rewrites the on-site repulsion term in terms of average occupation numbers $\langle n_i \rangle$ and single particle operators,

$$\begin{aligned} n_i n_{i+1} &= a_i^\dagger a_i a_{i+1}^\dagger a_{i+1} \\ &\approx \langle a_i^\dagger a_i \rangle a_{i+1}^\dagger a_{i+1} + a_i^\dagger a_i \langle a_{i+1}^\dagger a_{i+1} \rangle \\ &- \langle a_i^\dagger a_{i+1} \rangle a_{i+1}^\dagger a_i - a_i^\dagger a_{i+1} \langle a_{i+1}^\dagger a_i \rangle. \end{aligned} \tag{2.7}$$

This approximation leads to four terms, two are diagonal and two are off-diagonal. Rewriting the Hubbard Hamiltonian,

$$\begin{aligned} H = &-t \sum_i ((1 - \langle a_{i+1}^\dagger a_i \rangle) a_i^\dagger a_{i+1} + (1 - \langle a_i^\dagger a_{i+1} \rangle) a_{i+1}^\dagger a_i) \\ &+ U \sum_i \langle a_i^\dagger a_i \rangle a_{i+1}^\dagger a_{i+1} + a_i^\dagger a_i \langle a_{i+1}^\dagger a_{i+1} \rangle \end{aligned} \tag{2.8}$$

it is seen that the Hartree-Fock terms lead to a modification of the hopping parameter. The work in Chapter (4) relies on a phenomenological description of a gapped system. The Hartree-Fock approximation to the Hubbard model returns a general form of such a system:

$$\begin{aligned} H = &-J \sum_i (a_i^\dagger a_{i+1} + a_{i+1}^\dagger a_i) \\ &+ V \sum_i a_{i+1}^\dagger a_{i+1} + a_i^\dagger a_i \end{aligned} \tag{2.9}$$

with the Hartree-Fock terms contained in the renormalized hopping parameter J and gap V.

2.3 One-dimensional correlated systems

In one-dimension, correlated systems have dramatically different behavior compared to $d \geq 2$ systems. First, a discussion of the Luttinger liquid and bosonization methods outline the foundations of the spin-less fermion model used in later chapters. The combination of the Hartree-Fock approximation and the Hubbard model leads to the discussion of the general two-band model in Section (2.3.2).

2.3.1 The Luttinger liquid

In systems with spatial dimension $d > 1$, the Fermi liquid of interacting particles can be evolved from the non-interacting system (the Fermi gas) by adiabatically turning on interactions. As a result, the gas particles are evolved into quasi-particle

states which are long-lived and weakly interacting. Excitations in the interacting system are now single particle excitations of a quasi-particle above the Fermi surface, and the creation of a hole beneath the Fermi surface. As a result, an interacting electron system can be treated as non-interacting, or weakly interacting quasi-particles. There are many systems that exhibit Luttinger liquid behavior, these were outlined in the paper by Haldane [33]. Of importance to this dissertation are the connections to the Sine-Gordon solitons, and spinless fermion models.

The Fermi liquid description fails in one dimension. Fundamentally, any one-dimension system is correlated: the dimensionality of the system means any motion by an electron results in the motion of neighboring particles. Secondly, the one-dimensional lattice at half-filling is unstable when interactions between electrons are introduced, no matter how small. The resulting symmetry breaking is known as the Peierl's instability and leads a non-interacting, half-filled band (which is a metallic system) to become a filled band with a gap (an insulating system) when interactions are turned on. Due to the collective motion inherent in any one-dimensional system, excitations in the charge or spin spectra are density waves.

Solutions of the Luttinger liquid are built on the bosonic nature of density waves. Through the technique of bosonization [35], the Luttinger liquid can be described by operators that obey bosonic commutation rules. Notable results from this method are the separation of the spin and charge spectra and the finer points of the method can be found in Refs. [33, 128–130]. The purpose of this section is to show a connection between the Sine-Gordon model and interacting fermion systems (the connection was also highlighted by Haldane [33]). Also, this is the final piece to support the use of a spinless fermion system to describe an interacting electron system.

In the Luttinger liquid, the concept of a Fermi surface is reduced to a set of Fermi points in the energy spectrum. The energy spectrum can be linearized near the Fermi points. After linearization, the system has two energy branches which correspond to the two kinds of particles in the system, left movers and right movers. Particles that move to the right have energy $\epsilon_1 = -kv_F$, particles that move to the left have energy $\epsilon_2 = kv_F$.

The Luttinger liquid is described with the Hamiltonian [126],

$$H = H_0 + H_{int} = v_F \sum_{k,s} k(a^\dagger_{1,k,s} a_{1,k,s} - a^\dagger_{2,k,s} a_{2,k,s}) + H_{int}. \tag{2.10}$$

Where H_0 is the kinetic energy term, and H_{int} contains all the two-body interaction terms ((k, s) label the momentum and spin). Beginning with just the non-interacting electrons will show the nature of particles and excitations in a one-dimensional electron

system. There are two sets of creation and destruction operators, these are necessary to distinguish between the right $(a_1, a_1^\dagger)$ and left $(a_2, a_2^\dagger)$ moving electrons.

Following the derivations of [36,126], creation and annihilation operators can be defined for the charge density and spin density excitations. The charge density operator (defined in [126]) $\rho(k)$ is given by,

$$\rho(k) = \rho_1(k) + \rho_2(k) = \sum_{p>0,s} a^\dagger_{(p-\frac{k}{2}),s} a_{(p+\frac{k}{2}),s} + \sum_{p<0,s} a^\dagger_{(p-\frac{k}{2}),s} a_{(p+\frac{k}{2}),s}. \tag{2.11}$$

Similarly for the spin density operator $\sigma(k)$,

$$\sigma(k) = \sigma_1(k) + \sigma_2(k) = \sum_{p>0,s} s a^\dagger_{(p-\frac{k}{2}),s} a_{(p+\frac{k}{2}),s} + \sum_{p<0,s} s a^\dagger_{(p-\frac{k}{2}),s} a_{(p+\frac{k}{2}),s}. \tag{2.12}$$

A charge-density wave is a periodic modulation in the charge, a spin-density wave is a periodic modulation of the spin. The operators $\rho(k), \sigma(k)$ follow bosonic commutation rules and can be used to redefine the non-interacting Luttinger Hamiltonian. This redefined Hamiltonian can be separated into two parts, describing a spin spectrum and charge spectrum.

For the interacting Luttinger model, the two-body operators can also be written as bosonic operators. The bosonization of the operators (a_1, a_2) was derived by Luther and Peschel [129]. The authors avoided the direct calculation of (a_1, a_2) by defining a new set of operators that has the same equation of motion as the field operators, and the same commutator algebra as bosonic density operators [129].

Using the redefined field operators, the spin-charge separation of the non-interacting Hamiltonian also occurs in the full Hamiltonian [130], there are no terms that mix ρ and σ operators. Depending on the strength of the interactions, and the scattering processes allowed, the result is either the charge or spin spectrum becomes gapped. The bosonized forms of the backscattering and Umklapp processes have the same form, but depend on either the spin boson field, or the charge boson field (respectively). In Ref. [131], the general form of these scattering terms is found to be proportional to $\cos(\phi_{\rho,\sigma})$, and the Hamiltonian of the bosonic field theory (for charge or spin fields) has the same form as the quantized Sine-Gordon model. Backscattering processes contribute to a gap in the spin spectrum, Umklapp processes contribute to a gap in the charge spectrum. At half-filling, Umklapp processes cannot be omitted. As a result, the one-dimensional, interacting electron system at half-filling can be studied using a system of spinless electrons.

2.3.2 General two-band system

The general two-band theory of a tight-binding lattice model begins with an undriven, non-interacting many-body system. The electrons on odd or even lattice sites are identified by the creation operators $\alpha_k^\dagger, \beta_k^\dagger$, respectively. In the absence of the perturbation or the driving force, the system consists of a hopping term $(-t)$ which describes hopping between odd and even sites. The simple, non-interacting tight-binding model has a sum over the N-particles,

$$H_{tb} = -t \sum_k (\alpha_k^\dagger \beta_{k+a} + \beta_k^\dagger \alpha_{k+a}) \tag{2.13}$$

where (a) is the lattice spacing. In the momentum basis it can be represented by an $N \times N$ Hamiltonian,

$$H = \begin{pmatrix} & \ddots & -t & 0 & 0 & \dots & & \\ 0 & -t & 0 & -t & 0 & 0 & \dots & \\ \dots & 0 & -t & 0 & -t & 0 & 0 & \dots \\ \dots & 0 & 0 & -t & 0 & -t & 0 & \dots \\ \dots & \dots & 0 & 0 & -t & 0 & -t & \dots \\ & \dots & \dots & 0 & 0 & -t & \ddots & \end{pmatrix}. \tag{2.14}$$

For a tight-binding model, the annihilation and creation operators can be expanded in Fourier modes with respect to the quasi-momentum (k), the wavefunction of the $N \times N$ Hamiltonian is an N-length vector:

$$\psi_n(k) = \begin{pmatrix} \vdots \\ \alpha \\ \beta e^{ika} \\ \alpha e^{i2ka} \\ \beta e^{i3ka} \\ \alpha e^{i4ka} \\ \vdots \end{pmatrix}. \tag{2.15}$$

The Schrödinger equation for such a system gives a set of N-coupled equations describing the energy states:

$$\begin{aligned} -t\beta e^{ika} &= i\dot{\alpha} \\ -t\alpha - t\alpha e^{i2ka} &= i\dot{\beta} e^{ika} \\ -t\beta - t\beta e^{i3ka} &= i\dot{\alpha} e^{i2ka} \\ -t\alpha - t\alpha e^{i4ka} &= i\dot{\beta} e^{i3ka} \\ &\vdots \end{aligned} \tag{2.16}$$

These can be reduced to two coupled equations, since each new equation for $\dot{\alpha}$ or $\dot{\beta}$ can be generated with a translation of $ka \to ka + a$.

$$-t\alpha - t\alpha e^{i2ka} = i\dot{\beta}e^{ika} \tag{2.17}$$

$$-t\beta - t\beta e^{i3ka} = i\dot{\alpha}e^{i2ka} \tag{2.18}$$

which reduces to,

$$-2t\cos(ka)\alpha = i\dot{\beta} \tag{2.19}$$

$$-2t\cos(ka)\beta = i\dot{\alpha} \tag{2.20}$$

giving a simple two-level description of the N-body, non-interacting tight-binding model ($H_{tb}\psi = \epsilon_{tb}(k)\psi$).

$$\begin{pmatrix} 0 & -2t\cos(ka) \\ -2t\cos(ka) & 0 \end{pmatrix} = \epsilon \begin{pmatrix} \alpha \\ \beta \end{pmatrix} \tag{2.21}$$

which can be rotated into a diagonal form ($\epsilon(k) = -2t\cos(ka)$):

$$H_{sys} = \epsilon(k)\sigma^z = \begin{pmatrix} \epsilon(k) & 0 \\ 0 & -\epsilon(k) \end{pmatrix}. \tag{2.22}$$

There are no interactions between the two bands. In the absence of the weak potential the system's eigenvalues give the energy spectrum, which is identical to $\epsilon(k)$.

$$\begin{pmatrix} \epsilon(k) - \lambda & 0 \\ 0 & -\epsilon(k) - \lambda \end{pmatrix}. \tag{2.23}$$

$$-(\epsilon(k)^2 - \lambda^2) = 0 \tag{2.24}$$

$$\lambda = \sqrt{\epsilon(k)^2} = \pm\epsilon(k). \tag{2.25}$$

The addition of interactions leads to a gap in the energy spectrum. From the discussion of the Hartree-Fock approximation given in Section (2.2.1), when interactions are present the off-diagonal terms in Eq. (2.23) are non-zero:

$$H_{sys} = \epsilon(k)\sigma^z + \delta\sigma^x = \begin{pmatrix} \epsilon(k) & \delta \\ \delta & -\epsilon(k) \end{pmatrix}. \tag{2.26}$$

Additionally, the interactions cause a renormalization of the hopping parameter. The self-consistent calculation of the Hartree-Fock term will not be used, rather the hopping parameter will be renamed: $t \to J$, where J is a phenomenological constant describing

the hopping in an interacting system. The energy spectrum can again be found from the eigenvalues of the matrix for H_{sys}. The characteristic polynomial,

$$\begin{pmatrix} \epsilon(k) - \lambda & \delta \\ \delta & -\epsilon(k) - \lambda \end{pmatrix}, \tag{2.27}$$

results in the eigenvalues,

$$-(\epsilon(k)^2 - \lambda^2) - \delta^2 = 0 \tag{2.28}$$

$$\lambda = \sqrt{\epsilon(k)^2 + \delta^2} \tag{2.29}$$

The addition of interactions causes a gap to open at the mid-point of the Brillouion zone.

Using the gauge transformation methods defined in Section (2.6), the strong driving field can be incorporated into the unperturbed Hamiltonian through the minimal coupling shift $\bar{k} = k + \frac{d\alpha}{dx} = k + A(t)$. With the full system Hamiltonian given by,

$$H_{sys} = \epsilon(k + A(t))\sigma^z + \delta\sigma^x, \tag{2.30}$$

the interaction Hamiltonian can be defined, using the methods described in Section (2.5).

2.4 Floquet - Bloch formalism

Many physical systems have dynamics which can be described using differential equations which have a periodic symmetry. Quasi-periodic systems have a dynamical structure which repeats after one period (either in space or time), but with the addition of a phase.

In the chapters that follow, the systems studied are periodic in space and time. Time-independent, spatially periodic systems, such as electrons in a metal can be expanded in terms of Bloch functions [132]. Time periodic systems, such as systems under AC field driving, can be expanded in terms of Floquet modes [53, 133]. Both expansions will define new quantities for the momentum and energy, called the quasi-momentum and quasi-energy, respectively. By working in the space defined by these quantities, it will be seen that the system is recast in an effective space of slowly varying energy levels [133].

Both formalisms rely on the fact that the periodic symmetry of the Hamiltonian is shared by the solutions of the Schrödinger equation. In this initial section, the systems

considered will not have any perturbations present and the equation of motion is given by,

$$-i\frac{\partial}{\partial t}\psi(x,t) = H(x,t)\psi(x,t) \tag{2.31}$$

The time periodic system is considered first. If the system has a time-periodicity $H(t) = H(t+\tau)$, the wavefunction $\psi(x,t)$ can be expanded in a series of time-periodic functions and a phase term. The eigenfunctions of the periodic Schrödinger's equation have the form:

$$\psi(x,t) = e^{i\epsilon_m t} f_m(x,t) \tag{2.32}$$

where $f_m(x,t) = f_m(x,t+\tau)$ shares the periodicity of the Hamiltonian. The phase term defines the Floquet quasi-energy, which is unique up to a factor of $m\omega, m = \pm 1, 2, \ldots,$ $\omega = 2\pi/\tau$. This first description expands $\psi(x,t)$ in terms of a Floquet mode (m). Substitute the Floquet mode form of $\psi(x,t)$ into the original equation of motion and the result is the equation:

$$\begin{aligned} -i\frac{\partial}{\partial t}\psi(x,t) &= H(x,t)\psi(x,t) \\ -i\frac{\partial}{\partial t}e^{i\epsilon_m t} f_m(x,t) &= H(x,t)e^{i\epsilon_m t} f_m(x,t) \\ e^{i\epsilon_m t}\left[\epsilon_m - i\frac{\partial}{\partial t}\right] f_m(x,t) &= e^{i\epsilon_m t} H(x,t) f_m(x,t) \\ (\epsilon_m) f_m(x,t) &= \mathcal{H}(x,t) f_m(x,t) \end{aligned} \tag{2.33}$$

Where the Hamiltonian operator is redefined as $\mathcal{H}(x,t) = H(x,t) + i\frac{\partial}{\partial t}$. This equation can be used to define the energy of a given Floquet mode and further manipulated to recast the driven Hamiltonian as a series of time-independent equations.

The periodicity of the function $u(x,t)$ allows it to be expanded into a Fourier series:

$$f_m(x,t) = \sum_n e^{in\omega t} u_{m,n}(x,t) \tag{2.34}$$

leading to the complete expression for $\psi(x,t)$,

$$\psi(x,t) = \sum_n e^{i(\epsilon_m + n\omega)t} u_{m,n}(x,t). \tag{2.35}$$

So it is seen that a single Floquet mode ϵ_m contains many harmonics. Finally, the Hamiltonian is also expanded in a periodic series:

$$H(x,t) = \sum_m H_m(x) e^{im\omega t}. \tag{2.36}$$

The Floquet formalism casts a time-periodic Hamiltonian into an infinite series of time-independent bands, with the Fourier modes of $H(x,t)$ separated by a gap determined

by the periodicity $\Delta = \omega$, $\omega = 2\pi/\tau$,

$$H = \begin{pmatrix} \ddots & 0 & 0 & 0 & 0 & \dots \\ \dots & H_{(-2)}(x) - 2\omega & 0 & 0 & 0 & \dots \\ \dots & 0 & H_{(-1)}(x) - \omega & 0 & 0 & \dots \\ \dots & 0 & 0 & H_{(0)}(x) & 0 & \dots \\ \dots & 0 & 0 & 0 & H_{(1)}(x) + \omega & \dots \\ \dots & \dots & 0 & 0 & 0 & \ddots \end{pmatrix}. \tag{2.37}$$

By recasting a time-dependent Hamiltonian into the Floquet representation, the time-dependent spectrum is rewritten as a ladder of time-independent levels, separated by a spacing $\Delta\epsilon = \omega$. In the work that follows, the spacing between Floquet levels is important. In order to ensure a particle will most likely scatter within a single band, the separation between levels has to be large enough to ensure neighboring Floquet bands do not overlap. The bandwidth of a Floquet level is a renormalization of the original bandwidth ($\widetilde{J}$), this lead to a hierarchy for the system parameters: $\Delta < \widetilde{J} < \omega < J$.

The theory of particles in a periodic potential is described using Bloch theory, the analysis follows a similar method to Floquet theory. If a Hamiltonian is time-independent, and spatially periodic ($H(\bar{r}) = H(\bar{r}+\bar{R})$), then the wavefunction is defined by a spatially periodic function and a phase term:

$$\psi(\bar{r}) = e^{-i\bar{k_m}\cdot\bar{r}} f_m(\bar{r}). \tag{2.38}$$

The dynamics of a particle in a periodic potential is that of a plane wave with a spatially-periodic amplitude given by $f_m(\bar{r}) = f_m(\bar{r}+\bar{R})$. Since the systems considered here only have one spatial dimension the vector notation will be dropped $\bar{r} = x$. As with the Floquet modes, the first decomposition of $\psi(x)$ is given in terms of a single Bloch mode, defined with the quasimomentum k, which is unique up to a factor $2m\pi/R, m = \pm 1, 2, \dots$.

An additional expansion of the function $f_m(x)$ is done in terms of spatial harmonics, called Wannier functions [132]:

$$\psi(x) = \sum_R e^{ikR} \phi_n(x - R). \tag{2.39}$$

The advantage to expanding the Floquet mode into Fourier harmonics, and expanding the Bloch mode into Wannier functions, is that the final periodic functions $u_{m,n}(x,t)$ and $\phi_n(x-R)$ are orthogonal.

2.5 Interaction representation

The systems studied in this work are driven by strong, highly-oscillatory fields. To study the effects of strong driving and small perturbations on the Hamiltonians, perturbation expansions are used. In the case of quantum systems (the gapped electron system and the single band renormalization) the small perturbations are resolved using the interaction representation. The general form of the system's Hamiltonian,

$$H_{sys} = H_0 + H_D + H_P, \tag{2.40}$$

is composed of three terms: H_0 is the un-driven system with known eigenfunctions, H_D is the time-dependent driving, and H_P includes any other external potential terms. The system is time-dependent and rapidly oscillating. Additionally, the driving force amplitude is large, and cannot be treated as a perturbation.

In the systems that follow, the term H_0 has a set of know eigenfunctions ψ_0 (either tight-binding Wannier functions or free electrons). The time-dependence from the driving force is treated by defining a gauge field and is discussed in the next section. The small potential given by H_{ext} is treated by transforming into the interaction representation and from there defining a cumulant expansion which will be truncated at the appropriate order. A time-dependent, unitary operator is defined which will evolve the system in time ($U(t)$). The full operator $U(t)$ is decomposed into two factors,

$$U(t) = U_0(t)S(t). \tag{2.41}$$

The time dependence of the wave-function $\phi(t)$ is found from the differential equation of the known Schrödinger equation for H_0,

$$\dot{\phi}(t) = -iH_0\phi(t). \tag{2.42}$$

Comparing the time-dependent Schrödinger equation with the definition of U_0, it is seen there is an equivalent way to describe the time evolution of the wave-function:

$$\phi(t) = U_0\phi(t=0), \tag{2.43}$$

$$\dot{\phi}(t) = \frac{d(U_0\phi(t=0))}{dt} = \dot{U}_0\phi(t=0). \tag{2.44}$$

The time-dependence of U_0 can be determined through an equation similar to the time-dependent Schrödinger equation:

$$\dot{U}_0 = -iH_0U_0. \tag{2.45}$$

For systems which are time-independent, the equation can be easily integrated:

$$U_0(t) = e^{-iH_0 t} \tag{2.46}$$

When a small perturbation term (H') is included to the time-independent Hamiltonian, the definition of the unitary operator changes to an operator $U(t)$ which will evolve the full system ($H_{sys} = H_0 + H'$),

$$U(t) = U_0(t)S(t). \tag{2.47}$$

Where $S(t)$ is a factor which accounts for the change in system evolution due to the perturbation. There are now two time evolution equations which can be written:

$$\dot{U}_0 = -iH_0 U_0 \tag{2.48}$$

$$\dot{U} = -iH_{sys} U \tag{2.49}$$

The last equation can be rewritten in terms of U_0, and S:

$$\dot{U} = (\dot{U}_0 S + U_0 \dot{S}) = -i(H_0 + H')(U_0 S). \tag{2.50}$$

Terms which can be cancelled are identified by multiplying the unperturbed evolution equations on the right by the operator S,

$$(\dot{U}_0)S = (-iH_0 U_0)S, \tag{2.51}$$

and the time evolution operator for U reduces to:

$$U_0 \dot{S} = -iH' U_0 S \tag{2.52}$$

Multiplying through by $U_0^\dagger$ allows the equation to be written as an evolution equation for $S(t)$,

$$\dot{S}(t) = -iH_{int} S(t) \tag{2.53}$$

$$\dot{S}(t) = -iU_0^\dagger H' U_0 S(t) \tag{2.54}$$

The interaction Hamiltonian is identified $H_{int} = U_0^\dagger H' U_0$. Once the interaction representation is identified, the complete dynamics of the operator $S(t)$ can be approximated through a perturbation series. Assuming the amplitude of H' is small the series can be truncated at a low order.

The iterative solution of the equation above for $S(t)$ begins at time $t = 0$. The initial conditions for the operator$S(t)$ are defined as $S(t = 0) = 1$. Additionally, at $t = 0$, the full system evolution operator $U(t = 0) = 1$. From the time evolution equation

defined above, the evolution of $S(t)$ is determined by the interaction representation of the Hamiltonian. To find the full form of $S(t)$, the equation is integrated:

$$\dot{S}(t) = -i(U_0^\dagger H' U_0)S(t) \tag{2.55}$$

$$\int_0^{\mathcal{T}} dt\dot{S}(t) = -i\int_0^{\mathcal{T}} dt(U_0^\dagger H' U_0)S(t) \tag{2.56}$$

The left-hand side of the equation is evaluated:

$$S(\mathcal{T}) - S(0) = S(\mathcal{T}) - 1 \tag{2.57}$$

The equation for $S(t)$ is given in terms of an integral:

$$S(t) = 1 - i\int_0^t dt' H_{int}(t')S(t'). \tag{2.58}$$

Likewise, for $S(t')$,

$$S(t') = 1 - i\int_0^{t'} dt'' H_{int}(t'')S(t''). \tag{2.59}$$

So after two iterations, the equation for $S(t)$ is given,

$$S(t) = 1 - i\int_0^t dt' H_{int}\left[1 - i\int_0^{t'} dt'' H_{int}S(t'')\right] \tag{2.60}$$

$$= 1 - i\int_0^t dt' H_{int}(t') + (-i)^2\int_0^t dt'\int_0^{t'} dt'' H_{int}(t')H_{int}(t'')S(t'') \tag{2.61}$$

A more compact form can be given by defining the integrals with time-ordered operators [126]. Time ordering of two operators organizes the arguments such that operators that act earlier in time are placed to the right.

$$\mathcal{T}[H_{int}(t_1)H_{int}(t_2)] = \Theta(t_1 - t_2)H_{int}(t_1)H_{int}(t_2) + \Theta(t_2 - t_1)H_{int}(t_2)H_{int}(t_1) \tag{2.62}$$

By time-ordering operators, the upper limit for all integrals goes to (t). The second order expansion of S(t) can be generalized to m-order,

$$\begin{aligned} S(t) = 1 - i\int_0^{t_0} dt_1\, H_I(t_1) + \frac{(-i)^2}{2}\int_0^{t_1}\int_{t_1}^{t_2} dt_1 dt_2\, [H_I(t_1), H_I(t_2)] \\ + \cdots + \frac{(-i)^m}{m!}\int_0^t dt_j\, \mathcal{T}_t H_I^m, \end{aligned} \tag{2.63}$$

and written as an exponential operator,

$$S(t) = \mathcal{T}_t e^{-i\int_0^t dt'\, H_{int}(t')} \tag{2.64}$$

2.6 Gauge field definition

The strong driving field is incorporated by minimal coupling to a gauge field. First the gauge will be found for the case of a driven free particle, then for a driven tight-binding model. The exact form of the driving force is not important at this stage, but it is assumed to be dependent on time and the position operator $F = F(\hat{x}, t)$. The full Hamiltonian is given by,

$$\widetilde{H}(\hat{p}, \hat{x}, t) = H_0(\hat{p}) + H_{driving}(\hat{x}, t) \tag{2.65}$$

The undriven free-particle Hamiltonian is only dependent on the momentum operator ($\hat{p}$). A unitary operator, $U(t)$ can be defined in the following form:

$$U(t) = e^{-i\alpha(\hat{x},t)} U_0(t), \tag{2.66}$$

$$U_0(t) = e^{\int dt \widetilde{H}(\hat{p},\hat{x},t)}. \tag{2.67}$$

$U(t)$ is defined by the evolution of the driven system and the factor $\alpha(\hat{x}, t)$. The above equations can be rearranged for a definition of $U_0(t)$ and used in the time-evolution equation: This equation can be solved for the gauge field $\alpha(\hat{x}, t)$, and also a gauge transformed form of the driven, unperturbed, Hamiltonian. Rearranging the equation for $U(t)$ to give a definition of $U_0(t)$ and using it in the time evolution equation:

$$U_0(t) = e^{i\alpha(\hat{x},t)} U(t), \tag{2.68}$$

$$\dot{U}_0(t) = \frac{d}{dt}\left[e^{i\alpha(\hat{x},t)} U(t)\right] = -iHU_0. \tag{2.69}$$

$$\tag{2.70}$$

Fully expanded,

$$\left(i\dot{\alpha} e^{i\alpha(\hat{x},t)} U(t) + e^{i\alpha(\hat{x},t)} \dot{U}(t)\right) = -i\left[H_0(\hat{p}) + H_{driving}(\hat{x}, t)\right]\left(e^{i\alpha(\hat{x},t)} U(t)\right), \tag{2.71}$$

and after multiplying on the left by the exponential operator $e^{-i\alpha(\hat{x},t)}$:

$$\left(ie^{-i\alpha(\hat{x},t)} \dot{\alpha} e^{i\alpha(\hat{x},t)} U(t) + \dot{U}(t)\right) \tag{2.72}$$

$$= -i\left[e^{-i\alpha(\hat{x},t)} H_0(\hat{p}) e^{i\alpha(\hat{x},t)} + e^{-i\alpha(\hat{x},t)} H_{driving}(\hat{x}, t) e^{i\alpha(\hat{x},t)}\right] U(t). \tag{2.73}$$

The exponential operators are expanded according to the Baker-Campbell-Hausdorff formula:

$$e^{i\hat{A}} \hat{B} e^{-i\hat{A}} = \hat{B} + \left[\hat{A}, \hat{B}\right] + \frac{1}{2!}\left[\hat{A}, \left[\hat{A}, \hat{B}\right]\right] + \ldots \tag{2.74}$$

and for position and momentum operators, the series truncates after the second term.

$$e^{-i\alpha(\hat{x},t)}\dot{\alpha}e^{i\alpha(\hat{x},t)} = \dot{\alpha}(\hat{x},t) \tag{2.75}$$

$$e^{-i\alpha(\hat{x},t)}F(\hat{x})e^{i\alpha(\hat{x},t)} = F(\hat{x}) \tag{2.76}$$

$$e^{-i\alpha(\hat{x},t)}\hat{p}e^{i\alpha(\hat{x},t)} = \hat{p} + \frac{d}{dx}\alpha(\hat{x},t) = \tilde{p} \tag{2.77}$$

The third line gives the gauge transformed momentum operator $\tilde{p}$. To form the gauge transformed Hamiltonian, $\bar{H}$, the momentum operator in H_0 is replaced by the gauge-transformed momentum:

$$\bar{H} = H_0(\tilde{p}) = H_0\left(\hat{p} + \frac{d}{dx}\alpha(\hat{x},t)\right) \tag{2.78}$$

As a result, Eq. ((2.73)) reduces to:

$$i\dot{\alpha}(\hat{x},t) + \dot{U} = -i\bar{H}U - iF(\hat{x},t)U, \tag{2.79}$$

which is allows for the following identifications:

$$i\dot{\alpha}(\hat{x},t)U(t) = -iF(\hat{x},t)U(t), \tag{2.80}$$

$$\dot{U} = -i\bar{H}U. \tag{2.81}$$

So that once a driving force of the form $F(\hat{x},t)$ is known, the gauge transform can be defined:

$$\alpha(x,t) = \int dt F(\hat{x},t) \tag{2.82}$$

Once the gauge transformed Hamiltonian $H_0(\tilde{p})$ is found, it can be used in the above expansion to define the interaction representation of a small perturbation. The gauge-transformed system is effectively in an accelerated frame, the potential the particles are bound to is considered stationary and the effects of the driving force are seen in the motion of the reference frame.

2.7 Driven field dynamics

To further probe the existence of gap closure, a DC field was added to the driving force. For a sinusoidal system under AC driving, the dynamics of a single particle or a collection of particles due to a weak DC field is studied. The advantages of using the sinusoidal system are due to the Bloch oscillations possible and the possibility of a band insulating system.

Bloch oscillations are the periodic motion of the electron's quasi-momentum. From semi-classical equations of motion, the time dependence for k, and v are determined by the applied field (E). For the quasi-momentum,

$$\dot{k} = -eE \tag{2.83}$$

$$k(t) = k_0 - eEt. \tag{2.84}$$

The value for k is periodic, when k reaches the boundary at $\frac{\pi}{a}$ it is Bragg reflected back to the opposite edge, $-\frac{\pi}{a}$. For the velocity,

$$v = \dot{r} = \frac{\partial \epsilon(k)}{\partial k} \tag{2.85}$$

$$v = -J\sin(ka) = J\sin((k_0 - eEt)a). \tag{2.86}$$

The velocity oscillates with period $eE\tau = \frac{2\pi}{a}$. Thus, the electron in a static electric field will oscillate around an average position (in real space). Likewise, for a particle that begins at the leftmost edge of the quasi-momentum zone at $t = -\frac{\pi}{a}$, at time $t = \tau$ the particle will be at $k = \frac{\pi}{a}$ and will reflected back to its original value. The periods of oscillations for real and momentum space are equal.

To calculate the electric current of a driven two-band system, the possibility that the system may have multiple states occupied needs to be considered. The electric transport of one (or many) electrons in the two-band system was calculated using the quantum master equation. The general two-band system and its associated eigenvalues (λ_i) and eigenvectors ($|\psi_i\rangle$) are given by,

$$H = \epsilon(k)\sigma_z + V\sigma_x \tag{2.87}$$

$$\lambda_{1,2} = \pm\sqrt{\epsilon(k)^2 - V^2} \tag{2.88}$$

$$H\psi_1 = \lambda_1\psi_1 \tag{2.89}$$

$$H\psi_2 = \lambda_2\psi_2. \tag{2.90}$$

where the indices $(1, 2)$ indicate which band a particle occupies. For example, $\lambda_1 = -\sqrt{\epsilon(k)^2 - V^2}$ corresponds to the energy of a particle in the lower band, and $\psi_1 = \binom{0}{1}$. For a closed system, the master equation is defined as the time evolution of the density matrix, describing the probability of each the system's eigenfunctions being occupied,

$$\dot{\rho} = -i[H, \rho]. \tag{2.91}$$

From the eigenfunctions of a system $|\psi_i\rangle$, the density matrix ρ is constructed from their inner product,

$$\rho = \sum_i p_i |\psi_i\rangle\langle\psi_i|, \tag{2.92}$$

and a factor p_i which gives the probability that a system is in the state given by $|\psi_i\rangle$. These probabilities are defined by the thermal probability that a state is occupied ($\beta = 1/T$, where T is the temperature),

$$P(\lambda_i, \beta) = \frac{1}{e^{\lambda_i \beta} + 1}. \tag{2.93}$$

.

This formalism was applied to the following situations: the electric current generated by a single particle, and the net electric current generated by a full electron band. Defining the system's dynamics with the density matrix allows for the incorporation of the system's temperature, though for the closed system it will not account for additional heating or energy dissipation. For a given observable in the system, the density matrix leads to a direct method of evaluating the expected value,

$$\langle \widehat{M} \rangle = \frac{\mathrm{Tr}(\rho \widehat{M})}{\mathrm{Tr}(\rho)}. \tag{2.94}$$

The calculation of the average electric current for a single electron used the the operator $\widehat{M} = \frac{dH}{dA}$,

$$\langle i_k(t) \rangle = \frac{\mathrm{Tr}(\rho \frac{dH}{dA})}{\mathrm{Tr}(\rho)}. \tag{2.95}$$

For a collection of electrons in a band, the total current is found by summing all momentum values,

$$I(t) = \int dk \ \langle i_k(t) \rangle \tag{2.96}$$

where the integration is over the entire Brillouin zone.

2.8 Keldysh formalism

The quantum systems studied in this work involve a strong AC field to create a modified Floquet spectrum which exhibits such qualities as band-gap suppression or band inversion. In addition, the systems are also driven with a weak DC field to determine how a particle will behave in the modified Floquet spectrum. In the previous section it was discussed how the dynamics of a single electron, or a collection of electrons can be determined for a closed system through the use of a quantum master equation. Central to the work in Chapter (5) is the derivation of a master equation when the system is strongly driven far from equilibrium and also is coupled to a dissipated heat bath (phonon modes).

Green's functions are a standard method of calculating properties in quantum many-body systems and the brief discussion here follows standard texts [70, 126]. For

equilibrium systems, they give probability amplitudes for the creation and annihilation of particles at given positions and time [126] and can be used to propagate a wavefunction between two states. Interactions, such as a heat bath coupling, are incorporated through a perturbative expansion in terms of self-energy functions. There are several forms of the Green's function ($G^{R,A,<,>}(\bar{r}',t',\bar{r},t)$) which are useful in defining physical quantities for quantum systems and can be defined for fermions, bosons and phonons (the phonon Green's function is denoted as $D^{R,A,<,>}(\bar{r}',t',\bar{r},t)$). In particular, the lesser Green's function $G^<$ can be connected to the electron distribution function of a system, with the use of the spectral function ($G^<(\bar{r}',t',\bar{r},t) = i\mathbb{A}(\bar{r}',t',\bar{r},t)n(\bar{r}',t',\bar{r},t)$). The time-evolution of the electron distribution is defined by the quantum transport equation known as the Boltzmann equation.

For the discussion of general Green's functions and their definitions, the Hamiltonian has the general form,

$$H = H_0 + V \tag{2.97}$$

where H_0 may or many not be time-dependent and V contains the interactions. The equilibrium Green's function is defined by the time-ordered product of operators,

$$G(\bar{r}',t',\bar{r},t) = \langle \mathcal{T} a(\bar{r}',t') a^\dagger(\bar{r},t) \rangle \tag{2.98}$$

describing the probability that a particle is destroyed at $(\bar{r},t)$ and created at $(\bar{r}',t')$. To simplify the coordinate notation, we follow Rammer's notation of $1 \equiv (\bar{r},t)$ and $1' \equiv (\bar{r}',t')$. Of the four types of Green's functions, $G^{R,A,<,>}$, only the retarded (G^R) and the lesser ($G^<$) are discussed here, they are integral to the derivation of quantum transport equations in the nonequilibrium system. The retarded and lesser Green's functions are derived from the general form by rewriting the time-ordered operators as commutators,

$$G^R(1,1') = -i\theta(t-t')\langle \{a(\bar{r},t), a^\dagger(\bar{r}',t')\} \rangle \tag{2.99}$$

$$G^<(1,1') = i\langle a^\dagger(\bar{r},t) a(\bar{r}',t') \rangle \tag{2.100}$$

The addition of interactions requires an perturbative expansion in terms of self-energy functions $\Sigma^{R,A,<,>}$. This expansion defined the Dyson equations,

$$G = G_0 + G_0 \Sigma G \tag{2.101}$$

from which the time evolution of a Green's function can be defined. For interactions due to electron-phonon coupling, the self-energy will depend on the electron Green's functions and the phonon Green's functions.

When systems are driven far from equilibrium, it require redefinition of known equilibrium Green's functions into the nonequilibrium Green's function formalism (NEGF) [73], also known as the Keldysh Green's function formalism [72]. For the strongly driven single band discussed in Chapter (5), the Keldysh formalism provides a description of the non-equilibrium electron dynamics using quantities very similar to those of equilibrium systems. Additionally, it provides a means to derive a quantum master equation which includes dissipative effects due to phonon scattering.

Green's functions are dependent on the time ordering of the field operators. In the nonequilibrium picture the time ordering is done with respect to a contour. To define the time contour, first the system evolve is described as follows: at some initial time t_i the system is in an equilibrium state with regards to a thermal bath, at a later time t, the strong driving field is turned on. The time contour begins at t_i, continues to $t' > t$, then returns to t_i. This modifies the time-ordering by splitting it into two-branches, those operators that sit on the branch $[t_i, t']$ and those that sit on the branch $[t', t_i]$. The definition of the Green's functions, and phonon propagator is similar to the equilibrium function, with the modification due to the contour ordering,

Chapter 3

Driven Sine-Gordon model

The study of correlated systems in external fields begins with a classical model. A well-known physical system that exhibits 'dynamical stabilization' is the pendulum with a vertically oscillating support (the Kapitza pendulum). In this chapter the effects of a strong, oscillating torque on a chain of pendulums are investigated. For the Kapitza pendulum dynamical stabilization results in an inverted pendulum, with a stable position in a vertical position over the support bar. Using a multi-scale approach, an effective potential is derived which assumes dynamical changes in the system occur on two time scales: gradual changes that accumulate over each period of the driving torque and rapid oscillations that have zero mean over each period of the driving torque. It is investigated if such a chain will exhibit dynamical stabilization. This stabilization will occur as a subset of the coupled pendulums are stable in an inverted position with respect to the horizontal support. It is shown that for a sinusoidal driving torque with amplitude and frequency that satisfy $F_0/\omega^2 = 2.4048$ the effective potential will have stable points both above and below the pendulum support. When the system is driven with these parameters, the driven Sine-Gordon equation is numerically integrated to find stationary waveform solutions. It is seen that a wide soliton can be created in the system with a dissipative term introduced to keep the motion from becoming chaotic. The driven Sine-Gordon equation provides a classical model of a correlated field theory and the connection between this classical field theory and a gapped quantum field theory will be discussed. Specifically the results in this chapter set the foundation for studies of how external driving forces will affect gapped quantum systems.

3.1 Introduction

The Sine-Gordon model and its soliton solutions has been an active area of research in both classical and quantum dynamics. Classically, the Sine-Gordon model is a nonlinear system with stationary wave solutions. These solutions (called *solitons*) have been well-established and many review articles exist, [13, 134, 135]. This classical model can be connected to quantum systems, such as the Frenkel-Kontorova model [11, 136, 137], and used in describing the physics of Josephson junctions [10]. In addition to the classical field theory, the quantization of the soliton fields resulted in a new way to study interacting fermionic systems [12, 138–141]. Of interest is the mapping of the Sine-Gordon model to a massive fermionic model, which results in a gapped spectrum. Through the use of bosonization, it is seen that the massive fermionic model is equal to a model with backscattering [35, 142]. The topological aspects of solitons has lead to renewed interest in the past decade [143–145].

Driven soliton systems have been extensively studied [146–154]. In this chapter we use an approach similar to that of Kivshar [146, 155], namely the expansion of the field variable φ in terms of harmonic functions which oscillate at the frequency of the external, driving field (or torque).

In the sections that follow, the Lagrangian and Hamiltonian dynamics of the Sine-Gordon model are discussed. First the qualities of the system including the waveforms known as *solitons* are described, and the effects of strong periodic driving are explored through the effective potential. The connection between the classical Sine-Gordon model and strongly correlated electron systems is discussed. The classical results are applicable for $(3+1)$ dimensions, however will be restricted to $(1+1)$ dimensions (one spatial dimension, one time dimension). In the classical field theory, the equations of motion that one obtains from the Lagrangian, for a time-independent field can be generalized to given the equations of motion of a particle in an effective field.

The general Lagrangian density of a field theory in $(1+1)$ space has the form,

$$\mathcal{L}(\varphi(x,t)) = \frac{1}{2}(\dot{\varphi})^2 - \frac{m^2}{2}\left(\varphi'\right)^2 - V(\varphi) \tag{3.1}$$

where the differential operator defined $\partial = (\partial/\partial t, -\partial/\partial x)$. There are many nonlinear field theories which exhibit kinks and solitons. We are focusing here on the Sine-Gordon equation, a second-order differential equation which has a periodic potential term $V(\varphi) = m^2(1-\cos(\varphi))$. The classical field Lagrangian density for the Sine-Gordon

equation is given by [13]:

$$\mathcal{L}(\varphi(x,t)) = \frac{1}{2}(\partial\varphi)^2 - V(\varphi), \tag{3.2}$$

$$V(\varphi) = \left(\frac{m^4}{\lambda}\right)\cos\left[\left(\frac{\sqrt{\lambda}}{m}\right)\varphi\right]. \tag{3.3}$$

The form of the Sine-Gordon potential is chosen such that the Taylor expansion around $\varphi = 0$ will result in the Klein-Gordon potential. Inside the cosine function, the factor $\sqrt{\lambda}/m$ is the coupling constant of the model. Through a rescaling of the field variable, the equations of motion derived from the Lagrangian above of a one-dimensional field $\varphi(x,t)$ is given by,

$$-\frac{d^2\phi}{dt^2} + \frac{d^2\phi}{dx^2} = \lambda^2 \sin(\phi). \tag{3.4}$$

Solutions to eq. (3.4) have known waveforms called *solitons* [156]. The physical properties of solitons are well-established, of importance to this work is the particle-like nature of excitations in the Sine-Gordon model. These excitations are commonly called *kinks*, in the x-direction they has a hyperbolic tangent shape. Asymptotically, as $x \to -\infty$ the solution $\phi(x) = -1$ and for $x \to \infty$ the solution $\phi(x) = 1$. The soliton shape is recognized as a narrow region where there field $\phi(x)$ goes from $-1 \to 1$. A physical interpretation of a set of horizontal pendulums would show a soliton wave as a twist, as the pendulums rotate from a stable position below the support, through the vertical position over the support and return to a stable position below.

3.2 Effective Potential of a driven Sine-Gordon model

3.2.1 Driven system without damping

Beginning from the general Sine-Gordon equation in (3.4), the driving torque $f(t)$ is added to the right hand side of the system,

$$\ddot{\varphi} - \varphi'' + \lambda^2 \sin(\varphi) = F_0 \cos(\omega t). \tag{3.5}$$

To incorporate the effects of the driving torque on the dynamics of the soliton solution, the undriven solution $\varphi_0(x,t)$ is rescaled by the addition of a time dependent function $\xi(t)$, effectively shifting the system into a moving reference frame. The function $\xi(t)$ is assumed to be periodic with the same frequency as the driving torque,

$$\varphi(t) = \varphi_0(t) + \xi(t). \tag{3.6}$$

In the function $\varphi(x,t)$, the term $\varphi_0(x,t)$ contains the slow dynamics of the system, it was change gradually over a period of the driving torque. The term $\xi(x,t)$ contains the

fast dynamics of the system, it will have a zero mean over one period of the driving. The choice of $\xi(x,t)$ will be used to incorporate the effects of the driving torque and eventually derive an effective potential for the driven, damped system.

The first choice for $\xi(x,t)$ is a simple shift by a periodic function with a constant amplitude:

$$\varphi(x,t) = \varphi_0(x,t) + \xi(x,t) = \varphi_0(t) + \mathcal{C}\cos(\omega t). \tag{3.7}$$

The constant amplitude $\mathcal{C}$ is yet undetermined. Under the rescaling eqtn (3.6), the terms in eqtn (3.5) change accordingly:

$$\ddot{\varphi} = \ddot{\varphi}_0 - \left(\mathcal{C}\omega^2\right)\cos(\omega t), \tag{3.8}$$

$$\varphi'' = \varphi_0'', \tag{3.9}$$

$$\sin(\varphi) = \sin(\varphi_0 + \mathcal{C}\cos(\omega t)). \tag{3.10}$$

The shifted Sine-Gordon equation becomes,

$$\begin{aligned} \ddot{\varphi}_0 - \varphi_0'' + \lambda^2 \sin(\varphi_0 + \mathcal{C}\cos(\omega t)) \\ - \left(\mathcal{C}\omega^2\right)\cos(\omega t) = F_0\cos(\omega t). \end{aligned} \tag{3.11}$$

With the choice of $\mathcal{C} = -\frac{F_0}{\omega^2}$, it is seen how the function $\xi(t)$ can be used to cancel the driving term on the right hand side of (3.5). The field equations of (3.5) are now:

$$\ddot{\varphi}_0 - \varphi_0'' + \lambda^2 \sin(\varphi_0 - \frac{F_0}{\omega^2}\cos(\omega t)) = 0. \tag{3.12}$$

An expansion of the potential term begins by separating the slow and fast terms:

$$\begin{aligned} \sin(\varphi_0 - \frac{F_0}{\omega^2}\cos(\omega t)) = \sin(\varphi_0)\cos(\frac{F_0}{\omega^2}\cos(\omega t)), \\ - \cos(\varphi_0)\sin(\frac{F_0}{\omega^2}\cos(\omega t)). \end{aligned} \tag{3.13}$$

The nested trigonometric functions are expanded in series according to the Jacobi-Anger expansion:

$$\cos(\frac{F_0}{\omega^2}\cos(\omega t)) = J_0\left(\frac{F_0}{\omega^2}\right) + 2\sum_{n=1}^{\infty}(-1)^n J_{2n}\left(\frac{F_0}{\omega^2}\right)\cos(2n\omega t), \tag{3.14}$$

$$\sin(\frac{F_0}{\omega^2}\cos(\omega t)) = -2\sum_{n=1}^{\infty}(-1)^n J_{2n-1}\left(\frac{F_0}{\omega^2}\right)\cos((2n-1)\omega t). \tag{3.15}$$

Assuming $\frac{F_0}{\omega^2} \ll 1$, justifies keeping only the lowest order terms. Equation (3.12) becomes:

$$\ddot{\varphi}_0 - \varphi_0'' + \widetilde{\lambda}^2 \sin(\varphi_0) - 2\lambda^2 J_1\left(\frac{F_0}{\omega^2}\right)\cos(\omega t)\cos(\varphi_0) = 0 \tag{3.16}$$

$$\ddot{\varphi}_0 - \varphi_0'' + \widetilde{\lambda}^2 \sin(\varphi_0) - \widetilde{\lambda}^2\left(\frac{F_0}{2\omega^2}\right)\cos(\omega t)\cos(\varphi_0) = 0 \tag{3.17}$$

where the rescaled parameter $\widetilde{\lambda} = \lambda^2 J_0\left(\frac{F_0}{\omega^2}\right)$ is introduced and the second equation comes from an approximation to the first Bessel function. From the recursive relation between Bessel functions,

$$J_0(z) + J_2(z) = \frac{2}{z} J_1(z) \tag{3.18}$$

$$J_1(z) = \frac{z}{2}\left(J_0(z) + J_2(z)\right) \tag{3.19}$$

$$J_1(z) \approx \frac{z}{2} J_0(z) \quad (z \ll 1) \tag{3.20}$$

This simple shift will be the zeroth order approximation of the driven system.

If now a more general shift expression is used, higher orders of approximation can be found. The general expansion of a waveform,

$$\begin{aligned}\psi(x,t) &= \varphi(x,t) + \sum_n a_n(x,t)\sin(n\omega t) + \sum_n b_n(x,t)\cos(n\omega t) \\ &= \left[\varphi_0(x,t) - \frac{F_0}{\omega^2}\cos(\omega t)\right] + \sum_n a_n(x,t)\sin(n\omega t) + \sum_n b_n(x,t)\cos(n\omega t)\end{aligned} \tag{3.21}$$

includes the zeroth order term and higher (Floquet) harmonics. In the general expansion it is assumed the coefficients a_n, b_n have small amplitude $|a_n|, |b_n| \ll 1$. As above, the individual terms of the Sine-Gordon equation are listed separately. First the time derivatives,

$$\begin{aligned}\ddot{\psi}(x,t) = \ddot{\varphi}_0(x,t) &+ \frac{F_0}{\omega^2}\cos(\omega t) \\ &+ \sum_n \left(\ddot{a}_n(x,t)\sin(n\omega t) + 2(n\omega)\dot{a}_n(x,t)\cos(n\omega t) - (n\omega)^2 a_n(x,t)\sin(n\omega t)\right) \\ &+ \sum_n \left(\ddot{b}_n(x,t)\cos(n\omega t) - 2(n\omega)\dot{b}_n(x,t)\sin(n\omega t) - (n\omega)^2 b_n(x,t)\cos(n\omega t)\right);\end{aligned} \tag{3.22}$$

and next the spatial derivatives,

$$\psi''(x,t) = \varphi_0''(x,t) + \sum_n a_n''(x,t)\sin(n\omega t) + \sum_n b_n''\cos(n\omega t). \tag{3.23}$$

Finally an expression for the driven Sine-Gordon equation with the general expansion (3.21) (the x and t dependencies of ψ, φ,a_n, b_n are dropped for the remainder of this section) is established,

$$\ddot{\psi} - \psi'' + \lambda^2 \sin(\psi) = F_0 \cos(\omega t), \tag{3.24}$$

becomes:

$$\begin{aligned}
&\ddot{\varphi}_0(x,t) + \sum_n \left(\ddot{a}_n(x,t)\sin(n\omega t) + 2(n\omega)\dot{a}_n(x,t)\cos(n\omega t) - (n\omega)^2 a_n(x,t)\sin(n\omega t)\right) \\
&\quad + \sum_n \left(\ddot{b}_n(x,t)\cos(n\omega t) - 2(n\omega)\dot{b}_n(x,t)\sin(n\omega t) - (n\omega)^2 b_n(x,t)\cos(n\omega t)\right) \\
&\quad - \left(\varphi_0''(x,t) + \sum_n a_n''(x,t)\sin(n\omega t) + \sum_n b_n''\cos(n\omega t)\right) \\
&\quad \lambda^2 \sin\left(\varphi_0 - \frac{F_0}{\omega^2}\cos(\omega t) + \sum_n a_n \sin(n\omega t) + \sum_n b_n \sin(n\omega t)\right) = 0
\end{aligned} \tag{3.25}$$

To establish the perturbation expansion in our system, first the many terms with nested trigonometric functions must be expanded. In the final term of (3.25), the function $\sigma(x,t)$ is defined,

$$\sigma(x,t) = \varphi_0 + \sum_n a_n \sin(n\omega t) + \sum_n b_n \cos(n\omega t), \tag{3.26}$$

separating the term $\frac{F_0}{\omega_2}\cos(\omega t)$, and allowing for the expansion of the sine function:

$$\begin{aligned}
&\sin\left(\varphi_0 - \frac{F_0}{\omega^2}\cos(\omega t) + \sum_n a_n \sin(n\omega t) + \sum_n b_n \sin(n\omega t)\right) \\
&= \sin\left(\sigma(x,t) - \frac{F_0}{\omega^2}\cos(\omega t)\right) \\
&= \sin(\sigma(x,t))\cos\left(\frac{F_0}{\omega^2}\cos(\omega t)\right) - \cos(\sigma(x,t))\sin\left(\frac{F_0}{\omega^2}\cos(\omega t)\right)
\end{aligned} \tag{3.27}$$

Again the expansion of nested trigonometric functions is done with the Jacobi-Anger expansion, and the potential of the Sine-Gordon equation becomes,

$$\begin{aligned}
\lambda^2 \Bigg\{ &\sin(\sigma)\Big[J_0\left(\frac{F_0}{\omega^2}\right) + 2\sum_{n=1}^{\infty}(-1)^n J_{2n}\left(\frac{F_0}{\omega^2}\right)\cos(2n\omega t)\Big] \\
&+ \cos(\sigma)\Big[2\sum_{n=1}^{\infty}(-1)^n J_{2n-1}\left(\frac{F_0}{\omega^2}\right)\cos((2n-1)\omega t)\Big]\Bigg\}
\end{aligned} \tag{3.28}$$

The expansion of the terms $\sin(\sigma), \cos(\sigma)$ can be simplified from the assumption about the terms in the series: $a_n, b_n, \sin(n\omega t), \cos(n\omega t)$. Assuming the magnitude of each term of the series are very small, $|a_n|, |b_n| \ll 1$, the sum of the series is also assumed to

be small. This allows for approximations of terms accordingly,

$$\sin\left(\sum_n a_n \sin\left(n\omega t\right)\right) \approx \sum_n a_n \sin\left(n\omega t\right) \tag{3.29}$$

$$\sin\left(\sum_n b_n \cos\left(n\omega t\right)\right) \approx \sum_n b_n \cos\left(n\omega t\right) \tag{3.30}$$

$$\cos\left(\sum_n a_n \sin\left(n\omega t\right)\right) \approx 1 \tag{3.31}$$

$$\cos\left(\sum_n b_n \cos\left(n\omega t\right)\right) \approx 1. \tag{3.32}$$

Additionally, it is assumed that terms of the form $\sin\left(\dots\right)\cos\left(\dots\right)$ will add destructively in the series, and as a result may be dropped.

After all expansions and simplifications have been made, the final expression of (3.25) is,

$$\begin{aligned}
&\ddot{\varphi}_0 - \varphi_0'' + \sum_n \left(\ddot{a}_n - a_n'' - 2(n\omega)\dot{b}_n - (n\omega)^2 a_n\right)\sin\left(n\omega t\right) \\
&\quad + \sum_n \left(\ddot{b}_n - b_n'' - 2(n\omega)\dot{a}_n - (n\omega)^2 b_n\right)\cos\left(n\omega t\right) \\
&\quad + \lambda^2\Bigg\{\sin\left(\varphi\right)\left(J_0\left(\frac{F_0}{\omega^2}\right) + 2\sum_{n=1}^{\infty}(-1)^m J_{2m}\left(\frac{F_0}{\omega^2}\right)\cos\left(2m\omega t\right)\right) \\
&\quad + \cos\left(\varphi_0\right)\left(J_0\left(\frac{F_0}{\omega^2}\right)\left(\sum_n \left(a_n \sin\left(n\omega t\right) + b_n \cos\left(n\omega t\right)\right) + \sum_n b_{2n} J_{2n}\left(\frac{F_0}{\omega^2}\right)\right)\right) \\
&\quad + \cos\left(\varphi_0\right)\left(2\sum_{n=1}^{\infty}(-1)^n J_{2n-1}\left(\frac{F_0}{\omega^2}\right)\cos\left((2n-1)\omega t\right)\right) \\
&\quad + \sin\left(\varphi_0\right)\left(\sum_{n=1}^{\infty} b_{2n-1} J_{2n-1}\left(\frac{F_0}{\omega^2}\right)\right)\Bigg\}
\end{aligned} \tag{3.33}$$

From equation (3.33) the terms are separated according to slow and fast dynamics. The slow terms are identified as those independent of $\sin\left(\dots\right), \cos\left(\dots\right)$. Additionally, the series over $\sin\left(n\omega t\right), \cos\left(n\omega t\right)$ are separated into sums over even or odd harmonics. Then equation (3.33) is separated into dynamic equations for slow dynamics, and the fast dynamics determined by a_n, b_n. The terms will be kept to lowest order, which will be $\mathcal{O}(\lambda^2)$. Terms proportional to $\lambda^2 a_n$ or $\lambda^2 b_n$ are dropped. The slow dynamics are determined by the equation:

$$\begin{aligned}
&\ddot{\varphi}_0 - \varphi_0'' + \lambda^2 \sin\left(\varphi_0\right) J_0\left(\frac{F_0}{\omega^2}\right) \\
&\quad + \lambda^2\left[\sum_{n=1}^{\infty} b_{2n-1} J_{2n-1}\left(\frac{F_0}{\omega^2}\right) + \cos\left(\varphi_0\right)\left(\sum_{n=1}^{\infty} b_{2n} J_{2n}\left(\frac{F_0}{\omega^2}\right)\right)\right] \\
&\quad = 0
\end{aligned} \tag{3.34}$$

The terms proportional to $\sin(n\omega t)$, separated in even or odd harmonics:

$$\begin{aligned}\ddot{a}_{2n} - a''_{2n} - 2(2n\omega)\dot{b}_{2n} - (2n\omega)^2 a_{2n} \\ + \lambda^2 \cos(\varphi_0)\left[\sum_n a_{2n} J_0\left(\frac{F_0}{\omega^2}\right)\sin(2n\omega t)\right] = 0\end{aligned} \tag{3.35}$$

$$\begin{aligned}\ddot{a}_{2n-1} - a''_{2n-1} - 2((2n-1)\omega)\dot{b}_{2n-1} - ((2n-1)\omega)^2 a_{2n-1} \\ + \lambda^2 \cos(\varphi_0)\left[\sum_n a_{2n-1} J_0\left(\frac{F_0}{\omega^2}\right)\sin((2n-1)\omega t)\right] = 0\end{aligned} \tag{3.36}$$

The terms proportional to $\cos(n\omega t)$, separated into even or odd harmonics,

$$\begin{aligned}&\ddot{b}_{2n} - b''_{2n} + 2(2n\omega)\dot{a}_{2n} - (2n\omega)^2 b_{2n} \\ &+ \lambda^2\Bigg[\sin(\varphi_0)\left(2\sum_{l=1}^{\infty}(-1)^l J_{2l}\left(\frac{F_0}{\omega^2}\right)\cos(2l\omega t)\right) \\ &+ \cos(\varphi_0)\left(J_0\left(\frac{F_0}{\omega^2}\right) b_{2n}\cos(2n\omega t)\right) \\ &+ \cos(\varphi_0)\left(\sum_{l=1}^{\infty}(-1)^l b_{2n} J_{2l}\left(\frac{F_0}{\omega^2}\right)\Big[\cos(2[n-l]\omega t) + \cos(2[n+l]\omega t)\Big]\right) \\ &- 2\sin(\varphi_0)\left(\sum_{l=1}(-1)^l J_{2l-1}\left(\frac{F_0}{\omega^2}\right)\cos([2l-1]\omega t)\right)\Bigg] = 0\end{aligned} \tag{3.37}$$

$$\begin{aligned}&\ddot{b}_{2n-1} - b''_{2n-1} + 2([2n-1]\omega)\dot{a}_{2n-1} - ([2n-1]\omega)^2 b_{2n-1} \\ &+ \lambda^2\Bigg[\cos(\varphi_0)\Big(\sum_{l=1}^{\infty}(-1)^l J_{2l}\left(\frac{F_0}{\omega^2}\right)\Big[\cos([2(2n-1-l)-1]\omega t) \\ &+ \cos([2(2n+2l-1)-1]\omega t)\Big]\Big) b_{2n-1} \\ &- 2\sin(\varphi_0)\left(\sum_{l=1}(-1)^l J_{2l-1}\left(\frac{F_0}{\omega^2}\right)\cos([2l-1]\omega t)\right) b_{2n-1}\Bigg] = 0\end{aligned} \tag{3.38}$$

We seek a solution to the driven dynamics which results in a quasi-stationary state. In the slow dynamics equation we need to establish the coefficients a_n, b_n, which will be found from the terms proportional to $\sin(n\omega t), \cos(n\omega t)$. The equations for the harmonic dynamics are used to establish a recursive solution. To find the quasi-stationary state, the terms $\dot{a}_n, \ddot{a}_n, \dot{b}_n, \ddot{b}_n$ are set to zero, resulting in quasi-static equations:

$$\begin{aligned}-a''_{2n} - (2n\omega)^2 a_{2n} = 0 \\ -a''_{2n-1} - ((2n-1)\omega)^2 a_{2n-1} = 0\end{aligned} \tag{3.39}$$

$$\begin{aligned}-b''_{2n} - (2n\omega)^2 b_{2n} \\ + \lambda^2\left[2\sum_l (-1)^l J_{2l}\left(\frac{F_0}{\omega^2}\right)\sin(\varphi_0)\right] = 0\end{aligned} \tag{3.40}$$

$$
\begin{aligned}
&-b''_{2n-1} - ([2n-1]\omega)^2 b_{2n-1} \\
&\qquad - \lambda^2 \left[2\cos(\varphi_0) \sum_{l=1}^{\infty} (-1)^l J_{2l-1}\left(\frac{F_0}{\omega^2}\right) \right] = 0
\end{aligned}
\tag{3.41}
$$

Equations (3.39)-(3.41) are solved recursively to find solutions for a_n, b_n. The zeroth order approximation sets the spatial derivatives to zero and the solved for$a_n^{(0)}, b_n^{(0)}$.

Immediately it is seen from (3.39) that the coefficients a_n vanish for all orders of approximation:

$$
-(2n\omega)^2 a_{2n}^{(0)} = 0 \tag{3.42}
$$

$$
-((2n-1)\omega)^2 a_{2n-1}^{(0)} = 0 \tag{3.43}
$$

Equation (3.40) is solved for the b_{2n} coefficients:

$$
(2n\omega)^2 b_{2n}^{(0)} = 2\lambda^2 \sin(\varphi_0) \left[\sum_l (-1)^l J_{2l}\left(\frac{F_0}{\omega^2}\right) \right] \tag{3.44}
$$

$$
b_{2n}^{(0)} = \frac{2\lambda^2}{(2n\omega)^2} \left[\sum_l (-1)^l J_{2l}\left(\frac{F_0}{\omega^2}\right) \right] \sin(\varphi_0) \tag{3.45}
$$

and equation (3.41) is solved for the b_{2n-1} coefficients:

$$
((2n-1)\omega)^2 b_{2n-1}^{(0)} = 2\lambda^2 \cos(\varphi_0) \left[\sum_l (-1)^l J_{2l-1}\left(\frac{F_0}{\omega^2}\right) \right] \tag{3.46}
$$

$$
b_{2n-1}^{(0)} = \frac{2\lambda^2}{([2n-1]\omega)^2} \left[\sum_l (-1)^l J_{2l-1}\left(\frac{F_0}{\omega^2}\right) \right] \cos(\varphi_0) \tag{3.47}
$$

The next order of approximation is found by using the zeroth order solutions in equations 3.40,(3.41).

$$
\begin{aligned}
b_{2n}^{(1)} &= 2\lambda^2 \sin(\varphi_0) \frac{\sum_l (-1)^l J_{2l}\left(\frac{F_0}{\omega^2}\right)}{2n\omega^2} - \frac{1}{(2n\omega)^2} (b_{2n}^{(0)})'' \\
b_{2n}^{(1)} &= \frac{2\lambda^2}{(2n\omega)^2} \sum_l (-1)^l J_{2l}\left(\frac{F_0}{\omega^2}\right) \left(\sin(\varphi_0) - \frac{\sin(\varphi_0)''}{(2n\omega)^2} \right)
\end{aligned}
\tag{3.48}
$$

$$
\begin{aligned}
b_{2n-1}^{(1)} &= \frac{2\lambda^2}{([2n-1]\omega)^2} \left[\sum_l (-1)^l J_{2l-1}\left(\frac{F_0}{\omega^2}\right) \right] \cos(\varphi_0) + \frac{1}{([2n-1]\omega)^2} (b_{2n-1}^{(0)})'' \\
b_{2n-1}^{(1)} &= \frac{2\lambda^2}{([2n-1]\omega)^2} \left[\sum_l (-1)^l J_{2l-1}\left(\frac{F_0}{\omega^2}\right) \right] \left(\cos(\varphi_0) + \frac{\cos(\varphi_0)''}{((2n-1)\omega)^2} \right)
\end{aligned}
\tag{3.49}
$$

The slow dynamics equation is used to define the effective potential of the driven system. After the first order approximations are found, they are used in the slow

dynamics equation,

$$\begin{aligned}
&\ddot{\varphi}_0 - \varphi_0'' \\
&\quad + \lambda^2 \Bigg[\sin(\varphi_0) \left(J_0\left(\frac{F_0}{\omega^2}\right) + \sum_{n=1}^{\infty} b_{2n-1}^{(1)} J_{2n-1}\left(\frac{F_0}{\omega^2}\right) \right) \\
&\quad + \cos(\varphi_0) \left(\sum_{n=1}^{\infty} b_{2n}^{(1)} J_{2n}\left(\frac{F_0}{\omega^2}\right) \right) \Bigg] = 0
\end{aligned} \tag{3.50}$$

and a set of coefficients A_1, A_2, A_3, A_4 are defined, containing the summations over even and odd harmonics of Bessel functions. Beginning with the even harmonics, the explicit forms for A_1, A_2 are found:

$$A_1 = \frac{2\lambda^4}{\omega^2} \sum_n \frac{(-1)^n}{(2n)^2} J_{2n}\left(\frac{F_0}{\omega^2}\right) \sum_l (-1)^l J_{2l}\left(\frac{F_0}{\omega^2}\right), \tag{3.51}$$

$$A_2 = \frac{2\lambda^4}{\omega^4} \sum_n \frac{(-1)^n}{(2n)^4} J_{2n}\left(\frac{F_0}{\omega^2}\right) \sum_l (-1)^l J_{2l}\left(\frac{F_0}{\omega^2}\right). \tag{3.52}$$

Similarly for the odd harmonics, the explicit forms for A_3, A_4 are found:

$$A_3 = \frac{2\lambda^4}{\omega^2} \sum_n \frac{(-1)^n}{[2n-1]^2} J_{2n-1}\left(\frac{F_0}{\omega^2}\right) \sum_l (-1)^l J_{2l-1}\left(\frac{F_0}{\omega^2}\right) \tag{3.53}$$

$$A_4 = \frac{2\lambda^4}{\omega^4} \sum_n \frac{(-1)^n}{[2n-1]^4} J_{2n-1}\left(\frac{F_0}{\omega^2}\right) \sum_l (-1)^l J_{2l-1}\left(\frac{F_0}{\omega^2}\right) \tag{3.54}$$

The coefficients are evaluated numerically at given values of F_0, ω in subsequent sections. The resulting equation of motion for the driven Sine-Gordon model is given in terms of the slowly varying term φ_0. It is seen that the coupling constant λ factor multiplying $\sin(\varphi_0)$ acquires an additional factor $J_0(F_0/\omega^2)$.

$$\begin{aligned}
&\ddot{\varphi}_0 - \varphi_0'' + \lambda^2 J_0\left(\frac{F_0}{\omega^2}\right) \sin(\varphi_0) + \left(A_1(\cos(\varphi_0)) - A_2(\cos(\varphi_0)'')\right) \sin(\varphi_0) \\
&\quad + \left(A_3(\sin(\varphi_0)) - A_4(\sin(\varphi_0)'')\right) \cos(\varphi_0) = 0
\end{aligned} \tag{3.55}$$

Since the system is assumed to be in a quasi-stationary state, the term $\ddot{\varphi}_0$ will be dropped. The terms $\cos(\varphi_0)\sin(\varphi_0)$ are rewritten in terms of the double angle argument, $(1/2)\sin(2\varphi_0)$ and both sides are multiplied by φ_0',

$$\begin{aligned}
&(\varphi_0')(\varphi_0'') + A_2 \cos(\varphi_0)'' \sin(\varphi_0)\varphi_0' + A_4 \sin(\varphi_0)'' \cos(\varphi_0)\varphi_0' \\
&\quad = \lambda^2 J_0\left(\frac{F_0}{\omega^2}\right) \sin(\varphi_0)\varphi_0' + \frac{(A_1 + A_3)}{2} \sin(2\varphi)\varphi_0'
\end{aligned} \tag{3.56}$$

and integrated by parts. The terms in the slow dynamics equation can be simplified by

identifying terms accordingly:

$$\begin{aligned}
\left(\frac{df(x)}{dx}\right)\left(\frac{d^2f(x)}{dx^2}\right) &= \left(\frac{1}{2}\right)\frac{d}{dx}\left[\left(\frac{df(x)}{dx}\right)^2\right] \\
(\varphi_0')(\varphi_0'') &= \frac{1}{2}\left[(\varphi_0)'\right]' \\
\cos(\varphi_0)''\sin(\varphi_0)\varphi_0' &= \cos(\varphi_0)''\left[-\cos(\varphi_0)\right]' = -\frac{1}{2}\left[\cos(\varphi_0)'\right]' \\
\sin(\varphi_0)''\cos(\varphi_0)\varphi_0' &= \sin(\varphi_0)''\left[\sin(\varphi_0)\right]' = \frac{1}{2}\left[\sin(\varphi_0)'\right]' \\
\sin(2\varphi_0)\varphi_0' &= -\frac{1}{2}\left[\cos(2\varphi_0)\right]' \\
\sin(\varphi_0)\varphi_0' &= -\left[\cos(\varphi_0)\right]'
\end{aligned} \tag{3.57}$$

This results in an equation,

$$\begin{aligned}
&\frac{1}{2}\left[(\varphi_0')^2\right]' - \frac{1}{2}A_2\left[(\cos(\varphi_0)')^2\right]' + \frac{1}{2}A_4\left[(\sin(\varphi_0)')^2\right]' \\
&\qquad = -\lambda^2 J_0\left(\frac{F_0}{\omega^2}\right)\left[\cos(\varphi_0)\right]' - \left(\frac{A_1+A_3}{4}\right)\left[\cos(2\varphi_0)\right]',
\end{aligned} \tag{3.58}$$

which is easily integrated ($\mathcal{C}$ is a constant due to integration):

$$\begin{aligned}
&\frac{1}{2}(\varphi_0')^2 - \frac{1}{2}A_2(\cos(\varphi_0)')^2 + \frac{1}{2}A_4(\sin(\varphi_0)')^2 \\
&\qquad = -\lambda^2 J_0\left(\frac{F_0}{\omega^2}\right)\cos(\varphi_0) - \left(\frac{A_1+A_3}{4}\right)\cos(2\varphi_0) + \mathcal{C},
\end{aligned} \tag{3.59}$$

This equation is simplified further to find an expression for $\mathcal{U}(\varphi_0) = \frac{1}{2}(\varphi_0')^2$,

$$\begin{aligned}
&\frac{1}{2}(1 + A_2\sin(\varphi_0)^2 + A_4\cos(\varphi_0)^2)(\varphi_0')^2 \\
&\qquad = -\lambda^2 J_0\left(\frac{F_0}{\omega^2}\right)\cos(\varphi_0) - \left(\frac{A_1+A_3}{4}\right)\cos(2\varphi_0) + \mathcal{C}.
\end{aligned} \tag{3.60}$$

The final expression for the effective potential is given as:

$$\mathcal{U}(\varphi_0) = -\frac{1}{2}(\varphi_0')^2 = \frac{\lambda^2 J_0\left(\frac{F_0}{\omega^2}\right)\cos(\varphi_0) + \left(\frac{A_1+A_3}{4}\right)\cos(2\varphi_0) + \mathcal{C}}{1 + A_2\sin(\varphi_0)^2 + A_4\cos(\varphi_0)^2} \tag{3.61}$$

It is seen in (3.61), that by choosing the driving torque amplitude and frequency such that $\frac{F_0}{\omega^2} = 2.4048$, the numerator term proportional to $\cos(\varphi_0)$ will vanish. The result will be the slow dynamics behaving according to a potential proportional to $\cos(2\varphi_0)$.

3.2.2 Numerical analysis of driven system without damping

To explore the period doubling in the driven Sine Gordon model, the effective potential is evaluated numerically. The summations in the coefficients A_1, A_2, A_3, A_4 converge rapidly and the series' can be truncated after 10 elements. Additionally, the

coefficient $\lambda^2 J_0\left(\frac{F_0}{\omega^2}\right)$ is defined as A_0. Depending on the values chosen for the driving amplitude and frequency the periodicity of the effective potential can be tuned from τ to 2τ, shown in figure 3.1. The simulation is valid for systems with a weak potential $\lambda \ll 1$. When $\frac{F_0}{\omega^2} \approx 2.4048$ the term A_0 is suppressed and the effective potential is proportional to $\cos(2\varphi_0)$. As the driving amplitude is increased it affects the stability

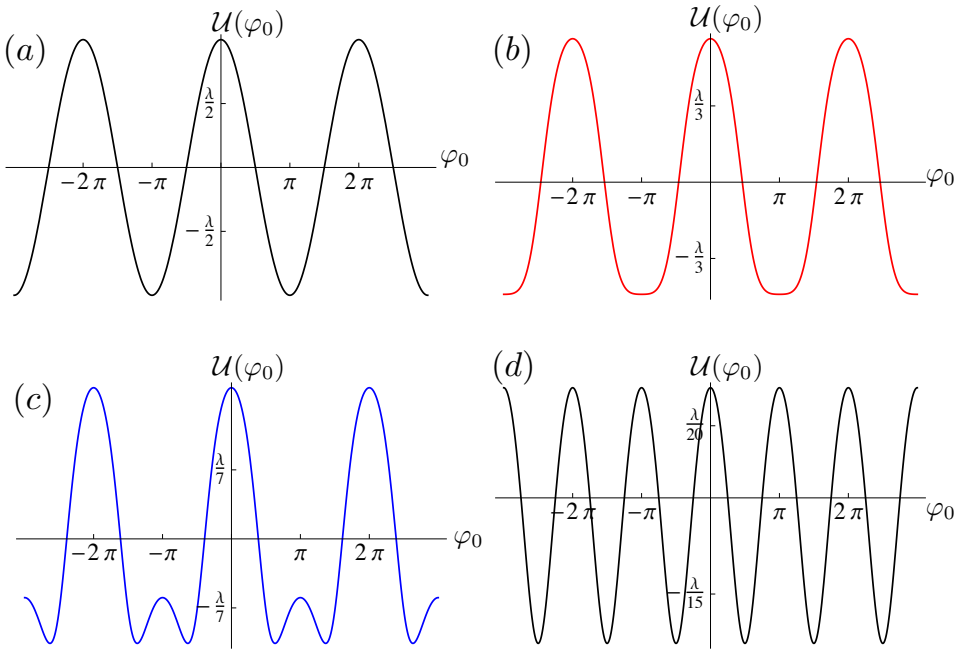

Figure 3.1: Emergence of period doubling in the driven Sine Gordon model. As the driving amplitude is tuned towards a root of the zeroth Bessel function, the effective potential changes periodicity. Shown are simulations for $\omega = 1.0$ and $F_0 = \{0.1, 1.0, 1.8, 2.405\}$ (a) - (d), respectively.

points of the system. For small driving amplitudes, the system behaves as a Sine-Gordon model with the dominant terms of the potential proportional to $\cos(\varphi)$. In figure 3.1(a) such a system has an effective potential with stable positions at $\varphi = 0, 2\pi$. Increasing the driving amplitude such that the dominant term of the potential is now $\cos(2\varphi)$ corresponds to the system having stable points at $\varphi = 0, \pi, 2\pi$.

For values of F_0, ω which do not correspond to a root of J_0, it is seen that A_0 is the dominant term in the effective potential (see figure 3.2).

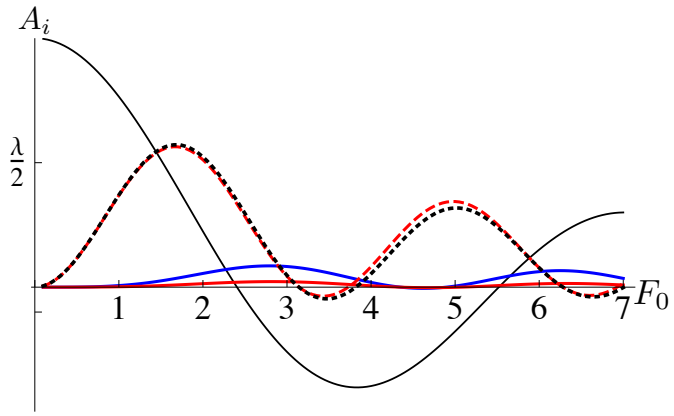

Figure 3.2: Dependence of A_i on driving amplitude. Shown are A_0 (black, solid), A_1 (blue, solid), A_2 (red, solid), A_3 (red, dashed), A_4 (black, dotted). $\omega = 1$ and $\lambda = 1$. Where A_0 vanished, the remaining coefficients are non-zero, leading to period doubling.

3.2.3 Driven system with damping

The system studied is an one-dimensional Sine-Gordon (SG) model with a driving torque of amplitude (F_0) and a dissipative term with constant amplitude α,

$$\frac{d^2\varphi}{dt^2} - \frac{d^2\varphi}{dx^2} = -\alpha\frac{d\varphi}{dt} - \lambda^2 \sin(\varphi) + F_0 \cos(\omega t). \tag{3.62}$$

The solution to the un-driven SG model, where no dissipation is present is labelled as (φ_0). These solutions are well known waveforms known as solitons.

With the driving torque present, the un-driven solution is modified by the addition of a function ($\xi(t)$). As described in [3], this splits the solution of the driven system into two terms: $\varphi_0(x,t)$ is assumed to change slowly over one period of the driving torque while $\xi(x,t)$ is assumed to oscillate rapidly. The form of $\xi(t)$ is chosen as ($\xi(t) = \mathcal{B}\sin(\omega t) + \mathcal{C}\cos(\omega t)$), when averaged over one period of the driving torque the additional term vanishes. The shifted field $\varphi(x,t)$ has the general form,

$$\varphi(x,t) = \varphi_0(x,t) + \xi(t) = \varphi_o(x,t) + \mathcal{B}\sin(\omega t) + \mathcal{C}\cos(\omega t). \tag{3.63}$$

Using the equation (3.63) in equation (3.62),

$$\begin{aligned}\frac{d^2\varphi_0}{dt^2} - \frac{d^2\varphi_0}{dx^2} = \\ -\alpha\frac{d\varphi_0}{dt} - \lambda^2 \sin(\varphi_o(x,t) + \mathcal{B}\sin(\omega t) + \mathcal{C}\cos(\omega t) + F_0\cos(\omega t)) + \\ (\mathcal{B}\omega^2 + \alpha\mathcal{C}\omega)\sin(\omega t) + (\mathcal{C}\omega^2 - \alpha\mathcal{B}\omega + F_0)\cos(\omega t)\end{aligned} \tag{3.64}$$

The coefficients $\mathcal{B}, \mathcal{C}$ can be chosen to exactly cancel the terms proportional to $\sin(\omega t)$,

and $\cos(\omega t)$,

$$\mathcal{B} = \frac{(\alpha F_0)}{(\omega(\omega^2+\alpha^2))} \qquad ,\mathcal{C} = \frac{(-F_0)}{(\omega^2+\alpha^2)}, \tag{3.65}$$

it is noted that for vanishingly small damping $\alpha \to 0$ the coefficients $\mathcal{B}, \mathcal{C}$ reduce to the undamped values $\mathcal{B} \to 0$, and $\mathcal{C} \to -\frac{F_0}{\omega^2}$. The resulting expression for the soliton is

$$\varphi(x,t) = \varphi_0(x,t) - \left(\frac{F_0}{(\omega^2+\alpha^2)}\right)\cos(\omega t) + \left(\frac{F_0\alpha}{\omega(\omega^2+\alpha^2)}\right)\sin(\omega t) \tag{3.66}$$

The derivation of the effective potential follows closely the derivation in Section 3.2.1. The solution of equation (3.62) is expressed in a series expansion,

$$\varphi(x,t) = \varphi_0 + \xi(t) + \sum_n a_n \sin(n\omega t) + \sum_n b_n \cos(n\omega t) \tag{3.67}$$

The derivatives of φ for use in the driven, damped Sine-Gordon model:

$$\begin{aligned}
\ddot{\varphi} &= \ddot{\varphi}_0 - \mathcal{B}\omega^2 \sin(\omega t) - \mathcal{C}\cos(\omega t) \\
&\sum_n (\ddot{a}_n \sin(n\omega t) + 2(n\omega)\dot{a}_n \cos(n\omega t) - a_n(n\omega)^2 \sin(n\omega t) \\
&\sum_n (\ddot{b}_n \cos(n\omega t) - 2(n\omega)\dot{b}_n \sin(n\omega t) - b_n(n\omega)^2 \cos(n\omega t) \\
\varphi'' &= \varphi'' + \sum_n (a_n'' \sin(n\omega t)) + \sum_n (b_n'' \cos(n\omega t)) \\
\dot{\varphi} &= \dot{\varphi}_0 + \mathcal{B}\omega\cos(\omega t) - \mathcal{C}\omega\sin(\omega t) \\
&+ \sum_n (\dot{a}_n \sin(n\omega t) + a_n(n\omega)\cos(n\omega t)) \\
&+ \sum_n (\dot{b}_n \cos(n\omega t) - b_n(n\omega)\sin(n\omega t))
\end{aligned} \tag{3.68}$$

The expansion of $\sin(\varphi)$ uses the same smallness arguments as in Section 3.2.1, no assumption of smallness is made with respect to the damping term. First, separating the terms in the argument

$$\begin{aligned}
\varphi(x,t) &= \alpha(x,t) + \gamma(x,t) \\
\alpha(x,t) &= \varphi_0 + \sum_n a_n \sin(n\omega t) + \sum_n b_n \cos(n\omega t) \\
\gamma(x,t) &= \mathcal{B}\sin(\omega t) + \mathcal{C}\cos(\omega t)
\end{aligned}$$

$$\sin(\varphi) = \sin(\alpha)\cos(\gamma) + \cos(\alpha)\sin(\gamma)$$

Simplifying the terms $\sin(\alpha), \cos(\alpha)$ by using the fact that $|a_n|, |b_n| \ll 1$.

$$\alpha(x,t) = \varphi_0 + \chi(x,t) \tag{3.69}$$

$$\chi(x,t) = \sum_n a_n \sin(n\omega t) + \sum_n b_n \cos(n\omega t) \tag{3.70}$$

$$\sin(\alpha) = \sin(\varphi_0 + \chi) = \sin(\varphi_0)(1) + \cos(\varphi_0)\sin(\chi) \tag{3.71}$$

$$\cos(\alpha) = \cos(\varphi_0) - \sin(\varphi_0)\chi \tag{3.72}$$

Expanding the terms $\cos(\gamma), \sin(\gamma)$;

$$\begin{aligned} \sin\gamma &= \sin(\mathcal{B}\sin(\omega t))\cos(\mathcal{C}\cos(\omega t)) + \\ &\quad \cos(\mathcal{B}\sin(\omega t))\sin(\mathcal{C}\cos(\omega t)) \\ &= I + II \\ \cos\gamma &= \cos(\mathcal{B}\sin(\omega t))\cos(\mathcal{C}\cos(\omega t)) - \\ &\quad \sin(\mathcal{B}\sin(\omega t))\sin(\mathcal{C}\cos(\omega t)) \\ &= III + IV \end{aligned} \tag{3.73}$$

The nested trigonometric functions are rewritten in terms of Bessel functions via the Jacobi-Anger expansions. The result is four terms.

$$\begin{aligned} I &= J_0(\mathcal{B})J_0(\mathcal{C}) + 2J_0(\mathcal{C})\sum_n J_{2n}(\mathcal{B})\cos(2n\omega t) + 2J_0(\mathcal{B})\sum_n (-)^n J_{2n}(\mathcal{C})\cos(2n\omega t) \\ &\quad + 4\sum_{n,m}(-)^m J_{2n}(\mathcal{B})J_{2m}(\mathcal{C})\cos(2n\omega t)\cos(2m\omega t) \\ &= J_0(\mathcal{B})J_0(\mathcal{C}) + 2J_0(\mathcal{C})\sum_n J_{2n}(\mathcal{B})\cos(2n\omega t) + 2J_0(\mathcal{B})\sum_n (-)^n J_{2n}(\mathcal{C})\cos(2n\omega t) \\ &\quad + 2\sum_n (-)^n J_{2n}(\mathcal{B})J_{2n}(\mathcal{C}) \end{aligned} \tag{3.74}$$

$$\begin{aligned} II &= 2(\sum_n J_{2n-1}(\mathcal{B})\sin((2n-1)\omega t))(-2\sum_n J_{2n-1}(\mathcal{C})\cos((2n+1)\omega t)) \\ &= 0 \end{aligned} \tag{3.75}$$

$$\begin{aligned} III &= 2J_0(\mathcal{C})\sum_n J_{2n-1}(\mathcal{B})\sin((2n-1)\omega t) \\ &\quad + 4\sum_{n,m} J_{2n-1}(\mathcal{B})J_{2m}(\mathcal{C})\sin((2n-1)\omega t)\cos(2m\omega t) \\ &= 2J_0(\mathcal{C})\sum_n J_{2n-1}(\mathcal{B})\sin((2n-1)\omega t) \end{aligned} \tag{3.76}$$

$$
\begin{aligned}
IV &= -2J_0(\mathcal{B})\sum_m J_{2m-1}(\mathcal{C})\cos\left((2m-1)\omega t\right) \\
&\quad - 4\sum_{n,m} J_{2n}(\mathcal{B})J_{2m-1}(\mathcal{C})\cos\left(2n\omega t\right)\cos\left((2m-1)\omega t\right) \\
&= -2J_0(\mathcal{B})\sum_m J_{2m-1}(\mathcal{C})\cos\left((2m-1)\omega t\right)
\end{aligned}
\tag{3.77}
$$

The full expansion of the term $\sin(\varphi)$, in terms of (I, II, III, IV);

$$
\sin(\varphi) = (\sin(\varphi_0) + \chi(x,t)\cos(\varphi_0))(I + II) + (\cos(\varphi_0) - \chi(x,t)\sin(\varphi_0))(III + IV)
\tag{3.78}
$$

The full expression for the system, now expanded with φ, is divided into slowly evolving terms, terms proportional to $\sin(\omega t)$ and terms proportional to $\cos(\omega t)$.

3.2.4 Full Expansion

The full expansion of the driven, damped Sine-Gordon equation, given in (3.62) and reproduced here,

$$
\ddot{\varphi} - \varphi'' = -\alpha\dot{\varphi} - \lambda^2\sin(\varphi) + F_0\cos(\varphi)
\tag{3.79}
$$

is found by using the shifted series expansion defined above.

$$
\begin{aligned}
&\Bigg[\ddot{\varphi_0} - \mathcal{B}\omega^2\sin(\omega t) - \mathcal{C}\omega^2\cos(\omega t) + \sum_n\Bigg(\ddot{a_n}\sin(n\omega t) + 2(n\omega)\dot{a_n}\cos(n\omega t) \\
&\quad - a_n(n\omega)^2\sin(n\omega t)\Bigg) + \sum_n\Bigg(\ddot{b_n}\cos(n\omega t) - 2(n\omega)\dot{b_n}\sin(n\omega t) - b(n\omega)^2\cos(n\omega t)\Bigg)\Bigg] \\
&\quad - \Bigg[\varphi_0'' + \sum_n(a_n''\sin(n\omega t)) + \sum(b_n''\cos(n\omega t))\Bigg] \\
&\quad = -\alpha\Bigg[\dot{\varphi_0} + \mathcal{B}\omega\cos(n\omega t) - \mathcal{C}\omega\sin(n\omega t) + \sum_n\Bigg(\dot{a_n}\sin(n\omega t) + a_n(n\omega)\cos(n\omega t)\Bigg) \\
&\quad + \sum_n\Bigg(\dot{b_n}\cos(n\omega t) - b_n(n\omega)\sin(n\omega t)\Bigg)\Bigg] \\
&\quad - \lambda^2\Bigg([I]\sin(\varphi_0) + [III]\cos(\varphi_0) + [IV]\cos(\varphi_0) \\
&\quad + [(2\sum_n(-1)^n J_{2n}(\mathcal{B})J_{2n}(\mathcal{C}))(\sum(a_n\sin(n\omega t)) + \sum(b_n\cos(n\omega t)))] \\
&\quad + (J_0(\mathcal{C})\sum_n J_{2n}(\mathcal{B})b_{2n} + J_0(\mathcal{B})\sum J_{2n}(\mathcal{C})b_{2n})\cos(\varphi_0) \\
&\quad - (J_0(\mathcal{C})\sum_n J_{2n+1}(\mathcal{B}a_{2n+1})\sin(\varphi_0) + (J_0(\mathcal{B})\sum J_{2n+1}(\mathcal{C})b_{2n+1})\sin(\varphi_0)\Bigg) \\
&\quad + F_0\cos(\omega t)
\end{aligned}
\tag{3.80}
$$

Again, as in the previous section, the full expansion is separated according to slow dynamics, and terms proportional to even and odd harmonics of $\sin(n\omega t), \cos(n\omega t)$. The slow dynamics are determined by the terms in the full expansion which are independent of $\sin(n\omega t), \cos(n\omega t)$,

$$\begin{aligned}\ddot{\varphi_0} - \varphi_o'' = -\alpha\dot{\varphi_0} - (\lambda^2)[[J_0(\mathcal{B})J_0(\mathcal{C}) - \\ J_0(\mathcal{C})\sum_m J_{2m-1}(\mathcal{B})a_{2m-1} + 2\sum_m (-)^m J_{2m}(\mathcal{B})J_{2m}(\mathcal{C})]\sin(\varphi_0) + \\ \Big(J_0(\mathcal{C})\sum_n J_{2n}(\mathcal{B}) + J_0(\mathcal{B})\sum_n J_{2n}(\mathcal{C})\Big)b_{2n}\cos(\varphi_0) + \\ (J_0(\mathcal{B})\sum J_{2n-1}(\mathcal{C})b_{2n-1})\sin(\varphi_0)]\end{aligned} \tag{3.81}$$

The even and odd harmonics of $\sin(n\omega t), \cos(n\omega t)$ are used to define the equations of motion for the coefficients of the series expansion. The even harmonics of $\sin(n\omega t)$,

$$\begin{aligned}(\ddot{a}_{2n} - (2n\omega)a_{2n}) - 2(2n\omega)^2\dot{b}_{2n} - a_{2n}'' \\ = -\alpha(\dot{a}_{2n} - (2n\omega)b_{2n}) - (\lambda)^2(J_0(\mathcal{B})J_0(\mathcal{C})a_{2n} \\ + 2(\sum_k (-)^k J_{2k}(\mathcal{B})J_{2k}(\mathcal{C}))a_{2n}\cos(\varphi_0)\end{aligned} \tag{3.82}$$

the odd harmonics of $\sin(n\omega t)$,

$$\begin{aligned}(\ddot{a}_{2n+1} - ((2n+1)\omega)^2 a_{2n+1}) - 2((2n+1)\omega)\dot{b}_{2n+1} - a_{2n+1}'' \\ = -\alpha(\dot{a}_{2n+1} - ((2n+1)\omega)b_{2n+1}) - (\lambda)^2\Big(J_0(\mathcal{B})J_0(\mathcal{C})a_{2n+1} \\ + 2(\sum_k (-)^k J_{2k}(\mathcal{B})J_{2k}(\mathcal{C}))a_{2n+1}\cos(\varphi_0) + 2J_0(\mathcal{C})J_{2n+1}(\mathcal{B})\cos(\varphi_0)\Big)\end{aligned} \tag{3.83}$$

the even harmonics of $\cos(n\omega t)$,

$$\begin{aligned}(\ddot{b}_{2n} - (2n\omega)^2 b_{2n}) + 2(2n\omega)\dot{a}_{2n} - b_{2n}'' = \\ - \alpha(\dot{b}_{2n} + (2n\omega)a_{2n}) - (\lambda)^2(2(J_{2n}(\mathcal{B})J_0(\mathcal{C}) \\ + J_{2n}(\mathcal{C})J_0(\mathcal{B}))\sin(\varphi_0) + (J_0(\mathcal{C})J_0(\mathcal{B}) \\ + 2(\sum_k (-)^k J_{2k}(\mathcal{B})J_{2k}(\mathcal{C}))b_{2n}\cos(\varphi_0)\end{aligned} \tag{3.84}$$

and the odd harmonics of $\cos(n\omega t)$,

$$\begin{aligned}(\ddot{b}_{2n+1} - ((2n+1)\omega)^2 b_{2n+1}) + 2((2n+1)\omega)\dot{a}_{2n+1} - b_{2n+1}'' \\ = -\alpha(\dot{b}_{2n+1} + ((2n+1)\omega)a_{2n+1}) - (\lambda)^2(-2(J_{2m+1}(\mathcal{C})J_0(\mathcal{B})) \\ + (J_0(\mathcal{C})J_0(\mathcal{B}) + 2(\sum_k (-)^k J_{2k}(\mathcal{B})J_{2k}(\mathcal{C}))b_{2n+1}\cos(\varphi_0)\end{aligned} \tag{3.85}$$

From equations (3.82),(3.83),(3.84),(3.85), solutions for a_n, b_n are found by self-consistent calculation. The results are used in the slow term equation. To lowest order in (λ^2),

terms proportional to $(\lambda^2)a_n, (\lambda^2)b_n$ are dropped. The equations for a_{2n}, a_{2n+1} reduce to

$$\begin{aligned}
(\ddot{a}_{2n} - (2n\omega)^2 a_{2n}) - 2(2n\omega)\dot{b}_{2n} - a''_{2n} &= -\alpha(\dot{a}_{2n} - (2n\omega)b_{2n}) \\
(\ddot{a}_{2n+1} - ((2n+1)\omega)^2 a_{2n+1}) - 2((2n+1)\omega)\dot{b}_{2n+1} - a''_{2n+1} & \\
= -\alpha(\dot{a}_{2n+1} - ((2n+1)\omega)b_{2n+1}) - (\lambda)^2(J_0(\mathcal{B})J_0(\mathcal{C}))\cos(\varphi_0) &
\end{aligned} \tag{3.86}$$

The equations for b_{2n}, b_{2n+1},

$$\begin{aligned}
(\ddot{b}_{2n} - (2n\omega)^2 b_{2n}) + 2(2n\omega)\dot{a}_{2n} - b''_{2n} & \\
= -\alpha(\dot{b}_{2n} + (2n\omega)a_{2n}) - (\lambda)^2(2(J_{2m}(\mathcal{B})J_0(\mathcal{C}) + J_{2m}(\mathcal{C})J_0(\mathcal{B}))\sin(\varphi_0) & \\
(\ddot{b}_{2n+1} - ((2n+1)\omega)^2 b_{2n+1}) + 2((2n+1)\omega)\dot{a}_{2n+1} - b''_{2n+1} & \\
= -\alpha(\dot{b}_{2n+1} + ((2n+1)\omega)a_{2n+1}) - (\lambda)^2(-2(J_{2m+1}(\mathcal{C})J_0(\mathcal{B})) &
\end{aligned} \tag{3.87}$$

For a static solution, the time derivatives in the above equations are set to zero. The zeroth approximation to the $a_n^{(0)}, b_n^{(0)}$ is found by solving the above equations, where the spatial derivates are also set to zero,

$$\begin{aligned}
a_{2n}^{(0)} &= \left(\frac{-\alpha(\lambda^2)}{(2n\omega)^3 + \alpha^2(2n\omega)}\right)(2[J_0(\mathcal{C})J_{2n}(\mathcal{B}) + J_0(\mathcal{B})J_{2n}(\mathcal{C})\sin(\varphi_0) \\
b_{2n}^{(0)} &= \left(\frac{\alpha(\lambda^2)}{(2n\omega)^2 + \alpha^2}\right)(2(J_0(\mathcal{C})J_{2n}(\mathcal{B}) + J_0(\mathcal{B})J_{2n}(\mathcal{C})))\sin(\varphi_0)
\end{aligned} \tag{3.88}$$

$$\begin{aligned}
a_{2n+1}^{(0)} &= \left(\frac{\lambda}{(2n+1)\omega}\right)^2 (2J_0(\mathcal{C})J_{2n+1}(\mathcal{B})\cos(\varphi_0)) \\
&\quad - \left(\frac{\alpha}{(2n+1)\omega}\right)\left(\frac{\lambda^2}{((2n+1)\omega)^2 + \alpha^2}\right)\Big[\left(\frac{\alpha}{(2n+1)\omega}\right)(2J_0(\mathcal{C})J_{2n+1}(\mathcal{B})) \\
&\quad - (2J_0(\mathcal{B})J_{2n+1}(\mathcal{C}))\Big]\cos(\varphi_0) \\
b_{2n+1}^{(0)} &= \left(\frac{\lambda^2}{((2n+1)\omega)^2 + \alpha^2}\right)\Big[\left(\frac{\alpha}{(2n+1)\omega}\right)(2J_0(\mathcal{C})J_{2n+1}(\mathcal{B})) \\
&\quad - (2J_0(\mathcal{B})J_{2n+1}(\mathcal{C}))\Big]\cos(\varphi_0)
\end{aligned} \tag{3.89}$$

Collect terms in the expression for $a^{(0)}, b^{(0)}$,

$$a_{2n}^{(0)} = \mathcal{C}_1 \sin(\varphi_0) \qquad a_{2n}^{(0)\prime\prime} = \mathcal{C}_1 \sin(\varphi_0)'' \tag{3.90}$$

$$b_{2n}^{(0)} = \mathcal{C}_2 \sin(\varphi_0) \qquad b_{2n}^{(0)\prime\prime} = \mathcal{C}_2 \sin(\varphi_0)'' \tag{3.91}$$

$$a_{2n+1}^{(0)} = \mathcal{C}_3 \cos(\varphi_0) \qquad a_{2n+1}^{(0)\prime\prime} = \mathcal{C}_3 \cos(\varphi_0)'' \tag{3.92}$$

$$b_{2n+1}^{(0)} = \mathcal{C}_4 \cos(\varphi_0) \qquad b_{2n+1}^{(0)\prime\prime} = \mathcal{C}_4 \cos(\varphi_0)'' \tag{3.93}$$

The next approximation $a_n^{(1)}, b_n^{(1)}$ is found with $a_n^{(0)}, b_n^{(0)}$.

$$\begin{aligned}
a_{2n}^{(1)} &= \frac{-1}{(2n\omega)^2}[a_{2n}^{(0)\prime\prime} + \alpha(2n\omega)b_{2n}^{(1)}] \\
b_{2n}^{(1)} &= \frac{-1}{(2n\omega)^2}[b_{2n}^{(0)\prime\prime} - \alpha(2n\omega)a_{2n}^{(1)} - \\
&\quad (\lambda^2)(2[J_0(\mathcal{C})J_{2n}(\mathcal{B}) + J_0(\mathcal{B})J_{2n}(\mathcal{C})]\sin(\varphi_0))] \\
a_{2n+1}^{(1)} &= \frac{-1}{((2n+1)\omega)^2}[a_{2n+1}^{(0)\prime\prime} + \alpha((2n+1)\omega)b_{2n+1}^{(1)} - \\
&\quad (\lambda^2)(2J_0(\mathcal{C})J_{2n+1}(\mathcal{B}))\cos(\varphi_0)] \\
b_{2n+1}^{(1)} &= \frac{-1}{((2n+1)\omega)^2}[b_{2n+1}^{(0)\prime\prime} - \alpha((2n+1)\omega)a_{2n+1}^{(1)} + \\
&\quad (\lambda^2)(2J_0(\mathcal{B})J_{2n+1}(\mathcal{C}))\cos(\varphi_0)]
\end{aligned} \tag{3.94}$$

Using the expressions in equations (3.90)–(3.93)to solve equation (3.94),

$$\begin{aligned}
a_{2n}^{(1)} &= \frac{-1}{(2n\omega)^2}([\mathcal{C}_1 - \frac{\alpha^2}{(2n\omega)^2+\alpha^2}(\mathcal{C}_1 - \frac{(2n\omega)}{\alpha}\mathcal{C}_2)](\sin(\varphi_0)^{\prime\prime}) \\
&\quad - 2(\lambda^2)[J_0(\mathcal{C})J_{2n}(\mathcal{B}) + J_0(\mathcal{B})J_{2n}(\mathcal{C})]\sin(\varphi_0)) \\
b_{2n}^{(1)} &= \frac{-1}{(2n\omega)^2+\alpha^2}[(\mathcal{C}_2 + \frac{\alpha}{2n\omega}\mathcal{C}_1)\sin(\varphi_0)^{\prime\prime} \\
&\quad - 2(\lambda^2)[J_0(\mathcal{C})J_{2n}(\mathcal{B}) + J_0(\mathcal{B})J_{2n}(\mathcal{C})]\sin(\varphi_0)
\end{aligned} \tag{3.95}$$

$$\begin{aligned}
a_{2n+1}^{(1)} &= \frac{1}{((2n+1)\omega)^2+\alpha^2}[\left(\frac{\alpha\mathcal{C}_3}{(2n+1)\omega} - \mathcal{C}_4\right)\cos(\varphi_0)^{\prime\prime} \\
&\quad + \left[\frac{\alpha\lambda^2}{(2n+1)\omega}(2J_0(\mathcal{B})J_{2n+1}(\mathcal{C})) + \lambda^2(2J_0(\mathcal{C})J_{2n+1}(\mathcal{B}))\right]\cos(\varphi_0)] \\
b_{2n+1}^{(1)} &= \frac{-(\alpha\mathcal{C}_3 + \mathcal{C}_4)}{((2n+1)\omega)^2+\alpha^2}\cos(\varphi_0)^{\prime\prime} \\
&\quad + \frac{(2n+1)\omega}{((2n+1)\omega)^2+\alpha^2}\left[\frac{2\alpha\lambda^2}{((2n+1)\omega)^2}(J_0(\mathcal{C})J_{2n+1}(\mathcal{B}))\right. \\
&\quad \left. - 2\lambda^2(J_0(\mathcal{B})J_{2n+1}(\mathcal{C}))\right]\cos(\varphi_0)
\end{aligned} \tag{3.96}$$

Rewriting $b_{2n}^{(1)}, b_{2n+1}^{(1)}, a_{2n+1}^{(1)}$,

$$\begin{aligned}
a_{2n+1}^{(1)} &= \mathcal{D}_1(\alpha,\omega;2n+1)\cos(\varphi_0)^{\prime\prime} + \mathcal{D}_2(\alpha,\omega;2n+1)\cos(\varphi_0) \\
b_{2n}^{(1)} &= -\mathcal{D}_3(\alpha,\omega;2n)\sin(\varphi_0)^{\prime\prime} + \mathcal{D}_4(\alpha,\omega;2n)\sin(\varphi_0) \\
b_{2n+1}^{(1)} &= -\mathcal{D}_5(\alpha,\omega;2n+1)\cos(\varphi_0)^{\prime\prime} + \mathcal{D}_6(\alpha,\omega;2n+1)\cos(\varphi_0)
\end{aligned} \tag{3.97}$$

Use these expressions in the slow term equation (equation (3.81) rewritten here),

$$\begin{aligned}\ddot{\varphi_0} - \varphi_o'' = -\alpha\dot{\varphi_0} - (\lambda^2)[[J_0(\mathcal{B})J_0(\mathcal{C}) - \\ J_0(\mathcal{C})\sum_m J_{2m-1}(\mathcal{B})a_{2m-1}^{(1)} + 2\sum_m (-)^m J_{2m}(\mathcal{B})J_{2m}(\mathcal{C})]\sin(\varphi_0) + \\ [(J_0(\mathcal{C})\sum_n J_{2n}(\mathcal{B}) + J_0(\mathcal{B})\sum_n J_{2n}(\mathcal{C}))b_{2n}^{(1)} + \\ (J_0(\mathcal{B})\sum J_{2n-1}(\mathcal{C})b_{2n-1}^{(1)})]\cos(\varphi_0)]\end{aligned} \tag{3.98}$$

To solve for the static solution, the time derivatives of φ_0 are set to zero. The remaining terms are only dependent on φ_0, φ_0'. (The factors of $\mathcal{Z}_i$ are constants only dependent on α, ω)

$$\begin{aligned}\varphi_0'' = (\mathcal{Z}_1)\sin(\varphi_0) + (\mathcal{Z}_2)\cos(\varphi_0)''\sin(\varphi_0) + (\mathcal{Z}_3)\cos(\varphi_0)\sin(\varphi_0) \\ + (\mathcal{Z}_4)\sin(\varphi_0)''\cos(\varphi_0) + (\mathcal{Z}_5)\sin(\varphi_0)\cos(\varphi_0)\end{aligned} \tag{3.99}$$

The terms proportional to $\sin(\varphi_0)\cos(\varphi_0)$ are rewritten as double-angle terms.

$$\begin{aligned}\varphi_0'' = (\mathcal{Z}_1)\sin(\varphi_0) + (\mathcal{Z}_2)\cos(\varphi_0)''\sin(\varphi_0) \\ + \frac{(\mathcal{Z}_3 + \mathcal{Z}_5)}{2}\sin(2\varphi_0) + (\mathcal{Z}_4)\sin(\varphi_0)''\cos(\varphi_0)\end{aligned} \tag{3.100}$$

Using the same methods as in section 3.2.1, multiplying both sides of the equation above by φ_0' and integrating by parts, allows the equation to be rewritten as a collection of complete derivatives (using the fact that $g'(x)g''(x) = \frac{1}{2}(g'(x)^2)'$).

$$\begin{aligned}\varphi_0''\varphi_0' = (\mathcal{Z}_1)\sin(\varphi_0)\varphi_0' + (\mathcal{Z}_2)\cos(\varphi_0)''(-\cos(\varphi_0))' \\ + \frac{(\mathcal{Z}_3 + \mathcal{Z}_5)}{2}\left(-\frac{1}{2}\cos(2\varphi_0)\right)' + (\mathcal{Z}_4)\sin(\varphi_0)''(\sin(\varphi_0))'\end{aligned} \tag{3.101}$$

$$\begin{aligned}\frac{1}{2}((\varphi_0')^2)' = -(\mathcal{Z}_1)(\cos(\varphi_0))' - (\mathcal{Z}_2)\frac{1}{2}([\cos(\varphi_0)']^2)' \\ - \frac{(\mathcal{Z}_3 + \mathcal{Z}_5)}{2}\left(\frac{1}{2}\cos(2\varphi_0)\right)' + (\mathcal{Z}_4)\frac{1}{2}([\sin(\varphi_0)']^2)'\end{aligned} \tag{3.102}$$

This expression is easily integrated,

$$\begin{aligned}\frac{1}{2}((\varphi_0')^2) = -(\mathcal{Z}_1)(\cos(\varphi_0)) - (\mathcal{Z}_2)\frac{1}{2}(\cos(\varphi_0)')^2 \\ - \frac{(\mathcal{Z}_3 + \mathcal{Z}_5)}{2}\left(\frac{1}{2}\cos(2\varphi_0)\right) + (\mathcal{Z}_4)\frac{1}{2}([\sin(\varphi_0)']^2)\end{aligned} \tag{3.103}$$

and simplified to identify terms proportional to $(\varphi_0)'$,

$$\begin{aligned}\frac{1}{2}((\varphi_0')^2) = -(\mathcal{Z}_1)(\cos(\varphi_0)) - (\mathcal{Z}_2)(\sin(\varphi_0)^2)\frac{1}{2}((\varphi_0')^2) \\ - \frac{(\mathcal{Z}_3 + \mathcal{Z}_5)}{4}(\cos(2\varphi_0)) + (\mathcal{Z}_4)(\cos(\varphi_0)^2)\frac{1}{2}((\varphi_0')^2)\end{aligned} \tag{3.104}$$

$$\begin{aligned}\frac{1}{2}((\varphi_0')^2)\left[1+(\mathcal{Z}_2)(\sin(\varphi_0)^2)-(\mathcal{Z}_4)(\cos(\varphi_0)^2)\right]\\ =-(\mathcal{Z}_1)(\cos(\varphi_0))-\frac{(\mathcal{Z}_3+\mathcal{Z}_5)}{4}(\cos(2\varphi_0))\end{aligned}\tag{3.105}$$

We arrive an the final expression for the effective potential,

$$\begin{aligned}\mathcal{U}_{eff}&=-(\frac{1}{2})(\varphi_0')^2\\ &=\frac{(\mathcal{Z}_1)(\cos(\varphi_0))+(\mathcal{Z}_3+\mathcal{Z}_5)\frac{1}{4}(\cos(2\varphi_0))}{1+(\mathcal{Z}_2)(\sin(\varphi_0)^2)-(\mathcal{Z}_4)(\cos(\varphi_0)^2)},\end{aligned}\tag{3.106}$$

which has a similar for as the undamped effective potential in equation (3.61),

$$\mathcal{U}(\varphi_0)=-\frac{1}{2}(\varphi_0')^2=\frac{\lambda^2 J_0\left(\frac{F_0}{\omega^2}\right)\cos(\varphi_0)+\left(\frac{A_1+A_3}{4}\right)\cos(2\varphi_0)+\mathcal{C}}{1+A_2\sin(\varphi_0)^2+A_4\cos(\varphi_0)^2}\tag{3.107}$$

To fully evaluate the effective potential, the explicit forms of the coefficients Z_i, D_i, C_i are needed. Beginning with $\mathcal{Z}_1$ which is the collection of terms in the slow dynamics equation, independent of a_n, b_n:

$$\mathcal{Z}_1=\lambda^2\Big[J_0(\mathcal{B})J_0(\mathcal{C})+2\sum(-)^m J_{2m}(\mathcal{B})J_{2m}(\mathcal{C})\Big],\tag{3.108}$$

It is seen that as the damping vanishes, $\mathcal{Z}_1$ reduces to A_0 in the undamped equations. The remaining coefficients are also found,

$$\begin{aligned}\mathcal{Z}_2=-\lambda^2\Big[&J_0(\mathcal{C})\sum J_{2m-1}(\mathcal{B})\mathcal{D}_1(\alpha,\omega,2m-1)\\ &+J_0(\mathcal{B})\sum J_{2m-1}(\mathcal{C})\mathcal{D}_5(\alpha,\omega,2m-1)\Big],\end{aligned}\tag{3.109}$$

$$\begin{aligned}\mathcal{Z}_3+\mathcal{Z}_5=&-\lambda^2\Big[J_0(\mathcal{C})\sum J_{2m-1}(\mathcal{B})\mathcal{D}_2(\alpha,\omega,2m-1)\Big]\\ &+\lambda^2\Big[J_0(\mathcal{B})\sum J_{2m-1}(\mathcal{C})\mathcal{D}_6(\alpha,\omega,2m-1)\Big]+\lambda^2\Big[J_0(\mathcal{C})\sum J_{2m}(\mathcal{B})\mathcal{D}_4(\alpha,\omega,2m)\\ &+J_0(\mathcal{B})\sum J_{2m}(\mathcal{C})\mathcal{D}_4(\alpha,\omega,2m)\Big],\end{aligned}\tag{3.110}$$

and

$$\mathcal{Z}_4=-\lambda^2\Big[J_0(\mathcal{C})\sum J_{2m}(\mathcal{B})\mathcal{D}_3(\alpha,\omega,2m)+J_0(\mathcal{B})\sum J_{2m}(\mathcal{C})\mathcal{D}_4(\alpha,\omega,2m)\Big].\tag{3.111}$$

The coefficients $\mathcal{D}_i$ are found:

$$\mathcal{D}_1(\alpha,\omega,2n-1)=\Big(\frac{1}{((2n-1)\omega)^2+\alpha^2}\Big)\Big(\frac{\alpha\mathcal{C}_3^{(2n-1)}}{(2n-1)\omega}-\mathcal{C}_4^{(2n-1)}\Big)\tag{3.112}$$

$$\begin{aligned}&\mathcal{D}_2(\alpha,\omega,2n-1)\\ &=\Big(\frac{1}{((2n-1)\omega)^2+\alpha^2}\Big)\Big(\frac{\alpha\lambda^2}{(2n-1)\omega}(2J_0(\mathcal{B})J_{2n-1}(\mathcal{C})+2\lambda^2 J_0(\mathcal{C})J_{2n-1}(\mathcal{B}))\Big)\end{aligned}\tag{3.113}$$

$$\mathcal{D}_3(\alpha,\omega,2n) = \Big(\frac{1}{(2n\omega)^2+\alpha^2}\Big)\Big(\mathcal{C}_2^{(2n)} + \frac{\alpha}{2n\omega}\mathcal{C}_1^{(2n)}\Big) \tag{3.114}$$

$$\mathcal{D}_4(\alpha,\omega,2n) = \Big(\frac{1}{(2n\omega)^2+\alpha^2}\Big)\Big[2\lambda^2(J_0(\mathcal{C})J_{2n}(\mathcal{B}) + J_0(\mathcal{B})J_{2n}(\mathcal{C}))\Big] \tag{3.115}$$

$$\mathcal{D}_5(\alpha,\omega,2n-1) = \frac{(\alpha\mathcal{C}_3^{(2n-1)} - \mathcal{C}_4^{(2n-1)})}{(((2n-1)\omega)^2+\alpha^2)} \tag{3.116}$$

$$\begin{aligned}&\mathcal{D}_6(\alpha,\omega,2n-1)\\ &= \frac{(2n-1)\omega}{[((2n-1)\omega)^2+\alpha^2]^2}\Big[\frac{2\alpha\lambda^2}{((2n+1)\omega)^2}(J_0(\mathcal{C})J_{2n-1}(\mathcal{B}) - 2\lambda^2 J_0(\mathcal{B})J_{2n-1}(\mathcal{C}))\Big]\end{aligned} \tag{3.117}$$

Also, the coefficients $\mathcal{C}_i$:

$$\mathcal{C}_1^{(2n)} = \frac{(-\alpha\lambda^2)}{(2n\omega)^3+\alpha^2(2n\omega)}\Big(2[J_0(\mathcal{C})J_{2n}(\mathcal{B}) + J_0(\mathcal{B})J_{2n}(\mathcal{C})])\Big) \tag{3.118}$$

$$\mathcal{C}_2^{(2n)} = \frac{(\alpha\lambda^2)}{(2n\omega)^2+\alpha^2}\Big(2[J_0(\mathcal{C})J_{2n}(\mathcal{B}) + J_0(\mathcal{B})J_{2n}(\mathcal{C})])\Big) \tag{3.119}$$

$$\begin{aligned}\mathcal{C}_3^{(2n-1)} &= \left(\frac{\lambda}{(2n+1)\omega}\right)^2 (2J_0(\mathcal{C})J_{2n+1}(\mathcal{B}))\\ &- \left(\frac{\alpha}{(2n+1)\omega}\right)\left(\frac{\lambda^2}{((2n+1)\omega)^2+\alpha^2}\right)\Big[\left(\frac{\alpha}{(2n+1)\omega}\right)(2J_0(\mathcal{C})J_{2n+1}(\mathcal{B}))\\ &- (2J_0(\mathcal{B})J_{2n+1}(\mathcal{C}))\Big]\end{aligned} \tag{3.120}$$

$$\begin{aligned}\mathcal{C}_4^{(2n-1)} &= \left(\frac{\lambda^2}{((2n+1)\omega)^2+\alpha^2}\right)\Big[\left(\frac{\alpha}{(2n+1)\omega}\right)(2J_0(\mathcal{C})J_{2n+1}(\mathcal{B}))\\ &- (2J_0(\mathcal{B})J_{2n+1}(\mathcal{C}))\Big]\end{aligned} \tag{3.121}$$

3.2.5 Numerical simulations with varying dissipation term

The driven Sine-Gordon model and a stable soliton can easily devolve into chaotic motion. Numerical simulations of the soliton solution were done using the driven model with a time-dependent, decaying damping term. The initial waveform was taken to be a straight line. Since the solution varies slowly over the period of the driving torque, the soliton form was plotted after several periods of the driving torque had elapsed and the total driving time of the system was 99 driving periods. The time-dependence of the dissipation term was determined by varying the amplitude at $t = 0$ and decay rate. Other parameters, such as: system size, driving amplitude, driving frequency and mass term were kept constant and chosen to correspond to the period doubling seen in the effective potential. The driving torque parameters were $F_0 = 3.7972, \omega = 1.2566$ and the

coupling constant $\lambda = 0.25132$. The system was driven for many periods of the driving torque, sufficient time to develop a quasi-equilibrium state.

The values for F_0, ω, λ were chosen such that $J_0(\frac{F_0}{\omega^2}) \approx 0$, and $\frac{\lambda}{2\omega} = 0.1$. The dissipation constant, α, is a function of time and decays over the course of the simulation (see figure 3.3). Four functions for $\alpha(t)$ were used, and defined with the parameters: n an index, and k the size of the time step ($k = 0.005$). The decay rate was determined proportional to the total run time $t_f = 500$.

$$\begin{aligned} \alpha_1(t) &= \alpha_0 \\ \alpha_2(t) &= \alpha_0 \exp\left(-\frac{n*k}{25.0}\right) \\ \alpha_3(t) &= \alpha_0 \exp\left(-\frac{n*k}{200.0}\right) \\ \alpha_4(t) &= \alpha_0 \exp\left(-\frac{n*k}{500.0}\right) \end{aligned} \tag{3.122}$$

At the end of the simulation, the strength of $\alpha(t)$,

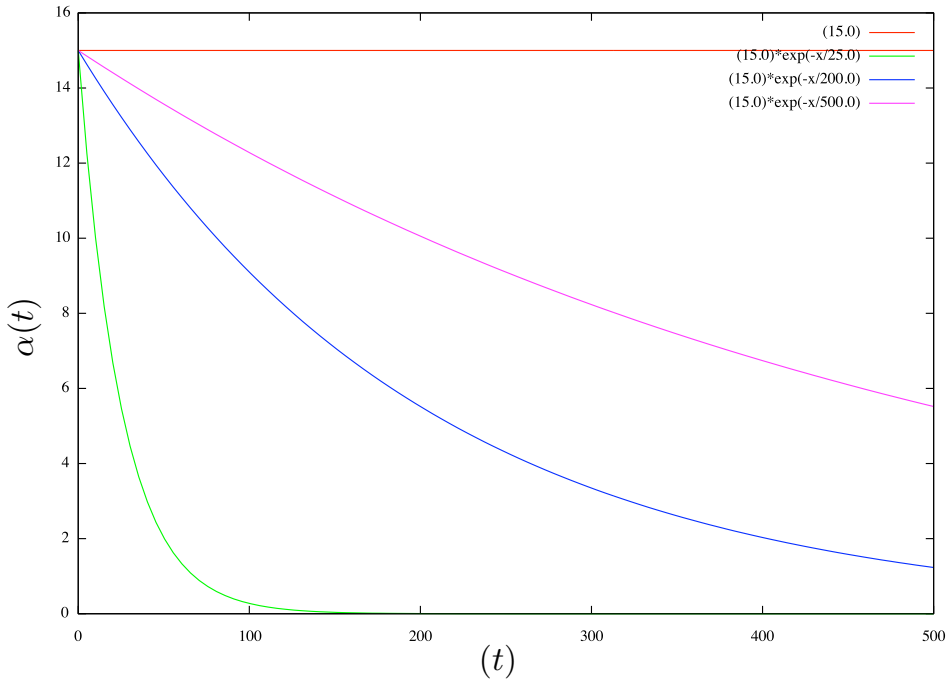

Figure 3.3: Time dependence of the dissipation coefficient

$$\begin{aligned}
\alpha_1(t = 500) &= \alpha_0, \\
\alpha_2(t = 500) &= 0, \\
\alpha_3(t = 500) &= (0.28)\alpha_0, \\
\alpha_4(t = 500) &= (0.36)\alpha_0.
\end{aligned} \tag{3.123}$$

Five values were used for the initial strength of α_0:

$$\begin{aligned}
&\alpha_0 = 0.1 \quad (\alpha_0 < \lambda < F_0) \\
&\alpha_0 = 1.5 \quad (\lambda < \alpha_0 < F_0) \\
&\alpha_0 = 2.9 \quad (\lambda < \alpha_0 < F_0) \\
&\alpha_0 = 5.0 \quad (\lambda < F_0 < \alpha_0) \\
&\alpha_0 = 15.0 \quad (\lambda < F_0 \ll \alpha_0).
\end{aligned} \tag{3.124}$$

Systems with $\alpha_0 = 2.9, \alpha_0 = 5.0, \alpha_0 = 15.0$ did not exhibit 2 π-solitons. The systems with $\alpha(t)$ slowly decaying or constant $(\alpha_1, \alpha_3, \alpha_4)$ converged to single solitons. The system with the rapidly decaying dissipation (α_2) did not converge to a soliton, or any stable solution. The time average of the soliton was computed, $u(x) = \frac{1}{T}\int_0^T (u(x,t))dt$ (integration over 1 period of the driving torque $T = \frac{2\pi}{\omega}$). The initial shape of the soliton is a straight line $(u(x, t = 0) = (\frac{2\pi}{2000}) * (n * h))$. n is an index and h is the size of the step in x (h = 0.01).

The final shape of the solitons are shown with the initial dissipations values: $\alpha_0 = 0.1$ (see figure 3.4), $\alpha_0 = 1.5$ (see figure 3.5). For the smaller initial value for α_0, the system reaches a stationary soliton that is quite broad. With the larger initial value of α_0 it is seen that the system reaches a stationary state that has a narrow soliton shape.

For the curve in Figure 3.4, with dissipation term $\alpha_3(t)$, many solutions reach a steady state with a broadened soliton. The soliton's evolution over several periods of the driving torque is shown in Figure 3.6.

3.3 Conclusions

Through the derivation of an effective potential, the driven Sine-Gordon model can be recast as motion of a single particle. It was shown that in the presence of a driving torque, it is possible to significantly alter the dynamics of the particle. In the absence of driving, there are well defined minima at $\varphi = \{0, \pm 2\pi\}$. The particle will reach an

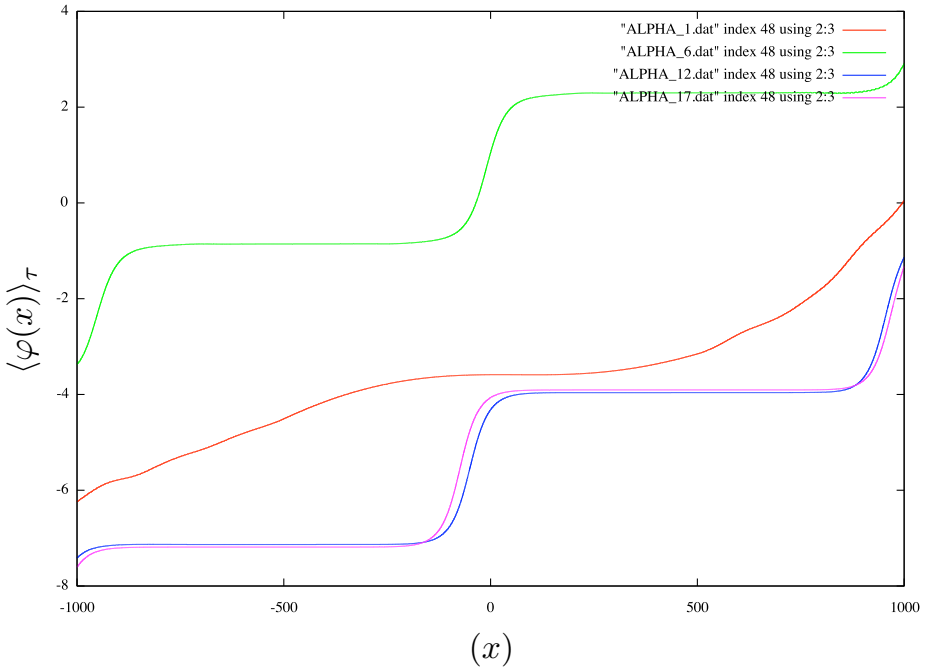

Figure 3.4: Stationary solution reached after several periods of driving for $\alpha_0 = 0.1$ and the dissipation constant has the decay rates given in equation(3.122): $\alpha_1(t)$ (purple), $\alpha_2(t)$ (red) , $\alpha_3(t)$ (green), $\alpha_4(t)$ (blue).

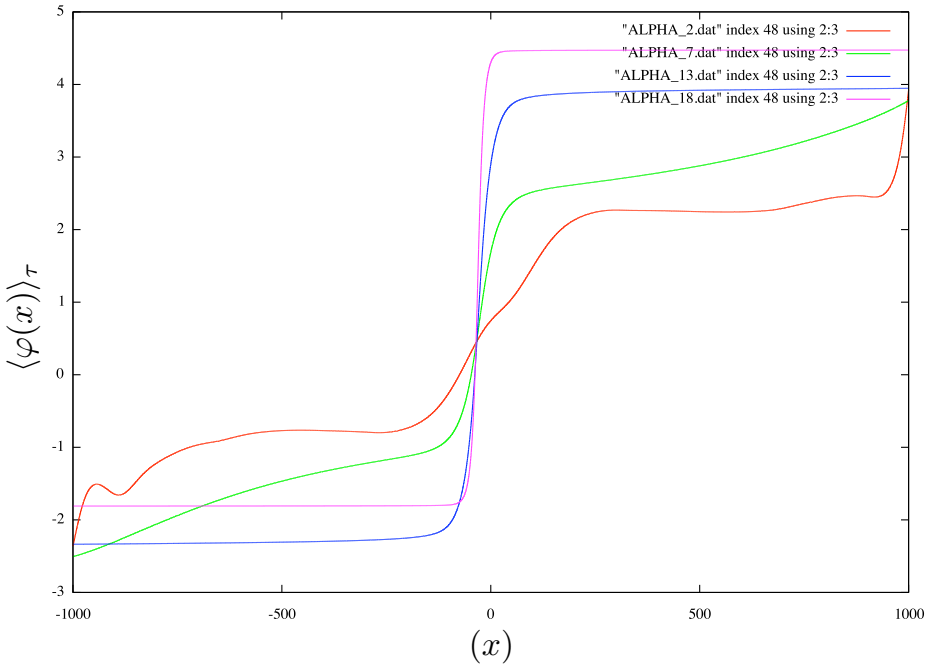

Figure 3.5: Stationary solution reached after several periods of driving for $\alpha_0 = 1.5$ and the dissipation constant has the decay rates given in equation(3.122): $\alpha_1(t)$ (purple), $\alpha_2(t)$ (red) , $\alpha_3(t)$ (green), $\alpha_4(t)$ (blue).

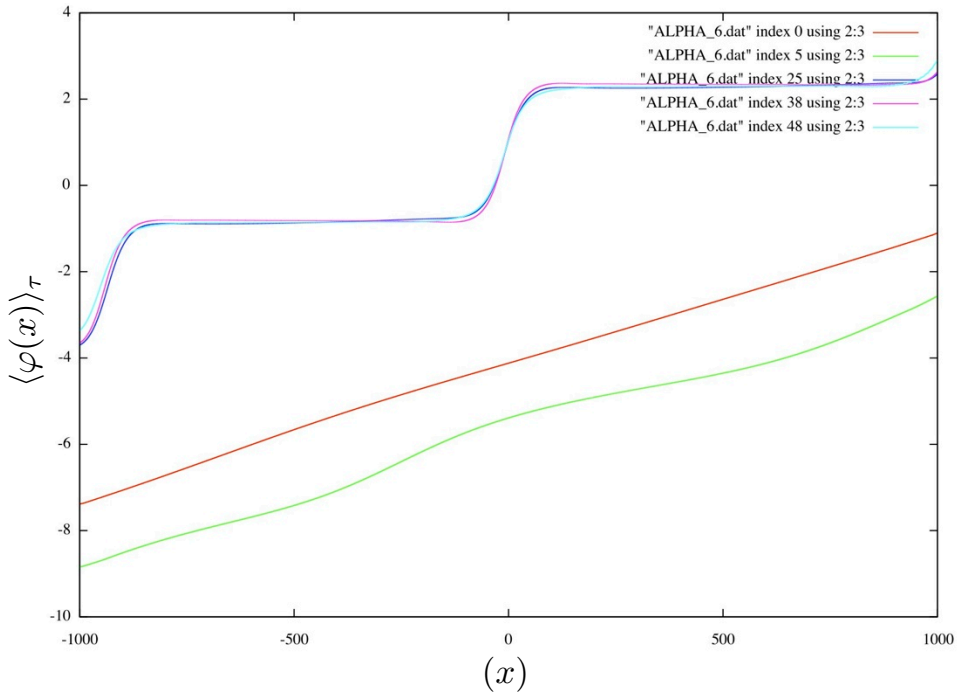

Figure 3.6: Time evolution of a soliton over several periods of the driving torque τ, with $\alpha = \alpha_3$ from Figure 2 at 0τ (red), 10τ(green), 50τ (dk blue), 79τ (purple), 99τ (lt blue)

equilibrium position at those minima. If it is weakly driven out of equilibrium, the particle will rapidly return to those stable points. In the presence of a strong driving torque, it is seen that the particle is moving in an effective potential and also that it is possible to drive the particle far from the initial stable points at $\varphi = \{0, \pm 2\pi, \dots\}$ and additionally new minima are formed at points which were previously unstable.

Chapter 4

Two-band delocalization

There are many connections between the classical Sine-Gordon model and quantum systems. The dynamical stabilization possible in the driven Sine-Gordon model (see Chapter (3)) suggests the possibility of dynamical effects in a driven gapped quantum system, particularly those with a gapped, hyperbolic spectrum. This chapter describes work done on interacting electrons on a lattice in hyperbolic and sinusoidal energy spectra and also a continuum model of a series of parabolic spectra. In the Hartree approximation, the interaction between particles opens a gap between neighboring levels and such gapped systems are driven by a large amplitude, highly oscillatory external field. The gap is treated as a perturbation and the system is studied in the interaction representation. The periodic nature of the driving force leads to the analysis of dynamical effects in the system as a gradual renormalization of the Floquet quasi-energy bands and the primary effect of the driving field is the gap suppression in a two-band system. Three systems are considered: a multi-band, continuum model with a parabolic energy spectrum, and two-band lattice models with either a linear spectrum or a sinusoidal spectrum. Numerical studies of the lattice models show the gap suppression due to the external field. It is also studied how gap suppression affects the electrical current that can be generated by an external field. For a system driven by a strong AC field in the gap suppression regime, a DC field is gradually introduced. For a single particle driven through the system as the gap is suppressed, the Bloch oscillations undergo a doubling of the period as the periodicity of the energy band is doubled. For a gapped system initially prepared as a filled band, the closure of the gap leads to a half-filled band and as a result a non-zero net current is generated by the DC field. A brief discussion of dissipation and temperature dependent effects are discussed, the Linblad operator model is introduced as an extension of the two-band model which will include phonon scattering. The full effects of phonon scattering is not considered in this work.

4.1 Introduction

In Chapter (3), a group of driven coupled pendulum exhibited unique stabilization effects. Similar to the driven vertical pendulum, it was possible to create a stable equilibrium point at points which are unstable in the un-driven system. Quantization of the Sine-Gordon model corresponds to a bosonic system with a gap due to back-scattering. The connection between the quantized Sine-Gordon model and a system of non-interacting particles with backscattering, leads to the work discussed in this chapter: an investigation into the dynamical effects of a driven two-band model. Since the back-scattering term leads to a gap in the quantized Sine-Gordon model, the two-band model studied in the chapter has a gap introduced by a weak, time-independent perturbation. The period doubling seen in the driven Sine-Gordon model is expected to occur in the two-band model as the suppression of the band-gap.

In Sections (2.2) and (2.3), the characteristics of a one-dimensional, strongly interacting system were discussed. Of importance is the metal-insulator transition present for interactions of any magnitude. In a one-dimensional lattice at half-filling, the introduction of interactions leads to the Peirels' shift, which destroys the original translation symmetry of the lattice (see Figure (4.1)). The doubling of the lattice spacing leads to a halving of the Brillouin zone and creates an insulating system. Instead of the Fermi liq-

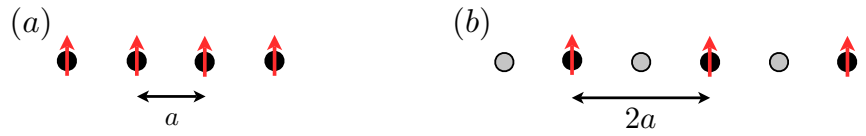

Figure 4.1: The instability of the one-dimensional lattice to interactions. In (a) the half-filled non-interacting system is shown. As interactions are introduced the symmetry of the original system is lost (shown in (b)). The instability is present no matter how small the interaction between particles.

uid picture, one-dimensional systems can be represented in the Luttinger liquid picture. Excitations in this representations are not quasi-particles, as in the Fermi liquid, but rather are density waves in the charge (CDW) or spin (SDW) degrees of freedom. The propagation of density waves through a correlated system is similar to the propagation of a soliton in the Sine-Gordon model. In a system with high repulsion between electrons, two ground states are possible (see Figure (4.2)(a)). When an excitation of a CDW is present, it travels through the lattice as a soliton moves through the Sine-Gordon model, as a narrow region of disturbance which connects regions in ground state configurations (see Figure (4.2)(b)). Both the soliton energy spectrum and the interacting electron

spectrum exhibit a gapped hyperbolic spectrum.

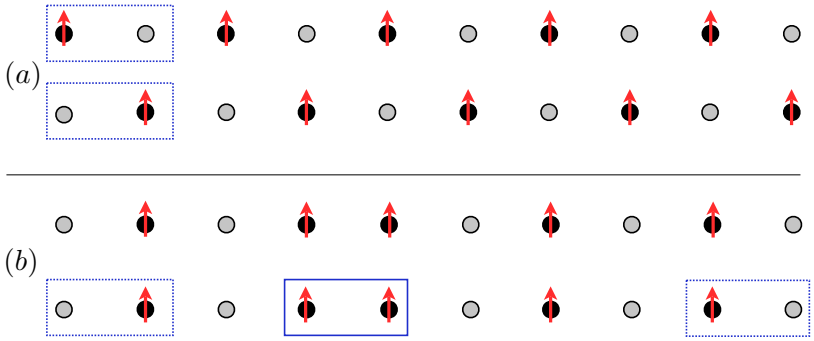

Figure 4.2: The connection between soliton waves and charge density waves in the one-dimensional lattice. In (a) the two periodic ground states for a strongly interacting lattice are shown with unit cells highlighted (blue dashed frames). In (b) the excitation of a CDW is shown and its connection to a soliton shape is highlighted: far from a narrow region of disturbance (solid blue frame) regions are in either ground state (blue dashed frames).

The quantized Sine-Gordon model can be mapped to a spinless fermion model [12, 157] through bosonization (discussed in Section (2.3.1)). A final note about the classical Sine-Gordon model is made here, to further highlight the similarities of the soliton energy spectrum and the Luttinger liquid spectrum. From the Sine-Gordon Lagrangian density discussed Section (3.1),

$$\mathcal{L} = \frac{1}{2}(\partial\varphi)^2 - V_{SG}(\varphi) \tag{4.1}$$

$$V_{SG}(\varphi) = \lambda^2(1 - \cos(\varphi)) \tag{4.2}$$

the Hamiltonian density is defined with the canonical momentum $p = \delta\mathcal{L}/\delta\varphi'$,

$$\begin{aligned} \mathcal{H} &= \left[p\left(\frac{\delta\mathcal{L}}{\delta\varphi'}\right) - \mathcal{L}\right] \\ &= \left[\frac{1}{2}(\partial\varphi)^2 + V_{SG}(\varphi)\right]. \end{aligned} \tag{4.3}$$

The variables are shifted into a moving reference frame through the Lorentz transformation $\xi = \lambda\gamma(x \pm vt)$ (where $\gamma = (1 - v^2)^{-1}$). The change of variables does not affect the potential $V_{SG}(\varphi)$ and the derivatives are transformed as follows,

$$\begin{aligned} \frac{1}{2}(\partial\varphi)^2 &= \frac{1}{2}(\partial_t\varphi(x,t))^2 + \frac{1}{2}(\partial_x\varphi(x,t))^2 \\ &= \frac{(\lambda\gamma)^2}{2}\left[1 + v^2\right]\left(\frac{\partial\varphi(\xi)}{\partial\xi}\right)^2. \end{aligned} \tag{4.4}$$

The final transformed Hamiltonian is,

$$H = \int \frac{d\xi}{\lambda\gamma}\mathcal{H} = \int \frac{d\xi}{\lambda\gamma}\left(\frac{(\lambda\gamma)^2}{2}\left[1+v^2\right]\left(\frac{\partial\varphi(\xi)}{\partial\xi}\right)^2 + \lambda^2(1-\cos(\varphi))\right). \tag{4.5}$$

To highlight the similarities of the Sine-Gordon and the Luttinger spetrum, the Hamiltonian (energy density) is further manipulated to give an expression in terms of an integral over the field variable φ. Using the Euler-Lagrange equations of motion, an expression for $\partial\varphi/\partial\xi$ is defined. First found in the (x,t) coordinates,

$$\frac{\partial^2\varphi}{\partial x^2} - \frac{\partial^2\varphi}{\partial t^2} = V_{SG}(\varphi)', \tag{4.6}$$

then transformed to the coordinate $\xi = x \pm vt$,

$$\left(\frac{\lambda^2}{2}\right)\frac{d^2\varphi}{d\xi^2} = V_{SG}(\varphi)' \tag{4.7}$$

the equations of motion are integrated by parts to find an expression for $d\varphi/d\xi$. Multiplying by $d\varphi/d\xi$ on each side and rewriting the left-hand side as a total derivative, gives an expression for $(d\varphi/d\xi)^2$ that can be integrated:

$$\left(\frac{d\varphi}{d\xi}\right)\frac{d^2\varphi}{d\xi^2} = \left(\frac{d\varphi}{d\xi}\right)\frac{1}{\lambda}V_{SG}(\varphi)' \tag{4.8}$$

$$\frac{1}{2}\left(\frac{d}{d\xi}\right)\left(\frac{d\varphi}{d\xi}\right)^2 = \left(\frac{d\varphi}{d\xi}\right)\frac{1}{\lambda}V_{SG}(\varphi)' \tag{4.9}$$

the ξ-integration follows directly;

$$\frac{1}{2}\left(\frac{d\varphi}{d\xi}\right)^2 = V_{SG}(\varphi) \tag{4.10}$$

and finally an expression for $d\varphi/d\xi$ is found,

$$\left(\frac{d\varphi}{d\xi}\right) = \sqrt{2V_{SG}(\varphi)} \tag{4.11}$$

Replacing the term $V_{SG}(\varphi)$ in the Lorentz transformed Hamiltonian is now possible,

$$\begin{aligned}\mathcal{H} &= \left(\frac{\partial\varphi(\xi)}{\partial\xi}\right)^2 + \lambda^2(1-\cos(\varphi)) \\ &= 2\left(\frac{\partial\varphi(\xi)}{\partial\xi}\right)^2.\end{aligned} \tag{4.12}$$

Finally, the energy density of a stationary soliton is given as an integral over φ:

$$\mathcal{E} = \int d\varphi(\varphi)' = \pm\int d\varphi 2\sqrt{2V_{SG}(\varphi)} \tag{4.13}$$

when the Sine-Gordon potential is substituted above, it is seen that the stationary soliton has a gapped spectrum near the points where $\cos(\varphi)$ vanish. This gap has a

width proportional to λ^2. From the studies of dynamical stabilization in Chapter (3) it was seen that stabilization occurs when the parameter λ is renormalized and may be suppressed. This suggests that a gapped spectrum may exhibit gap suppression. Additionally, in the vicinity of the gap, the soliton spectrum has a hyperbolic shape, similar to that of the Luttinger liquid.

As discussed in Sections (2.2) and (2.3), a system of strongly interacting electrons in one dimension can be described using a model of spin-less fermions in a gapped spectrum. The general form of the Hamiltonian of these systems is as follows:

$$H = -J \sum_i \left(a_i^\dagger a_{i+1} + a_{i+1}^\dagger a_i \right) + \frac{V}{2} \left(\langle n_i \rangle n_{i+1} + n_i \langle n_{i+1} \rangle \right). \tag{4.14}$$

The gap width V is not determined self-consistently, what is presented in this chapter are phenomenological results. The gap width is chosen to be small compared to the bandwidth ($V \ll J$), and the additional modifications to the hopping parameter due to Hartree-Fock terms are incorporated into J, which describes hopping between adjacent lattice sites.

The systems under consideration all share the following characteristics: a system in a periodic spatial potential of period $x_0 = 2\pi/k$ is subjected to a weak perturbation of amplitude V_0 which is periodic with period $x_0/2 = \pi/k$. The weak perturbation will cause a gap to open in the energy spectrum of the original system, the lowest order gap will be determined by the amplitude of the perturbation $\delta = 2V_0$.

With the addition of an oscillating driving force the gap between the two lowest bands will be effectively closed through a renormalization of the bandwidth. The gap closure will be seen explicitly in the energy spectrum and implicitly through the field generated electric field. Temperature dependence enters in the discussion of the electric current and finally a discussion of how these results could be extended to a simple model of an open quantum system is discussed.

4.2 Continuum model: parabolic model

The system in this section is a modification to the two-band model. It consists of an unperturbed parabolic spectrum, a weak periodic perturbation and a strong AC driving force. This effectively describes single particles isolated in wells separated by a spatial distance of $2k$ and oscillating about the bottom of the well. It can be considered a system of single particles in a deep sinusoidal potential, where the inter-well tunneling energy is much higher than the kinetic energy of the bound electrons. The weak perturbation adds a small barrier at the midpoint of the original band, which back-scatters

the electrons. When the weak perturbation is added to the system, the energy spectrum exhibits the same gap opening at the band midpoint as in two-band model. However it is not exactly $2V_0$. For a system of N wells the matrix representation of the Hamiltonian will be $N \times N$.

Without any perturbations, the system has a series of parabolic spectra (see Figure (4.3a) with exact crossings between the bands. With the weak perturbation (of amplitude V_0) present, a gap opens between the two lowest lying energy bands (see Figure (4.3b)). Additional gaps open at higher band crossings but have narrower widths.

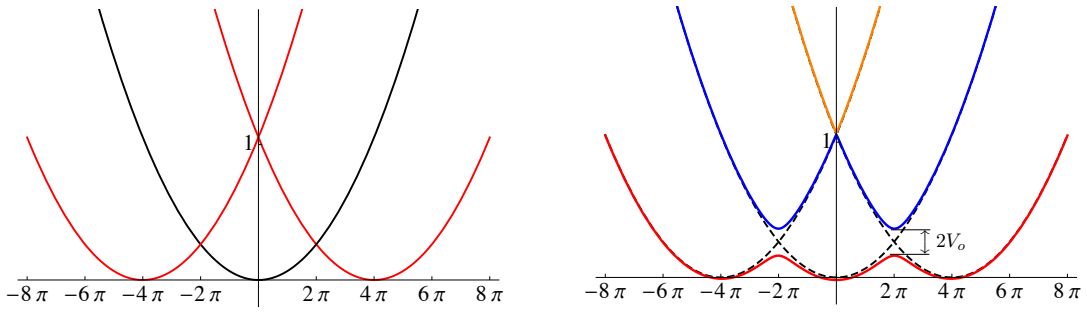

Figure 4.3: Development of gap in parabolic spectra: a subset of undriven parabolic spectra are shown. (a) In the absence of the periodic perturbation, there are exact crossings between the bands. Shown are the spectra for particles in wells at $k = 0$ (black) and the adjacent wells at $k \pm 4\pi$ (red). (b) With the weak perturbation present, the crossings between the lowest bands (red, blue lines) are not exact and have gap width of approximately $2V_0$. The crossing between the second and third band (blue, orange) is also gapped but has a narrower width.

The general system discussion in Section (2.3.2) shows how the weak perturbation leads to the gap opening in the energy spectra. In the case of the parabolic spectra, the matrix for H is not 2×2. The full system describes a system of N particles and as a result the full matrix will be $N \times N$. The form of such a matrix will be quite simple, with the diagonal terms describing the momentum for each particle and the off-diagonal terms describing the weak perturbation.

$$H = \begin{pmatrix} & \ddots & \frac{V_0}{2} & 0 & 0 & \dots & & \\ 0 & \frac{V_0}{2} & \epsilon(p-k) & \frac{V_0}{2} & 0 & 0 & \dots & \\ \dots & 0 & \frac{V_0}{2} & \epsilon(p) & \frac{V_0}{2} & 0 & 0 & \dots \\ \dots & 0 & 0 & \frac{V_0}{2} & \epsilon(p+k) & \frac{V_0}{2} & 0 & \dots \\ \dots & \dots & 0 & 0 & \frac{V_0}{2} & \epsilon(p+2k) & \frac{V_0}{2} & \dots \\ & \dots & \dots & 0 & 0 & \frac{V_0}{2} & \ddots & \end{pmatrix}, \tag{4.15}$$

The eigenvalues for the $N \times N$ system can be found and the spectrum will show a gap opening. In Figure (4.3b) the energy spectrum for a 3×3 system is shown, calculated from the eigenvalues of the matrix Hamiltonian.

The full system Hamiltonian contains three terms, describing the original system (H_0), the driving force ($H_D(\hat{x},t)$) and the weak spatial perturbation caused by interactions ($H_P(\hat{x})$):

$$\begin{aligned} H_{sys}(\hat{p},\hat{x},t) &= H_0(\hat{p}) + H_D(\hat{x},t) + H_P(\hat{x}), \\ &= \frac{(\hat{p})^2}{2m} + F_0\hat{x}\cos(\omega t) + V_0\cos(k\hat{x}). \end{aligned} \tag{4.16}$$

Where the momentum operator $\hat{p}$ is defined to be invariant under translations of $p+2k$ and the spatial perturbation shifts the momentum by $p+k$. As discussed in Chapter (2) the interaction representation can be used to describe the time evolution of this system in the presence of a weak perturbation. First, the driving force is incorporated into the momentum through a gauge transform. For a gauge field $\alpha(\hat{x},t) = F_0\hat{x}/\omega\sin(\omega t)$, the gauge-transformed Hamiltonian is given by:

$$\begin{aligned} \overline{H}(\overline{p},t) = \frac{\overline{p}^2}{2m} &= \frac{\left(\bar{p} + \frac{d\alpha}{dx}\right)^2}{2m} \\ &= \frac{1}{2m}\left(\hat{p}^2 + 2\frac{F_0}{\omega}\hat{p}\sin(\omega t) + \left(\frac{F_0}{\omega}\right)^2\sin(\omega t)^2\right). \end{aligned} \tag{4.17}$$

The unitary operator $U(t)$ is built from the operators $U_0(t)$ and $S(t)$:

$$U(t) = e^{-i\int_0^t dt'\left(\overline{H}(\bar{p},t)+H_P(\hat{x},t)\right)} \tag{4.18}$$

$$S(t) = e^{-i\int_0^t dt' H_I(t')} \tag{4.19}$$

$$U(t) = U_0(t)S(t) \tag{4.20}$$

Where U_0 is defined with the gauge transformed Hamiltonian in Equation (4.17), and $S(t)$ is dependent on the interaction representation of the weak periodic potential H_I, a term which will expanded in a perturbation series. With the unitary operator $U_0(t)$:

$$U_0 = e^{-i\int_0^t dt'\overline{H}(\bar{p},t')}, \tag{4.21}$$

$$= e^{-i\frac{1}{2m}[\hat{p}^2 t - 2\frac{F_0}{\omega^2}\hat{p}(1-\cos\omega t)) + \left(\frac{F_0}{\omega}\right)^2\left(\frac{t}{2}-\frac{1}{2}\sin(2\omega t)\right)]}, \tag{4.22}$$

the interaction representation is found:

$$H_I = U_0^\dagger H_P U_0 \tag{4.23}$$

$$= V_0\cos\left(k\left(x + \frac{1}{m}pt + \frac{F_0}{m\omega^2}\left[1-\cos(\omega t)\right]\right)\right). \tag{4.24}$$

The unitary operator for the time evolution of the system:

$$U(t) = e^{i\int_0^t dt' H_{sys}(t')} \tag{4.25}$$

can be evaluated directly with the full system Hamiltonian. Due to the complex time-dependence we will evaluate $U(t)$ through a perturbative expansion, as outlined in Chapter (2).

From the interaction form of the Hamiltonian (see Equation (4.25)), the first order terms are easily found by averaging over one period of the driving force ($\tau = 2\pi/\omega$) to fine $\langle H_I \rangle_\tau$. First, the momentum representation of H_I given in (4.24) is determined:

$$\begin{aligned} H_I(p,p') &= \langle p|H_I|p'\rangle \\ &= \langle p|V_0\cos\left(k\left(x + \frac{1}{m}pt + \frac{F_0}{m\omega^2}\left[1-\cos(\omega t)\right]\right)\right)|p'\rangle \\ &= \frac{V_0}{2}\big(e^{i(\frac{kt}{m}p' + \frac{k^2t}{2m} + \frac{F_0k}{m\omega^2}[1-\cos(\omega t)])}\delta_{p,p'+k} \\ &+ e^{-i(\frac{kt}{m}p' - \frac{k^2t}{2m} + \frac{F_0k}{m\omega^2}[1-\cos(\omega t)])}\delta_{p,p'-k}\big) \\ &= \frac{V_0}{2}\big(e^{i\theta_1(p',t)}\delta_{p,p'+k} + e^{-i\theta_2(p',t)}\delta_{p,p'-k}\big). \end{aligned} \tag{4.26}$$

After the delta function is evaluated the exponential arguments become,

$$\begin{aligned} \theta_1(p,t) &= \frac{kt}{m}(p-k) + \frac{k^2t}{2m} + \frac{F_0k}{m\omega^2}[1-\cos(\omega t)] \\ &= \frac{kt}{m}\left(p - \frac{k}{2}\right) + \frac{F_0k}{m\omega^2}[1-\cos(\omega t)] \\ \theta_2(p,t) &= \frac{kt}{m}(p+k) - \frac{k^2t}{2m} + \frac{F_0k}{m\omega^2}[1-\cos(\omega t)] \\ &= \frac{kt}{m}\left(p + \frac{k}{2}\right) + \frac{F_0k}{m\omega^2}[1-\cos(\omega t)] \end{aligned} \tag{4.27}$$

The time dependence of the scalar term is sinusoidal but can be written in terms of Bessel functions. The terms $e^{i\mathbf{C}\cos(\omega t)}$ (where $\mathbf{C} = \frac{F_0}{m\omega^2}$) are rewritten :

$$e^{\pm i\mathbf{C}\cos(\omega t)} = \sum_n (i^n) J_n(\mathbf{C}) e^{(in\omega t)} \tag{4.28}$$

and as a result the time dependence in the first order terms can be easily integrated and the time averaged first term of the perturbation series is found;

$$\begin{aligned} \int_0^\tau dt H_I(p) = &\int_0^\tau dt(\frac{V_0}{2})(e^{(i\mathbf{C})})e^{i\frac{kt}{m}(p-\frac{k}{2})}\left[\sum_n (i^n)J_n(\mathbf{C})e^{(in\omega t)}\right] \\ &+ \int_0^\tau dt(\frac{V_0}{2})(e^{(-i\mathbf{C})})(e^{-i\frac{kt}{m}(p+\frac{k}{2})})\left[\sum_n (i^n)J_n(\mathbf{C})e^{(in\omega t)}\right] \end{aligned} \tag{4.29}$$

So the first order term in the perturbation series is found as a sum over Floquet modes $(n\omega)$:

$$\begin{aligned}\langle H_I(p)\rangle = \frac{V_0}{2\tau}(e^{(i\mathbf{C})}\sum_n(-i)^n J_n(\mathbf{C})\left[\frac{(e^{(i\frac{k}{m}(p-\frac{k}{2})\tau)}-1)}{(i(\frac{kp}{m}-\frac{k^2}{2m}+n\omega)}\right])+\\ \frac{V_0}{2\tau}(e^{(-i\mathbf{C})}\sum_n(i)^n J_n(\mathbf{C})\left[\frac{(e^{(-i\frac{k}{m}(p+\frac{k}{2})\tau)}-1)}{(-i(\frac{kp'}{m}-\frac{k^2}{2m}-n\omega)}\right])\end{aligned} \tag{4.30}$$

Near the location of the gap, when the momentum has value $p' = \pm\frac{k}{2}$, the $n = 0$ term becomes very large and dominate the sum over n. Additionally, if the driving amplitude and frequency are chosen such that the term $\mathbf{C} = \frac{F_0}{m\omega^2}$ corresponds to the root of the J_0 Bessel function, the first order term can be suppressed completely. A plot of the gap suppression in a parabolic model is shown in Figure (4.6), found by numerically integrating the exact time evolution operator.

For completeness the second order terms are presented here, determined by the commutator of $H_I(t)$ at different times (t_1, t_2). The commutator is evaluated from the expansion of H_I into exponential terms and the Baker-Campbell-Hausdorff method of expanding exponentiated operators. The second term becomes (where the subscript (I) will be omitted for the remainder of the derivation),

$$\begin{aligned}[H(t_1), H(t_2)] = \left(\frac{V_0}{2}\right)^2 [(e^{i(\hat{\alpha}+\hat{\beta}(t_1))}e^{i\gamma(t_1)} + e^{-i(\hat{\alpha}+\hat{\beta}(t_1))}e^{i\gamma(t_1)}),\\ (e^{i(\hat{\alpha}+\hat{\beta}(t_2))}e^{i\gamma(t_2)} + e^{-i(\hat{\alpha}+\hat{\beta}(t_2))}e^{i\gamma(t_2)})]\\ = [e^{i(\hat{\alpha}+\hat{\beta}(t_1))}e^{i\gamma(t_1)}, e^{i(\hat{\alpha}+\hat{\beta}(t_2))}e^{i\gamma(t_2)}]\\ + [e^{i(\hat{\alpha}+\hat{\beta}(t_1))}e^{i\gamma(t_1)}, e^{-i(\hat{\alpha}+\hat{\beta}(t_2))}e^{-i\gamma(t_2)}]\\ + [e^{-i(\hat{\alpha}+\hat{\beta}(t_1))}e^{-i\gamma(t_1)}, e^{i(\hat{\alpha}+\hat{\beta}(t_2))}e^{i\gamma(t_2)}]\\ + [e^{-i(\hat{\alpha}+\hat{\beta}(t_1))}e^{-i\gamma(t_1)}, e^{-i(\hat{\alpha}+\hat{\beta}(t_2))}e^{-i\gamma(t_2)}]\end{aligned} \tag{4.31}$$

The argument of the cosine function was separated in to operator $(\hat{\alpha}, \hat{\beta}(t))$ and scalar terms $(\gamma(t))$. The scalar terms commute ($[\hat{\alpha}, \gamma(t)] = [\hat{\beta}(t), \gamma(t)] = [\gamma(t), \gamma(t)] = 0$) and can be simply separated from the operator terms:

$$e^{i(\hat{\alpha}+\hat{\beta}(t)+\gamma(t))} = e^{i(\hat{\alpha}+\hat{\beta}(t))}e^{i\gamma(t)}. \tag{4.32}$$

With the scalar terms pulled out of the commutators,

$$\begin{aligned}[H(t_1), H(t_2)] = [e^{i(\hat{\alpha}+\hat{\beta}(t_1))}, e^{i(\hat{\alpha}+\hat{\beta}(t_2))}]e^{i(\gamma(t_1)+\gamma(t_2))}\\ + [e^{i(\hat{\alpha}+\hat{\beta}(t_1))}, e^{-i(\hat{\alpha}+\hat{\beta}(t_2))}]e^{i(\gamma(t_1)-\gamma(t_2))}\\ + [e^{-i(\hat{\alpha}+\hat{\beta}(t_1))}, e^{i(\hat{\alpha}+\hat{\beta}(t_2))}]e^{-i(\gamma(t_1)-\gamma(t_2))}\\ + [e^{-i(\hat{\alpha}+\hat{\beta}(t_1))}, e^{-i(\hat{\alpha}+\hat{\beta}(t_2))}]e^{-i(\gamma(t_1)+\gamma(t_2))}\end{aligned} \tag{4.33}$$

The operator sums in the exponential terms can be separated,

$$e^{i(\hat{\alpha}+\hat{\beta}(t))} = e^{i\hat{\alpha}} e^{i\hat{\beta}(t)} e^{-\frac{1}{2}[\hat{\alpha},\hat{\beta}(t)]} \tag{4.34}$$

and since $\hat{\alpha}, \hat{\beta}$ are dependent on $\hat{x}, \hat{p}$, their commutator will generate an additional scalar term.

$$\begin{aligned}
[H(t_1), H(t_2)] = &[e^{i\hat{\alpha}} e^{i\hat{\beta}(t_1)}, e^{i\hat{\alpha}} e^{i\hat{\beta}(t_2)}] e^{i(\gamma(t_1)+\gamma(t_2))} e^{-\frac{1}{2}([\hat{\alpha},\hat{\beta}(t_1)]+[\hat{\alpha},\hat{\beta}(t_2)])} \\
&+ [e^{i\hat{\alpha}} e^{i\hat{\beta}(t_1)}, e^{-i\hat{\alpha}} e^{-i\hat{\beta}(t_2)}] e^{i(\gamma(t_1)-\gamma(t_2))} e^{-\frac{1}{2}([\hat{\alpha},\hat{\beta}(t_1)]-[\hat{\alpha},\hat{\beta}(t_2)])} \\
&+ [e^{-i\hat{\alpha}} e^{-i\hat{\beta}(t_1)}, e^{i\hat{\alpha}} e^{i\hat{\beta}(t_2)}] e^{-i(\gamma(t_1)-\gamma(t_2))} e^{\frac{1}{2}([\hat{\alpha},\hat{\beta}(t_1)]-[\hat{\alpha},\hat{\beta}(t_2)])} \\
&+ [e^{-i\hat{\alpha}} e^{-i\hat{\beta}(t_1)}, e^{-i\hat{\alpha}} e^{-i\hat{\beta}(t_2)}] e^{-i(\gamma(t_1)+\gamma(t_2))} e^{\frac{1}{2}([\hat{\alpha},\hat{\beta}(t_1)]+[\hat{\alpha},\hat{\beta}(t_2)])}
\end{aligned} \tag{4.35}$$

Note the operator $\hat{\alpha}$ is time-independent and dependent on the position operator $k\hat{x}$ only. When the commutator terms above are fully expanded, terms which are proportional to $e^{i\hat{\alpha}} e^{i\hat{\alpha}} = e^{i2\hat{\alpha}}$ or $e^{-i\hat{\alpha}} e^{-i\hat{\alpha}} = e^{-i2\hat{\alpha}}$ will be generated. In the momentum representation this operator would correspond to scattering between $p \to p \pm 2k$ which would allow particles to scatter into adjacent wells. The second term expansion is restricted to terms which conserve the momentum of the electrons, scattering into adjacent wells is suppressed by dropping terms which correspond to momentum transfer of $\pm 2k$.

The final form of the second order term is,

$$\begin{aligned}
&[H(t_1), H(t_2)] = \\
&\quad iV_0^2 \sin\left(\frac{3k^2}{2m}(t_2 - t_1)\right) \Bigg\{ \left[\cos\left(\frac{kp}{m}(t_1 - t_2)\right) \cos\left(\frac{F_0 k}{m\omega^2}(\cos(\omega t_2) - \cos(\omega t_1))\right)\right] \\
&\quad - \left[\sin\left(\frac{kp}{m}(t_1 - t_2)\right) \sin\left(\frac{F_0 k}{m\omega^2}(\cos(\omega t_2) - \cos(\omega t_1))\right)\right] \Bigg\}
\end{aligned} \tag{4.36}$$

In the perturbation series, the second order is integrated over the time variables t_1, t_2,

$$\langle [H(t_1), H(t_2)] \rangle = \int_0^{\tau} dt_1 \int_0^{t_1} dt_2 \, [H(t_1), H(t_2)] \tag{4.37}$$

and can be evaluated numerically, but a closed analytic form is not found. It is noted that in the momentum representation, the second order term is a diagonal term. The first order term is sufficient to investigate the parameters for gap suppression.

The parabolic spectrum gives an approximation of a Hartree-Fock system and an initial demonstration of a gap in a system that can be suppressed by a driving force. However it is of limited applicability. The singularity present in the first term $\langle H_I \rangle$

can cause the gap to increase to a very large size. The ambiguity in the definition of a bandwidth for a parabolic spectrum makes it difficult to define driving parameters that will ensure the Floquet spectrum has both well-separated quasi-energies and is driven at a frequency which will avoid chaotic motion. The many-well parabolic model will be replaced by a model of a generic two-band system with a gap.

4.3 Driven two-band tight-binding model

4.3.1 Undriven tight-binding model

The tight-binding model is a theoretical description of negatively-charged particles moving through a lattice of positive ions. It is built upon the idea that negatively charged particles will be localized near the positive ions. Each ion is labeled as a site by the index (i).

For a system of non-interacting electrons moving through a lattice, the tight-binding model Hamiltonian is expressed in terms of the creation and annihilation operators for the electrons,

$$H_{tb} = -J \sum_i (a_{i+1}^\dagger a_i + h.c). \tag{4.38}$$

The factor (J) denotes the hopping energy, the energy required to go between adjacent sites. From this Hamiltonian, the electronic energy spectrum can be derived,

$$E_{tb}(k) = -2J \cos(ka). \tag{4.39}$$

The parameters (k,a) are the quasi-momentum of the electrons and the lattice spacing, respectively. In the remainder of this section, it will be assumed the lattice has unit spacing $(a = 1)$.

Without the driving force present, and without the weak perturbation applied, we consider a modification of the system: where it consists of two species of sites, labeled (A) and (B). The particles moving between (A) sites and (B) sites do not interact. Such a system has a matrix representation similar to that of the two band model:

$$H_{AB} = E_{tb}(k)\sigma^z \tag{4.40}$$

The system is diagonal and scattering between the two bands is not possible.

4.3.2 Driven tight-binding model

The driving force is incorporated into the tight-binding model through an appropriate gauge definition. It is seen that the quasi-momentum of the electrons can be shifted to include the vector potential of the applied electric field: $k' = k + A(t)$.

In the tight-binding Hamiltonian, the addition of the gauge field appears as a phase term:

$$H_{driven} = -t\sum_i (e^{(iA(t))}a_{i+1}^\dagger a_i + h.c), \tag{4.41}$$

where A(t) is the vector potential. Choosing an appropriate gauge transform allows the vector potential to be defined by $A(t) = \nabla \int dt F_{DC}(t) = -e\int dt E(t)$. It is seen that the addition of the field modifies the energy spectrum:

$$E_{tb}(k') = -2J\cos(k') = -2J\cos(k + A(t)). \tag{4.42}$$

For the alternating lattice described in Section (4.3.1) the matrix becomes:

$$H_{AB}(t) = E_{tb}(k + A(t))\sigma^z \tag{4.43}$$

4.3.3 Perturbed system

The weak perturbation applied to the system introduces scattering between A and B sites. A spatial perturbation is defined which will shift the on-site energies of (A, B) sites by a constant amount V_0.

$$H = -J\sum_i \left(e^{(iA(t))}a_{i+1}^\dagger a_i + \text{h.c.}\right) + V_0\sum_i (-1)^i a_i^\dagger a_i \tag{4.44}$$

The result of this perturbation is a gap opening at the point $k = \frac{\pi}{2}$. In terms of the matrix representation,

$$H = E_{tb}(k')\sigma^z + V_0\sigma^x = \begin{pmatrix} E_{tb}(k') & V_0 \\ V_0 & -E_{tb}(k') \end{pmatrix}. \tag{4.45}$$

From the eigenvalues of this matrix, the driven, perturbed energy spectrum will be,

$$\epsilon(k', V_0) = \sqrt{V_0^2 - 2J\cos(k + A(t))}, \tag{4.46}$$

and the spectra are shown in Figure (4.4). As has been done in the previous sections, the interaction representation for the perturbed system is defined. The terms H_0 and H_1 are defined from the full system:

$$\begin{aligned} H_{sys}(t) &= H_{AB}(t) + H_1 \\ &= (-2J\cos(k + A(t))\sigma^z) + \left(\frac{V_0}{2}\sigma^x\right) \end{aligned} \tag{4.47}$$

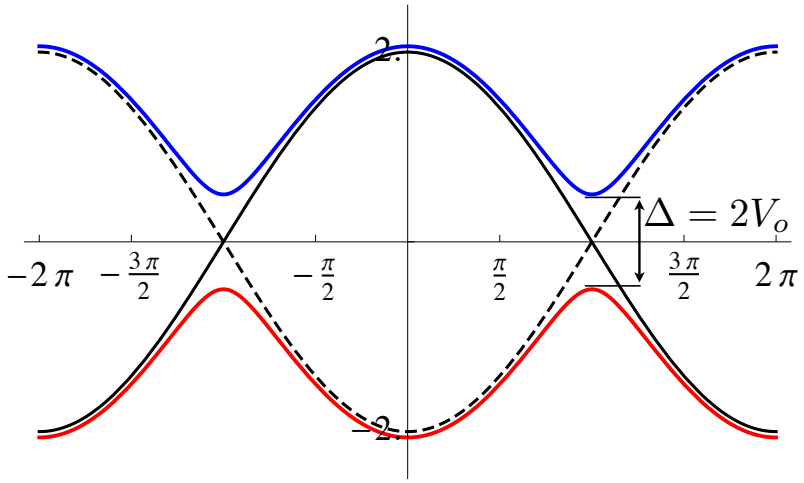

Figure 4.4: A segment of the undriven tight-binding spectra in the presence of weak spatial perturbations. In the absence of the perturbation, exact crossings between the left and right movers (black solid, black dashed) exist at the midpoint of the bands. With the perturbation present, a gap of width of $2V_0$ opens at the band midpoint (red, blue).

The interaction representation is found as described in Section (2.5):

$$\begin{aligned} H_I &= e^{i\int dt' H_0(t')} H_1 e^{-i\int dt' H_0(t')} \\ &= e^{i\int dt'(-2J\cos(k+A(t))\sigma^z)} \left(\frac{V_0}{2}\sigma^x\right) e^{-i\int dt'(-2J\cos(k+A(t))\sigma^z)} \\ &= e^{i\phi_k(t)\sigma^z} \left(\frac{V_0}{2}\sigma^x\right) e^{-i\phi_k(t)\sigma^z} \end{aligned} \tag{4.48}$$

In the final line the time integral of the energy band is replaced by a time-dependent phase. To evaluate the commutator between the Pauli spin matrices, the exponential operators are expanded,

$$e^{i\phi_k(t)\sigma^z} = (\cos(\phi_k(t))\mathbf{1} + i\sigma^z \sin(\phi_k(t))) \tag{4.49}$$

and the expression for H_I becomes a combination of simple products with Pauli matrices. The final step in evaluating H_I involves reducing multiple Pauli matrix products to a simple operator, which is easily done using the relation:

$$\sigma^i\sigma^j = i\,\epsilon_{ijk}\,\sigma^k \tag{4.50}$$

Thus the evaluation of H_I reduces and simplifies as follows,

$$\begin{aligned} H_I &= e^{i\int dt' H_0(t')} H_1 e^{-i\int dt' H_0(t')} \\ &= e^{i\phi_k(t)\sigma^z}\left(\frac{V_0}{2}\sigma^x\right)e^{-i\phi_k(t)\sigma^z} \\ &= \left(\cos\left(\phi_k(t)\right)\mathbf{1} + i\sigma^z\sin\left(\phi_k(t)\right)\right)\frac{V_0}{2}\sigma^x\left(\cos\left(\phi_k(t)\right)\mathbf{1} - i\sigma^z\sin\left(\phi_k(t)\right)\right) \\ &= \frac{V_0}{2}\left[\cos\left(2\phi_k[t]\right)\sigma^x - \sin\left(2\phi_k[t]\right)\sigma^y\right]. \end{aligned} \tag{4.51}$$

The time dependence in H_I comes in the time integral of the driven energy bands. As before, the full time evolution of the system is given exactly by integrating H_{sys} or through the perturbative expansion with H_I,

$$\begin{aligned} U(t) &= e^{-i\int dt' H_{sys}(t')} \\ U(t) &= U_0(t)S(t) \\ S(t) &= 1 + \int dt' H_I(t') + \ldots. \end{aligned} \tag{4.52}$$

where perturbative expansion for S(t) will be carried out to the second order.

For a cosine spectrum, a closed analytical description of the gap suppression cannot be found. The full solution for gap closure will be found numerically, either by direct numerical integration of the unitary operator defined by the driven Hamiltonian in Eq. (4.47) or by numerically integrating the unitary operator defined by a perturbative series in the interaction Hamiltonian (Eq. (4.51)).

Presented here is an approximation to the cosine phase, showing how gap closure is possible. From the definition of the phase and the vector potential,

$$\begin{aligned} \phi_k(t) &= \int_0^t dt' \epsilon[k + A(t')] \\ A(t) &= -\frac{F_0}{\omega}\cos\left(\omega t\right) \end{aligned} \tag{4.53}$$

and using the tight-binding energy spectrum,

$$\epsilon[k + A(t)] = (-2J)\cos\left(k - \frac{F_0}{\omega}\cos\left(\omega t\right)\right) \tag{4.54}$$

the nested trigonometric functions complicate the time integrations necessary to define the Floquet spectrum. These can be expanded using the Jacobi-Anger expansion. In the phase term,

$$\begin{aligned} \phi_k(t) &= (-2J)\left[\cos\left(k\right)\int_0^t dt' \cos\left[A(t)\right] - \sin\left(k\right)\int_0^t dt' \sin\left[A(t)\right]\right] \\ &= (-2J)\left[\cos\left(k\right)\left(J_0\left(\frac{F_0}{\omega}\right)t + 2\sum_{n=1}^{\infty} J_{2n}\left(\frac{F_0}{\omega}\right)\frac{\sin\left(2n\omega t\right)}{2n\omega}\right)\right. \\ &\left. - \sin\left(k\right)\left(-2\sum_{n=1}^{\infty}(-1)^n J_{2n-1}\left(\frac{F_0}{\omega}\right)\frac{\sin\left([2n-1]\omega t\right)}{[2n-1]\omega}\right)\right] \end{aligned} \tag{4.55}$$

if the driving frequency is very large, then the $J_0\left(\frac{F_0}{\omega}\right)$ term dominates. Truncating the series expansions results in an approximate expression,

$$\phi_k(t) \approx (-2J)\cos(k)J_0\left(\frac{F_0}{\omega}\right)t \tag{4.56}$$

which is linear in time. The first order term is simply the time average of the interaction representation (the time averaging is done with respect to the period of the driving force):

$$\langle H_I\rangle = \frac{1}{\tau}\int_0^\tau dt' - k\sigma^z + \cos\left(2\left(\frac{F_0}{\omega}\right)\sin(\omega t')\right)\sigma^x + \sin\left(2\left(\frac{F_0}{\omega}\right)\sin(\omega t')\right)\sigma^y. \tag{4.57}$$

The interaction representation of the driven tight-binding model given in eq. (4.51) can be used for any system with a Hamiltonian given in the general form:

$$H_{sys} = \epsilon(k,t)\sigma^z + \frac{V_0}{2}\sigma^x. \tag{4.58}$$

The only modification required is the generalization of the definition of $\phi_k(t)$:

$$\phi_k(t) = \int_0^t dt'\epsilon(k,t') \tag{4.59}$$

This general form will be of use in the following section, where the Floquet analysis is applied to a linear spectrum.

4.4 Driven lattice model: linear spectrum

For the driven tight-binding model, the previous section considered the effect of the driving force on all electrons trapped in a given band. For the case of a system with half-filled bands, the addition of the perturbation causes the system to transition from a metallic state to an insulating state. The gap closure in the driven system can be studied by focusing on the electrons which are localized near the Fermi surface, those have momenta close to the Fermi momentum. By restricting the system to these electrons, the Hamiltonian of the full tight-binding model can be linearized.

4.4.1 Undriven lattice model

From the unperturbed tight-binding model on a modified lattice, given in equation (4.39), the energy spectrum was defined with a cosine function. For a partially filled band, the Fermi-momentum is located at $k_F a = \pi/2$, if the band is half filled, this occurs at the midpoint of the band. When the perturbation term is present, the gap opens at the middle of the band. Linearizing the cosine spectrum at the Fermi-momentum gives

a linear spectrum for those electrons localized near the Fermi surface. Equation (4.39) is linearized as follows:

$$\epsilon(k = k_F + \delta) \approx \epsilon(k_F) + (\delta)\frac{\partial \epsilon(k)}{\partial k}\bigg|_{k=k_F} \tag{4.60}$$

so near the Fermi momentum the linear spectrum is:

$$\epsilon(k) = \pm 2Ja(k). \tag{4.61}$$

The positive (negative) sign differentiates between right (left) movers. In the absence of the perturbation, again the two branches have an exact crossing. As above, the two band system consists of two non-interacting species of particles: left and right movers with linear spectra.

It was shown in Section (2.3.2) that the original terms with left and right movers has a diagonal matrix representation. The energy spectra for the left and right movers are not gapped. The addition of a weak perturbation term results in scattering between branches and results in a gap opening at the midpoint of the Brillouin zone.

4.4.2 Driven linear model

The Hamiltonian of the driven, perturbed system is separated into two terms:

$$H_{sys} = H_0 + H' \tag{4.62}$$

$$H_0 = 2Ja\left(k + \frac{F_0}{\omega}\cos(\omega t)\right)\sigma^z \tag{4.63}$$

$$H' = \frac{V_0}{2}\sigma^x \tag{4.64}$$

with the same form as the full tight-binding system in equation (4.51). The analysis of Sections (4.3.2) and (4.3.3) is applied to the linear spectrum. This results in the same condition for delocalization:

$$\langle \cos(2\phi_k(t)) \rangle = 0 \tag{4.65}$$

The result for the linear spectrum differ from those of the cosine spectrum only in a modification to the phase term:

$$\phi_k(t) = \int_0^t dt' \epsilon(k, t') \tag{4.66}$$

$$= 2Ja\left(kt + \frac{F_0}{\omega^2}\sin(\omega t)\right). \tag{4.67}$$

For the linear spectrum, a closed form for the gap suppression can be found,

$$J_0\left(2Ja\frac{F_0}{\omega^2}\right) = 0. \tag{4.68}$$

One of the motivations for studying a gapped linear spectrum is the close connection to Sine-Gordon dynamics, particularly the similarities in the energy spectra. It was seen in Chapter (3) that dynamical stabilization for a soliton occurred at driving parameters that lead to a suppression of the $\cos(\varphi_0)$ term in the effective potential, where $J_0\left(\frac{F_0}{\omega^2}\right)$ vanished. With a similar hyperbolic spectrum, it is seen that the linear spectrum has dynamical gap suppression where $J_0\left(2Ja\frac{F_0}{\omega^2}\right)$ vanishes.

4.5 Numerical results: gap suppression

Two series of numeric simulations were carried out. The first investigated the gap closure in each of the three systems described above (the parabolic, cosine, and linear spectra), driving each system with only an AC field. The second investigated how driving a system into a gap suppressed state would affect the electric current generated by an additional DC field.

Studying the gap closure in each of the three spectra previously discussed was done by numerically integrating the unitary time operator. Then, after finding its time average over one period of the driving force, the average Floquet quasi-energies were defined. The unitary operator for a system was defined by the exact expression, involving the full driven Hamiltonian, and also through a perturbative expansion using the interaction Hamiltonian.

The perturbation series expansion of the operator $U(t)$ solves for the matrix $U(t)$ using the second order expansion of $S(t)$,

$$\begin{aligned} U(t) &= U_0(t)(\mathbf{1} + \langle H_I(t)\rangle + \frac{i^2}{2}\langle [H_I(t_1), H_I(t_2)]\rangle + \dots \\ &\approx U_0(t)(\mathbf{1} + \langle H_I(t)\rangle + \frac{i^2}{2}\langle [H_I(t_1), H_I(t_2)]\rangle), \end{aligned} \tag{4.69}$$

where the integration Hamiltonian (H_I) is averaged over one period of the driving force.

The driving force was implemented in the numeric system as a combined AC and DC field, rather than with a time-dependent AC field amplitude. With the DC field present the overall driving force had an envelope form with the overall amplitude of the field gradually increased over a fixed time interval.

4.5.1 Parabolic spectrum

For the simulation of the gap closure, the unitary operator $U(t)$ was numerically integrated from the full Hamiltonian. From the full unitary operator $U(t)$ the energy spectrum was found from the eigenvalues of the system. The matrix $U(t)$ can be

diagonalized with elements given by,

$$U_{ii}(t) = e^{i\mathcal{M}_i \tau} \tag{4.70}$$

with $\mathcal{M}_i$ the Floquet quasi-energy of the i-th level. In the momentum representation the first order term of the perturbation series connected states of different momenta and contributed to the gap. The conditions for gap closure were determined from Equation (4.30) where resonance in the $n = 0$ term at $p = \pm k/2$ lead to gap suppression at the root of the Bessel function ($J_0(F_0 k/m\omega^2) = 0$). In Figure (4.6), the possibility of gap closure is investigated for different driving frequencies. Defining the driving amplitude in terms of (k, m, ω),

$$F(\omega) = \frac{(2.4048)m\omega^2}{k} \tag{4.71}$$

it is seen that gap closure occurs if the driving frequency is large enough to ensure the Floquet spectrum has well-separated levels. Shown in Figure (4.5), the system used for numeric simulation was designed with a small gap compared to the width (J) of the lowest band.

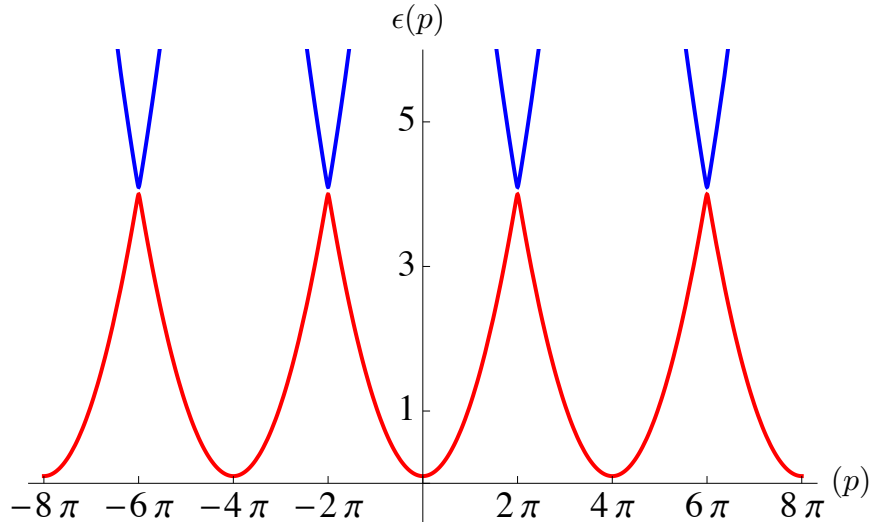

Figure 4.5: Shown is the gapped energy spectrum of an $N = 5$ parabolic well system. The parameters of the system $k = 4\pi$ and $V = 0.05$ were chosen to ensure the width of the lower band formed was much larger than the gap.

4.5.2 Cosine spectrum

For the simulation of the gap closure, the unitary operator $U(t)$ was numerically integrated from the full Hamiltonian. These results were compared to the perturbation

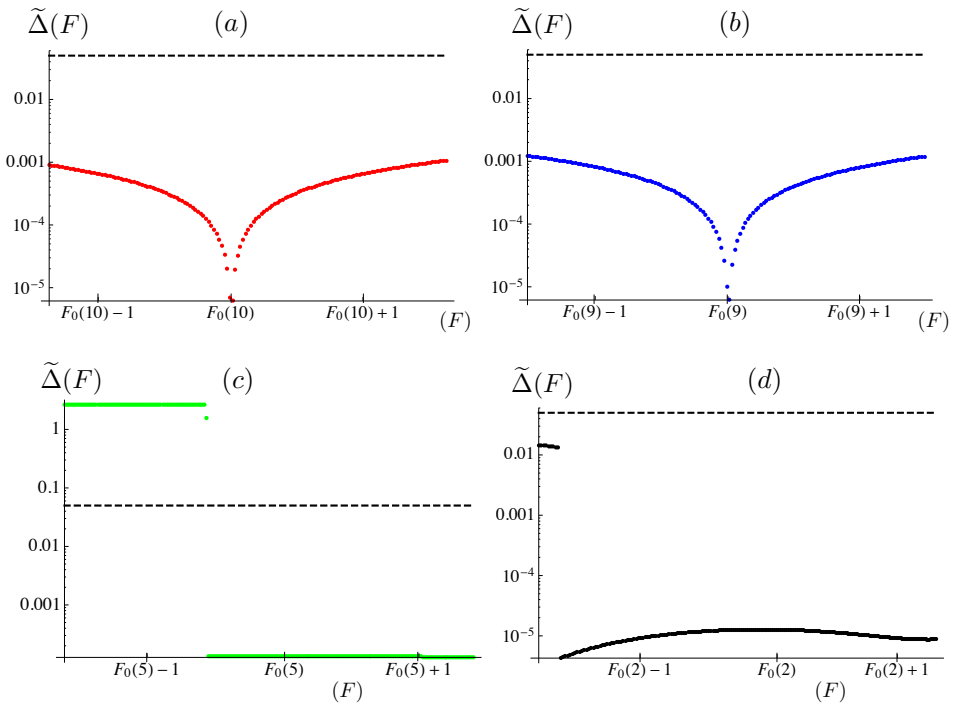

Figure 4.6: The gap width predicted from the first order perturbation expansion. For $\omega \gg J$ (a,b) the gap closes at the value predicted by $F_0(\omega)$. For $\omega \approx J$ (c) or $\omega < J$ (d) the possibility of gap closure is ambiguously defined and complicated by the overlap of Floquet levels.

series results. At the root of the Bessel function $J_0(z) = 0$ it was seen that gap suppression occurred. From the time averaged eigenvalues of the full unitary operator $U(t)$ the energy spectrum was found.

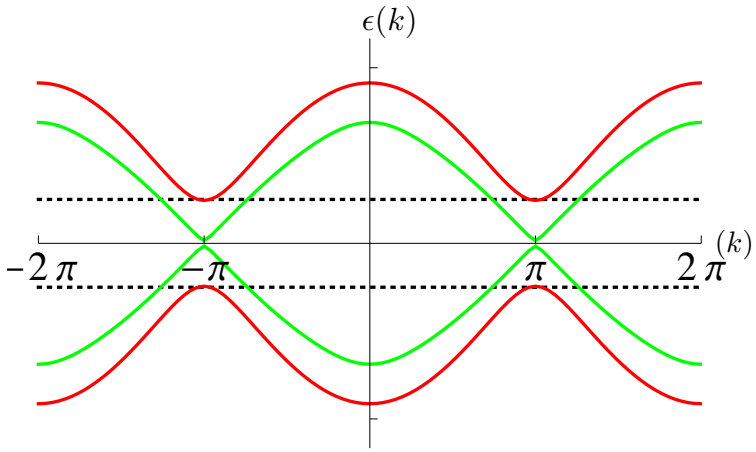

Figure 4.7: Shown is the energy spectrum found from exact integration of H_{sys}, showing the gap suppression near $k = \pm\pi$. The gap of $\Delta = \omega/4$ is shown (black dotted). At $F = .00235$ the gap is suppressed (green solild) and at $F = 0.00421$ the gap is present (red solid). The other parameters for the system are $J = 0.0013$ eV, $a = 0.5$ nm, $\omega = 1$eV. The y-axis is marked at $\pm\omega/2$

4.5.3 Linear spectrum

At the root of the Bessel function $J_0(z) = 0$ it was seen that gap suppression occurred. From the full unitary operator $U(t)$ the energy spectrum was found from the eigenvalues of the system. Only a single gap at $p = \frac{ka}{2}$ was considered, and was shifted to the origin. As demonstrated in the parabolic model, the dependence on the driving amplitude is observed (shown in Figure (4.11)) in both the cosine and linear spectra.

4.6 Numerical results: combined field driving

It is seen that a small gap caused by interactions between two electron bands can be effectively suppressed due to a strong AC field. The study of the two-band is concluded by observing how driving a system toward gap closure affects the dynamics of a single electron or a collection of electrons. With the parameters for gap closure identified, the sinusoidal spectrum was driven by both an AC field which would close a

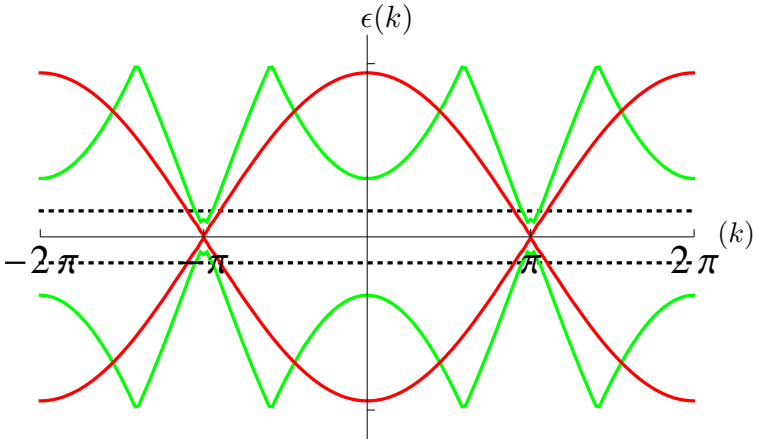

Figure 4.8: Shown is the energy spectrum found from integration of the perturbation series derived from H_I, showing the gap suppression near $k = \pm\pi$. The gap of $\Delta = 0.15\omega$ is shown (black dotted). At $F = .0005$ the gap is present (green solild) and at $F = 0.0054$ the gap is suppressed (red solid). The other parameters for the system are $J = 0.02$ eV, $a = 0.5$ nm, $\omega = 1$eV. The y-axis is marked at $\pm\omega/2$.

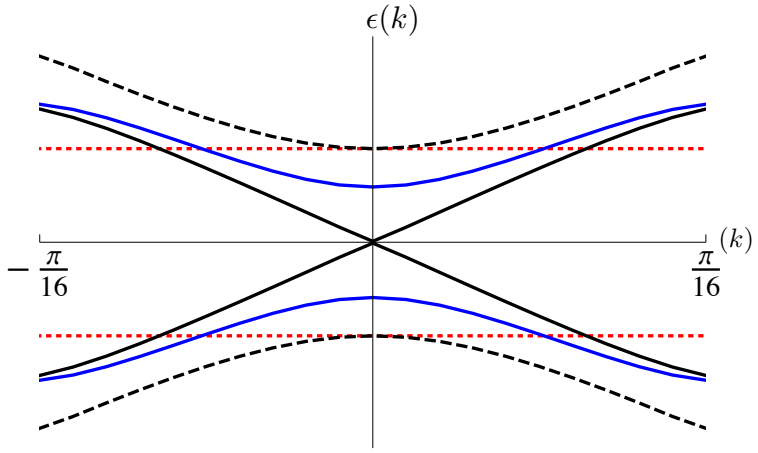

Figure 4.9: Shown is the gapped energy spectrum near k = 0, found from exact integration of H_{sys}. The gap of $\Delta = \omega/2$ is shown (red dotted). At approximately zero driving, the spectrum is gapped (black dashed). At $F = .00084$ the gap is reduced (blue solild) and at $F = 0.00156$ the gap is suppressed (black solid). The other parameters for the system are $v_F = 2J/a = 0.0067, \omega = 0.003$eV

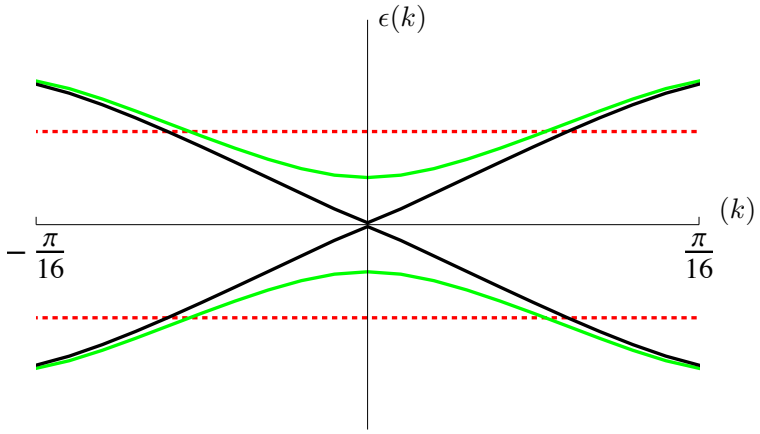

Figure 4.10: Shown is the gapped energy spectrum near k = 0, found from integration of the perturbation series derived from H_I. The gap of $\Delta = \omega/2$ is shown (red dotted). At $F = .00084$ the gap is reduced (green solid) and at $F = 0.00165$ the gap is suppressed (black solid). The other parameters for the system are $v_F = 2J/a = 0.0067, \omega = 0.003$eV

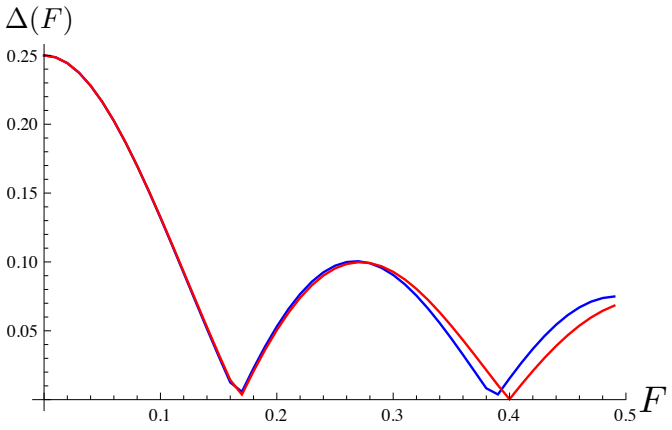

Figure 4.11: Shown is the dependence of the renormalized gap width on the driving amplitude. Gap widths for both the cosine (red) and linear (blue) are shown, both generated from systems with parameters $J = 2.0$, $\omega = 0.75$, $\Delta_0 = 0.25$.

band gap, and a weak DC field. The DC field with weak amplitude was turned on first and the AC field amplitude is gradually increased. Within several driving periods the system would be driven under both AC and DC fields. It was expected that a particle in the system would first exhibit motion due to the weak DC field and the gap. As the AC field gradually increases in amplitude, the gapped system would be driven into a gap-less system and it was investigated if the dynamics changed accordingly.

Two systems were prepared for the tight-binding model, a single electron and a collection of electrons. A single electron in the sinusoidal spectrum, under DC field driving, would exhibit Bloch oscillations. A collection of electrons would behave as a metal or an insulator depending on whether the band was completely filled or only partially filled. Shown in Figure (4.12)(a,b) are the expected results as a system is driven through a dynamical band closing. Also shown in Figure (4.12)(c) is a simplification of the combined field vector potential. The time dependence of the vector potential is chosen such that the DC field is gradually turned on, then the AC field is gradually turned on. The result is that the system is initially driven by only the DC field, then a combined AC and DC field. The AC field is turned off first, followed by the DC field.

4.6.1 Period doubling

The sinusoidal spectrum was driven with a combination AC-DC field. With the gap present it is expected that in the presence of only the DC field, the system will demonstrate Bloch oscillations in the gapped spectrum. As the AC field is tuned to the amplitude which corresponds to gap closure, it is expected that the system will undergo Bloch oscillations in the un-gapped spectrum.

Bloch oscillations were observed by calculating the electric current generated by a single particle oscillating in the periodic potential. The effective field generated by the motion of a single particle was discussed in Section (2.7). To study the motion of a particle rather than the shape of the energy bands, we solved for the two-state wave-functions of the initial Hamiltonian. These wavefunctions were used to define the density matrix of the two-band system. With a state initially prepared in the lower band, the density matrix was evolved in time with the DC and AC fields gradually turned on.

As the particle is driven to the edge of a Bloch band and reflected, the current is oscillatory with period given by the period of Bloch oscillations $\tau_B = 2\pi/eEa$, where the electric field is the DC field and a is the lattice spacing. With the gap present, the period of Bloch oscillations is $\tau_g = 2\pi/eEa_g$, and if the gap is closed, the period of Bloch

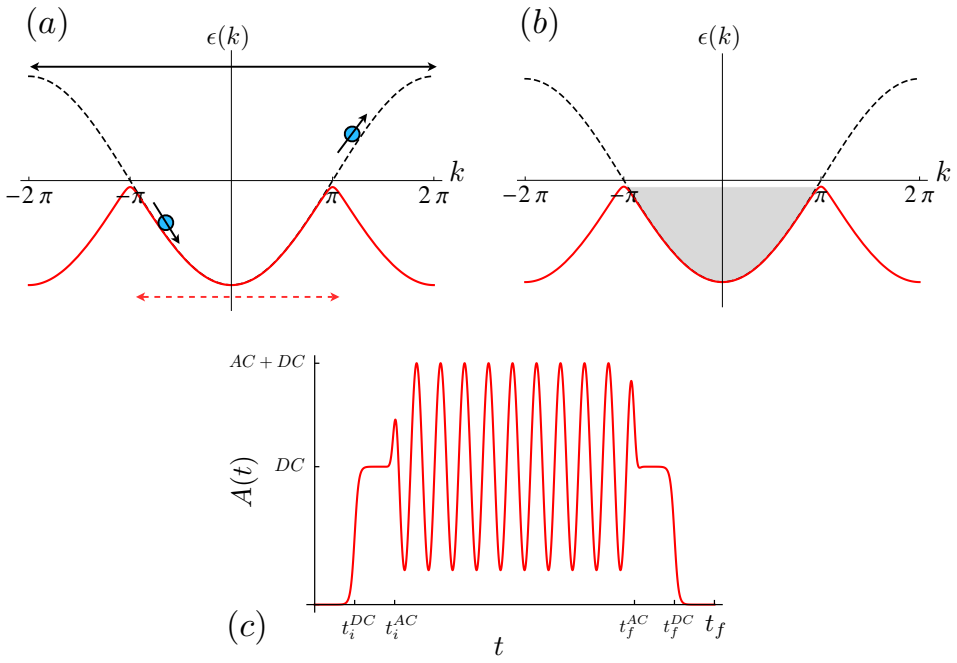

Figure 4.12: The expected dynamics of a system under AC and DC field driving. Shown in (a) are the single particle dynamics and the period doubling of Bloch oscillations. Initially an electron would oscillate with a period determined by Bloch oscillations in the lower band (red solid, dashed lines). As the gap is closed the electron would oscillate with a period determined by Bloch oscillations in the full band (black solid, dashed lines). Shown in (b) is the transition of a filled band (insulating) system becoming metallic as the bandwidth increases due to gap closure. Shown in (c) is a simplification of the combined AC and DC field vector potential.

oscillations would double to $\tau_g = 4\pi/eE(a_g)$.

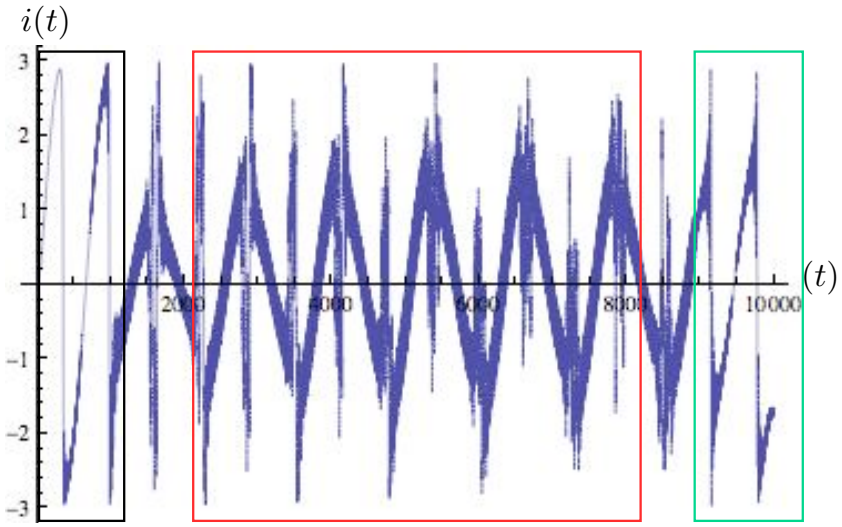

Figure 4.13: The current generated by a single particle driven by DC and AC fields. With initially only the DC field present, the current shows oscillations with a Bloch frequency determined by the width of the gapped band (black frame). As the AC field drives the system into gap closure, the period of oscillation doubles due to the doubling of the Brillouin zone width (red frame). As the AC field is turned off the current returns to it initial period of oscillation (green frame).

4.6.2 Driven net current

When the gap is present, the system is prepared in an initial state which is an insulator. The lower band is completely filled and it is expected that no net current will be generated by the external driving fields. However as the system is driven to a suppressed gap, the final state is metallic and a net current is expected.

4.7 Conclusions

Coherent destruction of tunneling is a perturbative effect which predicts the localization of a particle in an AC field. This localization is based on suppression of level splitting. We considered the suppression of a gap due to interactions between electrons in a one-dimensional system. Defining a perturbative expansion of the time-evolution operator, the effects of a strong AC driving force on the Floquet quasi-energy spectrum was investigated. It was seen that for a tight-binding model, certain driving parameters will lead to gap suppression, specifically those which satisfied $\langle \cos(2\theta(t)) \rangle =$

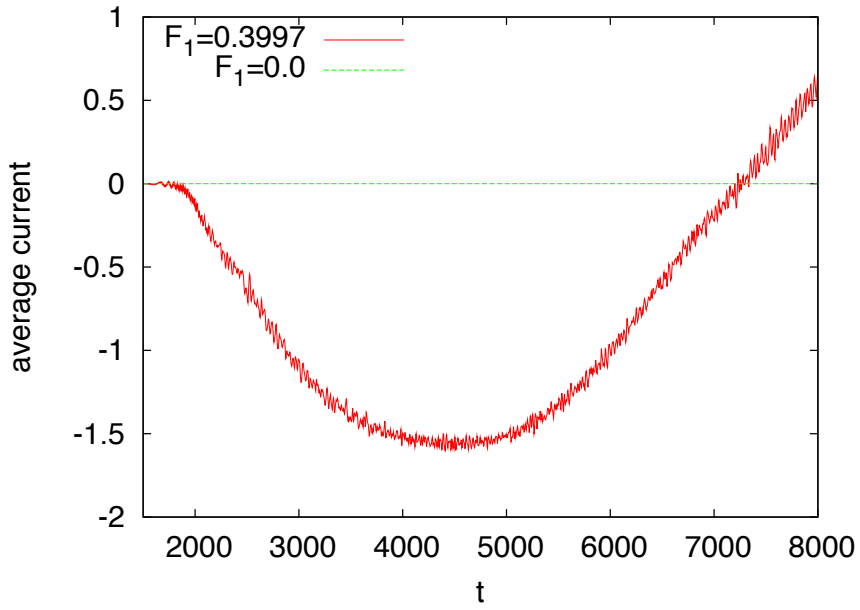

Figure 4.14: Net current generated with both AC and DC field driving. For zero AC driving (green dashed) the system remains in an insulating state and there is no net current. At AC driving the gap closure, the system has a net nonzero current for long enough driving (red).

0. An analytical form was found for the linearized spectrum, near the Fermi momentum. Additionally, a continuum model of parabolic wells was studied.

The possibility of gap suppression is due to the hybridization of Floquet levels. For the tight-binding lattice model, Floquet levels were well separated and did not overlap.

To further investigate how gap closure affects a system, a weak DC field was added to the driving force. It was observed through numerical simulation that the dynamics of a single electron, or a many-electron system, showed the effects of gap closure. For a single electron driven through a gap closure, the Bloch oscillations due to the DC field showed a doubling of period. For a gapped system prepared with a full band, an insulating system, driving such a system through gap closure led to the creation of a half-filled, metallic state. The net current for this system became nonzero when the gap was closed.

The work done on gap suppression for a two-band model was done on closed systems only. Heating by phonons was not considered. The long driving times needed to ensure gap closure would likely result in runaway phonon heating and the robustness of these results is questionable.

Chapter 5

Continuous third harmonic generation in a terahertz driven modulated nanowire

The material in this chapter was submitted for publication in ACS Nanoletters and has been published on the arXiv [158].

The driven single band system is a continuum model describing the effects of a strong driving force on electrons in a conduction band. Combining the Floquet quasi-energy spectrum with the Keldysh Green's function technique, we derive a phenomenological model of the semiclassical master equation for a one-dimensional band of strongly and rapidly driven electrons in the presence of weak scattering by phonons. When the strong driving force is present, the bandwidth of the energy spectrum is renormalized. The amplitude of the driving force can be used to create a flat band, in which no current will be generated. It is also possible to invert the energy band. With an inverted band, the system will equilibrate at points which were unstable in the absence of the driving force. This inverted distribution of particles leads to continuous higher harmonic generation, specifically the amplification of the third harmonic and the suppression of the primary harmonic. The system is derived as a closed system and also in the presence of dissipation. In the absence of scattering, the quantum efficiency of frequency tripling for such a system can be as high as 93%. Higher harmonic generation remains stable in a dissipative system, provided the phonon modes are dominated by surface modes of a nearby (higher-dimensional) substrate. The power absorbed from the driving field is continuously dissipated by phonon modes, leading to a quasi-equilibrium in the electron distribution. We use the Kronig-Penney model with varying effective

mass to establish growth parameters of an InAs/InP nanowire near optimal for third harmonic generation at terahertz frequency range.

5.1 Introduction

When electrons in a crystal band are driven by an external time-independent electric field, they move periodically across the Brillouin zone, creating characteristic Bloch oscillations [37, 159–162]. The frequency of the oscillations, $\omega_{\mathrm{B}} = eEa/\hbar$, where a is the unit cell size, coincides with the energy separation between neighboring states localized on a Wannier-Stark ladder [162, 163]. The effect has been observed for electrons/holes in semiconducting superlattices [164, 165], for atoms trapped in a periodic optical potential [166], and for light propagating in a periodic array of waveguides, with gradient of the temperature or of the refraction index working as an effective electric field [167–169].

Combining the effects of a strong, time-periodic driving field, with the nonlinearity of the Bloch oscillations leads to higher harmonic generation of the driving frequency [62, 170, 171]. This effect has recently been observed in bulk ZnO crystals strongly driven by a few-cycle pulsed infrared laser [64]. The application of the infrared field in short, 100-femtosecond, pulses was necessary to ensure that the absorbed energy could be transferred to the lattice and dissipated.

Semiconductor superlattices are an ideal system in which to observe these high-field effects. The transport of carriers through these structures can be described in terms of coherent motion through minibands in the energy spectrum [172]. Subsequently, the effects of intense driving fields can be described based on the modification of these minibands [173]. The mechanisms of charge transport in semiconductor superlattices in the presence of strong fields has been extensively studied in terms of miniband transport, Wannier-Stark hopping and photon-assisted transport [174, 175].

In this work, we suggest that frequency multiplication due to periodically-driven Bloch oscillations could also be observed in a steady-state setting, *e.g.*, a periodically modulated nanowire (or an array of such nanowires) continuously driven by high-amplitude terahertz radiation (see Fig. 5.1). In the weak-scattering limit, the quantum efficiency of frequency tripling for such a system can be as high as 93%. The high efficiency of third harmonic generation presents a novel means of Thz radiation and has been previously studied for GaAs superlattices [176, 177].

For a nanowire in mechanical contact with an insulating, optically transparent substrate, a quasi-equilibrium electron distribution will be reached as the power

absorbed from the driving field will be continuously dissipated into phonon modes. This distribution can be quite different from the initial, equilibrium Fermi distribution. In particular, at the driving field amplitude which is optimal for third harmonic generation, the distribution can be both broadened and inverted. The inversion of the distribution occurs once the driving field amplitude exceeds the dynamical localization threshold [57, 178].

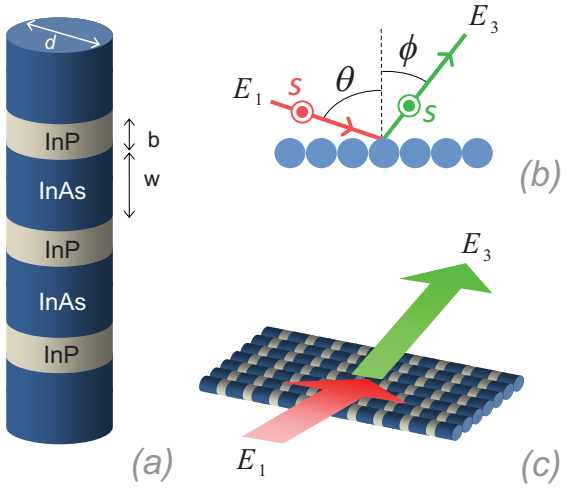

Figure 5.1: (a) A nanowire made with alternating InAs/InP regions. (b), (c) Schematic of the third harmonic generation with a planar array of such nanowires. The driving field is s-polarized so that the electric field E_1 be parallel to the nanowires. The generated third harmonic will have the same polarization but propagate at a different angle.

In our analytic derivation, we combine the Floquet quasi-energy description with the Keldysh Green's function technique to obtain the semiclassical master equation for a one-dimensional band of strongly and rapidly driven electrons in the presence of weak scattering by phonons. We solve these equations numerically to find the electron distribution function for a cosine energy band at a given driving field frequency (fixed at $\Omega/2\pi = 1\,\mathrm{THz}$) and the field amplitude chosen to suppress the generation of the principal harmonic. This electron distribution is used as an input for calculating the time-dependent current and the intensity radiated at different harmonics of the driving field frequency. We use these results to find the optimal dimensions of a periodically modulated InAs/InP nanowire, which would yield the most efficient frequency tripling of 1 THz radiation.

5.2 Nonequilibrium driven system

We consider a single-band one-dimensional metallic wire driven by a harmonic electric field with the amplitude E_0 and frequency Ω, and coupled to substrate phonons,

$$H = H_0 + H_{\rm e-ph} + H_{\rm ph}, \tag{5.1}$$

where the electron, electron-phonon, and phonon Hamiltonians are, respectively

$$H_0 = \sum_k \varepsilon\big(k + A(t)\big) c_k^\dagger c_k, \tag{5.2}$$

$$H_{\rm e-ph} = V^{-1/2} \sum_{\mathbf{q},k} M_{\mathbf{q},k} c_{k+q_\parallel}^\dagger c_k (b_{\mathbf{q}} + b_{-\mathbf{q}}^\dagger), \tag{5.3}$$

$$H_{\rm ph} = \sum_{\mathbf{q}} \omega_{\mathbf{q}} b_{\mathbf{q}}^\dagger b_{\mathbf{q}}. \tag{5.4}$$

Here c_k ($c_k^\dagger$) is the annihilation (creation) operator for an electron with one-dimensional momentum $\hbar k$ and energy $\varepsilon(k)$. To apply our results to a periodically modulated nanowire, we assume a tight-binding model with the electronic spectrum,

$$\varepsilon(k) = -2J\cos(ka), \tag{5.5}$$

where J is the hopping matrix element and a is the period of the potential along the chain. The electric field is incorporated into the Hamiltonian through the vector potential $A(t) = A_0 \sin\Omega t$ with $A_0 = eE_0/\hbar\Omega$ representing the vector potential of the driving field. Phonon annihilation (creation) operators $b_{\mathbf{q}}$ and $b_{\mathbf{q}}^\dagger$ are labeled with the three-dimensional wavevector $\mathbf{q} \equiv (q_\parallel, \mathbf{q}_\perp)$ and $\omega_{\mathbf{q}}$ is the phonon frequency (electron spin and phonon branch indices are suppressed). The factors $M_{\mathbf{q},k} = \alpha_{\mathbf{q},k}(\hbar/2\omega_{\mathbf{q}})^{1/2}$ are the matrix elements for electron-phonon scattering.

We ignore the effects of disorder or electron-electron interactions, and consider lattice phonons in thermal equilibrium at temperature $\hbar/k_B\beta$. We do not include directly the scattering by phonon modes of the nanowire, assuming that they are strongly hybridized with those of the substrate, with the corresponding effects incorporated in the matrix elements $M_{\mathbf{q},k}$. The electron-phonon coupling is considered to be weak, meaning that the phonon scattering time is long compared to the period $\tau \equiv 2\pi/\Omega$ of the driving field.

The dynamics of the strongly-driven electrons with the Hamiltonian (5.2) is characterized by non-monotonous phases

$$\varphi_k(t) = \int_0^t dt' \varepsilon\big(k + A(t')\big). \tag{5.6}$$

The phase accumulated over a period, $\varphi_k(\tau)$, can be expressed in terms of the average particle energy with the momentum $\hbar k$,

$$\langle \varepsilon(k+A) \rangle \equiv \tau^{-1} \int_0^\tau dt\, \varepsilon\big(k + A(t)\big); \tag{5.7}$$

clearly, this energy can be also identified as the Floquet energy of a single-electron state. While Eq. (5.7) does not include the usual additive uncertainty $m\Omega$, this particular choice has the advantage that in the weak-field limit, $A_0 \to 0$, $\langle \varepsilon(k+A) \rangle$ recovers the zero-field spectrum $\varepsilon(k)$.

The average energy (5.7) also coincides with that introduced in the theory of dynamical localization [57, 178]. Dynamical localization occurs when the effective band becomes flat, *i.e.*, $\langle \varepsilon(k+A) \rangle \to 0$. The corresponding condition is most easily obtained in the special case of tight-binding model with the spectrum (5.5),

$$\langle \varepsilon(k+A) \rangle = -2\widetilde{J} \cos(ka), \quad \widetilde{J} \equiv J\, J_0(A_0 a), \tag{5.8}$$

where $J_0(z)$ is the zeroth order Bessel function. With the driving field amplitude increasing from zero the bandwidth is gradually reduced; it switches sign at the roots of the Bessel function, $A_0\, a = \zeta_{0n}$. The first time this happens corresponds to the electric field $E_0 = \zeta_{01} \hbar\Omega / ea$, where $\zeta_{01} \approx 2.405$.

We obtain the instantaneous current by averaging the canonical velocity operator $\partial H / \partial A$ over the electron distribution function $f_k \equiv \langle c_k^\dagger c_k \rangle$,

$$i(t) = C_f(t)\, \sin A(t) a + S_f(t)\, \cos A(t) a, \tag{5.9}$$

where we assumed the tight-binding spectrum (5.5) and used the definitions

$$C_f(t) \equiv 2J \int \frac{dk}{2\pi} \cos(k) f_k, \quad S_f(t) \equiv 2J \int \frac{dk}{2\pi} \sin(k) f_k. \tag{5.10}$$

In the limit of weak scattering, the distribution function f_k is time- independent and always symmetric, $f_{-k} = f_k$. Thus, $S_f(t) = 0$ while $C_f(t) = C_f$ is a time-independent pre-factor. The Fourier components of the current are obtained directly,

$$i(t) = 2C_f \sum_{m=1,3,5,\ldots} J_m(A_0 a) \sin(m\Omega t), \tag{5.11}$$

where the summation is over the odd harmonics m. By choosing $A_0 a = \zeta_{11} \approx 3.8317$, the first harmonic can be fully suppressed, which leaves the third harmonic dominant. The maximal value for the fraction of the energy emitted into the third harmonic (93.34%) is found in close vicinity of this amplitude, see Fig. 5.2.

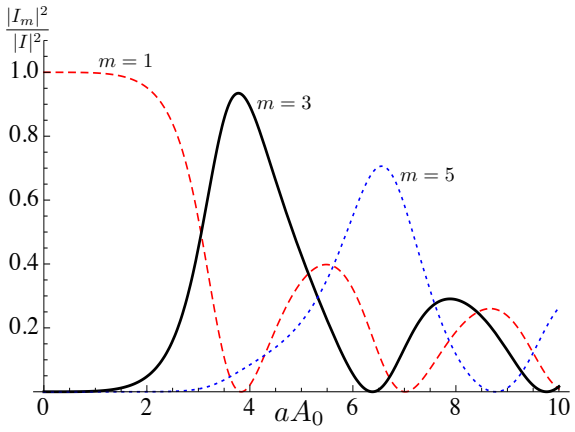

Figure 5.2: Normalized magnitude squared of the Fourier harmonics of the instantaneous current, $|I_m|^2$, for $m = 1$ (red dashed), $m = 3$ (black, solid), and $m = 5$ (blue, dotted) plotted as a function of the dimensionless amplitude of the vector potential of the driving field, see Eq. (5.2). The intensities $|I_m|^2$ correspond to the power emitted in the corresponding harmonics when multiple nanowires are used in a planar geometry, see Fig. 5.1 (b),(c).

We use the Keldysh non-equilibrium Green's function (GF) formalism [70, 72, 73, 179] along with a perturbation theory expansion with respect to the entire time-dependent electron Hamiltonian (5.2); the corresponding evolution is solved exactly in terms of the phases (5.6). Previously, related approaches have been used, *e.g.*, for describing ionization of atoms [180, 181] and the high-order harmonic generation [63] in the field of ultrashort laser pulses. Here, instead of solving the corresponding equations numerically, we take the limit of weak electron-phonon coupling and analytically derive the semiclassical master equation for electron distribution function averaged over the period of the driving field, see Eqs. (5.17) and (5.18). The same master equation can also be derived from the formalism by Konstantinov and Perel' [182] with the help of an appropriate resummation of the perturbation series [183].

In the interaction representation with respect to the time-dependent Hamiltonian (5.2), the electron operators acquire time-dependence $e^{-i\varphi_k(t)}c_k$ with quasiperiodic phases (5.6). We separate these phases by defining the "lower-case" GFs

$$g_k(t_2, t_1) = e^{-i\varphi_k(t_2)} G_k(t_2, t_1) e^{i\varphi_k(t_1)}, \tag{5.12}$$

where the "upper-case" $G_k(t_2, t_1)$ is any of the conventional GFs introduced in the Keldysh formalism [70, 72, 73, 179]. These phases introduce rapid oscillations in the self-energy, making the direct Wigner transformation difficult. We notice, however, that in the limit of weak electron-phonon coupling, the GFs (5.12) are expected to change only weakly when both time arguments are incremented by the driving period τ. This

implies that in the following decomposition,

$$g_k(t_2,t_1)=\sum_m g_{k,m}(t,T)e^{-im\Omega T}, \tag{5.13}$$

$t\equiv t_2-t_1$ is the "fast" time, while $T\equiv(t_2+t_1)/2$ is the "slow" time when it appears as an argument of thus defined Floquet components $g_{k,m}(t,T)$ of the GF. The Dyson equations for thus defined Keldysh $g^K_{k,m}$ and retarded $g^R_{k,m}$ GFs [73] have the form

$$(i\partial_T+m\Omega)g^K_{k,m}(t,T) = I^K_{\rm coll}, \tag{5.14}$$

$$i\partial_t g^R_{k,m}(t,T) = \delta_{m,0}\,\delta(t)+I^R_{\rm coll}, \tag{5.15}$$

where $I^K_{\rm coll}$ and $I^R_{\rm coll}$ are the collision integrals originating from the corresponding self-energy functions. The collision integrals being relatively small, both $g^K_{k,m}$ and $g^R_{k,m}$ are dominated by the $m=0$ components.

5.3 Master equation derivation

To derive the semiclassical master equation, we write the equations for the $m=0$ components of the "lesser" $g^<$ and "greater" $g^>$ GFs [73], perform the Wigner transformation replacing the fast time variable t by the frequency ω, and use a version of the Generalized Kadanoff-Baym approximation [184, 185]

$$g^<_{k,0}(\omega,T)=iA_{k,0}(\omega,T)f_k(T), \quad . \tag{5.16}$$

The corresponding spectral function, $A_{k,0}(\omega,T)=i[g^<_{k,0}(\omega,T)-g^>_{k,0}(\omega,T)]=2\,{\rm Im}g^R_{k,0}(\omega,T)$, is not solved for self-consistently, we assume a sharply peaked Lorentzian function in order to obtain a phenomenological study of the driven system and define the non-equilibrium electron distribution function $f_k(T)$ from the function $g^<$. The width of the Lorentzian Γ is a phenomenological constant and it not solved for self-consistently. It is assumed to be much smaller than the bandwidth of the system and much smaller than the frequency of the driving field ($\Gamma\ll 4J$, $\Gamma\ll\Omega$).

The use of the Kadanoff-Baym approximation restricts us to systems with momentum-independent scattering. Additionally the particle distribution must be sharply peaked. This requires that the electron-phonon coupling be weak, the bandwidth of the renormalized energy is sufficiently larger than the self-energy, and assumes that the electron spectrum renormalization has been included in the Hamiltonian (5.2).

The resulting master equation for weak electron-phonon interactions has the

following standard form

$$\frac{d}{dt}f_k(T) = \int \frac{dk'}{2\pi}\Big\{\Gamma_{k,k'}\,[1-f_{k'}(T)]f_k(T) - \Gamma_{k',k}\,f_{k'}(T)[1-f_k(T)]\Big\}, \tag{5.17}$$

where the transition rates are

$$\Gamma_{k,k'} = 2\sum_m |S_{k,k'}(m)|^2 \int_0^\infty d\omega\, W_{k,k'}(\omega) \times \Big[(n_\omega+1)\delta(\Delta\varepsilon^{(m)}_{k,k'}-\hbar\omega) + n_\omega\delta(\Delta\varepsilon^{(m)}_{k,k'}+\hbar\omega)\Big]. \tag{5.18}$$

Here $W_{k,k'}(\omega)$ is the phonon spectral function (density of states weighted by the square of the coupling) for a given momentum $q_\parallel = k'-k$ along the wire, see Eq. (5.3), $n_\omega \equiv [\exp(\beta\omega)-1]^{-1}$ is the phonon distribution function, and the energy increment

$$\Delta\varepsilon^{(m)}_{k,k'} \equiv \langle\varepsilon(k+A)\rangle - \langle\varepsilon(k'+A)\rangle - m\,\hbar\Omega, \tag{5.19}$$

is the energy carried in or out by phonons, depending on its sign. Note that this energy includes m quanta of the driving field, emitted or absorbed, depending on the sign of $m = 0, \pm1, \ldots$. The matrix elements $S_{k,k'}(m)$ are the Fourier expansion coefficients of the product of the two phase factors, $e^{i\delta\varphi_k(t)-i\delta\varphi_{k'}(t)}$, where $\delta\varphi_k(t) \equiv \varphi_k(t) - t\langle\varepsilon(k+A)\rangle$ is the periodic part of the phase. They satisfy the sum rule

$$\sum_{m=-\infty}^{\infty} |S_{k,k'}(m)|^2 = 1. \tag{5.20}$$

Clearly, the equilibrium Fermi distribution for f_k is only obtained in the limit of small electric field amplitudes, such that $S_{k,k'}(m)$ with $m=0$ gives the dominant contribution.

5.4 Numerical simulation

The following results have been obtained by numerically finding the stationary solution of the discretized version of the master equation (5.17) with transition rates (5.18). A simple model for the phonon spectral function, $W_{k,k'}(\omega) = \gamma^2\,\theta(\omega - s\,|k-k'|)$, was used, with the sound speed $s = 5\times10^3\,\mathrm{m/s}$ as appropriate for typical 3D acoustical phonons. Since we assume no other scattering mechanisms, the quasi-equilibrium distribution functions f_k and other results do not depend on the magnitude of the electron-phonon coupling γ^2. Additional results are found using a more comprehensive phonon model is used which includes both acoustic and optic phonons similar to the model used in Wacker's review paper [174]. For sufficiently sharp optic phonon modes, the qualitative behavior of the third harmonic is unaffected ($\Gamma_{opt} \sim 1K$).

We fix the phonon temperature at 4.2K, the lattice period $a = 8.64\,\mathrm{nm}$, the average electron filling at 1/2 and choose the driving field frequency $\Omega/2\pi = 10^{12}$ Hz (energy $\hbar\Omega \approx 4.14\,\mathrm{meV}$). Also, the amplitude $A_0 a = \zeta_{11} \approx 3.8317$ is fixed, which corresponds to the point where the first harmonic generation is fully suppressed [see Fig. 5.2]. At this point the effective coupling is $\widetilde{J} = J\,J_0(\zeta_{11}) \approx -0.403\,J$, which creates an inverted and somewhat narrowed band. The effective bandwidth is smaller than $\hbar\Omega$ for $J < 2.57\,\mathrm{meV}$.

In Fig. 5.3, we show the intensity $|I_3|^2$ of the radiated third harmonic (in arbitrary units) as a function of the tight-binding hopping parameter J. The overall upward trend reflects the linear scaling of the current with J. The plot has a series of pronounced maxima and minima related to the structure of the distribution function f_k, see Fig. 5.4. Indeed, at the first maximum of the radiated intensity $|I_3|^2$, $J = 2.7\,\mathrm{meV}$, the distribution function has a well-defined minimum at $k = 0$ and symmetric maxima at $k = \pm\pi/a$ [Fig. 5.4(b)]; notice the population inversion consistent with negative $\widetilde{J}$. On the other hand, the distribution in Fig. 5.4(c) corresponding to the first minimum of radiated intensity, $J = 4.5\,\mathrm{meV}$, is much flatter. This flattening can be traced to a sharp increase of the transition rates connecting the regions of momentum space near $k = 0$ and $k = \pi/a$. This is illustrated in Fig. 5.5, where transition rates between $k = 0$ and $k = \pi/a$ are shown. The corresponding phases $\delta\varphi_{\pi/a} = -\delta\varphi_0$ have only even harmonics $m\Omega$, $m = 2, 4, \ldots$, and the threshold values of J for different m correspond to sharp maxima of $\Gamma_{0,\pi/a}$.

In Fig. 5.6, we show how the average power $\mathcal{P}$ radiated into the phonon modes scales with the tight-binding parameter J. While general dependence on J is monotonic, at $J = 4.5\,\mathrm{meV}$, where the third harmonic has a minimum, $\mathcal{P}$ changes slope.

5.5 Proposed nanowire design

The simulation results discussed above suggest that the optimal system for third harmonic generation would be a one-dimensional metallic conductor with an unrenormalized bandwidth close to 2.6 times the energy $\hbar\Omega$ of the driving field quanta (bandwidth of about 11 meV for $\Omega/2\pi = 1\,\mathrm{THz}$ is needed), and a wide gap to reduce the absorption of the generated harmonics. One option to satisfy these requirements is to use modulated semiconductor nanowires. Here we estimate the growth parameters

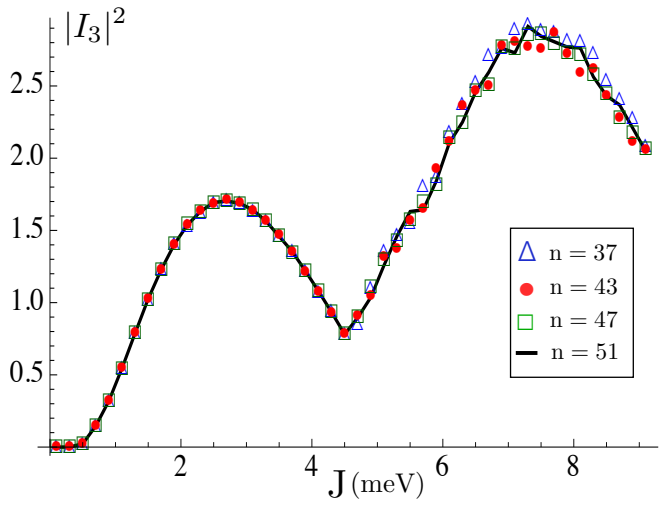

Figure 5.3: Magnitude squared of the third harmonic of the instantaneous current (arbitrary units), plotted as a function of the tight-binding parameter J, computed with $N_k = 37, 43, 47, 51$ discrete momentum points as indicated in the caption. See text for other simulation parameters. The pronounced minima are caused by the flattening of the distribution function near thresholds of m-photon-assisted scattering between the vicinities of $k = 0$ and $k = \pm\pi/a$, with m even.

of an InAs/InP nanowire [186], which would have a near optimal band structure for generating the third harmonic of a 1 THz driving field.

We calculate the band structure of the modulated nanowire modeling it as a stack of cylinders with isotropic (bulk) electron effective masses $m^*_{\rm InAs} = 0.073m_e$ and $m^*_{\rm InP} = 0.027m_e$ for the InAs and InP carriers respectively, as appropriate for the nanowire diameter we used [187]. We used the barrier height of $V_0 = 0.636\,$eV, found from the four-band model simulations, which is close to experimentally observed [186, 188] 0.6 eV. To ensure a relatively large gap, we chose the nanowire diameter $d = 20\,$nm, and InAs well width $w = 6.0\,$nm. Separating the radial and angular parts of the corresponding wave functions, we obtained a version of the Kronig-Penney model with effective mass modulation, and effective barrier dependent on the transverse momentum $\hbar\kappa_{nl}$. We plot the first few allowed energy bads as a function of InP barrier width b in Fig. 5.7.

In particular, we conclude that an InAs/InP nanowire of diameter $d = 20.0\,$nm, well width of $w = 6.0\,$nm, and barrier width of $b = 2.64\,$nm [Fig. 5.1 (a)] would have the lowest band with a width of approximately 10.9 meV. The next band would be separated by a gap of 280 meV [Fig. 5.7]. These parameters are near optimal for third harmonic generation at $\Omega/2\pi = 1\,$THz.

One possible device design could involve depositing of a number of parallel

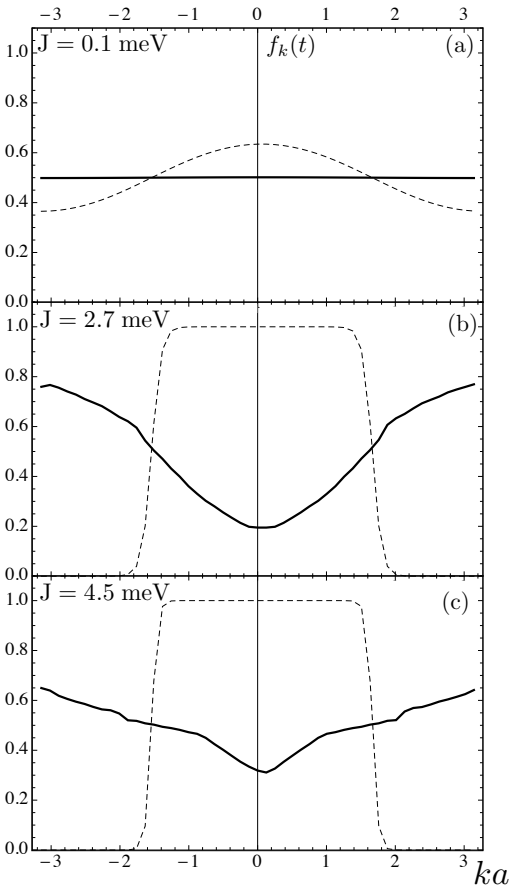

Figure 5.4: Solid lines: the stationary distribution functions obtained by solving discretized versions of Eqs. (5.17), (5.18) with $N_k = 51$ momentum points and the tight-binding parameters J as indicated. See text for other simulation parameters. Dashed lines: equilibrium Fermi distribution functions.

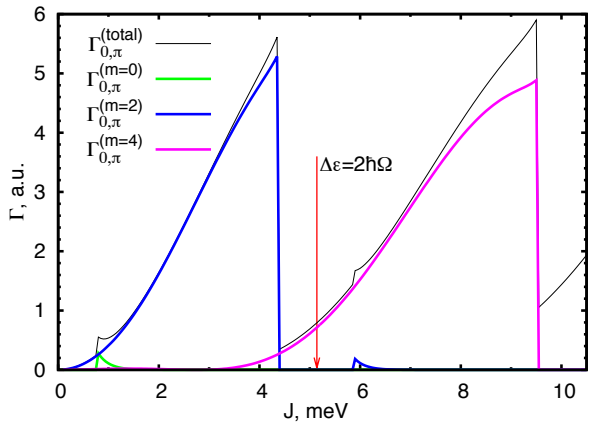

Figure 5.5: The transition rate (5.18) (arbitrary units) for scattering between the sites at $k = -\pi/a$ and $k = 0$ (black, solid) and the individual contributions from m-photon assisted processes as indicated. The vertical dashed line at $J = 5.1\,\mathrm{meV}$ indicates the threshold for the $m = 2$ transition, $|4\widetilde{J}| = 2\hbar\Omega$; the peaks to the left and to the right of this point correspond to phonon emission and absorption, respectively.

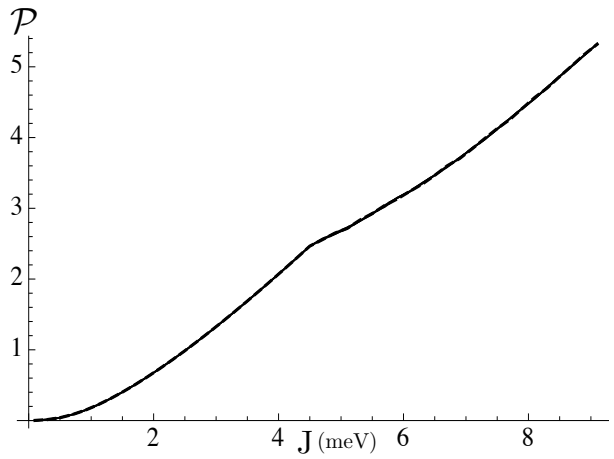

Figure 5.6: Scaling of the average power (arbitrary units) dissipated into the phonon modes as a function of the tight-binding parameter J. The four curves on top of each other correspond to the same numbers of discrete momentum points N_k as in Fig. 5.3.

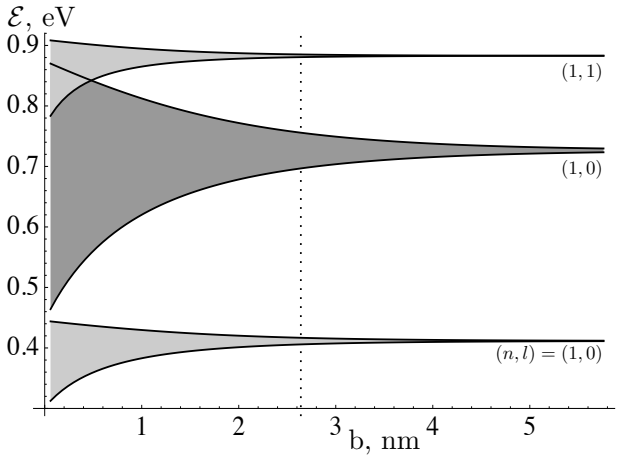

Figure 5.7: Energies of the three lowest bands computed using the Kronig-Penney model with effective mass modulation corresponding to an InAs/InP nanowire with diameter $d = 20\,\text{nm}$, InAs well width $w = 6.0\,\text{nm}$, plotted as a function of InP barrier width, b. The labels indicate the radial n and angular l quantum numbers of dimensional quantization. The dashed line at $b = 2.64\,\text{nm}$ gives a bandwidth 10.9 meV, or tight-binding parameter $J = 2.7$, corresponding to the first maximum of the third harmonic in Fig. 5.3.

modulated nanowires on a substrate, with an s-polarized driving field incident on the surface at angle θ so that the electric field of the wave be directed along the nanowires [Fig. 5.1 (b),(c)]. Then both the reflected signal and the first harmonic are going to be propagating at the same reflection angle θ, while the propagation direction of the third harmonic can be found from the Snell's law, $\sin\theta = 3\sin\phi$, which accounts for the wavelengths ratio.

To derive the semiclassical master equation, or a one-dimensional band of strongly and rapidly driven electrons, we combine the Floquet quasi-energy description with the Keldysh Green's function technique. The result is the master equation for a strongly driven system weakly coupled to phonon modes. We solve these equations numerically to find the electron distribution function for a cosine energy band at a given driving field frequency (fixed at $\Omega/2\pi = 1\,\mathrm{THz}$) and the field amplitude chosen to suppress the generation of the principal harmonic. This electron distribution is used as an input for calculating the time-dependent current and the intensity radiated at different harmonics of the driving field frequency.

We do not consider the effects of disorder or electron-electron interactions, and only consider lattice phonons in thermal equilibrium at temperature $\hbar/k_B\beta$. We do not include the scattering by phonon modes of the nanowire, assuming that they are strongly hybridized with those of the substrate. The electron-phonon coupling is considered to be weak, meaning that the phonon scattering time is long compared to the period $\tau \equiv 2\pi/\Omega$ of the driving field. The Hamiltonian of the system under consideration is given in Eq. (5.1).

5.6 Robustness of results to spectral function broadening

To derive the semiclassical master equation, the Kadanoff-Baym ansatz was used to define the electron distribution function from the zero-mode function $g^<$,

$$g^<_{k,0}(\omega, T) = iA_{k,0}(\omega, T) f_k(T), \quad . \tag{5.21}$$

The corresponding spectral function, $A_{k,0}(\omega, T) = i[g^<_{k,0}(\omega, T) - g^>_{k,0}(\omega, T)] = 2\,\mathrm{im} g^R_{k,0}(\omega, T)$, was approximated as a delta function.

We derive the master equation using a phenomenological model that has a spectral function with finite width. Beginning with the left-right subtracted Dyson

equations,

$$[g_0^{-1}, g_k^<(\omega,T)] = \int dq d\eta \sum_M |S_{k,k-q}(M)|^2 D_q^>(\eta) g_{k-q}^>(\langle\epsilon_k\rangle - \langle\epsilon_{k-q}\rangle + M\Omega - \omega - \eta, T) g_k^<(\omega,T)$$
$$- \int dq d\eta \sum_M |S_{k,k-q}(M)|^2 D_q^<(\eta) g_{k-q}^<(\langle\epsilon_k\rangle - \langle\epsilon_{k-q}\rangle + M\Omega - \omega - \eta, T) g_k^>(\omega,T), \tag{5.22}$$

the model is revised to include a broadened spectral function. As in the Kadanoff-Baym ansatz, we assume the functions $g^{<,>}$ can be connected to the electron distribution function through the spectral function. From the general definition of the spectral function $A_{k,0}(\omega,T) = i[g_{k,0}^<(\omega,T) - g_{k,0}^>(\omega,T)]$, the imaginary part of the Green's functions is kept finite as Γ and the redefined spectral function becomes $a_k(\omega,T) = \dfrac{2\Gamma}{(\omega)^2+\Gamma^2}$. The width is a phenomenological constant and it not solved for self-consistently.

After substituting for the functions $g^{<,>}$ in the Dyson equations, the equation is integrated over the transferred energy ω. The left-hand side of the Dyson equation is the same as when the Kadanoff-Baym ansatz is used;

$$\int \frac{d\omega}{2\pi} [g_0^{-1}, i a_k(\omega,T) f_k(T)] = i \frac{\partial}{\partial T} f_k(T). \tag{5.23}$$

On the right-hand side, the convolution of the spectral functions alters the transition rates,

$$\Gamma_{k-q,k} = \pi^2 \int d\eta \, \frac{d\epsilon}{2\pi} \sum_M |S_{k-q,k}(M)|^2 D_q^>(\eta) \big[a_{k-q}(\langle\epsilon_k\rangle - \langle\epsilon_{k-q}\rangle + M\Omega - \omega - \eta, \Gamma) a_k(\omega,\Gamma)\big]$$
$$\Gamma_{k,k-q} = 4\pi^2 \int d\eta \, \frac{d\epsilon}{2\pi} \sum_M |S_{k,k-q}(M)|^2 D_q^<(\eta) \big[a_k(\langle\epsilon_k\rangle - \langle\epsilon_{k-q}\rangle + M\Omega - \omega - \eta, \Gamma) a_{k-q}(\omega,\Gamma)\big] \tag{5.24}$$

From this model it is possible to obtain phenomenological results for the driven system and define a non-equilibrium electron distribution function $f_k(T)$ from the function $g^<$.

We show the effect of the width of the electron spectral function on the third harmonic amplitude is shown in Fig. 5.8. The results presented were calculated with a the spectral function modeled as a Lorentzian function, sharply peaked at the transferred energy ω and with finite width Γ. The width is assumed to be much smaller than the bandwidth of the system and much smaller than the frequency of the driving field ($\Gamma \ll 4J$, $\Gamma \ll \Omega$). The intensity $|I_3|^2$ of the radiated third harmonic (in arbitrary units) is plotted as a function of the tight-binding hopping parameter J. Acoustic phonon modes are the only scattering mode included. The width of the electron spectral

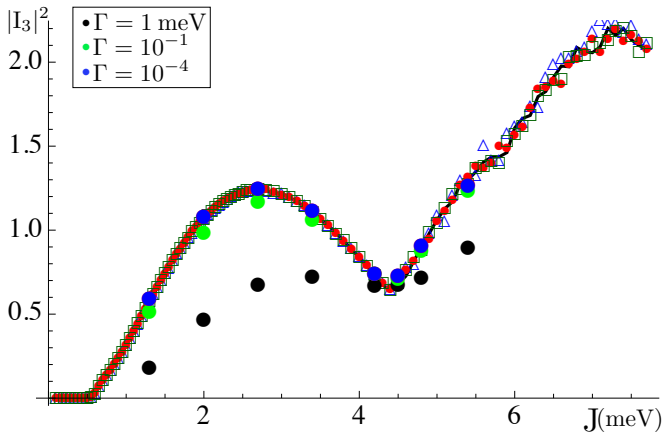

Figure 5.8: Magnitude squared of the third harmonic of the instantaneous current (arbitrary units), plotted as a function of the tight-binding parameter J, computed with $\Gamma = 10^{-4}$ meV,10^{-1} meV,1 meV as indicated in the caption. See text for other simulation parameters. The results are overlaid on the results discussed in Section (5.4).

function is varied and it is seen that for spectral widths less than the driving frequency, the qualitative shape of the third harmonic amplitude is unaffected.

The phonon spectral function $W(\omega)$ is determined by the modes used to thermalize the system. The results in the main text were obtained with a simple model for the phonon spectral function, $W_{k,k'}(\omega) = \gamma^2\,\theta(\omega - s\,|k - k'|)$, was used, with the sound speed $s = 5 \times 10^3\,\mathrm{m/s}$ as appropriate for typical 3D acoustical phonons. We include results for when the model is thermalized with acoustic and optic phonon modes. The optic mode is modeled as a Lorentzian distribution of width σ and peaked at a given energy ω_{opt}. The spectral function is modified as, $W_{k,k'}(\omega) = W_{acous} + W_{opt} = \gamma^2\,\theta(\omega - s\,|k - k'|) + \alpha\mathcal{L}(\omega - \omega_{opt}, \sigma)$. For sufficiently sharp optic phonon modes, the qualitative behavior of the third harmonic is unaffected ($\sigma \sim 1K$). Additionally, the intensity of the optic mode cannot be too large without severely affecting the third harmonic amplitude. The constant α is included to ensure the relative intensities of the acoustic and optic mode are of the same order.

We fix the phonon temperature at 4.2K, the lattice period $a = 8.64\,\mathrm{nm}$, the average electron filling at 1/2 and choose the driving field frequency $\Omega/2\pi = 10^{12}$ Hz (energy $\hbar\Omega \approx 4.14\,\mathrm{meV}$). Also, the amplitude $A_0 a = \zeta_{11} \approx 3.8317$ is fixed, which corresponds to the point where the first harmonic generation is fully suppressed. At this point the effective coupling is $\widetilde{J} = J\,J_0(\zeta_{11}) \approx -0.403\,J$, which creates an inverted and somewhat narrowed band. The effective bandwidth is smaller than $\hbar\Omega$ for $J < 2.57\,\mathrm{meV}$.

In Fig. 5.9, we show the intensity $|I_3|^2$ of the radiated third harmonic (in arbitrary units) as a function of the tight-binding hopping parameter J. The optic mode

amplitude α is determined by the relative intensities between the optic and acoustic modes,

$$\int_0^{\omega_{opt}} d\omega\, W_{acous}(\omega) = \alpha \int_0^{\omega_{MAX}} d\omega\, \mathcal{L}(\omega - \omega_{opt}, \sigma), \tag{5.25}$$

and modeled as a Lorentzian distribution with $\sigma = 0.4$ meV.

In Fig. 5.10, we show the intensity $|I_3|^2$ of the radiated third harmonic (in arbitrary units) as a function of the tight-binding hopping parameter J. The optic mode amplitude is fixed at 2.5% of the acoustic mode amplitude and modeled as a Lorentzian distribution of width 0.4 meV.

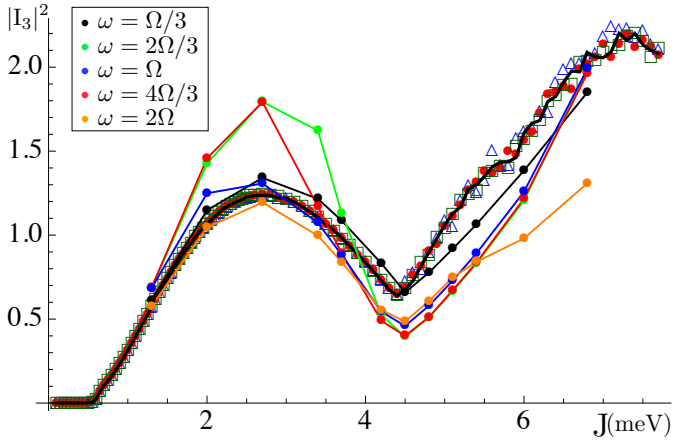

Figure 5.9: Magnitude squared of the third harmonic of the instantaneous current (arbitrary units), plotted as a function of the tight-binding parameter J, computed with $\omega_{opt} = \frac{\Omega}{3}, \frac{2\Omega}{3}, \Omega, \frac{4\Omega}{3}, 2\Omega$ as indicated in the caption. The scaling amplitude of the optic mode is dependent on the relative intensity of the optic and acoustic modes. See text for other simulation parameters. The results are overlaid on the results discussed in the previous sections.

5.7 Conclusions

In this work we suggest a possibility that frequency multiplication due to periodically-driven Bloch oscillation may be possible in a quas-istationary setting, with the help of a narrow-band one-dimensional conductor. A quasi-equilibrium electron distribution is possible because the energy absorbed from the driving field is continuously dissipated by the bulk phonons.

For a periodically modulated InAs/InP nanowire with the period $a = 8.64\,\mathrm{nm}$, and the driving field frequency $\Omega/2\pi = 1\,\mathrm{THz}$, the emission of the first harmonic is suppressed with the dimensionless vector potential amplitude $A_0\, a \approx 3.83$, which gives

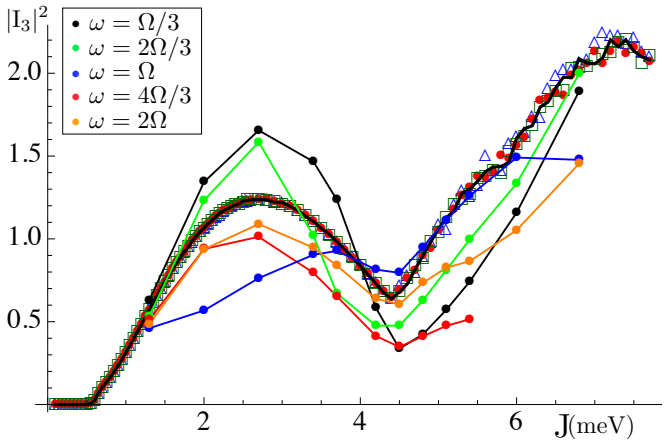

Figure 5.10: Magnitude squared of the third harmonic of the instantaneous current (arbitrary units), plotted as a function of the tight-binding parameter J, computed with $\omega_{opt} = \frac{\Omega}{3}, \frac{2\Omega}{3}, \Omega, \frac{4\Omega}{3}, 2\Omega$ as indicated in the caption. The scaling amplitude of the optic mode is fixed at 2.5% of the acoustic mode. See text for other simulation parameters. The results are overlaid on the results discussed in previous sections.

the electric field amplitude $E_0 = \hbar\Omega\, A_0/e \approx 1.8 \times 10^6\,\mathrm{V/m}$, corresponding to the energy flux of about $0.5\,\mathrm{MWt/cm^2}$. At this kind of power, many effects could lead to eventual run-away overheating of the system, *e.g.*, direct absorption by the substrate, or even a relatively weak disorder scattering in the nanowire. We hope that a quasi-continuous operation would still be possible, with the driving field pulse duration of a few microseconds, as opposed to few picoseconds in the experiment [64].

Chapter 6

Percolation theory

In a given space, either continuous or discrete, percolation can be defined by the probability that a random process will generate a connected object (cluster) that is infinitely large or contains a significant fraction of vertices. A connected discrete d-dimensional space is known as a graph and can be finite or infinite. It is defined by two sets, one a set of integers labeling points called *vertices* and another a set of $\mathbb{Z}^d$ vectors labeling the connections between vertices, called *edges*. The two sets fully describe a graph, $\mathbb{G} = (\mathbb{V}, \mathbb{E})$. This chapter introduces the language used to describe percolation on graphs, and the methods used to find the threshold of the percolation transition.

6.1 Definition of percolation on graphs

For a given graph $\mathbb{G} = (\mathbb{V}, \mathbb{E})$ a probability measure can be associated with either the vertex set or the edge set, which describes the probability that a given vertex is open or closed, or whether a given edge is open or closed. If the probability measure is associated with the elements of the vertex set being open or closed, then the process being described is that of *site percolation*. Whereas if the probability measure is associated with the elements of the edge set being open or closed, then the process is that of *edge percolation*. The two processes can be related to each other, if an edge is open, that can be mapped to the equivalent probability that two adjacent vertices are open.

Adjacency on a graph is defined by whether an edge exists between two vertices. The full set of connections on a graph can be catalogued and arraigned into a matrix, called the *adjacency matrix* which is helpful in studying percolation on graphs and will be further discussed in Section (6.3). Additionally, two vertices which are not adjacent may be connected by a connected set of edges, called a *path*. Finally, a vertex may be connected to itself if a path returns to the starting vertex, this path is called a *cycle*.

These concepts are shown in Figure (6.1). For site percolation, the vertices of a graph

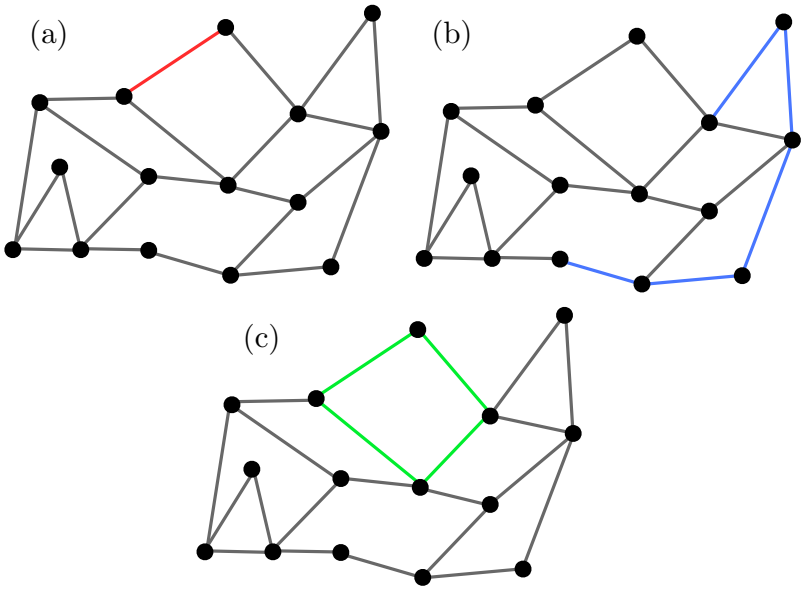

Figure 6.1: Generic graph definitions: (a) A generic graph $\mathbb{G} = (\mathbb{V}, \mathbb{E})$ with a pair of adjacent vertices highlighted (red). (b) Connection of two non-adjacent vertices by a path (blue). (c) Connection of a vertex to itself by a cycle (green).

can be assigned to the state 'open' with a probability (p) and 'closed' with probability $(1-p)$. For the general background given in this section, it will be assumed that all vertices have the same independent probability to be open or closed. In later sections the situation where probability is site-dependent is explored and also the situation where the probability of adjacent vertices being open is no longer independent (correlated percolation). When a percolation process is defined on a given graph, the result is a random sub-graph where $p|V|$ of the original vertices are retained. It is possible for the random graph generated after a percolation process to have a group of vertices which nearly cover the original graph. If adjacent vertices are both open, they form a group known as a *cluster* $C(n)$. The size of a cluster (n) is equal to the number of vertices contained in it. Shown in Figure (6.3)(a) are clusters of size $C(n=1), C(n=2)$ and in Figure (6.3)(b) $C(n=7)$. As is seen in Figure (6.2) it is possible for a cluster of open vertices to contain nearly all the vertices of the original graph. Such a cluster is said to *span* the graph. The percolation transition is defined in terms of the probability that such a spanning cluster exists, or in the instance of an infinite graph, the existence of an infinitely large cluster. For an infinite graph, where sites are open with probability

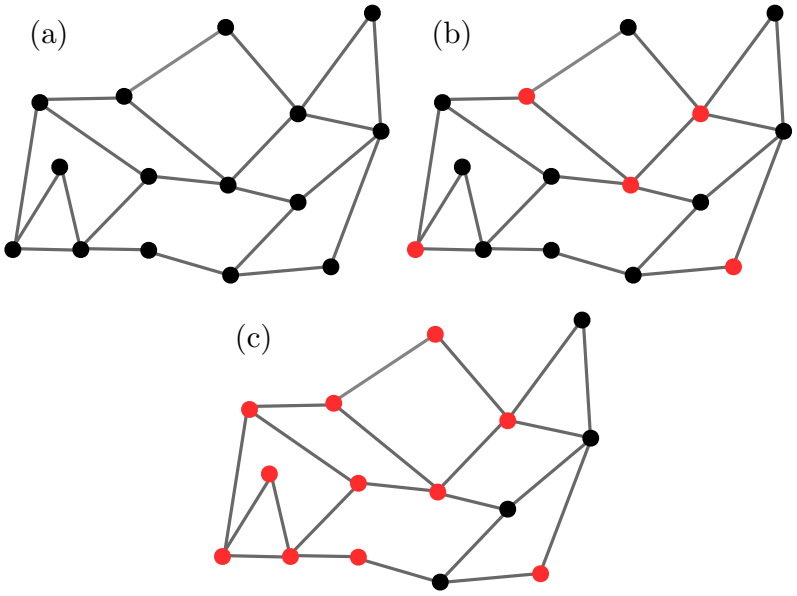

Figure 6.2: Generic percolation definitions (a) A generic graph $\mathbb{G} = (\mathbb{V}, \mathbb{E})$ before percolation. (b) After a process where $p|V|$ of the original vertices are opened. (c) Depending on the value of (p) is it possible that a large majority of the original vertices are retained, and for a group which nearly covers the original graph.

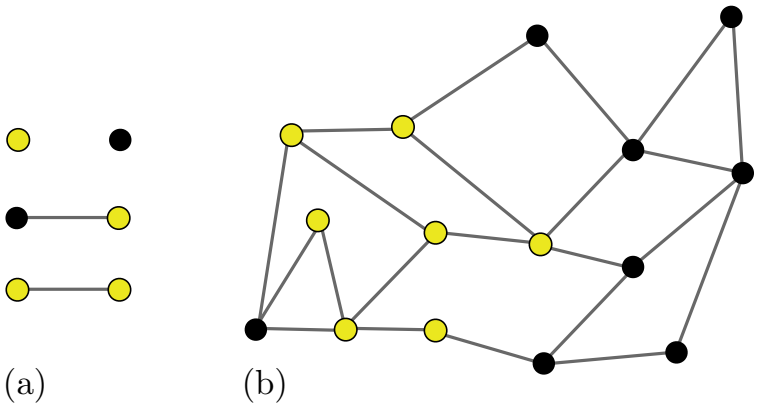

Figure 6.3: (a) Vertices on a graph may be open (yellow) or closed (black) and may be adjacent or not. If adjacent vertices are open they form a cluster. (b) A large cluster of open vertices.

(p) percolation is defined as the existence of an cluster of infinite size, $C(n = \infty)$. To describe this event, an additional probability quantity is defined, $\theta(p)$ which is the probability that percolation occurs. Explicitly,

$$\theta(p) = \mathbb{P}_p(C(n = \infty)). \tag{6.1}$$

It is easy to identify two values for $\theta(p)$. For $(p = 0)$, $\theta(p = 0) = 0$, that is if no vertices are open there is zero probability percolation occurs. Likewise for $(p = 1)$ then $\theta(p = 1) = 1$, if all vertices are open then percolation occurs with unit probability. Of interest is what happens to $\theta(p)$ as the probability of a vertex to be open is increased from $0 \to 1$. Specifically, is there a value for p_T for which $p < p_T$ there is probability of an infinite cluster, whereas for $p > p_T$ an infinite cluster occurs almost certainly.

6.2 Mean field theory

Mean field (MF) theory is a method for calculating macroscopic quantities of complex systems, fundamentally by only including complexity in immediate vicinity of a given point. First defined for polymerization, mean field theory was used to find the percolation threshold on trees [74,105–107]. The approach on a tree begins with defining the probability of a branch of finite length growing from a given root, arbitrarily chosen in a tree. The further growth of the branch is dependent only on the neighboring vertices of the root, and whether they are open or closed. The overall complexity of the tree graph is not considered, but the MF approach provides a lowest order approximation to complex graphs. In Chapter 7 the mean-field approach is extended to include second-generation connections.

6.3 Percolation threshold and adjacency matrix

Two vertices are adjacent if an edge exists between them. On a graph, the full set of connections can be arranged into a matrix $\mathbf{A}$, with nonzero elements a_{ij} if an edge exists between the vertices (i) and (j). The rows of $\mathbf{A}$ are defined by all vertices (j) that are connected from a given vertex (i) and the columns of $\mathbf{A}$ are defined by all vertices (i) that connect to a given vertex (j). Undirected edges (i, j) allow paths from $i \to j$ and $j \to i$, and the adjacency matrix $\mathbf{A}$ is symmetric. If the edges of a graph (i, j) only allows for a path to travel from $i \to j$, then the graph is directed and $\mathbf{A}$ is not symmetric. Undirected graphs will be distinguished as $\mathcal{G}$ and directed graphs as $\mathcal{D}$. In Chapter (7) a mean field theory is derived using non-backtracking, directed graphs. In Chapter (8) the process of correlated percolation is explored on undirected graphs.

From an adjacency matrix, the conditions that define a percolation threshold can be established. The average size of a connected cluster on a graph can be defined by higher orders of the adjacency matrix. As stated above, the elements of $\mathbf{A}$ are non-zero if a connection between vertices (i,j). The elements of $\mathbf{A} \times \mathbf{A} \ldots \mathbf{A} = \mathbf{A}^n$ defines the number of n-length walks between vertices (i,j).

A random graph $\mathcal{G} = \{V, E\}$ can be generated from an original graph $\mathcal{G}_0 = \{V_0, E_0\}$ by selectring random vertices of the original graph to be open with a predefined probability measure. As a result, the adjacency matrix of $\mathcal{G}$ is the adjacency matrix $\mathbf{A}$ defined from $\mathcal{G}_0$ with the elements weighted by p. The scaled matrix gives the connections possible from a given vertex (i) which is known to be open. The connections $i \to j$ are dependent on the probability that vertex (j) is open.

For uncorrelated, unweighted percolation, the probability measure is independent for all vertices and also equivalent for all vertices. Thus,

$$\mathbf{A}(\mathcal{G}) = \mathbf{A}(\mathcal{G}_0)p. \tag{6.2}$$

The n-order product $\mathbf{A}^n$ gives the n-length walks between any two vertices of $\mathcal{G}_0$. Replacing the original adjacency matrix with the scaled expression $\mathbf{A}^n p^n$ gives the n-length walks between any two vertices and is dependent on the probability all intermediate vertices on the walk are open.

Following the method in Ref. [125], the adjacency matrix is used to define the average cluster size. An N-length, normalized, vector is defined,

$$|\mathbf{1}\rangle = \frac{1}{\sqrt{N}}|11 \ldots 11\rangle, \tag{6.3}$$

where $N = |V_0|$. Using the scaled adjacency matrix and the all-one vector, all possible endpoints of an n-length walk beginning from all possible initial points can be defined, $\mathbf{A}^n p^n |\mathbf{1}\rangle$. Including the probability that the initial point is open,

$$\langle \mathbf{1}|p\mathbf{A}^n p^n|\mathbf{1}\rangle, \tag{6.4}$$

gives the probability that a cluster of size n exists on the graph $\mathcal{G}$. The sum over all cluster sizes defines the average cluster size:

$$\langle n\rangle = \sum_n \langle \mathbf{1}|p\mathbf{A}^n p^n|\mathbf{1}\rangle. \tag{6.5}$$

The sum over n is the sum over the spectral norm of $\mathbf{A^n}$,

$$\begin{aligned} \sum_n \langle \mathbf{1}|p\mathbf{A}^n p^n|\mathbf{1}\rangle &= p^{n+1}|\mathbf{A}^n|_2 \\ &\leq p^{n+1}|\mathbf{A}|_2^n = p^{n+1}\rho(\mathbf{A})^n \end{aligned} \tag{6.6}$$

If $\rho(\mathbf{A})p < 1$ is true, the sum converges and a bound on the average cluster size is established:

$$\langle n \rangle \leq \frac{p}{(1 - \lambda_{max}(\mathbf{A})p)}. \tag{6.7}$$

The spectral norm ($\rho(\mathbf{A})$) has been replaced by the maximum eigenvalue of $\mathbf{A}$. This method is applied to weighted and correlated percolation in Chapter (8) with appropriate re-definitions of the scaled adjacency matrix.

In Eq. 6.7 the average cluster size has a finite bound if the probability and the spectral radius of $\mathbf{A}$ satisfy $p\rho(\mathbf{A}) < 1$. If $p\rho(\mathbf{A}) = 1$ the average cluster size is unbounded and the system is above the percolation threshold.

Equivalently, the average cluster size can be expressed as a sum over a probability distribution,

$$\langle n \rangle = \sum_{n} n f(n). \tag{6.8}$$

If a threshold cluster size is established by a finite fraction of vertices being contained in a cluster:

6.4 Site dependent and correlated percolation

Site percolation, as described in Section (6.1) considers how likely an infinite cluster will form on a graph when individual sites are independently opened or closed. That is, the probability that a vertex is open (or closed) is the same for all vertices and independent of whether neighboring site are open or closed. It is also possible to have percolation processes where each vertex is assigned a specific probability to be open (or closed), ($v_i \in \mathbb{V}$) is open with probability p_i. This leads to the process of site-dependent percolation. Its effect on the percolation threshold is described in Section (8.5).

It is possible to consider a process by which percolation occurs with correlated, site-dependent probabilities. Instead of considering whether single sites are open or closed, a set of vertices of size (n) and a specific shape are defined as a *animal*. If an animal is placed on a given vertex, it is immediately known that the (n) vertices in the animal are all open. Percolation occurs by the overlap of animals. The growth of a cluster through the overlap of animals is shown in Figure (6.4).

6.5 Line graphs

In Chapter (7) a tighter bound is established which relies on the Hashimoto's matrix [189], defining the connections possible in a line digraph which has no backtrack-

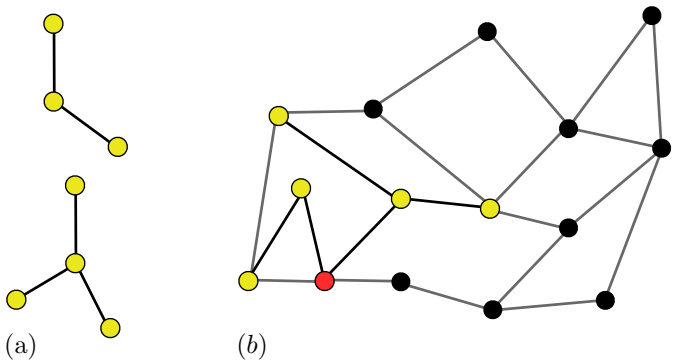

Figure 6.4: (a) Generic animals of size $n = 3$ and $n = 4$. (b) Growth of a cluster of size $n = 6$ by overlapping animals, overlapping vertex highlighted (red).

ing paths. The adjacency matrix discussed in Section (6.3) is defined by the adjacencies between vertices, there is also a matrix which describes the adjacent edges of a graph. Such a matrix is defined by a *line graph* and is well-known in graph theory [190]. From an initial graph $\mathcal{G} = \{\mathcal{V}, \mathcal{E}\}$ the line graph $\mathcal{L}(\mathcal{G})$ has a vertex set defined from the edge set $\mathcal{E}$. Now adjacencies are defined by undirected edges which are incident on the same vertex, or for the case of directed graph, two directed edges are adjacent if one is incident on a vertex while the second is incident from the same vertex. The Hashimoto's matrix is a specific class of line digraph which has no symmetric pairs and paths can only be defined in a forward direction.

The method of single cycle unwrapping, discussed in Chapter (7) generates a forward only line digraph (FOLD), such a matrix has adjacencies defined in a Hashimoto's matrix. From an initially undirected graph with cycles, a directed graph is defined by replacing all undirected edges with a symmetric pair of directed edges. Symmetric directed edges will generate symmetric pairs of edges in a line graph. From the directed graph, a line digraph is formed and symmetric edges are removed such that only forward paths are possible. After cycle unwrapping is done the result is a tree graph with directed edges that has no back-tracking paths.

Chapter 7

Tight lower bound for percolation threshold on an infinite graph

(The material in this section was submitted for publication in Physics Review Letters and a version of this paper has been published on the arXiv [191])

We construct a tight lower bound for the site percolation threshold on an infinite graph, which becomes exact for an infinite tree. The bound is given by the inverse of the maximal eigenvalue of the Hashimoto matrix used to count non-backtracking walks on the original graph. Our bound always exceeds the inverse spectral radius of the graph's adjacency matrix, and it is also generally tighter than the existing bound in terms of the maximum degree. We give a constructive existence proof in the case of a connected infinite quasi-transitive graph, a graph-theoretic analog of a translationally-invariant system.

7.1 Introduction

An ability to process and store large amounts of information lead to emergence of big data in many areas of research and applications. This caused a renewed interest in graph theory as a tool for describing complex connections in various kinds of networks: social, biological, technological, etc. [192–196] In particular, percolation transition on graphs has been used to describe internet stability, spread of contagious diseases, and emergence of viral videos. Percolation has also been applied to establish the existence of the decoding threshold in certain classes of quantum error-correcting codes [197].

A *degree* of a vertex in a graph is the number of its neighbors. Degree distribution is a characteristic easy to extract empirically. A simple approach for network modeling is to study random graphs with the given degree distribution [110, 198–201].

In the absence of correlations, the site percolation threshold on such a random graph is [110, 198–200]

$$p_c = \frac{\langle d \rangle}{\langle d^2 \rangle - \langle d \rangle}, \tag{7.1}$$

where $\langle d^m \rangle \equiv \sum_i d_i^m / n$ is the m-th moment of the vertex degree distribution and the *graph order*, n, is the number of vertices in the graph. While this result is very appealing in its simplicity, Eq. (7.1) has no predictive power for any actual network where correlations between degrees or enhanced connectivity ("clustering") of nearby vertices may be present. Substantial effort has been spent on attempts to account for such correlations [202–205] in random graphs. However, such approaches can only account for local correlations and are flawed when applied to artificial networks like the power grid, which may have a carefully designed robust backbone (e.g., as in Example 7.1). Such strong correlations make Eq. (7.1) or its versions accounting for local correlations seemingly irrelevant.

There are only a handful of results on percolation for general graphs [111, 206]. These include the exact lower bound for the site percolation threshold for any graph with the maximum vertex degree $d_{\max}$ [207],

$$p_c \geq (d_{\max} - 1)^{-1}, \tag{7.2}$$

which coincides with that for the bond percolation (Theorem 1.2 in reference [111]. Both bounds are achieved on d-regular tree $\mathcal{T}_d$. Unfortunately, for graphs with wide degree distributions, Eq. (7.2) may by far underestimate the percolation threshold.

An estimate of the percolation threshold for dense graphs (with some conditions) as the inverse *spectral radius* of the graph, $\rho(\mathcal{G}) \equiv \rho(A_{\mathcal{G}})$, defined as the maximum magnitude of an eigenvalue of its adjacency matrix, $A_{\mathcal{G}}$, has been suggested in Ref. [208]. Unfortunately, the conditions are rather restrictive, and the estimate is clearly not very accurate for sparse degree-regular graphs where the spectral radius $\rho(\mathcal{G}) = d$, as this estimate never reaches the lower bound in Eq. (7.2).

Example 7.1. *Consider a tree graph $\mathcal{T} \equiv \mathcal{T}_{d;r,L}$ constructed by attaching r chains of length L to each vertex of a d-regular tree $\mathcal{T}_d$, see Fig. 7.1. The percolation threshold coincides with that of $\mathcal{T}_d$, $p_c = p_c(T_d) = (d-1)^{-1}$. On the other hand, Eq. (7.1) gives $p_c \to 0$ if we take $L = 1$, r large, and $p_c \to 1$ if we take $r = 1$, L large. Similarly, the spectral radius is $\rho(\mathcal{T}_{d;r,1}) = d/2 + [(d/2)^2 + r]^{1/2}$ (we took $L = 1$); the corresponding estimated threshold varies in the range $0 < [\rho(\mathcal{G})]^{-1} \leq 1/d$, while the lower bound (7.2) varies in the range $0 < p_c^{\min} \leq (d-1)^{-1}$.*

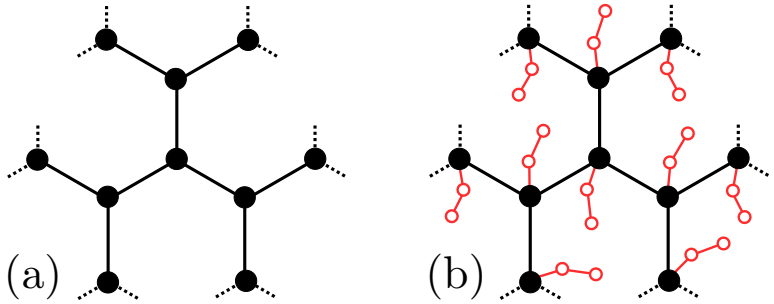

Figure 7.1: (a) A d-regular tree used for the backbone of the graph in Example 7.1. (b) The tree $\mathcal{T}_{d;r,L}$ is grown from the backbone by placing r chains of fixed length L (shown $d = 3$, $r = 1$, $L = 2$) at each vertex of the backbone.

Thus, Eq. (7.1), the lower bound (7.2), or the inverse spectral radius $[\rho(\mathcal{G})]^{-1}$ do not give accurate estimates of the percolation threshold for this graph family.

In this work we suggest a tight lower bound for the site percolation threshold p_c on an infinite graph. It is given by the inverse maximum eigenvalue of the linearized mean-field (MF) equations, $p_c \geq p_c^{(\min)} = 1/\lambda_{\max}$. These equations relate probabilities that neighboring bonds lead to infinite clusters; they are exact for tree graphs which do not have cycles. The matrix H corresponding to the MF equations was first introduced by Hashimoto [189] to generate non-backtracking walks on graphs. The infinite-dimensional matrix H is not symmetric; it is non-trivial that the maximum eigenvalue $\lambda_{\max} \equiv \lambda_{\max}(H)$ be real or non-zero. We show that the eigenvalue $\lambda_{\max}(H)$ gives a physically meaningful bound $0 < p_c^{(\min)} \leq 1$ and can be obtained as a solution of a finite eigensystem for any connected infinite *quasi-transitive graph* $\mathcal{G}$, a graph-theoretic analog of a translationally-invariant system with a finite number of inequivalent vertices. For such graphs we also give a constructive proof that our threshold is indeed a lower bound, by building a tree $\mathcal{T}$ locally equivalent to the original graph $\mathcal{G}$, except that a cycle on $\mathcal{G}$ is mapped to an open path connecting two equivalent vertices on $\mathcal{T}$. We also show that the inverse spectral radius $\rho(\mathcal{G})$ of the original graph gives a smaller (inexact) lower bound for the percolation threshold,

$$p_c \geq p_c^{(\min)} \equiv 1/\lambda_{\max}(H) > 1/\rho(\mathcal{G}). \tag{7.3}$$

7.2 Definitions

A graph $\mathcal{G} = (\mathcal{V}, \mathcal{E})$ with vertex set $\mathcal{V} \equiv \mathcal{V}(\mathcal{G})$ and edge set $\mathcal{E} \equiv \mathcal{E}(\mathcal{G})$ is called *transitive* iff for any two vertices i, j in $\mathcal{V}$ there is an automorphism (symmetry) of $\mathcal{G}$ mapping i onto j. Graph $\mathcal{G}$ is called *quasi transitive* if there is a finite set of vertices

$\mathcal{V}_0 \subset \mathcal{V}$ such that any $i \in \mathcal{V}$ is taken into $\mathcal{V}_0$ by some automorphism of $\mathcal{G}$. We say that any vertex which can be mapped onto a vertex $i_0 \in \mathcal{V}_0$ is in the equivalence class of i_0.

Let Γ be a group of automorphisms of a graph $\mathcal{G}$. The *quotient graph* $\mathcal{G}/\Gamma$ is the graph whose vertices are equivalence classes $\mathcal{V}(\mathcal{G})/\Gamma = \{\Gamma i : i \in \mathcal{V}(\mathcal{G})\}$, and an edge $(\Gamma i, \Gamma j)$ appears in $\mathcal{G}/\Gamma$ if there are representatives $i_0 \in \Gamma i$ and $j_0 \in \Gamma j$ that are neighbors in $\mathcal{G}$, $(i_0, j_0) \in \mathcal{E}(\mathcal{G})$. Same definition also applies in the case of a digraph $\mathcal{D}$, except that we need to consider directed edges, e.g., $(i_0 \to j_0) \in \mathcal{E}(\mathcal{D})$.

In *site percolation* on a graph $\mathcal{G}$, each vertex is open with probability p and closed with probability $1-p$; two neighboring open vertices belong to the same cluster. Percolation happens if there is an infinite cluster on $\mathcal{G}$. When graph is not connected, percolation happens independently on different connected components. In the following, we will only consider connected graphs.

7.3 Mean field equations

Let us first consider an infinite *tree* $\mathcal{T}$, a graph with no cycles. We will assume that the vertex degrees are bounded, so that according to Eq. (7.2), the corresponding percolation threshold be strictly non-zero, $p_c \equiv p_c(\mathcal{T}) > 0$. The percolation threshold can be found exactly by constructing a set of recursive equations starting with some arbitrarily chosen root [105–107]. For a given pair of neighboring open vertices i and j (denoted $i \sim j$), let us introduce the probability Q_{ij} that i is connected to a finite cluster through j. The corresponding recursive equations have the form

$$Q_{ij} = \prod_{l \sim j : l \neq i} (1 - p + pQ_{jl}), \tag{7.4}$$

where the product is taken over all neighbors l of j such that $l \neq i$ so that only so far uncovered independent branches be included. The growth of a branch into an infinite cluster is impeded by the site l being closed (probability $1-p$), or being open but connecting to a finite branch (probability pQ_{jl}).

Below the percolation threshold, $p < p_c$, Eqs. (7.4) are satisfied identically with $Q_{ij} = 1$. Right at the percolation threshold, we expect the probability of an infinite cluster to be vanishingly small, and the probabilities Q_{ij} can be expanded

$$Q_{ij} = 1 - \epsilon_{ij}, \quad i \sim j, \tag{7.5}$$

where ϵ_{ij} is infinitesimal. Expanding Eqs. (7.4) to linear order in ϵ_{ij}, we obtain the following eigenvalue problem at the threshold, $p = p_c$,

$$\lambda \epsilon_{ij} = \sum_{l \sim j : l \neq i} \epsilon_{jl}, \quad \lambda \equiv 1/p_c. \tag{7.6}$$

The percolation threshold corresponds to the largest real eigenvalue $\lambda = \lambda_{\max}$ corresponding to a non-negative eigenvector, $\epsilon_{ij} \geq 0$. To ensure the probability $p_c \leq 1$, the eigenvalue needs to be sufficiently large, $\lambda_{\max} \geq 1$.

Extending Eqs (7.4) to an arbitrary connected graph $\mathcal{G}$, we obtain a mean-field approximation to percolation. The probabilities Q_{ij} correspond to directed edges in $\mathcal{G}$, meaning that generally $Q_{ij} \neq Q_{ji}$, and this pair of variables is defined iff the corresponding component of the adjacency matrix is nonzero, $A_{ij} \neq 0$. Let us introduce a *symmetric digraph* $\tilde{\mathcal{G}}$ with the same adjacency matrix A. Namely, $\tilde{\mathcal{G}}$ has the same vertex set $\mathcal{V}(\tilde{\mathcal{G}})$ as $\mathcal{G}$ and the set of directed edges $\mathcal{E}(\tilde{\mathcal{G}}) \subseteq \mathcal{V} \otimes \mathcal{V}$ where each undirected edge $(i,j) \in \mathcal{E}(\mathcal{G})$ of the original graph $\mathcal{G}$ is replaced by a pair of directed edges $i \to j$ and $j \to i$. Then the matrix H of the eigensystem (7.6) has the components labeled by the directed edges of $\tilde{\mathcal{G}}$

$$H_{u,v} = \delta_{jj'}(1 - \delta_{li}), \quad u \equiv i \to j,\ v \equiv j' \to l, \tag{7.7}$$

where the second term in the product accounts for the non-backtracking condition $i \neq l$. Matrix H was originally introduced by Hashimoto [189] to generate non-backtracking walks on a digraph. This matrix can also be interpreted as the adjacency matrix of the oriented line (di)graph [209] (OLG) associated with the digraph $\tilde{\mathcal{G}}$. To simplify the notations, we will associate the Hashimoto matrix $H \equiv H_{\mathcal{G}}$ in Eq. (7.7) directly with the graph $\mathcal{G}$.

In the presence of cycles, the probabilities Q_{jl} and $Q_{jl'}$ for different branches leading to $l \neq l'$ are no longer independent. Both branches could lead to the same finite or infinite cluster. As a result of these correlations, the probability that both $j \to l$ and $j \to l'$ lead to finite clusters is generally smaller than the product of corresponding probabilities computed independently. Respectively, Eqs. (7.4) may have a non-trivial solution already for some $p < p_c(\mathcal{G})$. This implies that in the presence of cycles, the maximum eigenvalue $\lambda_{\max}$ of Eqs. (7.6) would give a lower bound on the percolation threshold, $p_c(\mathcal{G}) \geq 1/\lambda_{\max}(H)$, which is the first part of the inequality in Eqs. (7.3).

It is easy to check that the spectral radius $\rho(A)$ of the graph adjacency matrix A [which by definition equals to the spectral radius of the graph, $\rho(\mathcal{G}) \equiv \rho(A_{\mathcal{G}})$] cannot be smaller than any eigenvalue λ of H corresponding to a non-trivial solution $\epsilon_{ij} \geq 0$ of Eqs. (7.6), which implies $\lambda \geq 0$. Indeed, for a non-empty graph, A is a symmetric non-negative matrix with some non-zero matrix elements, thus $\rho(A) > 0$, and we only need to check the case $\lambda > 0$. Starting with the corresponding non-trivial solution $\epsilon_{ij} \geq 0$, we introduce vertex variables $x_j \equiv \sum_{i:i\sim j} \epsilon_{ij}$ and $y_j \equiv \sum_{l:j\sim l} \epsilon_{jl}$ where summation is over all edges incident to and incident from j, respectively. Summing Eqs. (7.6) over all

j neighboring with i, we obtain

$$y_i = A_{ij} y_j - x_i, \tag{7.8}$$

where the second term in the r.h.s. accounts for non-backtracking condition $l \neq i$. Now, by assumption the solution $\epsilon_{ij} \geq 0$ is such that $\epsilon_{i_0 j_0} > 0$ for some edge (i_0, j_0). Eq. (7.6) then implies that also $\epsilon_{j_0 l_0} > 0$ for some $l_0 \sim j_0$, so that at the vertex j_0 both $x_{j_0} > 0$ and $y_{j_0} > 0$. If we multiply Eq. (7.8) by y_i and sum over all i, we get

$$\lambda \|y\|^2 = y_i A_{ij} y_j - y_i x_i < y_i A_{ij} y_j \leq \rho(A) \|y\|^2 , \tag{7.9}$$

where $\|y\|^2 \equiv y_i^2 > 0$. This proves [cf. Eq. (7.3)]:

Theorem 7.2. *The spectral radius of the adjacency matrix $A_{\mathcal{G}}$ of any connected non-empty graph $\mathcal{G}$ is strictly larger than the maximum eigenvalue of the Hashimoto matrix $H_{\mathcal{G}}$ corresponding to a non-zero eigenvector with non-negative components, $\rho(A_{\mathcal{G}}) > \lambda_{\max}(H_{\mathcal{G}})$.*

7.4 Results for quasi-transitive graphs

The discussion of the MF equations (7.6) was at the "physical" level of rigorousness. We argued that the percolation threshold for an arbitrary infinite connected graph should be bounded from below by the inverse maximum positive eigenvalue $\lambda_{\max}(H)$ of Eqs. (7.6) corresponding to $\epsilon_{ij} \geq 0$, and proved that this bound is in turn larger than the inverse spectral radius of the graph.

Yet some questions remain: Eigensystem (7.6) has a non-symmetric matrix H. Under what conditions do we expect to get a real-valued eigenvalue $\lambda_{\max}(H) \geq 1$ which would correspond to a valid percolation threshold? Could we obtain $\lambda_{\max}(H)$ as a solution of some finite eigenvalue problem, or at least as a limit of some sequence of such problems? If yes, what are the convergence conditions? As an example, Theorem 7.3 states that for any finite tree Eqs. (7.6) give $\lambda_{\max}(H) = 0$. Of course, this makes perfect sense since these equations are exact on any tree, and the probability to have an infinite cluster on a finite tree is zero. However, the downside is that, at least in the case of an infinite tree graph, it is not sufficient to consider percolation on finite subgraphs.

In the following, we concentrate on the special case of infinite connected quasi-transitive graphs, and show that the maximum real eigenvalue $\lambda_{\max}(H)$ of the corresponding Hashimoto matrix (7.7) is finite, lies in the physical range $\lambda_{\max}(H) \geq 1$, and can be obtained by solving a single finite-dimensional spectral problem.

Let us first consider the eigensystem (7.6) for a finite graph $\mathcal{G}$. While the Hashimoto matrix $H_{\mathcal{G}}$ in Eq. (7.7) is non-symmetric, it is finite-dimensional and has non-negative matrix elements. The properties of the maximal real-valued eigenvalue $\lambda_{\max}$ of such matrices is addressed by the Perron-Frobenius theory of non-negative matrices [210–212]. In particular, an eigenvalue corresponding to a non-negative eigenvector always exists and it equals to the spectral radius of H, $\lambda_{\max}(H) = \rho(H)$, although in general one could have $\rho(H) = 0$.

For any $m \times m$ matrix H with non-negative matrix elements, a sufficient condition to have $\rho(H) > 0$ is expressed [212] in terms of the digraph $\mathcal{D}_H$ of order m with the adjacency matrix corresponding to non-zero elements of the square matrix H. Namely, there is a directed edge $u \to v$ whenever $H_{uv} > 0$ (or a loop $u \to u$ in the case of a diagonal matrix element $H_{uu} > 0$). In the case of the Hashimoto matrix, this graph is the OLG associated with the original graph, see discussion below Eq. (7.7). The spectral radius of H is positive, $\rho(H) > 0$, if the digraph $\mathcal{D}_H$ is *strongly connected*. This requires that for any pair of vertices u, v, there must be a directed path $(u_0 = u, u_1, \ldots, u_f \equiv v)$ connecting u and v such $u_{s-1} \to u_s$, $s = 1, \ldots, f$ is in the edge set of $\mathcal{D}_H$. In such a case, we also know that the eigenvalue $\lambda_{\max} = \rho(H)$ is non-degenerate, it is the only one with the magnitude equal to the spectral radius, $|\lambda| = \rho(H)$, and the corresponding eigenvector has all positive components [210–212].

We prove the following

Theorem 7.3. *For any finite connected graph $\mathcal{G}$, the spectral radius of the Hashimoto matrix $H_{\mathcal{G}}$ is zero iff $\mathcal{G}$ contains no cycles. Otherwise, $\rho(H_{\mathcal{G}}) \geq 1$. The eigenvector corresponding to $\lambda \equiv \lambda_{\max} = \rho(H_{\mathcal{G}})$ is non-negative.*

The interpretation is simple: on a finite tree, any non-backtracking walk eventually terminates at a *leaf* (degree-one vertex) with no outgoing edges; thus Eq. (7.6) with $\lambda \neq 0$ has only trivial solutions $\epsilon_{ij} = 0$. With one or more cycles present, recursively plucking off any leaves, we arrive at a *backbone* graph $\mathcal{B}$ with minimum degree $d_{\min}(\mathcal{B}) \geq 2$; the corresponding Hashimoto matrix $H_{\mathcal{B}}$ is strongly connected and its spectral radius is limited from below by $\rho(H_{\mathcal{B}}) \geq d_{\min}(\mathcal{B}) - 1 \geq 1$. Putting the leaves back recovers the original graph, but does not affect the spectral radius of the Hashimoto matrix.

Proof of Theorem 7.3 . For a finite tree, any non-backtracking path eventually terminates at a *leaf* (degree-one vertex) with no outgoing edges; thus Eq. (7.6) with $\lambda \neq 0$ has only trivial solutions $\epsilon_{ij} = 0$, which gives zero spectral radius of $H_{\mathcal{G}}$. Generally, it is easy to see that leafs on $\mathcal{G}$ have no effect on $\rho(H_{\mathcal{G}})$. Indeed, if $d_j = 1$ and $i \sim j$ is

the only neighbor on $\mathcal{G}$, then Eq. (7.6) gives $\epsilon_{ij} = 0$ regardless of its values elsewhere. Similarly, ϵ_{ji} is determined by λ and the values ϵ_{il} on the bonds neighboring with i, but this value has no effect on the components of the eigenvector elsewhere. Thus, removing a leaf does not change the eigenvalues of Eqs. (7.6) and therefore the spectral radius of the Hashimoto matrix $H_{\mathcal{G}}$, see Eq. (7.7).

Define a *backbone* $\mathcal{B}$ of a graph $\mathcal{G}$, a result of the recursive removal of all degree-one vertices. The spectral radius of the Hashimoto matrix associated with the backbone is the same as that for the original graph, $\rho(H_{\mathcal{B}}) = \rho(H_{\mathcal{G}})$. For any finite tree the backbone is empty, in which case $\rho(H_{\mathcal{G}}) = 0$. Otherwise, the backbone $\mathcal{B}$ satisfies $d_{\min}(\mathcal{B}) > 1$. If $\mathcal{G}$ is a connected graph, so is $\mathcal{B}$. For the backbone, the lower bound on the spectral radius of the $m \times m$ Hashimoto matrix $H \equiv H_{\mathcal{B}}$ can be found using the Collatz-Wielandt formula [see Eq. (8.3.3) in Ref. [212]]: $\rho(H) = \max_x f(x)$, where the maximum is taken over all vectors with non-negative components and

$$f(x) = \min_{1 \le i \le m,\, x_i \neq 0} \frac{[Hx]_i}{x_i}. \tag{7.10}$$

Indeed, if we take the vector x with the components $x_i = 1$, $i = 1, \ldots, m$, Eq. (7.10) gives $f(x) = \min_{1 \le i \le m} \sum_{j=1}^{m} [H]_{ij} = d_{\min}(\mathcal{B}) - 1$. Backbone has no degree-one vertices, thus $\rho(H_{\mathcal{B}}) \ge d_{\min}(\mathcal{B}) - 1 \ge 1$. The final statement of the Theorem is merely the reiteration of the Perron-Frobenius theorem for generic non-negative matrices, see p. 669 in Ref. [212]. □

We are not aware of an extension of the Perron-Frobenius theory to infinite matrices. However, in the case of a quasi-transitive graph which only has a finite set of inequivalent vertices, it is reasonable to expect that the solution $\epsilon_{ij} \ge 0$ of Eqs. (7.6) has the same symmetry as the original graph. Namely, for any pair of directed edges $i \to j$ and $i' \to j'$ which can be mapped to each other by an automorphism of $\mathcal{G}$, we request

$$\epsilon_{ij} = \epsilon_{i'j'}. \tag{7.11}$$

Such an ansatz reduces Eqs. (7.6) to a finite-dimensional eigensystem. Depending on the details, the corresponding matrix M may have elements which are greater than one, or non-zero elements along the diagonal. As we discuss in the proof, the non-zero elements of M uniquely correspond to non-zero elements of the Hashimoto matrix $H_{\mathcal{G}/\Gamma}$ corresponding to the quotient graph $\mathcal{G}/\Gamma$ with respect to the group Γ of automorphisms of $\mathcal{G}$. When the original infinite graph is connected, $\mathcal{G}/\Gamma$ necessarily has cycles. We prove

Theorem 7.4. *Consider an infinite connected quasi-transitive graph $\mathcal{G}$ with the group of automorphisms Γ. The invariant ansatz (7.11) with $\epsilon_{ij} \geq 0$ gives a valid solution of the MF Eqs. (7.6). The corresponding eigenvalue $\lambda = \rho(M)$ satisfies the inequalities*

$$\lambda_{\max}(H_{\mathcal{G}}) = \rho(M) \geq \rho(H_{\mathcal{G}/\Gamma}) \geq 1. \tag{7.12}$$

Proof. The ansatz forces identical values on any pair of directed edges which can be mapped into each other by an automorphism of $\mathcal{G}$. For a vertex-transitive graph, this leaves a finite eigensystem with a matrix M whose non-zero elements correspond to the Hashimoto matrix of the quotient graph $\mathcal{G}/\Gamma$. This latter graph cannot be a tree: it has to have at least one cycle (or a loop) since any non-backtracking walk on the infinite connected graph $\mathcal{G}$ has to eventually arrive to a point equivalent to that already in the walk. According to Theorem 7.3, this implies $\lambda_{\max}(H_{\mathcal{G}/\Gamma}) = \rho(H_{\mathcal{G}/\Gamma}) \geq 1$, with the corresponding eigenvector having non-negative components, $\epsilon_{ij} \geq 0$. In general, the corresponding matrix elements of M are greater or equal those of the adjacency matrix $A_{\mathcal{G}/\Gamma}$, $M \geq A_{\mathcal{G}/\Gamma}$. According to Perron-Frobenius theory [210–212], this implies that M also has an eigenvector with non-negative components and the eigenvalue $\lambda_{\max}(M) = \rho(M) \geq \rho(H_{\mathcal{G}/\Gamma}) \geq 1$. By construction, the obtained invariant symmetric eigenvector is also a non-negative eigenvector of the Hashimoto matrix $\mathcal{H}_{\mathcal{G}}$ corresponding to the original MF Eqs. (7.6), which implies $\lambda_{\max}(H_{\mathcal{G}}) \geq \lambda_{\max}(M)$. On the other hand, any non-negative eigenvector of $H_{\mathcal{G}}$ corresponding to $\lambda_{\max}(H_{\mathcal{G}})$ can be rendered to satisfy the invariant ansatz (7.11) by symmetrizing over the automorphisms group Γ. The resulting eigenvector is non-zero and corresponds to the same eigenvalue, which proves the equality in Eq. (7.12). □

Finally, we give a constructive proof of the first part of the inequality (7.3).

Theorem 7.5. *The percolation threshold for any infinite connected quasi-transitive graph $\mathcal{G}$ is bounded from below by the inverse maximum eigenvalue of the corresponding Hashimoto matrix corresponding to a non-negative eigenvector, $p_c(\mathcal{G}) \geq 1/\lambda_{\max}(H_{\mathcal{G}})$.*

The approach is to construct a tree graph $\mathcal{T}$ which is locally indistinguishable from the original graph $\mathcal{G}$, except that a closed walk on $\mathcal{G}$ goes over to a walk connecting equivalent points on $\mathcal{T}$. This is done by repeated application of *single cycle unwrapping* (SCU):

Definition 7.6 (SCU)**.** *Given a connected graph $\mathcal{G}$ and a bond $b \equiv (u, v) \in \mathcal{E}(\mathcal{G})$, such that the* two-terminal *graph $\mathcal{G}' \equiv \big(\mathcal{V}(\mathcal{G}), \mathcal{E}(\mathcal{G}) \setminus b\big)$ with source at v and sink at u is connected, define the cycle-unwrapped graph $\mathcal{C}_b\mathcal{G}$ as the series composition of an infinite*

chain of copies $\mathcal{G}'_i$, $i \in \mathbb{Z}$, of the graph $\mathcal{G}'$, with the source of $\mathcal{G}'_i$ connected to the sink of the $\mathcal{G}'_{i+1}$.

The SCU is illustrated in Fig. 7.2. Notice that for a graph with more than one cycle, unwrapping at b removes one cycle but creates an infinite number of copies of the remaining cycles. Nevertheless, for a locally finite graph, we prove that a countable number of SCUs is needed to remove all cycles. Further, we prove that an SCU does not change the maximum eigenvalue of the Hashimoto matrix, $\lambda_{\max}(H_{\mathcal{G}}) = \lambda_{\max}(H_{\mathcal{C}_b\mathcal{G}})$, whereas the percolation threshold cannot go up. Overall, this gives a constructive proof of Theorem 7.5.

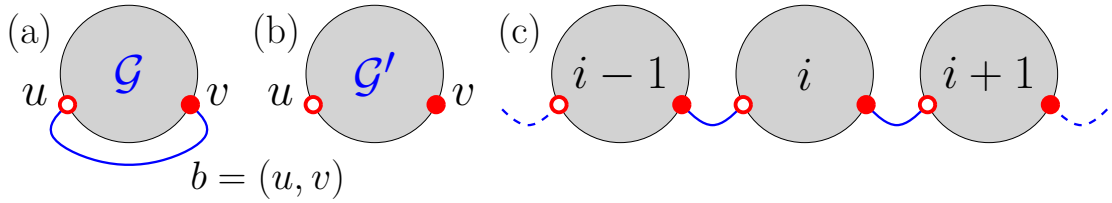

Figure 7.2: Illustration of SCU: (a) A graph $\mathcal{G}$ with a non-bridge bond $b \equiv (u, v)$ highlighted; (b) Two-terminal graph $\mathcal{G}'$; (c) The resulting graph $\mathcal{C}_b\mathcal{G}$ is a series composition of an infinite chain of copies of $\mathcal{G}'$.

We give a constructive proof of Theorem 7.5, by building a tree graph $\mathcal{T}$ which is locally indistinguishable from the original graph $\mathcal{G}$, except that a closed walk on $\mathcal{G}$ goes over to a walk connecting equivalent points on $\mathcal{T}$. We show that the maximal eigenvalues of Eqs. (7.6) corresponding to non-negative eigenvectors, $\epsilon_{ij} \geq 0$, are the same for the original graph and the tree, $\lambda_{\max}(H_{\mathcal{T}}) = \lambda_{\max}(H_{\mathcal{G}})$, while the percolation threshold on the tree cannot exceed that on $\mathcal{G}$, thus $p_c(\mathcal{G}) \geq p_c(\mathcal{T}) = 1/\lambda_{\max}(H_{\mathcal{G}})$.

The tree is built by a sequence of SCUs, see Definition7.6 and Fig. 7.2. For any connected graph, removal of a *bridge* bond creates a disconnected graph; each SCU must be done at a non-bridge bond. Notice that for a graph with more than one cycle, SCU at a non-bridge bond b removes one cycle but creates an infinite number of copies of the remaining cycles. Nevertheless, for a locally finite graph, a countable number of SCUs is needed to remove all cycles:

Lemma 7.7. *For a locally finite graph $\mathcal{G}_0 \equiv \mathcal{G}$, a sequence of SCUs $\mathcal{G}_{m+1} \equiv \mathcal{C}_{b_{m+1}}\mathcal{G}_m$ can be chosen so that in the $m \to \infty$ limit the resulting graph is a tree, $\mathcal{T} \equiv \mathcal{C}_\infty\mathcal{G} = \lim_{m\to\infty} \mathcal{G}_m$.*

Proof. Consider SCU $\mathcal{C}_b$ at a non-bridge bond $b \in \mathcal{E}(\mathcal{G})$. The cycle-unwrapped image of any path on $\mathcal{G}$ that does not include b will remain entirely within a single copy of

$\mathcal{G}'$. Thus, if at each SCU step we choose a bond b at distance r_b from some fixed origin vertex, such that only bridge bonds can be found closer to the origin, $r < r_b$, any copy of the remaining non-bridge bond introduced by the SCU is going to be at a distance $r > r_b$. Thus, each SCU reduces the number of non-bridge bonds at r_b, and does not introduce such bonds at $r < r_b$. For a locally finite graph, a finite number of SCUs is required to remove all non-bridge bonds at each of $r = 0, 1, 2, \ldots$. We arrive at a tree graph $\mathcal{T} = \mathcal{C}_\infty\mathcal{G}$ in the limit $r \to \infty$, after a countably many SCUs. □

The final theorem we prove establishes the spectral radius of the quasi-transitive graph, or the Hashimoto's matrix, is invariant under SCU.

Lemma 7.8. *For any simple quasi-transitive graph $\mathcal{G}$, SCU does not change the spectral radius of $\mathcal{G}$, $\rho(\mathcal{G}) = \rho(\mathcal{C}_b\mathcal{G})$, or the maximum eigenvalue of the Hashimoto matrix (7.7) corresponding to a non-negative eigenvector in Eqs. (7.6), $\epsilon_{ij} \geq 0$: $\lambda_{\max}(H_\mathcal{G}) = \lambda_{\max}(H_{\mathcal{C}_b\mathcal{G}})$.*

Proof. The symmetry of $\mathcal{C}_b\mathcal{G}$ implies that an eigenvector e can always be chosen to diagonalize both its adjacency matrix $A \equiv A(\mathcal{C}_b\mathcal{G})$, $Ae = \lambda e$, and the translation generator T, $Te = \mu e$. Translation group being Abelian, its representations are all one-dimensional, with $\mu = e^{ik}$, with $0 \leq k < 2\pi$. Let e_0 with non-negative components be the eigenvector of the matrix A with the eigenvalue equal to its spectral radius, $\lambda_{\max} = \rho(A)$ [Adjacency matrix is symmetric, and it is easy to see that Perron-Frobenius theorem applies]. Symmetrizing e_0 over $\mathbb{Z}$, gives a non-negative eigenvector e corresponding to the same $\lambda_{\max}$ and $k = 0$. This corresponds to the symmetric ansatz (7.11), thus $\rho(M') = \rho(A_{\mathcal{C}_b\mathcal{G}}) \equiv \rho(\mathcal{C}_b\mathcal{G})$, where M' is the reduced matrix corresponding to the symmetric eigenvector of A, cf. discussion below Eq. (7.11). Further, for a simple (di)graph $\mathcal{G}$, the matrix elements of M' satisfy $M'_{ij} \in \{0, 1\}$, thus $M' = A_\mathcal{G}$, which gives $\rho(\mathcal{G}) \equiv \rho(A_\mathcal{G}) = \rho(\mathcal{C}_b\mathcal{G})$, instead of the inequality in Theorem 7.4. The proof in the case of $H_{\mathcal{C}_b\mathcal{G}}$ is identical, except that we do not assume the applicability of Perron-Frobenius theorem and instead start with a non-negative eigenvector $\epsilon_{ij} \geq 0$ corresponding to $\lambda_{\max}(H_{\mathcal{C}_b\mathcal{G}})$. □

Proof of Theorem7.5. Quasi transitivity of $\mathcal{G}$ implies that a finite maximum degree exisits; according to Lemma 7.7, $\mathcal{G}$ can be transformed to a tree $\mathcal{T}$ by a series of SCUs. Each step of the sequence can be undone by a graph quotient, $\mathcal{G}_m = \mathcal{G}_{m+1}/\mathbb{Z}$. According to Theorem 1 in Ref. [206], the percolation threshold of a graph quotient cannot be below that of the original graph, thus $p_c(\mathcal{G}_m) = p_c(\mathcal{G}_{m+1}/\mathbb{Z}) \geq p_c(\mathcal{G}_{m+1})$; the entire sequence gives $p_c(\mathcal{G}) \geq p_c(\mathcal{T})$. On the other hand, Eqs. (7.6) are exact for the tree, they

give $p_c(\mathcal{T}) = 1/\lambda_{\max}(H_{\mathcal{T}})$. Moreover, each of the intermediate graphs of the sequence is vertex transitive and simple, thus the maximum eigenvalues of the corresponding Hashimoto matrices remain the same after each step, and $\lambda_{\max}(H_{\mathcal{T}}) = \lambda_{\max}(H_{\mathcal{G}})$, see Lemma 7.8. □

7.5 Conclusions

In conclusion, we suggested a spectral MF lower bound for the threshold of site percolation on an infinite graph. This bound accounts for local structure of the graph, and should be asymptotically exact for graphs with no short cycles. This bound goes over to the known lower bound (7.2) for degree-regular graphs, and otherwise improves on Eq. (7.2). We also demonstrated that the inverse spectral radius of the graph which was suggested previously as an estimate for the percolation threshold is always strictly smaller than our lower bound. In the case of a quasi-transitive graph, a graph-theoretical analog of a translationally-invariant system, we proved that the bound is in a physically meaningful range and can be found as a solution of a finite spectral problem.

Our results can be easily extended to the cases of Bernoulli (bond), combined site-bond, or non-uniform percolation, where the probabilities to have an open vertex may differ from site to site. A similar technique can also be used to prove the conjecture on the location of the threshold for vertex-dependent percolation on directed graphs [213].

After the original version of our manuscript appeared at the electronic archive [191], we were alerted to a forthcoming work by Newman, Karrer, and Zdeborova [125], who arrived at some of the same results using different arguments.

Chapter 8

Correlated percolation

In this chapter, the results from Chapter (7) and the methods of [125, 208] are extended to systems with correlated percolation. To define correlations in our system, we use connected sub-graphs, defined as *lattice animals*. Correlated percolation, as described in this chapter, is the random placement of lattice animals on a graph and defines a process where not just single sites are open or closed, but connected clusters of sites are simultaneously affected. By placing an animal on a vertex, if it is known that the given vertex is open, there is a set of connected neighbors that are also open. Three examples of correlated percolation are studied: correlated percolation on a regular lattice, correlated percolation on a random graph, and a combined process of site (uncorrelated) and correlated percolation on a random graph. A lower bound on the percolation threshold on general undirected graphs is defined using the spectral radius of the adjacency matrix($\rho(\mathcal{A})$), where the matrix $\mathcal{A}$ will be modified to include contributions from correlations. Also the diameter of the largest cluster on a graph is found to be finite below the threshold. The presence of correlations in a percolation system is found have a threshold dependent on the average animal size $\langle n^2 \rangle$. Finally, a discussion of weighted percolation shows how the methods for correlated percolation can be extended to vertex-dependent percolation.

8.1 Introduction

In the study of percolation on graphs, trees or discrete systems, the processes of site or bond percolation are defined by independent probabilities [74, 214]. There are many examples of systems where percolation is achieved by probabilistic processes which are not based on independent probabilities. In Section (1.3) many physical examples of percolation by clusters were given. Percolation on biological or sociological networks

may be defined by processes which affect specific subsets of the population simultaneously. Applying graph theory to computational systems involves the possibility of small sub-graphs being open simultaneously [215]. An initial approach is given in continuum systems, where percolation by overlapping shapes is the standard Poisson-Boolean model [216, 217] and can be considered as a process which affects a subset of points simultaneously. In continuum percolation it has been studied how the finite volume or area of a connected cluster can define the threshold of percolation [112, 218].

In our work we approach correlated percolation as percolation by overlapping lattice animals. The first approach approximates all lattice animals on a graph in $\mathbb{Z}^d$ as d-dimensional spheres and defines a connected cluster through the overlapping of random-sized spheres. This connects the continuum results to a discretized space and only requires the redefinition of a disk in terms of graph theoretic distances. A percolation threshold is established in terms of the average disk size.

On a graph which is not regular, either a tree or a random graph, the lattice animals on a graph can be approximated by adding vertices to a graph which are known to be open. These auxiliary vertices provide all the connections that are possible through connection to an animal. This approach avoids the exponential scaling encountered on sparse graphs.

8.2 Definitions

The discussion of correlated percolation and the methods used are based in continuum percolation concepts [112] and the adjacency matrix methods found in [125,208]. For a graph $\mathcal{G} = \{V, E\}$, the adjacency matrix is defined by the graph's connections. The matrix elements $a_{ij} \neq 0$ if there is an edge connecting vertex (i) to vertex (j). For undirected graphs, the adjacency matrix is symmetric. A random graph $\mathcal{G}'$ can be generated from $\mathcal{G}$ through a process which retains vertices with probability, p. Initially the probability will be considered vertex-independent. Edges are retained if both endpoints are open in $\mathcal{G}'$. When the probability is defined for independent vertices, this process will be defined as *uncorrelated percolation*. On $\mathcal{G}'$ there are clusters of open vertices, and if a cluster exists which spans or nearly covers the entirety of $\mathcal{G}$ then the system is above a threshold value of p, called the percolation threshold.

This chapter will focus on *correlated percolation* where the probability of a vertex being open is affected by its neighbors and the effect of correlations on the percolation threshold. Referring back to Section (6.4), a lattice animal is defined as a sub-graph. The overlap of animals leads to connected open clusters. For our definitions, the over-

lap of a single vertex between animals is sufficient. Weighted percolation is defined by vertex-dependent probabilities, $p = \{p_i\}, p_i = p(v_i)$. Using the methods described in Chapter (6), and methods used in continuum percolation models, the threshold for percolation will be established through a bound on the average cluster size.

8.3 Correlated percolation on a regular lattice

In Ref. [112], the existence of a percolation threshold was found to be dependent on the average size of shapes covering a space. Percolation was defined by a connected component, created by the overlap of random-sized objects, which spans the entire continuum space. For a system of d-dimensional space with randomly distributed spheres of random radii, the percolation threshold was defined by the finiteness of $\lambda\langle r^d\rangle$, where λ is the density of spheres in the system and $\langle r^d\rangle$ is the average volume of a sphere. For two-dimensional disks in $\mathcal{R}^2$ the average area of a disk determines the threshold. We show these results are obtainable by distributing random-sized shapes of dimension $D < d$, in d-dimensional space, starting from finite-width rings in $\mathcal{R}^2$ and continuing to one-dimensional rings (shown in Figure (8.5)). The ability to define a connected component for lower-dimensional objects is applied to discrete space (shown in Figure (8.6)). We assert then that percolation on a regular lattice can be defined similarly by placing random-sized disks on a lattice, where the average area and radius of a disk are defined by lattice points and the Manhattan distance (see Figure (8.2)).

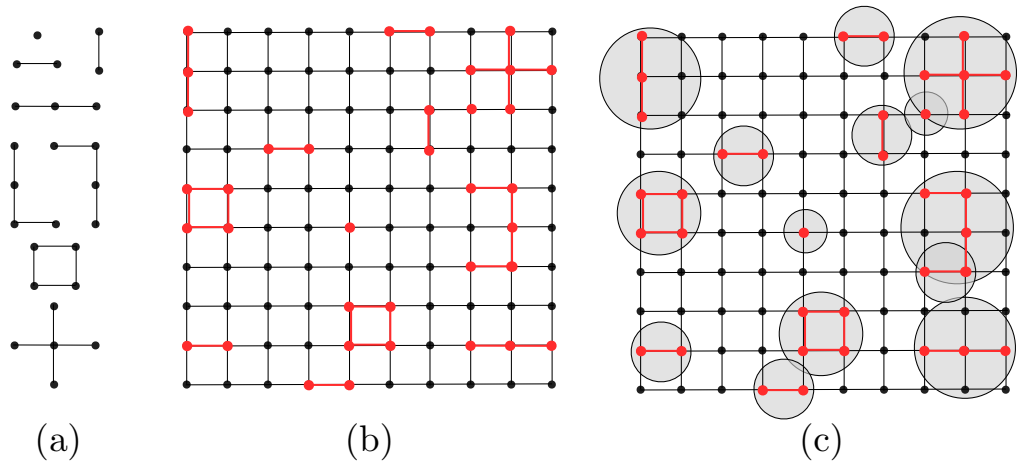

Figure 8.1: Correlated percolation on a regular graph using lattice animals: (a) A selection of lattice animals that can be formed, (b) placement of random-sized animals on the lattice (c) approximating the number of covered vertices using disks.

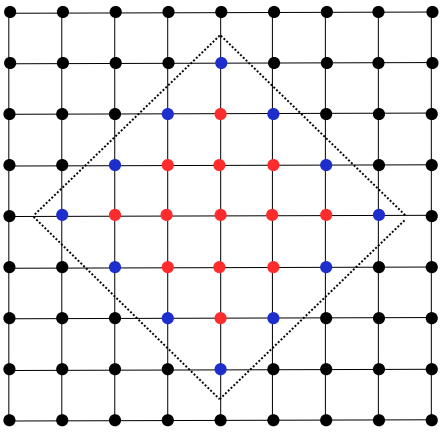

Figure 8.2: The interpretation of a solid disk on a lattice, using the Manhattan disk. The area of a disk is the number of points contained inside a disk of Manhattan radius $r = 3$ is $(r+1)^2 + r^2$ (red and blue points). The circumference of a disk of radius $r = 3$ consists of $4r$ points (blue).

8.4 Auxiliary vertex model: approximate correlated percolation on a random graph

In the previous section it was shown that the covered area of a disk can be applied to a regular graph and interpreted as the number of lattice points which are equidistant from the disk center. Using the graph theoretic distance it was seen that the area scaled as n^2, where n is the radius of a given disk. On a tree graph, this approach fails as the number of lattice points equidistant from a central vertex scales exponentially, rather than as a power law (see Figure (8.3)). Beginning with a simple

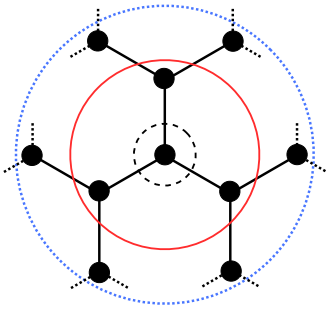

Figure 8.3: Exponential scaling of covered area on a degree regular tree. A $r = 0$ disk contains the central vertex (black dashed), $r = 1$ contains $z+1$ vertices (red solid), $r = 2$ contains $1 + z + z(z-1)$ vertices. The $r = d$ disk would contain at least z^d vertices.

fixed-degree tree, the number of points which are contained in a disk of radius d is given by the number of points contained in d-generations of growth away from a central

vertex. The number of vertices in the r^{th} generation is bounded above by z^r (or z_{max}^d for a degree-limited tree). An upper bound to the average size of a disk would require calculating,

$$\langle |B_2(0,r)| \rangle \leq \int z^r \nu(dr), \tag{8.1}$$

which leads to an exponentially small value for the threshold for percolation. In order for $\lambda \langle z^r \rangle$ to be finite the density of random-sized objects would be vanishingly small $\lambda \ll 1$.

We define an alternative approach to percolation by lattice animals, where a random animal is replaced with an auxiliary vertex which provides the same connections on the graph as the animal (see Figure (8.4)). It was established in [200] that a random network has a percolation threshold given by $\langle z \rangle / (\langle z^2 \rangle - \langle z \rangle)$ where the averages are taken with respect to the degree distribution of the original graph. With the addition of auxiliary vertices, the average degree $\langle z \rangle$ is taken over the new degree distribution.

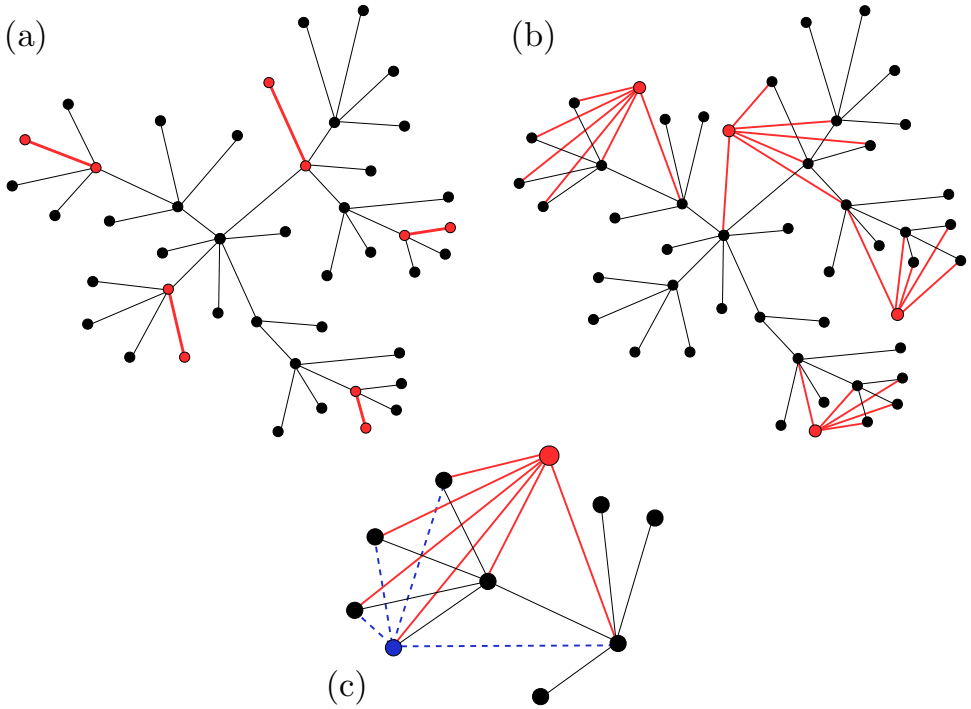

Figure 8.4: Percolation with lattice animals using auxiliary vertices. (a) Lattice animals distributed on a random graph, (b) Random graph with auxiliary vertices approximating lattice animals, (c) Detail of effects on the degree of a vertex (blue) by adding connections to the auxiliary vertex (red solid line) and allowing connections through the auxiliary vertex (blue dashed line).

The bound on the average cluster size is calculated first with a simplified model: a single lattice animal species (a connected subgraph containing ℓ vertices) randomly

distributed on a fixed degree tree. Considering the tree to contain N-total vertices, the N_1 lattice animals will cover ℓN_1-total vertices, an expression for the average degree can be written as,

$$\langle z \rangle = \sum_n z(n) f(n) \leq \frac{1}{N} \left[(N - N_2) z + N_1 z' + N_2 (z\ell) \right], \tag{8.2}$$

where N_1 is the number of higher-degree vertices added, and N_2 is the total number of vertices contained in all lattice animals and neighbors. Of the original graph's (N) vertices, the $(N - N_2)$ vertices which are neither in an animal nor are neighboring an animal will have unchanged degree. The connections due to a lattice animal is approximated by a single vertex of degree z', connected to all the lattice animal vertices and neighbors. In Figure (8.4)(b), the degree of the animal of size (ℓ) is bounded by, $z' \leq \ell z$. The number of vertices contained in all animals, and all neighbors is N_2 and these have a degree bounded by $z\ell$: increased by the connection to the auxiliary vertex of degree z', and by the additional connection to each other made possible by the (known open) auxiliary vertex (see Figure (8.4)(c)). Finally, it is noted that $N_2 < N_1(z\ell)$. Together these give a bound on the average degree of a graph with a single lattice animal species:

$$\begin{aligned} \langle z \rangle = \sum_n z(n) f(n) &\leq \frac{1}{N + N_1} \left(N z + N_1 \ell z + N_1 (\ell z)^2 \right) \\ &\leq \left((1 - \lambda) z + \lambda (\ell z + (\ell z)^2) \right). \end{aligned} \tag{8.3}$$

The percolation threshold scales as $p_T \sim 1/(\lambda(\ell)^2)$ where λ is the probability of a vertex being connected to an animal $(N_1/(N + N_1))$ and ℓ is the animal size. For a collection of lattice animals, with sizes distributed with a probability distribution $f(\ell)$ the percolation threshold scales as $p_T \sim 1/(\lambda \langle (\ell)^2 \rangle)$.

8.5 Weighted percolation

The auxiliary vertex model establishes an approximate lower bound to the correlated percolation threshold. Using the adjacency matrix of a system with percolation by lattice animals, a more exact bound will be found in the next section. In this section the general problem of weighted percolation is studied with the adjacency matrix method, which introduces vertex-dependent probabilities to a percolation process. The flexibility of the adjacency matrix approach is highlighted here.

In Section (6.3) the general method for deriving a percolation threshold from the n^{th}-order product of a graph's adjacency matrix was given. The general form only

considered unweighted, uncorrelated percolation. Before discussing the complex problem of correlated percolation, the process of weighted (vertex dependent) percolation is considered. For specific graphs (fixed degree and degree limited) the percolation threshold is determined.

Beginning with a graph $\mathcal{G}_0$, a random graph $\mathcal{G}'$ is generated from a random subset of vertices and edges. In unweighted percolation, the probability that a vertex is chosen to be in $\mathcal{G}'$ is independent of the vertex. For weighted percolation, this probability becomes vertex-dependent. Each vertex v_i has a probability p_i and there is no guarantee that two vertices (v_i, v_j) have the same probability of being included in $\mathcal{G}'$.

The adjacency matrix of $\mathcal{G}'$ is labelled $\mathbf{B}$, and is derived from the adjacency matrix of $\mathcal{G}_0$ ($\mathbf{A}$). The connections of the original graph may not exist on $\mathcal{G}'$, their existence is dependent on the existence of both endpoints in $\mathcal{G}'$. To incorporate the conditional nature of connections on $\mathcal{G}'$, the adjacency matrix of $\mathcal{G}_0$ is scaled by a diagonal matrix $\mathbb{P} = \mathrm{diag}(p_1, p_2, \ldots, p_N)$, defined by the vertex-dependent probabilities. The adjacency matrix of $\mathcal{G}'$ is defined as: $\mathbf{B} = \mathbf{A}\mathbb{P}$.

The number of n-length walks on $\mathcal{G}'$ from a known open vertex (v_i) to another vertex (v_j) is given by $(\mathbf{B}^n)_{ij}$ and is dependent on the probability of v_j existing in $\mathcal{G}'$. Defining the average cluster size as outlined in Section (6.3), requires a weighted matrix $\mathbf{M}$ rather than a scalar probability (p) and includes the probability that v_i needs to be open:

$$\begin{aligned}\langle n\rangle &= \sum_n \langle \mathbf{1}|\mathbb{P}^T\left(\mathbf{A}\mathbb{P}\right)^n|\mathbf{1}\rangle = \sum_n \langle \mathbf{1}|\mathbb{P}^{1/2}\left(\mathbb{P}^{1/2}\mathbf{A}\mathbb{P}^{1/2}\right)^n\mathbb{P}^{1/2}|\mathbf{1}\rangle, \\ &= \sum_n \langle \mathbf{1}|\mathbb{P}^{1/2}\left(\mathbf{M}\right)^n\mathbb{P}^{1/2}|\mathbf{1}\rangle.\end{aligned} \tag{8.4}$$

The matrix norm of $\mathbb{P}^{1/2}\left(\mathbf{M}\right)^n\mathbb{P}^{1/2}$ can be calculated using the spectral norm.

$$\begin{aligned}\|\mathbb{P}^{1/2}\left(\mathbf{M}\right)^n\mathbb{P}^{1/2}\|_2 &\leq \|\mathbb{P}^{1/2}\|_2\|\left(\mathbf{M}\right)^n\|_2\|\mathbb{P}^{1/2}\|_2 \\ &\leq \|\mathbb{P}^{1/2}\|_2\|\left(\mathbf{M}\right)\|_2^n\|\mathbb{P}^{1/2}\|_2 = \rho\left(\mathbb{P}^{1/2}\right)\rho\left(\mathbf{M}\right)^n\rho\left(\mathbb{P}^{1/2}\right)\end{aligned} \tag{8.5}$$

The spectral radius of the probability matrix is p_{max}, the largest probability a vertex is included in $\mathcal{G}'$, and the average cluster size is defined by the spectral radius of $\mathbf{M}$:

$$\begin{aligned}\langle n\rangle &= \sum_n \|\mathbb{P}^{1/2}\mathbf{M}^n\mathbb{P}^{1/2}\| \\ &\leq \sum_n p_{max}\lambda_{max}(\mathbf{M})^n = p_{max}\left(\frac{1}{1-\lambda_{max}(\mathbf{M})}\right).\end{aligned} \tag{8.6}$$

Again, the equivalence of the spectral radius and the maximum eigenvalue of a matrix has been used, and the final sum over (n) is possible only if $\lambda_{max}(\mathbf{M}) < 1$.

8.5.1 Weighted percolation threshold on graphs with known degree distributions

Equation (8.6) established that the average cluster size diverges when $\lambda_{max}(\mathbf{M}) = 1$. For certain graphs a bound on the spectral radius can be found using the rank-1 matrix norm, which is the maximum column sum:

$$\lambda_{max}(\mathbf{M}) \leq \|\mathbf{M}\|_1 = \sum_j m_{ij}. \tag{8.7}$$

Recalling the definition of the weighted matrix $\mathbf{M}$ rewrites the column sum over m_{ij} as a column sum over a_{ij}, the connections of the original graph.

$$\|\mathbf{M}\|_1 = \|\mathbb{P}^{1/2}\mathbf{A}\mathbb{P}^{1/2}\|_1 \leq (p_{max})\|\mathbf{A}\|_1. \tag{8.8}$$

In a fixed-degree graph, all vertices have the same degree (z) and the rank-1 norm is the same for all columns of $\mathbf{A}$. For a fixed-degree graph with weighted percolation:

$$\|\mathbf{M}\|_1 \leq (p_{max})\|\mathbf{A}\|_1 = p_{max}z, \tag{8.9}$$

and the threshold for percolation is $p_{max}z < 1$. In a degree-limited graph, the degree of a vertex is bounded by a maximum value z_{max}, which determines the rank-1 norm of $\mathbf{A}$. For a fixed-degree graph with weighted percolation:

$$\|\mathbf{M}\|_1 \leq (p_{max})\|\mathbf{A}\|_1 = p_{max}z_{max}, \tag{8.10}$$

and the threshold for percolation is $p_{max}z_{max} < 1$. As discussed in Chapter (7), the threshold for these models can be skewed by an single vertex of very high degree, or by a single vertex of very high probability.

8.6 Correlated and uncorrelated percolation on a random graph

In Section (8.5) the adjacency matrix of a random graph was used to define a bound on the average cluster size. The divergence of the average cluster size established a threshold for percolation. The process of correlated percolation is similar to weighted percolation, the probability of a vertex being randomly chosen from $\mathcal{G}_0$ is no longer independent of the vertex but is more complicated than just vertex-dependent probabilities. Correlated percolation is percolation by overlapping shapes (lattice animals) placed on a random graph. Vertices which are covered by lattice animals are automatically included in the random graph $\mathcal{G}'$. The method used in this section is based on how the

connections of $\mathcal{G}'$ relate to the adjacency matrix of $\mathcal{G}_0$ and the results given will be a more exact threshold bound then the results of Section (8.4).

Beginning with a connected graph $\mathcal{G}_0$, a random graph $\mathcal{G}'$ is generated by randomly selecting vertices with a vertex-independent probability (p) or by selecting groups of vertices by placing a lattice animal over them. On a graph, the entire set of lattice animals are defined as a set of vectors $\{\mathbf{c}\}$ where each vector represents a specific animal placed on a specific set of vertices of the original graph. The probability ($q(\mathbf{c})$) is the probability that the animal represented by $\mathbf{c}$ exists on the vertices contained in $\mathbf{c}$. On $\mathcal{G}'$ the connections that exist are the elements of the matrix $\mathbf{B}$,

$$b_{ij} = a_{ij}p + \sum_{\mathbf{c}} q(\mathbf{c})(\mathbf{M}(\mathbf{c})) \tag{8.11}$$

which is dependent on a matrix $\mathbf{M}(\mathbf{c})$ defined by an animal covering a set of vertices in the graph. A lattice animals of size (ℓ) is a connected sub-graph of $\mathcal{G}_0$ and the vertices it contains can be expressed as the weight-ℓ vector $\mathbf{c}$ that is non-zero at entries v_i where the animal is located. For $\mathbf{c}$ the matrix $\mathbf{M}(\ell)$ is,

$$\mathbf{M} = \mathbf{c}\mathbf{c}^T - \mathrm{diag}(\mathbf{c}). \tag{8.12}$$

The last term is necessary to ensure that self-loops are not created. The terms in Eq. (8.11) contributing to a connection between two vertices (v_i, v_j) in the graph $\mathcal{G}'$ are: ($a_{ij}p$) an edge connecting $i \leftrightarrow j$ in $\mathcal{G}_0$ and vertex v_j included, or, an animal exists which contains both vertices.

Defining the average cluster size is done by the same method used in Sections (6.3), (8.5). This introduces a simplification to the correlated system, in finding the n-length walks from $i \leftrightarrow j$ it is assumed that vertex (i) will be selected by an uncorrelated process only. The average cluster size is still defined by the spectral radius $\rho(\mathbf{B})$ but due to the complexity of the connections in $\mathbf{B}$, the bound on $\|\mathbf{B}\|_2$ by the rank-1 norm is used. The general result for the average cluster size on $\mathcal{G}'$ is:

$$\langle n \rangle \leq \frac{p}{1 - p\rho(\mathbf{B})}. \tag{8.13}$$

Again a threshold for a finite average cluster size is defined by $p\rho(\mathbf{B}) < 1$. However, evaluating the spectral norm $\rho(\mathbf{B})$ requires summing over the probabilities $q_i(\ell)$ for all possible animals on all vertices. A bound exists on the spectral norm which is easier to evaluate:

$$\|\mathbf{B}\|_2 \leq \sqrt{\|\mathbf{B}\|_1 \|\mathbf{B}\|_\infty} = \|\mathbf{B}\|_1 \tag{8.14}$$

On a symmetric graph, the rank-1 and rank-∞ norms are equivalent. The evaluation of $\|\mathbf{B}\|_1$ is the maximum value of the column sum of $\mathbf{B}$. Each column of $\mathbf{B}$ describes all

connections which include a fixed initial vertex (i), thus the column sum is expressed as:

$$\sum_j b_{ij} = \sum_j a_{ij}p + \sum_j \sum_\ell q(\ell)(\mathbf{M}(\ell))_{ij} \tag{8.15}$$

where the sum over the lattice animals is restricted to the subset of animals $\mathbf{c}_i \in \{\mathbf{c}\}$ which contain vertex i and the probability of an animal existing is $(q(\ell))$ the probability of vertex i being in an animal of weight ℓ. The expression is completed by rewriting $q(\ell) = \ell q(\ell)$ to account for the fact that vertex (i) can be any of the vertices in a weight-ℓ animal:

$$\|\mathbf{B}\|_1 = \sum_j a_{ij}p + \sum_j \sum_\ell \ell q(\ell)(\mathbf{M}(\ell))_{ij}. \tag{8.16}$$

In the second term, the matrix $\mathbf{M}$ is non-zero only on the $(\ell-1)$ entries which correspond to lattice animal vertices, omitting the self-connections. Thus the sum over the columns is invariant of i:

$$\begin{aligned}\sum_j \sum_\ell \ell q(\ell)(\mathbf{M}(\ell))_{ij} &= \sum_\ell \ell q(\ell) \sum_j (\mathbf{M}(\ell))_{ij} \\ &= \sum_\ell \ell(\ell-1)q(\ell) \\ &= (\langle \ell^2 \rangle - \langle \ell \rangle)\end{aligned} \tag{8.17}$$

8.6.1 Correlated percolation threshold on graphs with known degree distributions

The adjacency matrix method established a threshold for percolation through a bound on the average cluster size. If $\langle n \rangle$ is finite then no percolation occurs. In Section (6.3) it was seen that the geometric sum over $\rho(\mathbf{B})^n$ must converge, leading to the condition $\rho(\mathbf{B}) < 1$. In Section I8.5) the matrix $\mathbf{B}$ included terms due to vertex-dependent probabilities and in Eq. ((8.11)) the connectivity in a system with correlated percolation was found. To evaluate $\rho(\mathbf{B})$ exactly would require the inclusion of all possible positions of all possible weight-ℓ animals on a graph. This was reduced due to an upper bound established by the rank-1 norm. The summation over all animals which contain a specific vertex can be taken, but the column sum over the adjacency matrix $\mathbf{A}$ still remains to be evaluated. For specific classes of graphs, degree-limited and degree-fixed, these column sums can be found.

For a fixed-degree graph, the column sum $\sum_j a_{ij}$ is independent of the vertex (i). For unweighted percolation, this reduces $\sum_j a_{ij}p$ to pz. Additionally, the results of Section (8.5) can be used, for a system with weighted percolation, $\sum_j a_{ij}p \leq zp_{max}$. For

a degree-limited graph, the column sum is bounded by $z_{max}p$ for unweighted percolation and is bounded by $z_{max}p_{max}$ for weighted percolation.

Combining these results gives a lower bound on the percolation threshold for two kinds of systems which generate random graphs using two processes: unweighted percolation plus correlated percolation, or weighted percolation plus correlated percolation. Stating the results for unweighted percolation first, the threshold on a fixed-degree graph is established by,

$$\|\mathbf{B}\|_1 = zp + (\langle \ell^2 \rangle - \langle \ell \rangle) < 1, \tag{8.18}$$

and for a degree-limited graph,

$$\|\mathbf{B}\|_1 = z_{max}p + (\langle \ell^2 \rangle - \langle \ell \rangle) < 1. \tag{8.19}$$

For a system with weighted percolation plus correlated percolation, the threshold on a fixed-degree graph is,

$$\|\mathbf{B}\|_1 = zp_{max} + (\langle \ell^2 \rangle - \langle \ell \rangle) < 1, \tag{8.20}$$

and for a degree-limited graph,

$$\|\mathbf{B}\|_1 = z_{max}p_{max} + (\langle \ell^2 \rangle - \langle \ell \rangle) < 1. \tag{8.21}$$

8.7 Covered fraction with lower-dimension shapes

An inconsistency is now apparent in the models of correlated percolation. In the continuum model discussed in Ref. [112], the covered volume of the space was derived using shapes with the same dimensionality as the system. In $\mathbb{R}^2$ the space was covered by circular disks and the percolation threshold was determined by the finite bound on $\lambda\langle r^2 \rangle$. In Section (8.3), the percolation threshold for a regular lattice covered by solid disks was found using Manhattan disks and radii to approximate lattice animals. The average shape size was found to be dependent on the dimension of the lattice ($\langle n \rangle \propto r^2$), agreeing with the results in Ref. [112]. However, using the approximation of auxiliary vertices, or the exact method derived from the adjacency matrix, for a random graph the threshold was dependent on $\langle n^2 \rangle$. Applying this result to the regular lattice would correspond to a threshold dependent on $\lambda\langle r^4 \rangle$, much lower than the initial result based on Manhattan disks. In this section we investigate if a threshold of $\lambda\langle r^2 \rangle$ can be obtained in the continuum and regular lattice models. We replace the solid disks by lower dimension objects in the continuum model, or by lighter weight objects on the regular lattice.

Beginning with the continuum model: instead of solid, two-dimensional disks on $\mathbb{R}^2$, the space will be covered using finite-width rings (see Figure (8.5)(a,b)). Percolation in a continuum system can be defined by a cluster with an unbounded diameter,

and the derivation in Ref. [112] was based on the overlap of solid shapes. This lead to a bound on the connected cluster determined by the finiteness of a shape's d-dimensional volume. The entire area which is contained inside the connected cluster was included. For a distribution of rings with random radii it may be possible to form a connected cluster which has an unbounded diameter, though the area will not be explicitly covered.

A connected cluster is formed by solid disks when there is a non-empty region which is covered by both disks. The minimum amount the disks must overlap and contribute to non-zero growth of a cluster is localized near the perimeter of the disks. For example, a smaller disk which is nested inside a larger disk will not change the diameter of the larger disk. Likewise, the diameter of the cluster will be affected by rings which overlap by their outer radii, a ring nesting inside another will not contribute to the growth of a cluster with infinite diameter. Therefore the cluster formed by overlapping rings, and its dependence on the average are of a ring can be generalized to a system of overlapping circles by only considering the area swept out by the outer radius of a ring (see Figure (8.5)(c)). In the system of overlapping circles, only a single point is necessary to connect disks.

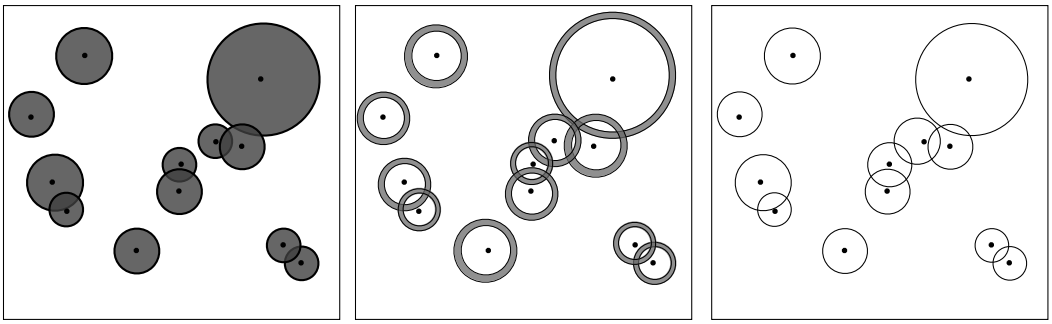

Figure 8.5: The connected cluster with solid, narrow and empty objects: (a) cluster generated by overlap of random-sized, two-dimensional disks in continuum system, (b) cluster generated by overlap of random-sized finite-width rings in discrete system, (c) cluster generated by overlapping circles.

In Figure (8.5) the connected component due to random-sized disks, rings and circles are shown. The space shown is $\mathbb{R}^2$ and the average size is given by $\langle r^2 \rangle = \int r^2 \nu(dr)$. This is the result given in [112] for $d = 2$. In Figure (8.5)(b), the solid disks are replaced with rings of random radii but finite width ϵ. Following the derivation in [112] the percolation threshold depends on the the area of a random shape. For a

ring of radius (r) and width ϵ centered at the origin, the Euclidean volume is

$$|B_2(0,r)| = \pi\left[(r+\epsilon)^2 - r^2\right], \tag{8.22}$$

and the average area of a system with random rings will be proportional to $\langle r^2\rangle$. To study the system of interlocking rings the limit of zero width is taken. In Eq. (8.22),

$$|B_2(0,r)|_{\epsilon\to 0} = 2\pi\epsilon r \tag{8.23}$$

the area of a ring vanishes, but the connected component can still have an infinite diameter. The bound for an infinite cluster's diameter will be dependent on the average circumference of a ring, and the percolation threshold determined by the finiteness of $\lambda\langle 2\pi r\rangle$.

On a regular lattice, the Manhattan disks defined in Section (8.3) are replaced by Manhattan rings. The connected cluster size still has a diameter which can grow to infinity. In Figure (8.6) it is shown how a connected cluster is formed by solid Manhattan

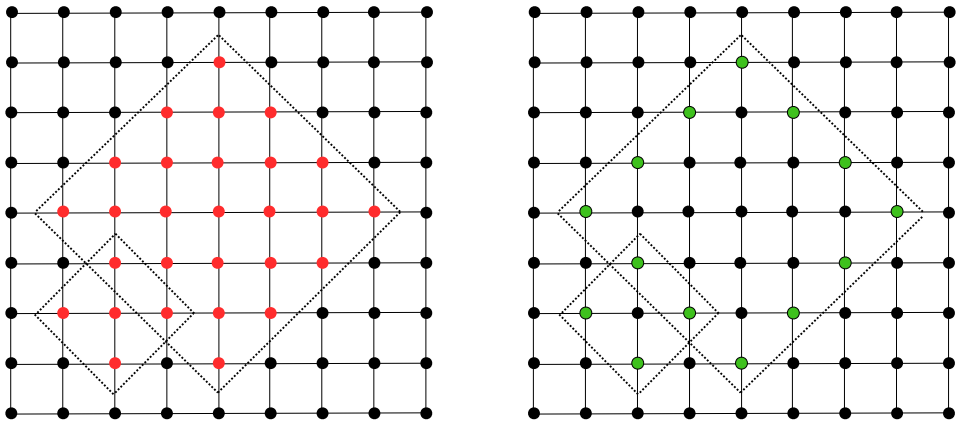

Figure 8.6: Percolation with lighter weight shapes on a regular lattice: (a) connected cluster formed by overlapping Manhattan disks, (b) connected cluster formed by overlapping Manhattan rings.

disks or by Manhattan rings. Previously the average animal size scaled with the area of a disk, $\langle n\rangle \propto \langle r^2\rangle$. For the regular lattice with lattice animals, but approximating their shape by Manhattan rings, the average animal size scales with the circumference of a ring: $\langle n\rangle \propto \langle r\rangle$. Now when the adjacency matrix results are applied to a regular lattice the dependence on $\langle n^2\rangle$ corresponds to $\langle r^2\rangle$.

8.8 Conclusions

The work discussed in this chapter derived methods for establishing the threshold for percolation in correlated systems. Three methods were discussed, all studying the threshold of percolation in systems where vertices are covered by lattice animals, rather than individually chosen to be open or closed. The size of the lattice animals was determined to be an important factor in establishing the percolation threshold, though the final section discussed whether the same results could be obtained with lighter weight objects.

First, the method of covered fraction, derived from continuum percolation models, was applied to regular lattices. The covered fraction was defined using objects with the same dimensionality as the lattice, specifically solid disks, and the results agreed with the continuum model results, a percolation threshold could be defined based on the covered area. However, applying these methods to random graphs or trees lead to limited usability. On a tree or random graph the number of points covered by a disk of radius scaled as z^r, leading to a percolation threshold that could only be defined for a distribution of objects with very low density.

The covered fraction approach was replaced by an approximation model for describing correlated percolation on random graphs. A random graph with lattice animals covering sets of vertices was approximated by a graph with additional vertices, accounting for the connections of the animal. The average degree of a graph with additional vertices was calculated and used to approximate the percolation threshold, following from previous known results for random graphs. For a simple system with only one animal species, it was seen that the average degree scaled with the size of the lattice animal.

Finally, the percolation threshold was studied from the adjacency matrix approach, focusing on how the connections generated by correlated percolation affected the average cluster size. An upper bound on the average cluster size was found, and included the uncorrelated percolation result plus a correction due to the lattice animal connections. The correction due to correlations was proportional to the animal size $\langle n^2 \rangle$.

Attempting to reconcile the random graph results and the continuum percolation results is hindered by the regular lattice. Covering the regular lattice by solid objects leads to a threshold which agrees with the continuum results, $\langle n \rangle \approx \langle r^2 \rangle$. However, applying the random graph results to the regular lattice would result in a threshold $\langle n^2 \rangle \approx \langle r^4 \rangle$. The use of solid disks or objects to approximate lattice animals overestimates the size of an animal and leads to a lower estimate on the percolation threshold.

In order for both the continuum results and the random graph results to be true on a regular lattice, the mechanism of how an infinite cluster is grown was investigated. As the growth of a connected component due to lattice animals only depends on the overlap of vertices located on the perimeter of the animal, we returned to the models of covered fraction in a continuum and regular lattice and investigated whether the same results could be obtained by objects with lower weight. These objects are closer in nature to the lattice animals on a random graph, which contain many points but do not cover much area. On the regular lattice, approximating lattice animals by empty rings lead to a percolation threshold $\langle n \rangle \approx \langle r \rangle$ which was dependent on the circumference (length) of the rings. The continuum and random graph results could now be connected, $\langle n^2 \rangle \approx \langle r^2 \rangle$.

Chapter 9

Conclusions

The work discussed in this dissertation developed the study of nonlinear effects in correlated systems along two directions: gradual changes in strongly driven many-body systems and the sudden changes of percolation. In the dynamical systems, the strong driving fields lead to gradual effects which resulted in dynamical stabilization, delocalization and band inversion. For the quantum systems which showed delocalization and band inversion, further driving by weak, static fields led to observation of a dynamical period doubling of Bloch oscillations, a dynamical insulator-metal transition, and higher harmonic generation.

Transport in quantum systems can also be described in terms of percolation on random graphs. In addition to the gradual changes of driven systems, the large-scale changes due to correlated effects were studied on random graphs. First, a connection between mean-field theory on a tree graph and random graphs was established. The mapping of a graph with cycles to a tree graph was done through a cycle-unwrapping scheme. Then, percolation by lattice animals was used to define correlated percolation on regular lattices and random graphs.

Turning to the phenomena of dynamical localization, which is possible under short pulse driving, and from the results that the behavior of a driven particle could be determined by an AC modified Floquet band, then the effects of driving a particle in an inverted band was studied. From the known effect of dynamical localization, which is a collapse of the Floquet band, the system driven into an inverted band was further driven and the possibility of third harmonic generation was studied. In the presence of a dissipative force (coupling to phonons) such frequency tripling was observed and additionally it was seen that the intensity of the frequency tripling was affected by phonon resonances. The phenomenological model established in Chapter (5) proved robust to a variety of phonon modes.

9.1 The driven Sine-Gordon model: dynamical stabilization

The analysis of strongly driven particle dynamics was made possible by analyzing the evolution of these driven systems along two separate time scales. This separation of time scales was first studied in the derivation of an effective potential for a strongly driven semiclassical system and was later applied to the evolution of Floquet states in strongly driven quantum systems. In the semiclassical Sine-Gordon model, it was established (refer to Chapter (3)) that strong driving will lead to period doubling and stabilization of a correlated system in previously unstable configurations.

In Chapter (3) the effects of a strong, rapidly-oscillating external driving force on a Sine-Gordon system was studied. The problem grew from the concept of dynamical stabilization in a vertical pendulum [1–3], where a pendulum is driving rapidly and oscillates with an equilibrium point above the support. It was determined that a horizontal series of coupled pendulums could exhibit dynamical stabilization. From the classical field theory of the Sine-Gordon model, the external driving field was first incorporated through time-dependent shift in the field variable $\varphi(x,t) = \varphi_0(x,t) + \xi(t)$, moving the system into a moving reference frame. In this lowest order approximation a renormalization of the system parameter $\widetilde{\lambda} = \lambda^2 J_0(F_0/\omega^2)$ based on the strength and frequency of the driving force (F_0, ω).

The next order expansion of the system expanded the field variable in a full series of the driving field harmonics. Once the full harmonic expansion was used in the Euler-Lagrange equations of motion, the slow and fast time dynamics were separated. Separating the field variable, $\varphi(x,t) = \varphi_0(x,t) + \xi(x,\omega,t)$, the function $\varphi_0(x,t)$ evolved gradually over each period of the driving force, while the function $\xi(x,\omega,t)$ rapidly oscillated. However, the form of ξ was chosen such that the average value $\langle\xi\rangle$ vanished over the driving period.

To fully evaluate the effective potential, the coefficients of the harmonic series were determined by a set of self-consistent equations. To lowest order they were assumed to be stationary. First order corrections were also found. In the final expression of the effective potential, it was seen that the driven system has a dominant term proportional to $\cos(\varphi_0)$, the same periodicity of the undriven potential, and a secondary term proportional to $\cos(2\varphi_0)$. The amplitudes of the dominant and secondary terms depend on the driving amplitude and frequency and when these parameters are tuned to $F_0/\omega^2 \approx 2.4048$ the dominant term can be suppressed.

When working with a stationary solution of the Sine-Gordon model, the equa-

tion of motion can be recast as a particle moving in the Sine-Gordon potential. This reasoning was extended to the driven model to explore the dynamics. From the effective potential it is seen that as the driving amplitude and frequency are tuned closer to 2.4048 the particle will travel slower as it passes through the inverted position (relative angle $\theta = \pi$). Eventually, when the dominant term is suppressed, the system develops a stable point at the inverted position. The evolution of the stable point at the inverted position implies dynamical stabilization would be possible in the coupled pendulum system.

The solution of the un-driven Sine-Gordon model is a soliton, a twisted waveform that corresponds to a set of pendulum rotated from $\theta = 0$ through $\theta = \pi$ and over to $\theta = 2\pi$. With minimal or no driving only a few pendulum are at the $\theta = \pi$ position. As the system is driven and tuned toward the inverted system the number of pendulum that can be kept in the inverted position is increased. Previous studies of driven solitons have established the concept of a π-soliton [14, 149], possible for strongly driven Sine-Gordon systems with high driving frequencies. In our work we study the possibility of a system to generate two π-solitons. We identify the driving parameters that lead to period doubling in the effective potential as the same that generate two π-soliton solutions.

The stationary waveform in a system driven with parameters in the period doubling regime was solved for numerically. Since the driven Sine-Gordon model can exhibit chaotic motion a slowly decaying dissipation term was included and the initial state was taken to be a straight line. By taking a time average over the period of the driving force, the slow dynamics could be isolated. Any effects due to the driving force accumulates over several periods of the driving force.

It was seen that with a dissipation term with weak initial amplitude ($\alpha_0 = 0.1$) that slowly decays a soliton form could be generated with a significant fraction of pendulum stable in the $\theta = \pi$ position. This waveform emerges after many periods of the driving force ($t > 10\tau$) and is stable once established.

The width of the driven two π-soliton can be interpreted as a broadening of a domain wall in a ferromagnetic system. From the results of the classical field theory, and based on the connection of the quantized Sine-Gordon model and fermionic systems [12, 35, 138], the next system studied was a correlated electron system.

9.2 Driven two-band model: dynamical delocalization

The hyperbolic shape and gapped spectrum of the Sine-Gordon soliton and the interacting Luttinger liquid led to studies of strongly driven many-body systems (refer

to Chapter (4)). Period doubling in the Sine-Gordon model was due to the suppression of the term λ, which corresponded to a reduction in the energy spectrum gap. It was seen that for strong amplitude, high-frequency AC field driving, the width of an interaction-induced gap in a two-band model of spinless fermions can be reduced and suppressed. Additionally, it was seen that a particle driven through the regime of gap closure will show dynamics of the suppressed gap band. However, the length of driving times required to observe such effects leaves these results vulnerable to heating effects, which were not included in the model.

Three such models were investigated, a continuum model and two models on a lattice. The gap-suppression was observed in the lattice models but not in the continuum model. Using the Hartree-Fock approximation, all three models were systems of spinless fermions, with a small interaction-induced gap, and driven with a strong external field. The strong driving field was incorporated through a simple gauge transformation, the gap was treated as a perturbation and an interaction representation of the systems were found, and used to define perturbative expansions of the time-evolution operators $U(t)$. The effects of the strong driving field were observed in the gradual changes to the Floquet spectrum. Gap suppression is identified by the suppression of the first-order term in the perturbation series expansion of $U(t)$, defined by the time-averaged interaction Hamiltonian.

Driving of electron systems with rapidly oscillating forces has been extensively studied as a system that demonstrates localization of particles. Two such phenomena are known: coherent destruction of tunneling (CDoT) and dynamical localization (DL). In the Floquet representation, CDoT is a perturbative effect that is linked to the suppression of tunneling between sites. For a system with degenerate energy levels, a perturbation which leads to level splitting can be suppressed through strong AC field driving [53]. In contrast, DL is an exact effect where the bandwidth of a driven system is effectively suppressed. This band collapse leads to suppression of a particle's kinetic energy [53]. The main results known for quantum systems in strong AC driving fields are renormalization effects, either gap renormalization or band renormalization. The first effect was the basis for the studies of strongly driven two-band systems and the second is the basis for the study of strongly driven single-band systems.

Building from the phenomena of CDoT, we investigate the suppression of a perturbation in a two-band system. In contrast to CDoT, where the perturbation suppressed the level splitting and results in localization, the weak perturbation we considered is due to interactions between electrons. The result of this interaction is a gap opening at band crossings, leading to localization in the absence of driving. Through

the strong driving force it was seen that in the Floquet representation, a small gap can be suppressed, leading to delocalization of particles.

The first model was a continuum, many-body system consisting of nearly free electrons weakly bound to ions of a one-dimensional lattice. In the absence of perturbations, the electrons travelled in parabolic energy bands. With the addition of interactions, a gap opened where neighboring wells overlap. The continuum model provided an initial investigation into how a small gap can be suppressed. In the first order perturbation term, the interaction Hamiltonian is dependent on the sum over Floquet modes, and was found to have a singularity in the $N = 0$ term. The presence of such a singularity lead to an approximation of $\langle H_I \rangle$, since the $N = 0$ term would dominate. When this term was suppressed, the gap was effectively suppressed, leading to the condition for gap closure: $J_0(F_0 k/m\omega^2) = 0$.

Once it was established that gap closure could exist, the continuum model was not studied further. There were many aspects of the parabolic spectrum which rendered it of limited use: primarily, the ambiguous definition of a bandwidth in the parabolic system lead to difficulty in showing gap closure except for very large driving frequencies. In the Floquet spectrum, multiple bands would overlap and the condition that a particle scatter within a single band ($N = 0$ term) could not be met. An additional complication was due to the singularity in the first order perturbation term. While such a singularity was useful in identifying the driving parameters which lead to gap closure, driving the system even slightly away from those parameters lead to significant increase in the gap size. This lead to a narrow range of driving amplitudes that would lead to reduction of a gap. Further study of the parabolic well model was not done.

The next models were Luttinger liquids, lattice models of spinless fermions with interaction-induced gaps. Two energy spectra were considered, sinusoidal bands (corresponding to a tight-binding model) and linear (corresponding to the linearized system near the Fermi points). From the interaction representation it was established that gap suppression would be possible. For the linear spectrum an exact expression for gap suppression was derived. For the sinusoidal spectrum a closed form could not be found. Further studies of these systems was done through numerical simulation.

Numerical simulations of all three systems involved exact evaluation of the time-evolution operator $U(t)$. Integrating for $U(t)$ using the original, time-dependent Hamiltonian $H_{sys}(t)$, lead to an expression which when diagonalized would given the Floquet spectrum of the driven system. In all three systems, gap closure was observed (see Figures (4.6), (4.11)). Additionally, the gap closure was observed in the Floquet spectrum of the lattice models (see Figures (4.7), (4.9)). Numerical simulation of the

perturbative expansion of $U(t)$ was also done for the lattice models. For a perturbation series up to second order, it was seen that gap closure was observed for both systems and showed strong agreement with the exact results (see Figure (4.8), (4.10)).

The expected dynamics of a particle in a sinusoidal potential were used to further establish the existence of the gap closure. In a tight-binding model with a sinusoidal spectrum, a weak DC field was added to the AC field driving. A particle driven by such a field is expected to undergo Bloch oscillations with a period determined by the Brillouin zone's periodicity. The DC field was applied to the system first, and the motion of the particle exhibited Bloch oscillations as expected. While the DC field was present, the amplitude of the AC field was gradually turned on. As the gapped spectrum was driven into a gapless spectrum, it was observed that the Bloch oscillations underwent a period doubling, consistent with the existence of gap closure.

The second investigation of the gap closure was done with a collection of electrons in a gapped sinusoidal potential. When the system was initially prepared in an insulating state, with a completely filled band below the gap. Driving such a system resulted in a zero net current, as expected. When the driving field was supplanted with an AC field, it was seen that a non-zero current could be generated. When the gap is suppressed, a band which is initially a band insulator is driven into a metallic system.

Gap closure was investigated for three systems, all which were closed. In the dynamics of electrons in bands driven through a gap closure, the effects of Bloch oscillation period doubling, or nonzero net current were observed only for very long driving times. This was necessary to ensure that the system could reach a quasi-stationary state. However, the effects of long driving times with very strong fields cannot be sufficiently explained without the addition of heating. It is likely such a system driven to a gapless spectrum would be beset by runaway heating, and the DC effects would become unobservable.

9.3 Driven single-band model: dynamical harmonic generation

The two-band model demonstrated that gap closure could be achieved with long driving times. However such systems would likely be affected by heating, which wasn't included in the models. The next driven system investigated included phonon scattering and also investigated an effect which would be achievable with shorter driving pulses: harmonic generation in band inverted systems. As the two-band effect was inspired by CDoT effects, the band inverted systems are a continuation of the physics involved

in dynamical localization. DL is due to complete band suppression in the Floquet spectrum, leading to a zero mean for a particle's kinetic energy. The renormalized bandwidth is proportional to the Bessel function $J_0(z)$ and suppression occurs at the root. In the single-band model, we considered a system which is driven past the point of band suppression, and into the regime where $J_0(z) < 0$.

A single conduction band in a semiconductor was driven by an external AC field and dissipation through phonon scattering was present. In the Floquet quasi-energy spectrum the driving field leads to a renormalization of the bandwidth. Dynamical localization occurs when the Floquet energies have effectively flat bands and in our work we focused on driving amplitudes and frequencies beyond the localization regime. The parameters for an AC field required to invert the band were determined from the Floquet quasi-energies. Since the inversion of a band requires high-amplitude and high-frequency fields, the dynamics of an electron in an inverted conduction band were derived from non-equilibrium Green's functions. The driving fields were incorporated through a quasi-periodic phase term $\phi_k(t)$. This phase lead to a redefinition of the electron operators and recast the Green's functions and self-energy functions in terms of a set of slow and fast time scales. Most importantly, it lead to the identification of terms which would evolve gradually over the driving period. It was these slowly evolving terms which provided a connection to a quantum kinetic equation, which was used to determine the driven current of the system.

When driven by both an AC and DC field, the conduction band system would drive an electrical current dependent on the inverted band. Based on harmonic analysis of the generated current: in the absence of scattering it was expected that an inverted band system could lead to a suppression of the fundamental driving field harmonic, and the amplification of higher harmonics of the driving field. Specifically the amplification of the third harmonic was studied.

The introduction of phonon scattering would result in a broadening of the electron distribution function, leading to a reduction in the higher harmonic generation. When phonon scattering was introduced, the amplification of higher harmonics was observed and not completely destroyed by thermalization. Additionally, it was seen that the total amplification of the third harmonic did not depend linearly on the initial bandwidth, which was expected. Rather the amplification had a dependence on the renormalized bandwidth and depending on the driving frequency a dramatic flatting of the band was possible when phonon scattering was resonant. The derivation was modified to include different phonon modes, and the third harmonic amplification was still observed.

Experimental parameters for a physical system which could be used to study higher harmonic generation were found. By designing a modulated nanowire which consists of alternating regions of InAs and InP, the initial bandwidth could be tuned. The remaining challenge would be to establish a device which could suspend such wires close enough to a substrate, such that the phonon modes responsible for scattering were surface modes of the substrate. The inclusion of phonon scattering was fundamental to dissipating the heat generated by the strong driving field. Due to the high-amplitude of the driving force and the likelihood of runaway heating, continuous driving of such a device would not be feasible. Instead, short pulsed driving fields are needed.

The harmonic generation in an inverted band was the last system studied with strong driving fields. In the systems studied, it was seen that strong driving fields result in significant changes in the dynamics of correlated systems. For the classical system, the results were the (partial) inversion of coupled linear pendulums. For the two-band system, the results were delocalization of electrons due to suppression of interaction-induced gaps. In the single band, the results were generation of harmonics as electrons reach equilibrium in an inverted band.

Finally, regarding the discussion of dynamical effects in quantum systems: the structure of the renormalized Floquet spectrum was integral to these results. The dynamical effects described in this dissertation are dependent on a large driving frequency, larger than the gap or the original system bandwidth. This results in the dominance of the fundamental Floquet mode, meaning an electron would most likely scatter within a single Floqeut band, rather than between bands. When there was overlap between bands, as in the parabolic well spectrum in Section (4.2), gap suppression was difficult to obtain.

9.4 Percolation on random graphs

Percolation theory focuses on the growth of clusters which are of infinite size, length or contain a significant fraction of points in a system. The random nature by which these clusters are generated leads to difficulty in determining a threshold for the percolation transition. A mean-field approach is applicable to tree graphs, where the lack of cycles reduces the possibility of a branch returning to itself. Through a process of "single cycle unwrapping," we established a mapping between graphs with cycles and an associated tree graph. On this tree graph an extended mean-field theory was defined, through the connectivity of the edges.

In the study of percolation on trees, the mean-field result leads to a strong

approximation to the percolation threshold. On random graphs the presence of loops leads to complications when describing the probability a process grows to infinite size, since it is possible to connect back to itself. We established a lower bound on the percolation threshold of a graph based on an unwrapping process call "single cycle unwrapping." Using this method, a graph of undirected bonds was extended into a quasi-transitive graph by removing bridge bonds of cycles and re-directing them to a subgraph defined by the graph. The process of cycle unwrapping defines a quasi-transitive graph from the original graph. By connecting multiple copies of an unwrapped graph, it was possible to remove all cycles.

A lower bound on the percolation threshold was established through an extended mean-field calculation. This was defined on the graph resulting from unwrapping all cycles, and using the probability of an infinite branch growing from an arbitrary vertex. Branch growth is hindered by closed vertices and those connected to finite branches. The connections from a given vertex also included second generation connections.

It was seen that through the adjacency matrix a percolation threshold can be established by determining conditions for a finite average cluster size. These results were used to study correlated percolation.

9.5 Correlated percolation

Correlated percolation was defined as a random process which affects connected subsets of vertices simultaneously. Rather than defining a process in terms of probabilities that single sites are open or closed, the probability that groups of connected sites are all open simultaneously is introduced and defined through the placement of lattice animals on a graph. The correlated percolation process was described in three cases: correlated percolation on a lattice, percolation on a random graph with lattice animals only, and percolation on a random graph with site percolation and lattice animals processes. In these three examples the exact percolation threshold was not determined, rather a lower bound on the threshold was established.

Based on the methods used in continuum percolation, the correlated percolation model was described by overlapping spheres on a given lattice or graph. Following methods which defined a threshold of percolation through the continuum system's average covered volume, we used analogous arguments to define an average covered volume of a discrete system. On a regular lattice, such an approach lead to covered volumes which scaled as $\langle n^2 \rangle$, the average size of a sphere in the discrete space. A non-trivial percolation threshold can be defined from this covered volume.

However, the same approach lead to limited results when applied to random graphs or trees. On such networks, the volume of a sphere scales exponentially as its radius increases. This results in a vanishingly small percolation threshold. On a random tree or graph percolation was considered to occur by lattice animals only, and the percolation threshold was defined using the average degree of the graph. To account for the long-range connections created by lattice animals, the average degree was defined using an auxiliary vertex model, which replaced animals by a single vertex of high connectivity.

To define a percolation threshold in a system which has both site (uncorrelated) and correlated percolation, the average length of a path connected to an arbitrary vertex was investigated. If such a path can be bounded, the system is below the percolation threshold. Using a modified adjacency matrix (which included contributions due to lattice animals) allowed for such a bound to be defined. Currently this method was only applied to fixed-degree or degree limited graphs. On these specific examples, when correlations are added the percolation threshold due to site percolation has a correction which is proportional to $\langle n^2 \rangle$, the average lattice animal size.

The more exact bound established through the average cluster size, calculated with the adjacency matrix, leads to a threshold which is dependent on $\langle n^2 \rangle$, which agrees with the approximation based on auxiliary vertices. On random graphs, the lattice animals which lead to correlated percolation contain many vertices, but do not cover a large area. The animal shape which dominates the cluster growth is branch-like is shape.

Applying this result to a regular lattice covered by disks would result in a threshold dependent on $\langle r^4 \rangle$. On a regular lattice, the approximation of lattice animals as disks over-estimates the number of points needed to grow a cluster of infinite length and results in a lower percolation threshold. In order for the continuum results and the random graph results to agree, the regular graph is covered with shapes similar to the random graph animals. An empty disk (ring) on the regular lattice would contain many points but cover a small amount of area. The percolation threshold on a regular lattice is re-derived using empty object to cover many points but a minimal amount of area. A connected cluster of the same size can be derived as in the case of solid disks, but the number of points needed is dependent on the circumference of a ring, $\langle n \rangle \propto \langle r \rangle$. Connecting the continuum and random graph results is now possible, the dependence $\langle n^2 \rangle = \langle r^2 \rangle$ holds.

The studies of correlated percolation establish a connection between continuum systems and discrete systems represented by regular lattices or random graphs.

Randomly distributed lattice animals on a regular lattice were approximated as random sized disks. This established the dependence of the percolation threshold on the average animal size. Applying this approach to random graphs led to a trivially small percolation bound. Through the auxiliary vertex model,which treated a random shape placed on a random graph as a single (open vertex) of high connectivity, a lower bound on the percolation threshold for a random graph was found which also showed a dependence on the average animal size. The results on a random graph were further refined through an auxiliary matrix treatment. The disagreement between the regular lattice and random graph was rectified by covering the regular lattice with lower weight objects. By defining random shapes of lighter weight on a lattice, a bound on the average connected cluster size can be established in terms of the average random shape size, which maps to the bound on the average shape size in continuum systems.

Bibliography

[1] Andrew Stephenson. Xx. On induced stability. *Philosophical Magazine Series 6*, 15(86):233–236, 1908.

[2] P. Kapitza. Dynamic stability of a pendulum when its point of suspension vibrates. *JETP*, 21:588–592, 1951.

[3] LD Landau and EM Lifshitz. *Mechanics*, volume 1 of *Course Of Theoretical Physics*. Butterworth-Heinemann, 1976.

[4] D. J. Acheson. A pendulum theorem. *Proceedings of the Royal Society of London. Series A: Mathematical and Physical Sciences*, 443(1917):239–245, 1993.

[5] Anindita Shit, Sudip Chattopadhyay, and Jyotipratim Ray Chaudhuri. Time-independent description of rapidly driven systems in the presence of friction: Multiple scale perturbation approach. *Chaos: An Interdisciplinary Journal of Nonlinear Science*, 22(1):–, 2012.

[6] Julia G. Fenn, Derek A. Bayne, and Bruce D. Sinclair. Experimental investigation of the effective potential of an inverted pendulum. *American Journal of Physics*, 66(11):981–984, 1998.

[7] Eugene I. Butikov. On the dynamic stabilization of an inverted pendulum. *American Journal of Physics*, 69(7):755–768, 2001.

[8] Gustavo J Mata and E Pestana. Effective hamiltonian and dynamic stability of the inverted pendulum. *European Journal of Physics*, 25(6):717, 2004.

[9] H. Goldstein, C. Poole, and J. Safko. *Classical Mechanics*. Pearson Education, 3 edition, 2002.

[10] G. Costabile, R. D. Parmentier, B. Savo, D. W. McLaughlin, and A. C. Scott. Exact solutions of the sine-gordon equation describing oscillations in a long (but finite) josephson junction. *Applied Physics Letters*, 32(9):587–589, 1978.

[11] O.M. Braun and Y.S. Kivshar. *The Frenkel-Kontorova Model: Concepts, Methods, and Applications*. Physics and Astronomy Online Library. Springer, 2004.

[12] Sidney Coleman. Quantum sine-gordon equation as the massive thirring model. *Phys. Rev. D*, 11:2088–2097, Apr 1975.

[13] R Rajaraman. *Solitons and instantons: an introduction to solitons and instantons in quantum field theory*. North-holland Amsterdam, 1982.

[14] Vadim Zharnitsky, Igor Mitkov, and Mark Levi. Parametrically forced sine-gordon equation and domain wall dynamics in ferromagnets. *Phys. Rev. B*, 57:5033–5035, Mar 1998.

[15] L.D. Landau. The theory of a fermi liquid. *Soviet Physics JETP*, 3(6):920–925, 1957.

[16] L.D. Landau. Oscillations in a fermi liquid. *Soviet Physics JETP*, 5(1):101–108, 1957.

[17] L.D. Landau. On the theory of the fermi liquid. *Soviet Physics JETP*, 35(1):70–74, 1959.

[18] R. K. Nesbet. Approximate methods in the quantum theory of many-fermion systems. *Rev. Mod. Phys.*, 33:28–36, Jan 1961.

[19] Attila Szabo and Neil S Ostlund. *Modern quantum chemistry: introduction to advanced electronic structure theory*. Courier Dover Publications, 2012.

[20] John Clarke Slater. *The self-consistent field for molecules and solids*, volume 4. McGraw-Hill New York, 1974.

[21] J. C. Slater. A simplification of the Hartree-Fock method. *Phys. Rev.*, 81:385–390, Feb 1951.

[22] Walter Kohn and Lu Jeu Sham. Self-consistent equations including exchange and correlation effects. *Physical Review*, 140(4A):A1133, 1965.

[23] G. Beni. Instability of the uniform antiferromagnetic chain. ii. Heisenberg interaction in the Hartree-Fock approximation. *The Journal of Chemical Physics*, 58(8):3200–3202, 1973.

[24] Junjiro Kanamori. Electron correlation and ferromagnetism of transition metals. *Progress of Theoretical Physics*, 30(3):275–289, 1963.

[25] N. F. MOTT. Metal-insulator transition. *Rev. Mod. Phys.*, 40:677–683, Oct 1968.

[26] John Hubbard. Electron correlations in narrow energy bands. *Proceedings of the Royal Society of London. Series A. Mathematical and Physical Sciences*, 276(1365):238–257, 1963.

[27] John Hubbard. Electron correlations in narrow energy bands. iii. an improved solution. *Proceedings of the Royal Society of London. Series A. Mathematical and Physical Sciences*, 281(1386):401–419, 1964.

[28] Masatoshi Imada, Atsushi Fujimori, and Yoshinori Tokura. Metal-insulator transitions. *Rev. Mod. Phys.*, 70:1039–1263, Oct 1998.

[29] Florian Gebhard. *The Mott Metal-Insulator Transition: Models and Methods*. Springer Tracts in Modern Physics. Springer-Verlag, 1997.

[30] Thierry Giamarchi. Quantum physics in one dimension, 2004.

[31] J Voit. One-dimensional fermi liquids. *Reports on Progress in Physics*, 58(9):977, 1995.

[32] J. M. Luttinger. An exactly soluble model of a manyfermion system. *Journal of Mathematical Physics*, 4(9):1154–1162, 1963.

[33] F D M Haldane. 'luttinger liquid theory' of one-dimensional quantum fluids. i. properties of the luttinger model and their extension to the general 1d interacting spinless fermi gas. *Journal of Physics C: Solid State Physics*, 14(19):2585, 1981.

[34] Daniel C. Mattis and Elliott H. Lieb. Exact solution of a manyfermion system and its associated boson field. *Journal of Mathematical Physics*, 6(2):304–312, 1965.

[35] Jan von Delft and Herbert Schoeller. Bosonization for beginners refermionization for experts. *Annalen der Physik*, 7(4):225–305, 1998.

[36] Gao Xianlong, M. Rizzi, Marco Polini, Rosario Fazio, M. P. Tosi, V. L. Campo, and K. Capelle. Luther-emery phase and atomic-density waves in a trapped fermion gas. *Phys. Rev. Lett.*, 98:030404, Jan 2007.

[37] Felix Bloch. Quantum mechanics of electrons in crystal lattices. *Z. Phys*, 52:555–600, 1928.

[38] J. B. Krieger and G. J. Iafrate. Time evolution of bloch electrons in a homogeneous electric field. *Phys. Rev. B*, 33:5494–5500, Apr 1986.

[39] Gregory H. Wannier. Wave functions and effective hamiltonian for bloch electrons in an electric field. *Phys. Rev.*, 117:432–439, Jan 1960.

[40] Emilio E Mendez and Gérald Bastard. Wannier-stark ladders and bloch oscillations in superlattices. *Physics Today*, 46(6):34–42, 2008.

[41] Markus Glück, Andrey R Kolovsky, and Hans Jürgen Korsch. Wannier–stark resonances in optical and semiconductor superlattices. *Physics Reports*, 366(3):103–182, 2002.

[42] Immanuel Bloch. Ultracold quantum gases in optical lattices. *Nature Physics*, 1(1):23–30, 2005.

[43] O Morsch, JH Müller, M Cristiani, D Ciampini, and E Arimondo. Bloch oscillations and mean-field effects of bose-einstein condensates in 1d optical lattices. *Physical Review Letters*, 87(14):140402, 2001.

[44] SR Wilkinson, CF Bharucha, KW Madison, Qian Niu, and MG Raizen. Observation of atomic wannier-stark ladders in an accelerating optical potential. *Physical review letters*, 76(24):4512, 1996.

[45] Qian Niu, Xian-Geng Zhao, GA Georgakis, and MG Raizen. Atomic landau-zener tunneling and wannier-stark ladders in optical potentials. *Physical review letters*, 76(24):4504, 1996.

[46] T. P. Grozdanov and M. J. Raković. Quantum system driven by rapidly varying periodic perturbation. *Phys. Rev. A*, 38:1739–1746, Aug 1988.

[47] Saar Rahav, Ido Gilary, and Shmuel Fishman. Time independent description of rapidly oscillating potentials. *Phys. Rev. Lett.*, 91:110404, Sep 2003.

[48] Saar Rahav, Eli Geva, and Shmuel Fishman. Time-independent approximations for periodically driven systems with friction. *Phys. Rev. E*, 71:036210, Mar 2005.

[49] Anindita Shit, Sudip Chattopadhyay, and Jyotipratim Ray Chaudhuri. Controlling activated processes of nonadiabatically, periodically driven dynamical systems: A multiple scale perturbation approach. *The Journal of Chemical Physics*, 136(23):–, 2012.

[50] Jon H Shirley. Solution of the schrödinger equation with a hamiltonian periodic in time. *Physical Review*, 138(4B):B979, 1965.

[51] Hideo Sambe. Steady states and quasienergies of a quantum-mechanical system in an oscillating field. *Phys. Rev. A*, 7:2203–2213, Jun 1973.

[52] André Nauts and Robert E. Wyatt. Theory of laser-molecule interaction: The recursive-residue-generation method. *Phys. Rev. A*, 30:872–883, Aug 1984.

[53] Milena Grifoni and Peter Hänggi. Driven quantum tunneling. *Physics Reports*, 304(5):229–354, 1998.

[54] F. Grossmann, T. Dittrich, P. Jung, and P. Hänggi. Coherent destruction of tunneling. *Phys. Rev. Lett.*, 67:516–519, Jul 1991.

[55] H Lignier, C Sias, D Ciampini, Y Singh, A Zenesini, O Morsch, and E Arimondo. Dynamical control of matter-wave tunneling in periodic potentials. *Physical review letters*, 99(22):220403, 2007.

[56] G Della Valle, M Ornigotti, E Cianci, V Foglietti, P Laporta, and S Longhi. Visualization of coherent destruction of tunneling in an optical double well system. *Physical review letters*, 98(26):263601, 2007.

[57] D. H. Dunlap and V. M. Kenkre. Dynamic localization of a charged particle moving under the influence of an electric field. *Phys. Rev. B*, 34:3625–3633, Sep 1986.

[58] Martin Holthaus. Collapse of minibands in far-infrared irradiated superlattices. *Phys. Rev. Lett.*, 69:351–354, Jul 1992.

[59] KW Madison, MC Fischer, RB Diener, Qian Niu, and Mark G Raizen. Dynamical bloch band suppression in an optical lattice. *Physical review letters*, 81(23):5093, 1998.

[60] Yosuke Kayanuma and Keiji Saito. Coherent destruction of tunneling, dynamic localization, and the landau-zener formula. *Phys. Rev. A*, 77:010101, Jan 2008.

[61] N. Tsuji, T. Oka, P. Werner, and H. Aoki. Dynamical band flipping in fermionic lattic systems: An ac-field-driven change of the interaction from repulsive to attractive. *Phys. Rev. Lett.*, 106:236401–236405, Jun 2011.

[62] F. H. M. Faisal and J. Z. Kamiński. Floquet-bloch theory of high-harmonic generation in periodic structures. *Phys. Rev. A*, 56, 1997.

[63] A. F. Kemper, B. Moritz, J. K. Freericks, and T. P. Devereaux. Theoretical description of high-order harmonic generation in solids. *New Journal of Physics*, 15, 2013.

[64] S. Ghimire, A. D. DiChiara, E. Sistrunk, P. Agostini, L. F. DiMauro, and D. A. Reis. Observation of high-order harmonic generation in a bulk crystal. *Nature Physics*, 7, 2011.

[65] Netanel H Lindner, Gil Refael, and Victor Galitski. Floquet topological insulator in semiconductor quantum wells. *Nature Physics*, 7(6):490–495, 2011.

[66] Y. H. Wang, H. Steinberg, P. Jarillo-Herrero, and N. Gedik. Observation of floquet-bloch states on the surface of a topological insulator. *Science*, 342(6157):453–457, 2013.

[67] Y. Mizumoto and Y. Kayanuma. Role of a nontrivial quantum phase in the dynamical band gap collapse. *Phys. Rev. A*, 86:035601, Sep 2012.

[68] Zhen Yao, Charles L Kane, and Cees Dekker. High-field electrical transport in single-wall carbon nanotubes. *Physical Review Letters*, 84(13):2941, 2000.

[69] A Leitenstorfer, S Hunsche, J Shah, MC Nuss, and WH Knox. Femtosecond high-field transport in compound semiconductors. *Physical Review B*, 61(24):16642, 2000.

[70] H. Haug and A. P. Jauho. *Quantum kinetics in transport and optics of semiconductors*. Springer: New York, 2 edition, 2008.

[71] Mukunda P Das and Frederick Green. Nonequilibrium mesoscopic transport: a genealogy. *Journal of Physics: Condensed Matter*, 24(18):183201, 2012.

[72] L. V. Keldysh. Ionization in the field of a strong electromagnetic wave. *Zh. Eksp. Teor. Fiz.*, 47, 1964.

[73] J. Rammer and H. Smith. Quantum field-theoretical methods in transport theory of metals. *Rev. Mod. Phys.*, 58, 1986.

[74] Dietrich Stauffer and Amnon Aharony. *Introduction to percolation theory*. Taylor and Francis, 1991.

[75] R.K. Pathria. *Statistical Mechanics*. Elsevier Science, 2011.

[76] Neil Ashcroft and David Mermin. *Solid State Physics*. Brooks-Cole, 1976.

[77] Pierre Weiss. L'hypothèse du champ moléculaire et la propriété ferromagnétique. *J. Phys. Theor. Appl.*, 6(1):661–690, 1907.

[78] H. A. Bethe. Statistical theory of superlattices. *Proceedings of the Royal Society of London. Series A, Mathematical and Physical Sciences*, 150(871):552–575, 1935.

[79] Shigetoshi Katsura and Makoto Takizawa. Bethe lattice and the bethe approximation. *Progress of Theoretical Physics*, 51(1):82–98, 1974.

[80] VI Litvinov and VK Dugaev. Ferromagnetism in magnetically doped iii-v semiconductors. *Physical review letters*, 86(24):5593, 2001.

[81] T. Jungwirth, Jairo Sinova, J. Mašek, J. Kučera, and A. H. MacDonald. Theory of ferromagnetic (iii,mn)v semiconductors. *Rev. Mod. Phys.*, 78:809–864, Aug 2006.

[82] Hannes Raebiger, Maria Ganchenkova, and Juhani von Boehm. Diffusion and clustering of substitutional mn in (ga,mn)as. *Applied Physics Letters*, 89(1):–, 2006.

[83] A. Kaminski and S. Das Sarma. Magnetic and transport percolation in diluted magnetic semiconductors. *Phys. Rev. B*, 68:235210, Dec 2003.

[84] Scott Kirkpatrick. Percolation and conduction. *Rev. Mod. Phys.*, 45:574–588, Oct 1973.

[85] G P Triberis and L R Friedman. A percolation treatment of the conductivity for the high-temperature small-polaron hopping regime in disordered systems. *Journal of Physics C: Solid State Physics*, 14(31):4631, 1981.

[86] B. J. Last and D. J. Thouless. Percolation theory and electrical conductivity. *Phys. Rev. Lett.*, 27:1719–1721, Dec 1971.

[87] M. Pollak. A percolation treatment of dc hopping conduction. *Journal of Non-Crystalline Solids*, 11(1):1 – 24, 1972.

[88] D.J. Thouless. Electrons in disordered systems and the theory of localization. *Physics Reports*, 13(3):93 – 142, 1974.

[89] K. D. Benkstein, N. Kopidakis, J. van de Lagemaat, and A. J. Frank. Influence of the percolation network geometry on electron transport in dye-sensitized titanium dioxide solar cells. *The Journal of Physical Chemistry B*, 107(31):7759–7767, 2003.

[90] N. Pinto, L. Morresi, M. Ficcadenti, R. Murri, F. D'Orazio, F. Lucari, L. Boarino, and G. Amato. Magnetic and electronic transport percolation in epitaxial $ge_{1-x}mn_x$ films. *Phys. Rev. B*, 72:165203, Oct 2005.

[91] L. Bergqvist, O. Eriksson, J. Kudrnovský, V. Drchal, P. Korzhavyi, and I. Turek. Magnetic percolation in diluted magnetic semiconductors. *Phys. Rev. Lett.*, 93:137202, Sep 2004.

[92] W. Q. Chen, S. T. Lim, C. H. Sim, J. F. Bi, K. L. Teo, T. Liew, and T. C. Chong. Optical, magnetic, and transport behaviors of ge1xmnxte ferromagnetic semiconductors grown by molecular-beam epitaxy. *Journal of Applied Physics*, 104(6):–, 2008.

[93] SAIFUL IZWAN ABD RAZAK, SHARIF HUSSEIN SHARIF ZEIN, and Abdul Latif Ahmad. Mno2-filled multiwalled carbon nanotube/polyaniline nanocomposites: effect of loading on the conduction properties and its percolation threshold. *Nano*, 6(01):81–91, 2011.

[94] CP Collier, RJ Saykally, JJ Shiang, SE Henrichs, and JR Heath. Reversible tuning of silver quantum dot monolayers through the metal-insulator transition. *Science*, 277(5334):1978–1981, 1997.

[95] J. Kassim, Christopher A. Nolph, Matthieu Jamet, Petra Reinke, and Jerrold A. Floro. Silicide formation during mn doping of ge/si (001) self-assembled quantum dots. *Journal of Materials Research*, 28:3210–3217, 12 2013.

[96] Sasha Stankovich, Dmitriy A. Dikin, Richard D. Piner, Kevin A. Kohlhaas, Alfred Kleinhammes, Yuanyuan Jia, Yue Wu, SonBinh T. Nguyen, and Rodney S. Ruoff. Synthesis of graphene-based nanosheets via chemical reduction of exfoliated graphite oxide. *Carbon*, 45(7):1558 – 1565, 2007.

[97] Fangming Du, John E. Fischer, and Karen I. Winey. Effect of nanotube alignment on percolation conductivity in carbon nanotube/polymer composites. *Phys. Rev. B*, 72:121404, Sep 2005.

[98] CS Suchand Sangeeth, Pablo Jiménez, Ana M Benito, Wolfgang K Maser, and Reghu Menon. Charge transport properties of water dispersible multiwall carbon nanotube-polyaniline composites. *Journal of applied physics*, 107(10):103719, 2010.

[99] A.J Nozik. Quantum dot solar cells. *Physica E: Low-dimensional Systems and Nanostructures*, 14(12):115 – 120, 2002.

[100] Albert-László Barabási. The network takeover. *Nature Physics*, 8(1):14–16, 2012.

[101] Sergey V Buldyrev, Roni Parshani, Gerald Paul, H Eugene Stanley, and Shlomo Havlin. Catastrophic cascade of failures in interdependent networks. *Nature*, 464(7291):1025–1028, 2010.

[102] James P. Gleeson. Cascades on correlated and modular random networks. *Phys. Rev. E*, 77:046117, Apr 2008.

[103] Sergey N Dorogovtsev, Alexander V Goltsev, and José FF Mendes. Critical phenomena in complex networks. *Reviews of Modern Physics*, 80(4):1275, 2008.

[104] Romualdo Pastor-Satorras and Alessandro Vespignani. Epidemic dynamics and endemic states in complex networks. *Phys. Rev. E*, 63:066117, May 2001.

[105] Paul J. Flory. Molecular size distribution in three dimensional polymers. I. Gelation. *J. Am. Chem. Soc.*, 63(11):3083–3090, 1941.

[106] Paul J. Flory. Molecular size distribution in three dimensional polymers. II. Trifunctional branching units. *J. Am. Chem. Soc.*, 63(11):3091–3096, 1941.

[107] Paul J. Flory. Molecular size distribution in three dimensional polymers. III. Tetrafunctional branching units. *J. Am. Chem. Soc.*, 63(11):3096–3100, 1941.

[108] Z V Djordjevic, H E Stanley, and A Margolina. Site percolation threshold for honeycomb and square lattices. *Journal of Physics A: Mathematical and General*, 15(8):L405, 1982.

[109] M. F. Sykes and J. W. Essam. Exact critical percolation probabilities for site and bond problems in two dimensions. *Journal of Mathematical Physics*, 5(8):1117–1127, 1964.

[110] Duncan S. Callaway, M. E. J. Newman, Steven H. Strogatz, and Duncan J. Watts. Network robustness and fragility: Percolation on random graphs. *Phys. Rev. Lett.*, 85:5468–5471, Dec 2000.

[111] R. van der Hofstad. Percolation and random graphs. In Ilya Molchanov and Wilfrid Kendall, editors, *New Perspectives on Stochastic Geometry*, chapter 6, pages 173–247. Oxford University Press, 2010. ISBN 978-0-19-923257-4.

[112] Jean-Baptiste Gouéré. Subcritical regimes in the poisson boolean model of continuum percolation. *Ann. Probab.*, 36:1209–1220, 2008.

[113] J W Essam. Percolation theory. *Reports on Progress in Physics*, 43(7):833, 1980.

[114] SG Whittington and CE Soteros. Lattice animals: Rigorous results and wild guesses. *Disorder in Physical Systems*, pages 323–335, 1990.

[115] J. Theodore Cox, Alberto Gandolfi, Philip S. Griffin, and Harry Kesten. Greedy lattice animals i: Upper bounds. *The Annals of Applied Probability*, 3(4):pp. 1151–1169, 1993.

[116] Mireille Bousquet-Mlou and Andrew Rechnitzer. Lattice animals and heaps of dimers. *Discrete Mathematics*, 258(13):235 – 274, 2002.

[117] Mireille Bousquet-Mlou. New enumerative results on two-dimensional directed animals. *Discrete Mathematics*, 180(13):73 – 106, 1998. Proceedings of the 7th Conference on Formal Power Series and Algebraic Combinatorics.

[118] Mireille Bousquet-Mlou. Percolation models and animals. *European Journal of Combinatorics*, 17(4):343 – 369, 1996.

[119] Alan Hammond. A lattice animal approach to percolation. arXiv:math/0402026v1.

[120] Alan Hammond. Critical exponents in percolation via lat-tice animals. *Electronic Communications in Probability*, 10:45–59, 2005.

[121] Jens Feder. Random sequential adsorption. *Journal of Theoretical Biology*, 87(2):237 – 254, 1980.

[122] J. W. Evans. Random and cooperative sequential adsorption. *Rev. Mod. Phys.*, 65:1281–1329, Oct 1993.

[123] J.J. Ramsden. Review of new experimental techniques for investigating random sequential adsorption. *Journal of Statistical Physics*, 73(5-6):853–877, 1993.

[124] J. Talbot, G. Tarjus, P.R. Van Tassel, and P. Viot. From car parking to protein adsorption: an overview of sequential adsorption processes. *Colloids and Surfaces A: Physicochemical and Engineering Aspects*, 165(13):287 – 324, 2000.

[125] Brian Karrer, M. E. J. Newman, and Lenka Zdeborova. Percolation on sparse networks. unpublished, 2014.

[126] Gerald D Mahan. *Many particle physics*. Springer, 2000.

[127] Michael E Peskin and Daniel V Schroeder. *An introduction to quantum field theory*. Westview, 1995.

[128] D. Mathis and E. Lieb. Exact solution of a many-fermion systemand its associated boson field. *Journal of Mathematical Physics*, 6:304–312, 1965.

[129] A. Luther and Peschel I. Single-particle states, kohn anomaly, and pairing fluctuations in one dimension. *Physical Review B*, 9:2911–2919, 1974.

[130] V. J. Emery, A. Luther, and I. Peschel. Solution of the one-dimensional electron gas on a lattice. *Physical Review B*, 13:1272–1276, 1976.

[131] David Senechal. An introduction to bosonization. In *Theoretical Methods for Strongly Correlated Electrons*, pages 139–186. Springer, 2004.

[132] Michael P Marder. *Condensed matter physics*. John Wiley & Sons, 2010.

[133] H.P Breuer and M Holthaus. A semiclassical theory of quasienergies and floquet wave functions. *Annals of Physics*, 211(2):249 – 291, 1991.

[134] Alwyn C Scott, FYF Chu, and David W McLaughlin. The soliton: a new concept in applied science. *Proceedings of the IEEE*, 61(10):1443–1483, 1973.

[135] A. Barone, F. Esposito, C.J. Magee, and A.C. Scott. Theory and applications of the sine-gordon equation. *La Rivista del Nuovo Cimento*, 1(2):227–267, 1971.

[136] Oleg M Braun and Yuri S Kivshar. Nonlinear dynamics of the frenkel–kontorova model. *Physics Reports*, 306(1):1–108, 1998.

[137] Oleg M. Braun and Yuri S. Kivshar. Nonlinear dynamics of the frenkel-kontorova model with impurities. *Phys. Rev. B*, 43:1060–1073, Jan 1991.

[138] S. Mandelstam. Soliton operators for the quantized sine-gordon equation. *Phys. Rev. D*, 11:3026–3030, May 1975.

[139] Bo-Sture K. Skagerstam. Generalized quantum sine-gordon equation and its relation to the thirring model in quantum field theory. *Phys. Rev. D*, 13:2827–2831, May 1976.

[140] R. Heidenreich, B. Schroer, R. Seiler, and D. Uhlenbrock. The sine-gordon equation and the one-dimensional electron gas. *Physics Letters A*, 54(2):119 – 122, 1975.

[141] F. D. M. Haldane. Nonlinear field theory of large-spin heisenberg antiferromagnets: Semiclassically quantized solitons of the one-dimensional easy-axis néel state. *Phys. Rev. Lett.*, 50:1153–1156, Apr 1983.

[142] L. Šamaj and Z. Bajnok. *Introduction to the Statistical Physics of Integrable Many-body Systems*. Cambridge University Press, 2013.

[143] Eugene Demler and Andrei Maltsev. Semiclassical solitons in strongly correlated systems of ultracold bosonic atoms in optical lattices. *Annals of Physics*, 326(7):1775–1805, 2011.

[144] N. Manton and P. Sutcliffe. *Topological Solitons*. Cambridge Monographs on Mathematical Physics. Cambridge University Press, 2004.

[145] Ying Ran, Ashvin Vishwanath, and Dung-Hai Lee. Spin-charge separated solitons in a topological band insulator. *Phys. Rev. Lett.*, 101:086801, Aug 2008.

[146] Yuri S. Kivshar and Boris A. Malomed. Dynamics of solitons in nearly integrable systems. *Rev. Mod. Phys.*, 61:763–915, Oct 1989.

[147] Yuri S Kivshar and Karl H Spatschek. Nonlinear dynamics and solitons in the presence of rapidly varying periodic perturbations. *Chaos, Solitons & Fractals*, 5(12):2551–2569, 1995.

[148] Franz G. Mertens, Niurka R. Quintero, and A. R. Bishop. Nonlinear schrdinger solitons oscillate under a constant external force. *Phys. Rev. E*, 87:032917, Mar 2013.

[149] Vadim Zharnitsky, Igor Mitkov, and Niels Grønbech-Jensen. π kinks in strongly ac driven sine-gordon systems. *Physical Review E*, 58(1):R52, 1998.

[150] Niurka R Quintero and Angel Sánchez. ac driven sine-gordon solitons: dynamics and stability. *The European Physical Journal B-Condensed Matter and Complex Systems*, 6(1):133–142, 1998.

[151] Niels Grnbech-Jensen and Yuri S. Kivshar. Inverted kinks in ac driven damped sine-gordon chains. *Physics Letters A*, 171(56):338 – 343, 1992.

[152] M. B. Fogel, S. E. Trullinger, A. R. Bishop, and J. A. Krumhansl. Dynamics of sine-gordon solitons in the presence of perturbations. *Phys. Rev. B*, 15:1578–1592, Feb 1977.

[153] M. Bttiker and H. Thomas. Periodic and solitary states of the driven sine-gordon chain. *Physics Letters A*, 77(5):372 – 374, 1980.

[154] AR Bishop and PS Lomdahl. Nonlinear dynamics in driven, damped sine-gordon systems. *Physica D: Nonlinear Phenomena*, 18(1):54–66, 1986.

[155] Yuri S. Kivshar, Niels Gro/nbech-Jensen, and Mogens R. Samuelsen. π kinks in a parametrically driven sine-gordon chain. *Phys. Rev. B*, 45:7789–7794, Apr 1992.

[156] Gert Eilenberger. *Solitons: mathematical methods for physicists*, volume 19 of *Solid-State Sciences*. Springer-Verlag, 1981.

[157] Sidney Coleman. Quantum sine-gordon equation as the massive thirring model. *Physical Review D*, 11(8):2088, 1975.

[158] Kathleen E Hamilton, Alexey A Kovalev, Amrit De, and Leonid P Pryadko. Continuous third harmonic generation in a terahertz driven modulated nanowire. *arXiv preprint arXiv:1303.2275*, 2013.

[159] V. A. Yakovlev. *Sov. Phys.-Solid State*, 3, 1961.

[160] V. A. Yakovlev. *Sov. Phys. JETP - USSR*, 13, 1961.

[161] L. V. Keldysh. *Sov. Phys. JETP-USSR*, 16, 1963.

[162] G. H. Wannier. Dynamics of band electrons in electric and magnetic fields. *Rev. Mod. Phys.*, 34, 1962.

[163] Hidetoshi Fukuyama, Robert A. Bari, and Hans C. Fogedby. Tightly bound electrons in a uniform electric field. *Phys. Rev. B*, 8:5579–5586, Dec 1973.

[164] C. Waschke, H. G. Roskos, R. Schwedler, K. Leo, H. Kurz, and K. Köhler. Coherent submillimeter-wave emission from bloch oscillations in a semiconductor superlattice. *Phys. Rev. Lett.*, 70, 1993.

[165] E. E. Mendez and G. Bastard. Wannier-stark ladders and bloch oscillations in superlattices. *Physics Today*, 46, 1993.

[166] M. Ben Dahan, E. Peik, J. Reichel, Y. Castin, and C. Salomon. *Phys. Rev. Lett.*, 76, 1996.

[167] T. Pertsch, P. Dannberg, W. Elflein, A. Bräuer, and F. Lederer. *Phys. Rev. Lett.*, 83, 1999.

[168] R. Morandotti, U. Peschel, J. S. Aitchison, H. S. Eisenberg, and Y. Silberberg. Experimental observation of linear and nonlinear optical bloch oscillations. *Phys. Rev. Lett.*, 83:4756–4759, Dec 1999.

[169] Demetrios N Christodoulides, Falk Lederer, and Yaron Silberberg. Discretizing light behaviour in linear and nonlinear waveguide lattices. *Nature*, 424(6950):817–823, 2003.

[170] Ashish Kumar Gupta, Ofir E. Alon, and Nimrod Moiseyev. Generation and control of high-order harmonics by the interaction of an infrared laser with a thin graphite layer. *Phys. Rev. B*, 68:205101, Nov 2003.

[171] D. Golde, T. Meier, and S. W. Koch. High harmonics generated in semiconductor nanostructures by the coupled dynamics of optical inter-and intraband excitations. *Phys. Rev. B*, 77, 2008.

[172] L. Esaki and R. Tsu. Superlattice and negative differential conductivity in semiconductors. *IBM Journal of Research and Development*, 14, 1970.

[173] M. Holthaus. Collapse of minibands in far-infrared irradiated superlattices. *Physical Review Letters*, 69, 1992.

[174] A. Wacker. Semiconductor superlattices: a model system for nonlinear transport. *Physics Reports*, 357, 2002.

[175] G. Platero and R. Aguado. Photon-assisted transport in semiconductor nanostructures. *Physics Reports*, 395, 2004.

[176] C. Wanke, M., A. G. Markelz, K. Unterrainer, S. J. Allen, and R. Bhatt. Hot carriers in semiconductors. Plenum Press: New York, 1996.

[177] X. L. Lei. Current suppression and harmonic generation by intense terahertz fields in semiconductor superlattices. *Journal of Applied Physics*, 82(2):718–721, Jul 1997.

[178] F. Grossmann, T. Dittrich, P. Jung, and P. Hänggi. Coherent destruction of tunneling. *Phys. Rev. Lett.*, 67, 1991.

[179] A. Kamenev. Nanoscopic quantum transport. Lectures notes for 2004 Les Houches Summer School on Nanoscopic Quantum Transport. 2004.

[180] P. L. DeVries. Calculation of harmonic generation during the multiphoton ionization of the hydrogen atom. *J. Opt. Soc. Am. B*, 7, 1990.

[181] C. J. Joachain, N. J. Kylstra, and R. M. Potvliege. *Atoms in Intense Laser Fields*. Cambridge University Press: Cambridge, UK, 2011.

[182] O. V. Konstantinov and V. I. Perel. *Zh. Exp. Teor. Fiz.*, 39, 1960.

[183] L. P. Pryadko and P. Sengupta. Quantum kinetics of an open system in the presence of periodic refocusing fields. *Phys. Rev. B*, 73:085321, 2006.

[184] L. P. Kadanoff and G. Baym. *Quantum Statistical Mechanics*. Benjamin: New York, 1962.

[185] P. Lipavský, V. Špička, and B. Velický. Generalized kadanoff-baym ansatz for deriving quantum transport equations. *Physical Review B*, 34, 1986.

[186] M. T. Bjork, B. J. Ohlsson, T. Sass, A. I. Persson, C. Thelander, M. H. Magnusson, K. Deppert, L. R. Wallenberg, and L. Samuelson. One-dimensional heterostructures in semiconductor nanowhiskers. *Applied Physics Letters*, 80, 2002.

[187] M. D. Moreira, P. Venezuela, and R. H. Miwa. Inp and inas nanowires hetero-and homojunctions: energetic stability and electronic properties. *Nanotechnology*, 21, 2010.

[188] C. Thelander, M. T. Björk, M. W. Larsson, A. E. Hansen, L. R. Wallenberg, and L. Samuelson. Electron transport in inas nanowires and heterostructure nanowire devices. *Solid State Communications*, 131, 2004.

[189] K. Hashimoto. Zeta functions of finite graphs and representations of p-adic groups. In K. Hashimoto and Y. Namikawa, editors, *Automorphic Forms and Geometry of Arithmetic Varieties*, volume 15 of *Advanced Studies in Pure Mathematics*, pages 211–280. Kinokuniya, Tokyo, 1989.

[190] F. Harary. *Graph Theory*. Addison-Wesley Series in Mathematics. Addison-Wesley Longman, Incorporated, 1969.

[191] Kathleen E. Hamilton and Leonid P. Pryadko. Tight lower bound for percolation threshold on a quasi-regular graph. unpublished, 2014.

[192] Réka Albert, Hawoong Jeong, and Albert-László Barabási. Error and attack tolerance of complex networks. *Nature*, 406:378–382, 2000.

[193] Réka Albert and Albert-László Barabási. Statistical mechanics of complex networks. *Rev. Mod. Phys.*, 74:47–97, Jan 2002.

[194] Katy Börner, Soma Sanyal, and Alessandro Vespignani. Network science. *Annual Review of Information Science and Technology*, 41(1):537–607, 2007.

[195] Leon Danon, Ashley P. Ford, Thomas House, Chris P. Jewell, Matt J. Keeling, Gareth O. Roberts, Joshua V. Ross, and Matthew C. Vernon. Networks and the epidemiology of infectious disease. *Interdisciplinary Perspectives on Infectious Diseases*, 2011:284909, 2011.

[196] Luciano da Fontoura Costa, Osvaldo N. Oliveira, Gonzalo Travieso, Francisco Aparecido Rodrigues, Paulino Ribeiro Villas Boas, Lucas Antiqueira, Matheus Palhares Viana, and Luis Enrique Correa Rocha. Analyzing and modeling real-world phenomena with complex networks: a survey of applications. *Advances in Physics*, 60(3):329–412, 2011.

[197] A. A. Kovalev and L. P. Pryadko. Fault tolerance of quantum low-density parity check codes with sublinear distance scaling. *Phys. Rev. A*, 87:020304(R), Feb 2013.

[198] M. Gordon. Good's theory of cascade processes applied to the statistics of polymer distributions. *Proceedings of the Royal Society of London. Series A. Mathematical and Physical Sciences*, 268(1333):240–256, 1962.

[199] Michael Molloy and Bruce Reed. A critical point for random graphs with a given degree sequence. *Random structures & algorithms*, 6(2-3):161–180, 1995.

[200] Reuven Cohen, Keren Erez, Daniel ben Avraham, and Shlomo Havlin. Resilience of the internet to random breakdowns. *Phys. Rev. Lett.*, 85:4626–4628, Nov 2000.

[201] M. E. J. Newman, S. H. Strogatz, and D. J. Watts. Random graphs with arbitrary degree distributions and their applications. *Phys. Rev. E*, 64:026118, Jul 2001.

[202] Romualdo Pastor-Satorras, Alexei Vázquez, and Alessandro Vespignani. Dynamical and correlation properties of the internet. *Phys. Rev. Lett.*, 87:258701, Nov 2001.

[203] A. V. Goltsev, S. N. Dorogovtsev, and J. F. F. Mendes. Percolation on correlated networks. *Phys. Rev. E*, 78:051105, Nov 2008.

[204] M. E. J. Newman. Random graphs with clustering. *Phys. Rev. Lett.*, 103:058701, Jul 2009.

[205] A. Niño and C. Muñoz Caro. Quantitative modeling of degree-degree correlation in complex networks. *Phys. Rev. E*, 88:032805, Sep 2013.

[206] Itai Benjamini and Oded Schramm. Percolation beyond z^d, many questions and a few answers. *Electronic Communications in Probability*, 1:71–82, 1996.

[207] J. M. Hammersley. Comparison of atom and bond percolation processes. *J. Math. Phys.*, 2:728, 1961.

[208] Béla Bollobás, Christian Borgs, Jennifer Chayes, and Oliver Riordan. Percolation on dense graph sequences. *The Annals of Probability*, 38(1):150–183, 2010.

[209] Motoko Kotani and Toshikazu Sunada. Zeta functions of finite graphs. *J. Math. Sci. Univ. Tokyo*, 7(1):7–25, 2000.

[210] O. Perron. Zur theorie der matrizen. *Math. Ann.*, 64:248–263, 1907.

[211] G. Frobenius. Über Matrizen aus nicht negativen elementen. *Sitzungsber. Königl. Preuss. Akad. Wiss.*, pages 456–477, 1912.

[212] Carl Meyer. *Matrix analysis and applied linear algebra*, chapter 8. SIAM, 2000.

[213] Juan G. Restrepo, Edward Ott, and Brian R. Hunt. Weighted percolation on directed networks. *Phys. Rev. Lett.*, 100:058701, Feb 2008.

[214] M. Newman. *Networks: An Introduction*. OUP Oxford, 2010.

[215] Imre Derényi, Gergely Palla, and Tamás Vicsek. Clique percolation in random networks. *Phys. Rev. Lett.*, 94:160202, Apr 2005.

[216] Ronald Meester. *Continuum percolation*. Number 119. Cambridge University Press, 1996.

[217] Peter Hall. On continuum percolation. *The Annals of Probability*, pages 1250–1266, 1985.

[218] Ronald Meester, Rahul Roy, and Anish Sarkar. Nonuniversality and continuity of the critical covered volume fraction in continuum percolation. *Journal of Statistical Physics*, 75(1-2):123–134, 1994.